# DEVELOPMENT AND ENHANCEMENT OF VARIOUS MECHANICAL OSCILLATORS FOR APPLICATION IN VIBRATIONAL ENERGY HARVESTING

Malcolm McRobb

A thesis for the degree of Doctor of Philosophy (PhD)

Submitted to the College of Science and Engineering,
University of Glasgow

January 2014

[This page is intentionally blank]

"If knowledge can create problems, it is not through ignorance that we can solve them."

ISAAC ASIMOV

(1920 - 1992)

# Acknowledgements

First and foremost, I would like to express my deepest thanks to Professor Matthew Cartmell for all his support and encouragement throughout the course of my research. I feel very privileged to have been given the opportunity to work with such a brilliant academic, and sincere person. I would also like to thank Calum Cossar for his great support along the way too, and for providing invaluable insight into the field of electrical generators and power conversion technologies, all of which has worked its way into my research in some form or another. And to Christopher Murray, who had the misfortune of sharing an office with me, and who was constantly subjected to a plethora of questions over the years. Despite the undoubtedly irritating nature of many of these, which according to Chris could always be solved with the magical use of "*vectors*", he was always willing to take the time to help.

Ultimately, however, it is with the support of my closest friends and family that has made it possible for me to struggle through and come out at the other side. I thank each and every one of them for this, especially my wife, who has witnessed the whole process from beginning to end. All her patience, love and support makes me realise just how lucky I truly am to have her in my life.

Finally, to my darling Mother who is responsible for setting me on this path.....what shall we race for next?

# Abstract

The context of this thesis surrounds the development and study of the effectiveness of three mechanical-to-electrical energy converter concepts that are based upon oscillatory systems with a view of discovering techniques to enhance their normal functioning throughputs.

The field of energy harvesting has experienced significant growth over recent years with the increased popularity of portable electronic devices and wireless sensors. However, with demand, so too rises the need for increased operating lifetimes not only for extended use for some personal devices, but also to reduce the frequency of periodic battery replacements for remote sensors that may be deployed in potentially hazardous environments.

In light of this need, the proceeding chapters will discuss the development of three conceptual energy harvesters. The first is based upon a simple Euler strut that is intended to harvest known steady-state periodic vibrations applied axially to the beam. The assumption here is that the periodic vibrations would arise from ambient conditions, whether naturally occurring or as a form of waste energy from man-made structures. This concept has built into it the facility to apply a static axial pre-load with which, it will be shown, can be used to passively enhance the energy throughput of the device.

However, it will also be shown that the periodic concept has an inherent sensitivity to excitation frequencies, where even minor shifts can result in significantly reduce outputs. To this end, the second harvester was proposed to relieve this limitation by instead harvesting stochastic inputs. With this in mind, the new concept is again based upon a simple and realisable Euler strut but with the stochastic input applied laterally to the supporting structure. By retaining the facility to apply both static and

dynamic axial loads, it will be shown that the cumulative effects of the deterministic and stochastic input can be manipulated to actively enhance the throughput of this system also. However, given the active nature of this form of control that will consume work during its implementation, an approach for ensuring that the net energy will be reduced by this additional work will be discussed. In this way, a conservative estimate of the harvestable energy may be made.

The final energy harvester to be discussed is based upon a planar pendulum that can integrate mechanical accelerations out of the full three degrees of freedom realisable by planar constructs. This begins with the development of a suitable approach to applying rotational excitations to the device, followed by the development of a set of loading terms used to represent the resistive torque that would be exerted upon the system by a suitable power take-off device. This is followed by a comprehensive parameter study of the proposed concept with a mindset towards optimising the operational performance of the device.

# Keywords

Absolute frame of reference
Body frame of reference
Coupled excitations
Decoupled excitations
Deterministic
Dynamic axial load
Enhanced energy throughput
Euler strut
Fourier series approximation
Harmonic solutions
Harvestable energy
Instantaneous power
Mechanical oscillator
Nonlinear
Numerical simulations
Operational bandwidth
Periodic excitation
Planar pendulum
Power take-off
Pre-curvature
Principle parametric resonance
Rectified response
Response trajectory
Rotational excitation
Static axial load
Stochastic resonance
Translational excitation
Torque
Vibrational energy harvesting

# Abbreviations

| | |
|---|---|
| CHAD | Central Hub And Daughter sections |
| DSM | Data Storage Module |
| IMU | Inertial Measurement Unit |
| MEMS | Micro Electro-Mechanical Systems |
| PPR | Principle Parametric Resonance |
| PV | Photovoltaic |
| SR | Stochastic Resonance |
| TEG | Thermo Electric Generator |

# Contents

# List of Tables

# List of Figures

# Nomenclature

| | |
|---|---|
| $a$ | static displacement |
| $A$ | cross sectional area |
| $c$ | linear viscous damping |
| $E$ | Young's modulus |
| $E(t)$ | instantaneous energy |
| $E_{acc}$ | accumulated energy |
| $E_{total}(t)$ | total energy |
| $f$ | dynamic displacement |
| $g$ | gravity |
| $I$ | second moment of area |
| $k$ | fundamental stiffness |
| $l$ | length |
| $L_{Fourier}$ | external load |
| $L_{square}$ | external load |
| $m$ | mass |
| $M$ | bending moment |
| $N(t)$ | stochastic input |
| $OXZ$ | absolute frame of reference |
| $P(t)$ | instantaneous power |
| $P_{crit}$ | critical buckling load |
| $P_{dynamic}(t)$ | dynamic axial load |
| $P_{net}(t)$ | instantaneous net power |
| $P_{static}$ | static axial load |
| $pxz$ | body frame of reference |
| $p'x'z'$ | secondary body frame of reference |
| $q$ | additional load per unit length |
| $Q_\phi$ | generalised force |
| $t$ | time |
| $t_n$ | end time |
| $t_0$ | start time |
| $T$ | kinetic energy |
| $T_0$ | external torque |
| $T_1$ | external torque |
| $T_p$ | external torque |
| $u(t)$ | horizontal translation |
| $U$ | potential energy |
| $U_0$ | magnitude of horizontal excitation |

| | |
|---|---|
| $v(t)$ | dynamic lateral displacement as measured from initial unstressed pre-curvature |
| $v_{static}$ | unstressed pre-curvature position |
| $V(f)$ | effective potential |
| $w(t)$ | vertical translation |
| $W_0$ | magnitude of vertical excitation |
| $x$ | longitudinal position |
| $\alpha$ | phase angle |
| $\delta$ | user quantity selecting work done |
| $\delta_a$ | definition of $\delta$ by McInnes *et al* (2008) |
| $\delta_a$ | definition of $\delta$ by the author |
| $\zeta$ | damping ratio |
| $\lambda(t)$ | rotational excitation |
| $\lambda_0$ | magnitude of rotational excitation |
| $\xi$ | damping ratio |
| $\rho$ | density |
| $\tau$ | torque generated by gravity acting upon an end mass |
| $\phi(t)$ | angular displacement |
| $\dot{\phi}(t)$ | average angular velocity |
| $\psi_{noise}$ | average magnitude of white noise |
| $\omega_n$ | fundamental natural frequency |
| $\Omega$ | modulating/excitation frequency |
| $\Omega_u$ | horizontal excitation frequency |
| $\Omega_w$ | vertical excitation frequency |
| $\Omega_\lambda$ | rotational excitation frequency |

# Chapter 1

# Introduction

Modern conjecture reserves the use of the term *energy harvesting* or *energy scavenging* to describe the process by which energy is harvested from ambient resources such as wind, solar radiation, thermal gradients and vibrations/motions to be either stored or used directly to power low-energy electronics (typically in the microwatt region). This field has seen considerable interest in recent years due to advances in wireless and micro electro-mechanical systems (*MEMS*) technology that has driven the demand for a new age of portable electronics and wireless sensors. However, the conventional power supply for such devices has thus far typically come from batteries which have to be incorporated into the design of said device. Batteries present a number of fundamental problems that researchers have long sought to overcome, namely, they restrict miniaturisation and have an inherent finite lifespan that once consumed, requires either recharging or disposal (leading often to the release of toxic chemicals into landfill sites).

To put this into perspective, consider batteries as the power supply for a wireless sensor node that is deployed in a remote, possibly hostile location. Once the stored energy within the battery has been depleted, there is often no option but to recover the device physically to replace the power supply, often at great inconvenience and significant costs [1–4]. Consider also the rising consumer trend to produce portable devices that are smaller and lighter with increased battery lives. It is often the battery power supply for these devices that accounts for the majority of the volume and mass [5] and still, with each technological iteration that inevitably supports greater processing

powers (consuming more power) the demand for extended battery life increases also [3]. Addressing these concerns, modern energy harvesting techniques now offer a method for autonomous battery recharging and in some situations even eliminate the need for batteries altogether, thus indefinitely extending the lifetime of these devices [6].

Strictly speaking however, energy harvesting on the macro-scale (or *energy conversion* as it shall be referred to as) has been exploited by humans for centuries if one considers the use of watermills and windmills [5, 7]. In these situations the mechanical energy from the flow of water in a river, or the wind across a field, was captured and put to serviceable use for simple tasks such as the grinding of flour and crushing ore that would normally required considerable physical effort. Today, this practice has advanced considerably to include devices capable of harnessing natural renewable resources such as biomass, wind, geothermal, solar, hydropower etc. [8] to be converted into useful electrical power typically in the range of kilowatts to gigawatts [8–10]. These are usually referred to as *renewable energy* devices and are considered vital in the effort to address the effects that carbon emissions from burning fossil fuels is having upon the $CO_2$ levels within the atmosphere (whilst providing an alternative power supply in light of ever increasing fuel and energy prices) [11, 12].

The following thesis will explore and develop a number of energy harvesting strategies aimed at converting mechanical accelerations from ambient conditions. To this end, the first body of work deals with the proposal and development of an Euler strut based energy harvester that can be excited axially by *known* steady-state periodic vibrations. Initially this system exists in a uni-stable state, but it will be shown that with the careful application of a static axial load, a pre-curvature can be applied to the beam. The result of this is a bistable system that, if controlled properly, can cause the periodic vibrations to initiate regular jumps between both potential wells such that the response will be greatly enhanced. This would be considered a form of *passive* control and would not therefore require continual power to maintain the enhanced state of performance.

However, as will be shown, such a device will be inherently sensitive to excitation frequencies, and if these were prone to drift then the response of the system may become compromised. This effectively limits the potential application of the harvester

to scenarios with known and stable vibrations. In an attempt to relive this limiting sensitivity, effort is then focussed upon the concept of a stochastically resonating device. This is an attractive solution because stochastic vibrations may be more readily available from ambient conditions. Furthermore, the concept only requires minor modifications to the periodically excited Euler strut, where instead the periodic forcing terms are used to *actively* modulate the beam as it is excited laterally by the stochastic input. It will be demonstrated that by forcing the system into a bistable state again with the application of a static pre-load, the coupling behaviour can be manipulated such that the deterministic and stochastic inputs will culminate in a stochastically resonant oscillator. Under such conditions the response of the system is enhanced and the net available energy for harvesting can be greatly offset from the energy required to actively modulate the beam.

The final body of work of the thesis focusses on the development of a novel pendulum-based energy harvester aimed at harvesting the rectified output produced by accelerated motion acting upon the concentrated end mass from the realisable degrees of freedom. This study focusses upon the planar pendulum with the understanding that it can be later expanded into a full spherical pendulum system. First, various approaches for accurately describing rotational excitations of the pendulum are examined, followed by the introduction of a suitable set of external loading terms to represent the resistive torque of a generated by a power take-off device. This is then concluded with a comprehensive parameter study aimed at optimising the energy throughput of the system.

However, prior to the actual thesis research material, it is appropriate to provide an understanding of the broader field of energy harvesting in order to establish a context for the greater discussion. Therefore, the proceeding chapter will briefly explore the fascinating history behind some of the fundamental principles of energy harvesting. This will be followed by a discussion of available energy resources with a review of the state-of-the-art technologies for exploiting these. An emphasis upon vibration/motion based techniques will be given to reflect the topic of this thesis.

## 1.1 A Brief History of the Origins of Energy Harvesting

If we consider the use of energy harvesting to harvest energy in the form of useful electrical power from a natural resource, then the first documented observation of this dates back to 1826 when Thomas Johann Seebeck discovered that a current would be induced in a circuit made of two dissimilar metals which are maintained at different temperatures [7, 13]. This suitably became known as the *Seebeck effect*. Without this discovery and the subsequent development of the *thermoelectric effect* in the proceeding three decades, the field of thermometry, aspects of power generation and even alternative refrigeration (for which thermoelectric cooling is the most established method) may have been setback years. Then in 1911 E. Altenkirch derived the thermoelectric efficiency that paved the way for decades of scientific and technological progress [14].

Not long after Seebeck's discovery, Edmund Becquerel discovered the *photovoltaic effect* in 1839 whilst experimenting with an electrolytic cell comprising of two metal electrodes [7,15,16]. But it was not until 1883 that Charles Fritts had the mind to melt selenium into a thin sheet on a metal substrate and press an silver-leaf on as the top contact. By doing so, Fritts noted that "the current, if not wanted immediately, could be either stored where produced, in storage batteries...or transmitted a distance and there used" [17]. This was perhaps the earliest example of PV technology applied to energy harvesting. The modern era of PV technology arose in 1940 when Russell Ohl at Bell Telephone Laboratories in New Jersey, discovered by accident that a piece of selenium generated a voltage when a flash light was shone onto it [18]. Further investigation led to the development of the *p-n junction* that, together with improvements made in the techniques for preparing selenium material, allowed for huge advancements to be made in solar cell performance throughout the 1950s [7, 17, 18].

Hans Christian Oersted made a discovery in 1820 that an electric current flowing through a wire could exert a influence upon a neighbouring compass needle [19]. This was an early demonstration that an electric current possessed the properties of magnetism and was the driving force behind a decade of rapid research into the

phenomenon by individuals such as Michael Faraday, André-Marie Ampére and James Clerk Maxwell [20]. However, it was not until 1831 that Faraday made the discovered that a moving magnet is also capable of producing an electric current [21] and hence the principle of producing electricity from magnetism, or *electromagnetism*, was born.

The discovery that energy could also be harvested in the form of charge was made in 1880 by the Curie brothers who predicted and proved experimentally that when particular crystals are subjected to a mechanical stress, they exhibit a surface charge [7]. This effect became known as *piezoelectricity*. However, with electromagnetism dominating the markets at the time, it was not until 1921 with the development of quartz crystal stabilised electrical oscillators that major improvements in piezoelectric devices were made. In 1924 radio transmitters with crystal stabilised oscillators were placed into service and by the end of the 1930s all high frequency radio transmitters were built with this technology [22, 23]. However, the strength of piezoelectric devices was made clear in 1946 after the demonstration that barium titanate ceramics, a *ferroelectric*, could be easily fabricated at low costs and be made piezoelectric via an electrical poling process [23].

Electrostatic generators are another method for producing electrical charge, the principles of which we are all made aware of as children with simple experiments involving nylon rods and synthetic cloths (and dare I say it, rubbing a balloon against ones head). Otto von Guericke can be credited as the inventor of the first electrostatic generator in 1663 who achieved charge separation by friction on a rotating sulphur sphere [24]. Variations of his machine were produced throughout the 18th and early 19th century, but in 1775 Alessandro Volta invented a device based upon *electrostatic induction*. This was the principle that later superseded friction based electrostatic generators in the 1860s when August Toepler and Wilhelm Holtz invented plate induction machines [25]. Then in 1883 James Wimshurst built a new generator that was considered the culmination of all induction-based electrostatic generators and played an important role in producing electrical discharges in vacuums and X-rays for radiography and electrotherapy [24, 25].

## 1.2 Resourcing and Exploiting Energy Harvesting

The principles of piezoelectricity, electromagnetism, photovoltaic and thermoelectric effects have all played their part throughout history and yet, still today in their more advanced forms they remain vital to the understanding and advancement of modern energy harvesting. It is the inherent mechanisms behind these principles that have allowed scientists and engineers to developed more effective approaches capable of capturing energy from ambient resources to be transduced into the more useful form of electrical power for either storage or direct exploitation. From Table 1.1, Roundy *et al* (2005) [1] demonstrate how these types of energy harvesting devices compare to other perhaps more established power sources, and provides an indication of the available power there is to be captured from various ambient conditions.

| Power Source | Power ($\mu$W)/cm$^3$ | Energy (Joules)/cm$^3$ | Power ($\mu$W)/cm$^3$/yr | Secondary Storage Required? | Voltage Regulation? |
|---|---|---|---|---|---|
| Primary Battery | N/A | 2880 | 90 | No | No |
| Secondary Battery | N/A | 1080 | 34 | N/A | No |
| Micro Fuel Cell | N/A | 3500 | 110 | Maybe | Maybe |
| Ultracapacitor | N/A | 50-100 | 1.6-3.2 | No | Yes |
| Heat Engine | 1x10$^6$ | 3346 | 106 | Yes | Yes |
| Radioactive ($^{63}$Ni) | 0.52 | 1640 | 0.52 | Yes | Yes |
| Solar (outside) | 15000[A] | N/A | N/A | Usually | Maybe |
| Solar (inside) | 10[A] | N/A | N/A | Usually | Maybe |
| Temperature | 40[A,B] | N/A | N/A | Usually | Maybe |
| Human Power | 330 | N/A | N/A | Yes | Yes |
| Air Flow | 380[C] | N/A | N/A | Yes | Yes |
| Pressure Variation | 17[D] | N/A | N/A | Yes | Yes |
| Vibrations | 375 | N/A | N/A | Yes | Yes |

Table 1.1: Comparisons of energy and power sources as originally reported by Roundy *et al* (2005) [1];
[A] *Measured in power per cm$^2$ instead of power per cm$^3$,*
[B] *Demonstrated from a 5° C temperature differential,*
[C] *Assuming an air velocity of 5m/s and 5% conversion efficiency,*
[D] *Based on 1 cm$^3$ closed volume of He undergoing a 10° C change once a day.*

## 1.3 Energy Harvesting from Temperature Gradients

Thermoelectric generators (TEGs) possess several distinct advantages over other technologies for energy harvesting purposes, including:

- Possess no moving parts (therefore low maintenance and silent in operation).
- High operating life (known to exceed 100,000 hours of steady-state operation).
- Can function in severe environments.
- Do not require any periodic replenishment of materials during operation.

These devices operate in the Seebeck mode where thermoelectric circuits convert thermal energy into electrical energy [26, 27]. A simple construct of a thermocouple is shown in Fig. 1.1, consisting of two pillars made of a thermoelement connected in series by a metallic conducting strip (typically copper) [13, 28]. When a temperature gradient exists between the top and the bottom of the pillars a voltage will develop across points (a) and (b), given by:

$$V = \alpha_1 \Delta \mathrm{T} - \alpha_2 \Delta \mathrm{T} \tag{1.1}$$

where $\alpha_1$ and $\alpha_2$ are the Seebeck coefficients.

In the case where the pillars are made of *p-type* and *n-type* semiconductors in light of their large Seebeck coefficients, opposing doping can be used to make the Seebeck coefficients for each of the pillars themselves opposing. From Eq. 1.1 it can be seen that the effect of this would be to sum the contributions from both pillars to the voltage produced across (a) and (b) [13].

In situations where thermoelectric generators are used for energy harvesting, a large number of thermocouples will be connected electrically in series and thermally

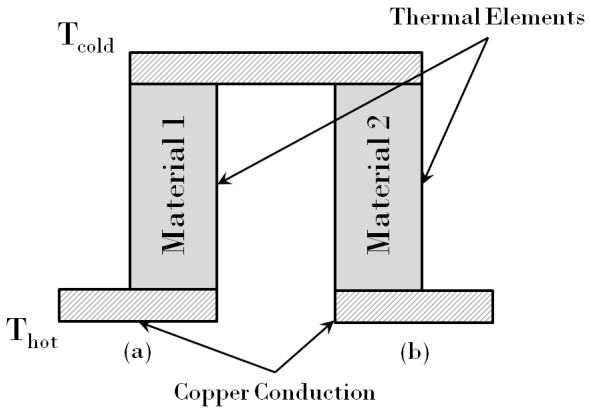


Figure 1.1: Schematics of a simple thermocouple capable of producing voltages in the presence of temperature gradients.

in parallel in order to create a *multicouple thermoelectric module*, or for applications in calorimetry, a *thermopile* [13, 27, 29]. Unfortunately, the relatively low efficiency of typical thermoelectric generators of approximately 5% [27, 30, 31] has limited their use to specialised fields such as the military, medical, remote power and even space applications. However, as cited by Thacher *et al* (2007) [32], interest has been revived in recent years with the development of thin-film quantum well materials used to manufacture thermocouples which boast potential efficiencies of approximately 22-24%. This, together with the realisation that in situations where energy in the form of heat is usually wasted, the low operating efficiency of these devices is no longer an overriding factor.

Yang (2005) [33] goes on to report that for typical gasoline internal combustion engine vehicles, only about 25% of the energy released by the fuel is used for the actual vehicle mobility and accessories, with the remainder lost by waste heat, friction and parasitic losses. An example of the waste heat generated by specific components of a large US army truck diesel engine was reported in [31], originally compiled by Bass *et al* (1991), and which is reproduced in Table 1.2.

| Source | Max' Temp' °C | Power Available kW | Fluid | Flow Rate |
|---|---|---|---|---|
| Radiator | 95.6 | 144 | Coolant | 369 L/min |
| Inter-cooler | 134.4 | 89 | Air | 39 Kg/min |
| Lubricant Oil | 118.3 | 29 | Oil | 123 L/min |
| Turbo Exhaust | 460.0 | 315 | Gas | 40 Kg/min |

Table 1.2: Waste heat inventory of a US Army truck diesel engine (Bass *et al* (1991)).

Recent studies by Thacher *et al* (2007) [32] demonstrated promise in increasing the overall efficiency of automotive engines by harvesting the waste heat of exhausts, but they found this to be highly dependent upon a number of factors including thermal management where insulating the exhaust and lowering the coolant temperature dramatically affected power production. Other limitations include the availabilty of space in the underbody of the vehicle. Indeed, this observation was corroborated by Karri *et al* (2011) [34] who employed a modeling approach in their research and were only able to report 5.3-5.8kW power production under optimised conditions, resulting in fuel savings of approximately 3%.

Of course, it is possible to apply a similar approach for harvesting waste heat, but instead on an industrial scale where available space is not an overriding factor. A review by Riffat *et al* (2003) [27] cited studies undertaken by Yodovard *et al* (2001) [35] to assess the potential to harvest the waste heat generated by diesel cycle and gas turbine cogeneration in factories across Thailand. It was estimated that the diesel cycle and gas turbine cogeneration systems produced electricity at 40% and 30% efficiency, respectively. The useful waste heat from the stack exhaust of these systems was estimated to be approximately 20% for the gas turbines and 10% for the diesel cycles, resulting in a potential net power generation of approximately 100MW.

Riffat *et al* (2003) [27] also highlight the fact that despite advancements in thermoelectric design, these generators still dissipate significant amounts of unconverted heat. The concept of *symbiotic* generation has the potential to address this and fulfil dual purposes; power generation and heat exchanging. A schematic of a symbiotic thermoelectric generator is shown in Fig. 1.2 and works on the premise that the heat which is not transduced into electricity due to inherently low conversion efficiencies, is diverted and used as a preheat instead of simply being discharged to the environment.

In the example of a central heating system in a domestic home, the diverted heat could be used to preheat radiator fluid, thus reducing the work needed by the conventional system to bring the fluid to the desired temperature. This concept of energy-harvesting devices being able to provide multiple functions is an increasing trend, where normally low conversion efficiencies are offset by an increase in functionality.

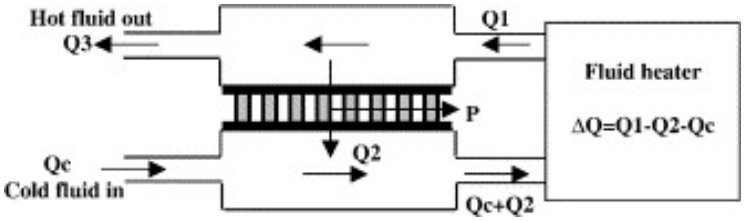


Figure 1.2: An example of a symbiotic thermoelectric generator operating as a fluid preheating/parasitic generation device. Dissipated heat for the thermoelectric generator is used to preheat the fluid [27].

## 1.4 Energy Harvesting of Solar Power

Solar cells are devices that convert solar radiation, or light energy, into electrical energy [36]. In fact, in the realm of renewable energies, the sun possesses the greatest potential of all by delivering approximately 124PW (PW= $10^{15}$Watts) globally to the surface of the Earth. Put into context, this is approximately eight thousand times greater than the total world energy consumed in 2004 [37].

The term used for solar radiation striking a surface is *insolation*, and does of course vary over time across the Earth's surface due to multiple factors; geographical locations (longitude and latitude), localised weather conditions, the distance between the sun and the Earth, and the availability of daylight are to name but a few [36, 38–41].

A photovoltaic (PV) solar electric system can be used to harness this abundant energy source, and in its basic form is made up of individual solar cells. When photons strike a solar cell like the semiconductor P-N junction in Fig. 1.3, they are either reflected, absorbed, or pass straight through the cell. Any absorption of the photon will result in the generation of an electron-hole pair that when separated across the P-N junction, will result in an electric potential difference across the interface [16, 43]

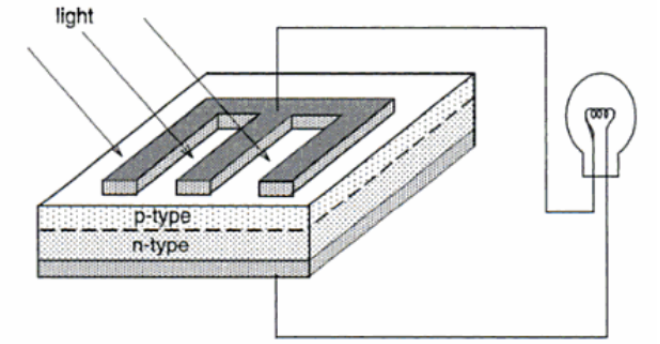


Figure 1.3: A typical solar cell arrangement as originally depicted by Gordon, J. & Society, I. S. E. (2001) [42], with a thin sheet semiconducting material into which the P-N junction has been formed.

and hence is the mechanism by which energy is converted. Each individual PV cell will typically produce half a volt of energy, but by connecting them together in series on the solar panel higher voltages may be generated [44, 45].

A comprehensive review of PV technologies conducted by Chaar *et al* (2011) [45] discussed four current major types of photovoltaic technologies, which are:

- Crystalline
- Thin film
- Compound
- Nanotechnology

The first generation of PVs were made of crystalline structures, the most dominant of which was arguably silicon [36, 37, 43]. Rather than becoming obsolete over the years, Chaar *et al* (2011) [45] report that instead the technology was constantly being developed to increased its capabilities and ultimately its efficiency. This has led to the development of mono-crystalline, poly-crystalline and emitter wrap through cells, all of which fall under the category of silicon based PVs [45].

Thin film technologies are considered as the second generation of PV cells, and are based upon thin layers ($< 10\mu$m thick) of semiconducting materials backed onto a solid material such as glass or stainless steel using sputtering techniques. This has allowed for the amount of semiconducting material to be greatly reduced as compared to silicon

based cells, and so reduces production costs [45, 46] and even opened up the capability of producing flexible PV modules.

Whilst it is true that the thinner layers used in these technologies does lead to less photovoltaic material available to absorb the incoming photons, the ability to deposit on many different materials can in fact lead to improved efficiencies [45]. Barnett *et al* (2001) [47] managed to produce thin film devices with power conversion efficiencies > 19%, which at the time of publication were considered to be the highest independently recorded performances for a thin film silicon layer on a ceramic substrates by utilising light trapping and back-surface passivation approaches [47].

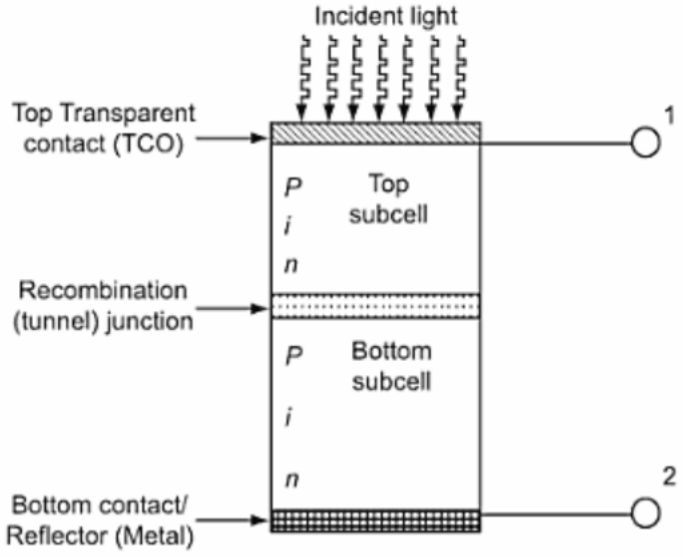


Figure 1.4: Schematic of a multi-junction (dual) solar cell stacked in the P-I-N configuration with two electrical terminals as produced by McEvoy *et al* (2012) [48], where light first enters the top sub-cell and any light remaining enters the below sub-cell. With the two sub-cells being electrically in series, the same current will subsequently circulate through each of them.

Compound solar cells (also know as tandem or multi-junction solar cells) are the evolutionary next step of single-junction cells that have been developed to overcome the relatively low efficiencies and poor stability problems of previous technologies [49]. By stacking crystalline layers with different band gaps in a manner similar to that shown in Fig. 1.4, such devices can be tailored to absorb most of the solar radiation present at the site of deployment. Using this approach, efficiencies as high as 39% have been recorded with gallium arsenide (GaAs)/indium gallium phosphide (InGaP) multiple-junction devices [45]. However, due to the increased complexity of these devices in

both design and manufacture, the associated costs are appropriately increased, but often this will be offset by the gains in operating efficiencies [50].

The inclusion of nanotechnology in PV cells provides methods for enhancing the effective optical paths for photons and decreases the likelihood of charge recombination events (a process that results in the annihilation of free charge carriers in the semiconductor) [51]. They also afford the ability to control the energy band-gap thus providing both flexibility and interchangeability [45] in design. Two types of nanotechnologies that are receiving significant interest are: carbon nanotubes that can be used to increase the surface area able to produce electricity [45]; and quantum dots that are very effective light emitters and can subsequently increase the device efficiency by adapting to the incoming light spectrum [51]. Other branches of nanotechnology are dye-sensitized cells which include photoelectrochemical cells [43], polymer cells and nanocrystal cells, which together with quantum dot technologies are broadly considered as the third generation of photovoltaics [51]. This demonstrates the growing interest in the field of solar energy harvesting and should lead to the technology being adopted for more and more applications.

## 1.5 Energy Harvesting of Vibrations and Motion

Mechanical vibrations are considered by many to be one of the most effective methods for implementing energy harvesting devices [4]. As an ambient energy source, these vibrations and accelerated motions are widely available, easily accessible and often have need of portable or wireless devices. An example of this could be bridges, tunnels or buildings where autonomous structural sensors are required to assess continually the vibration levels and the integrity of the structure whilst at the same time, being powered by those same vibrations, and transmitting data via wireless link for processing [4, 52, 53].

### 1.5.1 Vibration-Based Transducers

A means to recharge or replace batteries that have up until now been the primary power supply for wireless sensors and portable electronics has long been searched for. By employing suitable transducer technology, researchers have been able to build and test mechanical vibration-based generators capable of harvesting ambient vibrations to generate more useful electrical energy. As concluded by Roundy *et al* (2005) [1], the most effective transducer will often depend on the specific application and researchers will often compare these transducers based upon their inherent energy storage density. The three basic types of vibration based transducers have been compared by this method in Table 1.3, and typical characteristics of each of these are listed in Table 1.4.

| Type | Mechanisms Involved | Practical Maximum[A] ($mJ/cm^3$) | Aggressive Maximum[B] ($mJ/cm^3$) |
|---|---|---|---|
| Electromagnetic | A magnet acting as a proof mass passing a coil to induce a voltage. | 24.8 | 400 |
| Piezoelectric | Employs piezoelectric materials capable of converting induced strain into electricity. | 35.4 | 335 |
| Electrostatic | Induces a voltage when the distance or overlap of two electrodes of a polarized capacitor changes as a result of vibrations to the device. | 4 | 44 |

Table 1.3: Vibration-based transducers and their energy storage densities [13, 54, 55];
[A] *what was achievable at time of original publication (2004)*,
[B] *what was considered theoretically possible at time of original publication (2004).*

| Transduction Method | Characteristics |
|---|---|
| Electromagnetic | Well established commercially.<br>High output currents (at the expense of low AC voltages).<br>Output voltage scales down with size.<br>Can be used in a wide variety of spring/mass configurations.<br>Can be made with various materials that have been proven in cyclically stressed applications.<br>Difficult to construct sub-millimetre and wafer scaled devices. |
| Piezoelectric | Considered simplest approach for vibration based applications.<br>Can be used in force and impact-coupled applications.<br>Typically high output impedance levels (>100k$\Omega$).<br>The latter produces high voltages (but with low currents).<br>Current scales down with size.<br>Wide range of available piezoelectric materials.<br>Well suited to microengineering. |
| Electrostatic | Well suited to MEMS applications.<br>Energy density can be increased by decreasing the capacitor spacing.<br>Energy density is decreased by reducing the capacitor surface area.<br>At low frequencies, high transduction damping is achievable with small capacitor gaps and high voltages.<br>Requires the device to oscillate at a magnitude in the region of microns whilst maintaining a minimum capacitive air gap of $\leq$ 0.5$\mu$m.<br>Requires initial polarising voltage or charge.<br>Very high output impedance.<br>High output voltage (>100 V).<br>Risk of stiction or electrode shorting in wafer-scaled applications. |

Table 1.4: Characteristics of the three methods of transduction compiled from studies by S. Roundy (2005) [1] and Beeby *et al* (2006) [56].

### 1.5.2 General Theory of a Resonant Generator

The majority of cases for vibration energy harvesting employ the principle of inertia, irrespective of the chosen transducer. Demonstrating this principle, Fig. 1.5 shows a simple scheme discussed by Williams and Yates (1996) [55], and which is continually referenced throughout the literature including Stephen (2006) [52] and Beeby *et al* (2006) [56]. It depicts a second-order, spring-mass system with a *proof mass*, $m$ (also referred to as the *seismic mass*) suspended by a spring of stiffness, $k$, inside a frame. The frame itself may be fixed to a vibrating source and any displacement of this frame, denoted by *y(t)* that we assume to be of the form $y(t) = Y_0 \sin(\omega t)$, will result in relative motion *z(t)* of the mass with respect to its static equilibrium position. This displacement will be sinusoidal in amplitude and can be used to drive a transducer to convert the kinetic energy into electrical energy. In this scenario the energy losses within the system may comprise of parasitic losses, $c_p$, and the electrical energy extracted by the transducer, $c_e$, which are together represented by a dashpot, $c_t$.

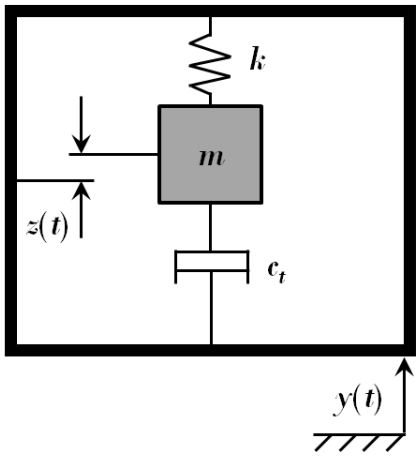


Figure 1.5: Schematic of a vibration based generator.

By assuming that the mass of the vibrating source is significantly greater than the proof mass in Fig. 1.5, and therefore not influenced by its presence, it is possible to derive the differential equation used to describe the motion of the proof mass with respect to the surrounding frame:

$$m\ddot{z}(t) + d\dot{z}(t) + kz(t) = -m\ddot{y}(t) \tag{1.2}$$

The standard steady-state solution for the displacement of the proof mass for this simple *linear* system can be given by:

$$z(t) = \frac{\omega^2}{\sqrt{\left(\frac{k}{m} - \omega^2\right)^2 + \left(\frac{c_t\omega}{m}\right)^2}} Y_0 \sin(\omega t - \phi) \tag{1.3}$$

where $\phi$ is the phase angle given by:

$$\phi = \tan^{-1}\left(\frac{c_t\omega}{(k - \omega^2 m)}\right) \tag{1.4}$$

The force on the proof mass must also be equal to the force, $F$ exerted on the mass-spring-damper, such that:

$$F = -m\ddot{y}(t) \tag{1.5}$$

Next, Williams and Yates (1996) [55] show that the *instantaneous power* transfer in the proof mass, *p(t)* is the product of the force acting upon the mass and its velocity:

$$p(t) = -m\ddot{y}(t)\left[\dot{y}(t) + \dot{z}(t)\right] \tag{1.6}$$

As a consequence of the damping created by the electrical transducer and the parasitic losses, there is a net transfer of mechanical power into electrical power within the system, which is given by [55, 56]:

$$P_d = \frac{m\zeta_t Y_0^2 \left(\frac{\omega}{\omega_n}\right)^3 \omega^3}{\left[1 - \left(\frac{\omega}{\omega_n}\right)^2\right]^2 + \left[2\zeta_t\left(\frac{\omega}{\omega_n}\right)\right]^2} \tag{1.7}$$

where $\zeta_t$ is the *total damping ratio* ($\zeta_t = c_t / 2m\omega_n$), $\omega_n$ is *natural frequency* of the system measured in *radians per second* ($\omega_n = \sqrt{\frac{k}{m}}$), $\omega$ is the forcing frequency and $Y_0$ the amplitude of this forcing.

Fig. 1.6 depicts the typical traits of a linear system where maximum power is generated at resonance, which is to say, when the undamped natural frequency of the mass-spring-damper system is equal to the frequency of vibrations applied to the frame, ($\omega_n = \omega$). It can be seen that even marginal deviations from $\omega_n$ may result in dramatic

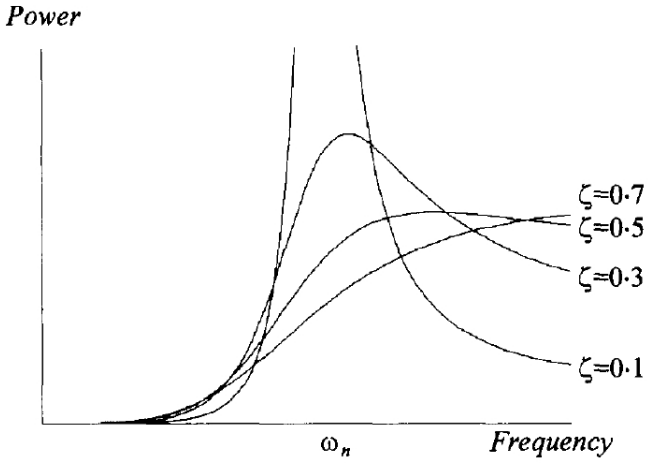


Figure 1.6: Frequency spectrum of power generation for the system in Fig. 1.5 around resonance for various $\zeta_t$, produced by Williams and Yates (1996) [55].

decreases in the throughput of the system.

Perhaps even more telling of observations of Fig. 1.6 is that peak power is achieved with lower damping factors, but with narrower operating bandwidths. Conversely, for higher damping factors the power generated is lower, but the operating bandwidth is extended. Therefore, if the spectra of the vibrating source is well understood and concentrated around a particular frequency, then a low damping ratio will yield optimum performances, whereas if the excitation frequency varies with time, a higher damping ratio would be better suited [52, 55, 56]. Based upon this observation that the maximum power generated occurs at resonance, Eq. 1.7 can be simplified such that:

$$P_d = \frac{m{\omega_n}^3{Y_0}^2}{4\zeta_t} \tag{1.8}$$

As these are steady-state solutions the generated power will not tend towards infinity as the damping ratio tends towards zero. The maximum power that can be extracted by the transducer, $P_e$, can be expressed by including both the parasitic damping ratio and the transducer damping ratio [56]:

$$P_e = \frac{m\zeta_e A^2}{4\omega_n \left(\zeta_p + \zeta_e\right)^2} \tag{1.9}$$

where $A$ is an expression for the excitation acceleration levels, and can be derived from $A = {\omega_n}^2 Y_0$. Note that $P_e$ is maximised when $\zeta_p = \zeta_e$.

Beeby *et al* (2006) [56] make the observation in their review of general resonant generator theory that since the power output is inversely proportional to the natural frequency of the system for a given acceleration, as shown in Eq. 1.9, it will be preferable to operate the generator at the lowest fundamental frequency. This is supported by the fact that acceleration levels of ambient vibration sources tend to reduce with ever increasing frequencies [56]. However, subsequent studies by DuToit and Wardle (2007) [57] have shown that essential features of the coupled electromechanical responses have previously been neglected and that operating at both resonance and antiresonance can result in near identical generated powers. Renno *et al* (2009) [58] developed this further and discovered that for damping ratios well below the bifurcation damping ratio there will exist two power maxima (at resonance and antiresonance) and one minima. Beyond the bifurcation damping ratio only one maxima exists.

### 1.5.3 Tunable Vibration-Based Energy Harvesting

Of course, the ultimate goal of any energy harvester is to transfer as much of the generated power to the electrical load. However, based upon previous observations of linear resonant systems, they all share one common limitation: that truly effective power generation is only really possible when operated at resonance (or in some situations, antiresonance). It has also been shown that the bandwidth of such systems may be very narrow and hence typical harvesters will be particularly sensitive to even minor deviations in excitation frequency that move away from the natural frequency of the device. Therefore, the idea of controlling design parameters has received much attention from many researchers as a way to optimise energy harvesters [58], and indeed to provide some kind of tuning element. However, tuning a generator is only a viable option if the procedure used to actually adjust the resonant frequency consumes less than the average power the device is capable of generating so that a net gain is produced [59, 60].

*Continuous* tuning (or *active* tuning as it is sometimes known as), operates under a continuous power supply in order to achieve the required resonance change by

controlling the effective stiffness, mass or damping. Roundy *et al* (2005) [61] have assessed the feasibility of tuning the resonant frequency of vibration-based generators with this method using actuators and concluded that the continuous tuning mechanism could never prove effective because the continuous power required to tune the resonant frequency will always exceed any resulting increase in output power. However, Zhu *et al* (2010) [62] showed that the approach employed by Roundy *et al* (2005) did not apply to all cases because the *maximum* power for actuation was used rather than the *average* power. In addition to this, only the situation where the tuning force was proportional to the displacement or acceleration of the generator was studied.

Examples of continuous tuning come from Adams *et al* (1998) [63] where electrostatic actuators that behaved analogously to mechanical springs were used to control stiffness of their harvester. Wu *et al* (2006) [64] demonstrated the effect of *impedance matching* (when the load matches the impedance of the generator to achieve maximum power transfer [65]) by using a variable capacitive load that shifted the gain curve of a cantilever beam to match the external vibration frequency in real time.

Conversely, many consider *intermittent* or *passive* tuning to be a more effective approach because it requires only an initial power supply (or some other disturbance) to achieve resonance change [61], thus no continuous power is consumed to maintain a tuned state. This may involve moveable clamps which can change the length (and stiffness) of a flexible structure, a moveable mass, or tensioning of the structure. An approach where axial loads are applied for intermittent tuning have been investigated by many, including Leland and Wright (2006) [66], Hu *et al* (2007) [67] and Zhu *et al* (2010) [68]. Masana and Daqaq (2011) [69] present a particularly interesting example of an intermittently tunable harvester that is relevant to the studies presented in the current thesis. They demonstrated that by applying a static axial load, $P$, to an Euler strut that was clamped on both sides in order to alter the stiffness of the flexural beam (see Fig. 1.7), it was possible to tune the resonant frequency to resonance up to 65% about the untuned frequency. In this particular instance, piezoelectric (PZT) patches were used as the electrical transduction devices whereby the induced mechanical strain would be converted into electricity.

The current thesis will investigate in depth enhanced vibration using a similar Euler

strut setup and it is speculated that the two approaches could perhaps be incorporated in an effective manner.

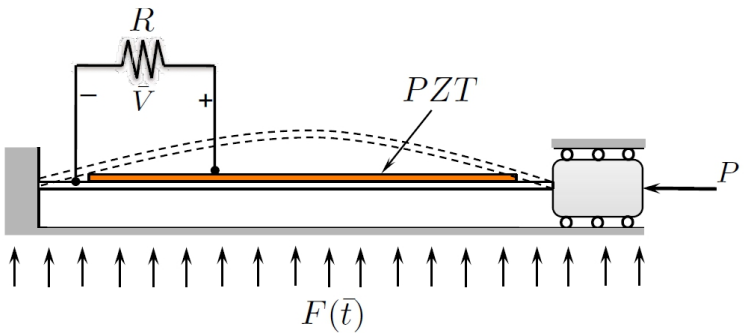


Figure 1.7: Schematic of an axially loaded intermittent tunable vibrational energy harvester proposed by Masana and Daqaq (2011) [69].

*Semi-active* tuning approaches have also been explored, such as that proposed by Challa *et al* (2008) [70], shown in Fig. 1.8. Here, repulsive and attractive forces from permanent magnets are used to alter the stiffness of the cantilevered structure by varying the separation distance between the respective magnets and the tip mass. This approach was shown to provide an operating bandwidth of ±20% about the untuned resonant frequency, producing powers of 240–280 $\mu$W from low level vibrations over the frequency range 22–32 Hz. Later, Challa *et al* (2011) [71] developed their concept further to develop a similar construct capable of tuning autonomously and increased the operating bandwidth from -27% to +22% of the untuned resonant frequency, producing powers peaking at 1mW at 0.1g accelerations for a beam of length=480mm, width=20mm, thickness=0.6mm with an effective mass of 0.0256kg.

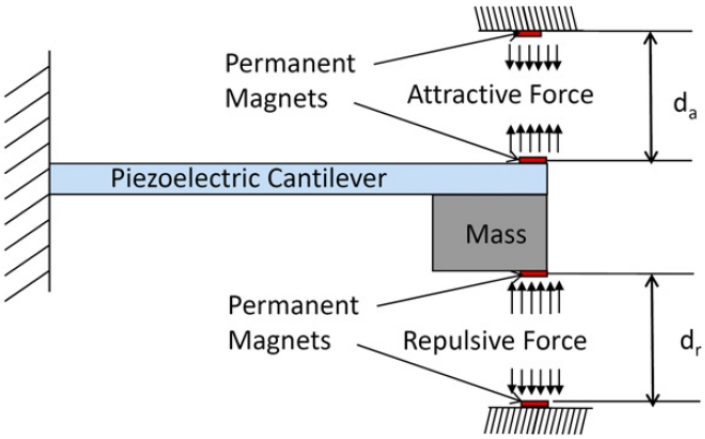


Figure 1.8: Experimental setup for a semi-active tunable energy harvesting device by Challa *et al* (2008) [70].

### 1.5.4 Broadband Vibration-Based Energy Harvesting

Although the approaches developed to tune vibration-based energy harvesters have been shown to be effective, they remain limited by the inherent characteristics of linear systems which exhibit resonance typically only within a narrow frequency range. Therefore, if the excitation frequencies are out with the tunable range of the harvester, or of a time-varying nature (such as noise), then the magnitude of generated power will drop significantly. A solution to this problem has been studied by Sari *et al* (2008) [72] who proposed to extend the bandwidth of their harvester by implementing a number of cantilevered beams of varying lengths that are connected in series to produce a device with an array of natural frequencies. With this approach they have been able to generate energy effectively across a wide range of excitation frequencies (including a bandwidth of 800Hz for the device reported in [72]).

However, research in *nonlinear systems* has demonstrated that by intentionally introducing nonlinearities into the design of a harvester, the short-comings typical of linear systems can be overcome [73–78]. To explain, consider a uni-modal Duffing-type oscillator whose equation of motion may be defined as:

$$\ddot{x} + 2\zeta_t\omega\dot{x} + \omega^2 x + \alpha x^3 = F(t) \tag{1.10}$$

where $\zeta_t$ is the total coefficient of damping, $\alpha$ is a coefficient of stiffness nonlinearity

and $F(t)$ is an external excitation, possibly of the form $F(t) = F_0 \cos \omega t$.

When $\alpha > 0$, a *hardening* nonlinearity is applied to the system which has the effect of bending the steady-state frequency response to the right when excited by a fixed frequency in resonance [79]. When $\alpha < 0$, *softening* nonlinearities will be dominant and are manifested by the steady-state frequency response bending to the left.

Nayfeh and Mook (2008) [80] demonstrate these effects in Fig. 1.9 for a similar Duffing-type oscillator, where again $\alpha$ is the nonlinearity coefficient and $\sigma$ is the excitation frequency. It can be seen that the coupling effect between the excitations and the harvester result in a broadening of the effective bandwidth when under the influence of either forms of stiffness nonlinearity (highlighted in Fig. 1.9(b) and Fig. 1.9(c) by the region with superimposed arrows). A potentially unwelcome by-product of this is that regions where multiple solutions exist are created that can lead to a jump-phenomenon [80].

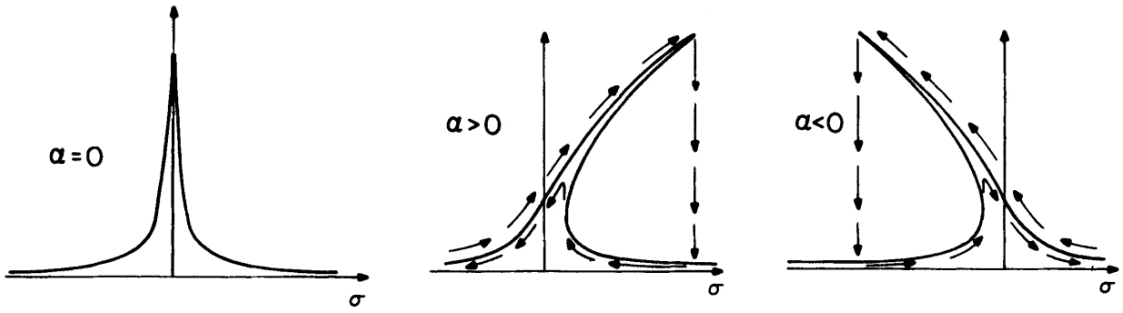


(a) Linear response.

(b) Hardening nonlinear response.

(c) Softening nonlinear response.

Figure 1.9: Frequency response curves depicting the effects of nonlinearities in a Duffing-type oscillator, where $\alpha$ is the nonlinearity coefficient and $\sigma$ is the excitation frequency. Originally produced by Nayfeh and Mook (2008) [80].

Several recent studies [76, 81–83] have investigated the effects of deliberately incorporating nonlinearities in statically *uni-stable* Duffing-type oscillators (a uni-stable device possess only a single potential energy well). Incredibly, Staton *et al* (2009) [82] demonstrated that by introducing softening to a cantilevered harvester, the response was actually able to outperform the linear response of the same system. This observation was conflicting with previous notions that linearly resonating systems represented the upper bound of generated energy. A limitation to this approach is that

it is only suited for excitations that have a slow frequency drift and it has been shown by F. and Daqaq (2010) [79] and Barton *et al* (2010) [84] that, in fact, nonlinearities in uni-stable systems can have an adverse effect when excited by random *coloured* vibrations with different bandwidths and center frequencies. Barton *et al* (2010) [84] observe that in such instances, the existence of low-level and high-level energy states began to average out and that sudden drops in vibrations occurred when the harvester fell into one of these low-level states (requiring some form of disturbance to put it back into a higher energy state).

Lim *et al* (2004) [85] took a different approach to exploiting the effects of nonlinearities. They modelled the dynamics of two coupled oscillators with opposing forms of nonlinearities (softening and hardening) and showed that controlled variation of the softening stiffness in a predominately hard system can mitigate the effects of both nonlinearities to give rise to an approximately linear response with enhanced performances.

Harvesters with a *bistable* energy potential have also been highlighted as a means to enhance the bandwidth and performance of harvesters [69, 83, 86–88]. A bistable system possess two potential energy wells separated by one unstable saddle (*potential barrier*), see Fig. 1.10(a). Inter-well oscillations can be activated when sufficient energy is supplied that allows for the system to jump from one stable energy state to the other [73, 86]. This behaviour can have the effect of extending the bandwidth of the device and to produce large amplitude responses. This is understood for steady-state fixed-frequency excitations, but the performance of such systems when exposed to random excitations of a stochastic nature is still in its infancy and may provide a more realistic representation for numerous naturally occurring environmental vibrations, and indeed will form a topic of discussion within the present thesis.

McInnes *et al* (2008) [90] are considered the first to exploit the role of *stochastic resonance* (SR) as a way to enhance the available power from a bistable vibrational energy harvester. Somewhat counter-intuitive, SR may manifest itself in nonlinear systems where a normally weak signal may be amplified by the assistance of noise. There are three prerequisites to achieving this [89]:

1. Some form of energetic activation barrier such as the potential barrier between

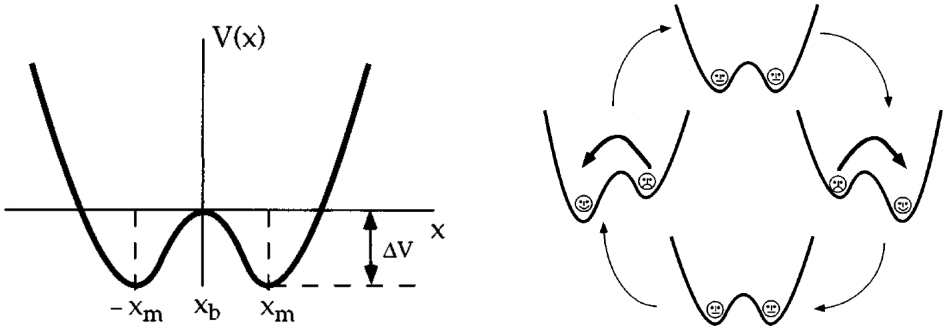


(a) Shape of the potential energy function for a bistable system.

(b) Demonstration of transitions between energy states during stochastic resonance.

Figure 1.10: Shape of the potential energy function in a bistable system suitable for stochastic resonance, originally produced by Gammaitoni *et al* (1998) [89].

two potential wells in a bistable system (see Fig. 1.10(a)).

2. A normally weak but coherent signal (such as a periodic forcing term).

3. A source of noise that is added to the coherent signal (this can be white Gaussian noise, coloured noise and even non-Gaussian noise [91]).

If the system is trapped within one of the potential wells, then the effect of the noise input will excite the dynamics locally with the likelihood of transitions between wells determined by the *Kramers rate* (1940) [89, 92]:

$$r_K = \frac{\omega_0 \omega_b}{2\pi\gamma} \exp\left(-\frac{\Delta \mathrm{V}}{D}\right) \tag{1.11}$$

where $\omega_0$ is the angular frequency of the potential one of the potential minima, $\pm x_m$, $\omega_b$ is the angular frequency at the top of the potential barrier, $x_b$, $\gamma$ is the viscous friction, $D$ is the strength of the noise and $\Delta$V is the height of the potential barrier.

From Eq. 1.11 it can be deduced that with large potential barriers, the likelihood of the system being able to jump from one potential well to the other as a result of noise is reduced. However, if a periodic force is introduced then the bistable wells will be modulated such that the height of the potential barrier will be oscillated (see Fig. 1.10(b)). If the same forcing that is normally too weak to induce a transition between wells on its own has a period equal to the mean time between transitions (inverse

of the Kramers rate) [90], then it will become synchronised with the noise induced hoping events, and thus achieve SR. This will produce large amplitude responses and significantly increase the generated power.

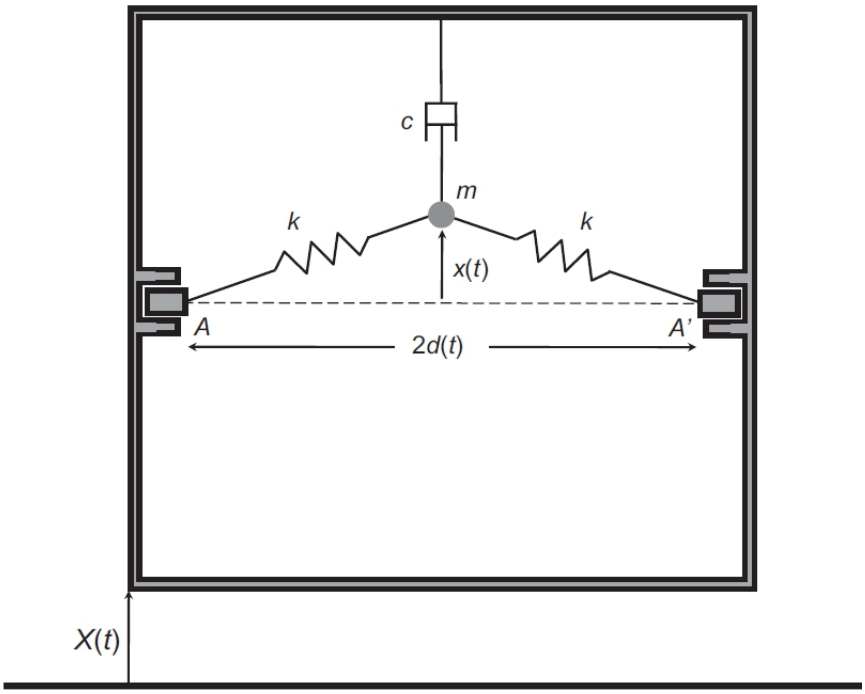


Figure 1.11: Conceptual model of a periodically forced stochastic resonator, proposed by McInnes *et al* (2008) [90].

McInnes *et al* (2008) [90] demonstrated the effectiveness of this approach using a simple conceptual model of a bistable clamped-clamped beam, shown in Fig. 1.11. Since then, many studies have been made into the concept, including by Gammaitoni *et al* (2009) [93], Cottone *et al* (2009) [94] and F. Daqaq (2011) [75], and indeed by the present author as is to be discussed in proceeding chapters.

## 1.6 Summarising Remarks

Now that an overview of energy harvesting has been given, it can be understood that their is great interest in the field the world over. Various techniques to enhance the throughput of vibrational-based devices have been explored, which included a review of stochastically resonant systems in which the response of a system may be significantly improved via the coupling behaviour between a stochastic input and periodic forcing.

Similarly, tuned systems have also been developed that require manipulation of the system to maintain optimum performance, but the main limitation of these approaches lie in that even minor deviations away from resonance can result in significant drops in performance. This is a condition that is difficult to avoid in practice without implementing complicated active or passive tuning techniques.

The proceeding chapters will seek to explore the use of a simple and realisable parametric mechanical construct under two separate regimes for harvesting the ambient vibrational energy from external sources. Firstly, the effectiveness of a parametric Euler strut for harvesting known steady-state periodic vibrations will be explored that will discuss methods for passively tuning the system by applying a static pre-load. This concept was inspired by the early work of Watt and Cartmell (1994) [95] which was pivotal because, to the knowledge of the author, it was the first to demonstrate successfully that a parametric system undergoing principle parametric resonance (PPR) is in fact capable of producing useful work. PPR is a resonance phenomenon that is seen in parametric systems whereby some parameter varies periodically in time. In such systems, and assuming linearity, then PPR occurs at twice the fundamental natural frequency of the system. However, when nonlinearities are introduced, it was suggested by Watt and Cartmell (1994) [95] that the work done by the system would only be bounded by the nonlinearities themselves. Following this, an external load should not be simply considered as a form of remote damping, but given that the damping within the system is low enough and the necessary resonant conditions are maintained, then such a system can indeed be capable of maintaining oscillatory motion. This was experimentally validated in [95] using a mechanical ratchet system as a power take-off that lifted a known mass during positive half-cycles, and with recovery half-cycles in between.

# Chapter 2

# Periodic Vibrational Energy Harvesting

This first harvester model explained in this chpater is to act as a precursor to the second proposed harvesting scheme which involves a similar Euler strut concept. This approach relieves the requirement for tuned conditions by exploiting the cumulative effects of both deterministic and stochastic inputs of the parametric system in such a way that significantly enhances the net harvestable energy. Furthermore, this concept will explore the requirement to apply an initial pre-curvature that satisfies, and exploits, the conditions for stochastic resonance.

## 2.1 Description of the Proposed System for Harvesting Known Periodic Vibrations

Fig. 2.1 shows a schematic of the proposed energy harvester in the form of a fully realisable Euler strut. The construct comprises a parametric oscillator that can be excited axially by periodic vibrations emanating *freely* from the environment. With the facility to apply an initial pre-curvature using a static pre-load, the inherent bistability of the system causes the beam to buckle to either side of the *unstressed zero reference line*.

The Euler strut harvester itself is simple in construction. The beam is hinged at both ends with the facility to apply both static and dynamic axial loads. By applying

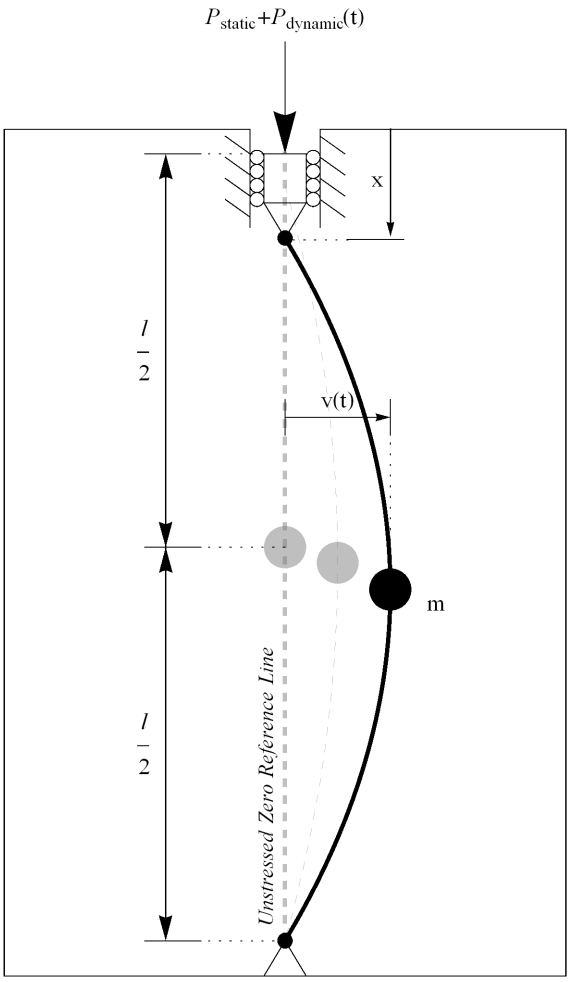


Figure 2.1: A buckling beam of length, $l$, with lumped mass, $m$, hinged at both ends, with static and dynamic loads applied axially, $P_{static}$ and $P_{dynamic}$ respectively.

a static load that exceeds the buckling capacity of the beam an initial pre-curvature may be formed. This has the effect of transitioning the system from a uni-stable state to a bistable state, the benefits of which will be discussed. The externally applied dynamic loads are what are to be considered as the harvestable vibrations that will excite the system. This will cause the potential barrier that separates the two basins of attraction in the bistable system to oscillate. By controlling the depth of the two basins of attraction via the static pre-load, the dynamic force will be able to force the system to jump from one basin of attraction to the other, thus potentially increasing the throughput of the system. The beam itself will be considered as a lumped mass system which will capture the essential behaviour of the responses.

Note that the response of the system will be measured as a lateral displacement of the lumped mass centre measured relative to the *unstressed zero reference line*.

## 2.2 Governing Equation of Motion of the Periodically Excited Euler Strut

The equation of motion for an Euler strut is well known and is based upon the Euler-Bernoulli partial differential equation. Using this, the provision for the initial pre-curvature, axial loads and inherent inertia and damping can then be built in. Two assumptions are made: that the longitudinal force in the beam is constant throughout its length, and that both the pre-curvature in the beam due to the static load and the lateral response of the beam are definable by half sine waves.

Therefore, by considering the equilibrium of an element within the beam, the basic equation of motion is [96, 97]:

$$\frac{\partial^2 M}{\partial x^2} + \left[P - \frac{EA}{2l}\int_0^l \left(\frac{\partial v_0}{\partial x}\right)^2 dx\right]\frac{\partial^2 v_0}{\partial x^2} + \left[P - \frac{EA}{2l}\int_0^l \left(\frac{\partial v}{\partial x}\right)^2 dx\right]\frac{\partial^2 v}{\partial x^2} - q = 0 \tag{2.1}$$

where $x$ is a longitudinal position coordinate, $M$ the total inertial bending moment, $P$ the total axial load acting upon the beam where $P = P_{static} + P_{dynamic}\cos\Omega t$, $E$ is the Young's modulus, $A$ the cross-sectional area, $l$ the length of the beam, $v_0$ and $v$ are

the unstressed lateral displacement and dynamic lateral displacement as measured the from the *unstressed zero reference line*, and $q$ is included as a potential additional load acting laterally upon the beam. Also, note that $\frac{EA}{2l}\int_0^l \left(\frac{\partial v_0}{\partial x}\right)^2 dx$ represents the axial stiffness within the beam.

The usual bending moment expression based upon the moment curvature relationship can be inserted:

$$-M = EI\left(v''\right) \tag{2.2}$$

Also, forces due to inertia and damping are taken into account as additional forces, such that:

$$q(x,t) = -m\ddot{v} - c\dot{v} \tag{2.3}$$

Note that the mass and damping terms are measured per metre i.e. $\frac{kg}{m}$ and $\frac{Ns/m}{m} = \frac{Ns}{m^2}$ as $q$ is the additional load per unit length of the beam acting laterally that is required to satisfy the form of $q = q(x,t)$.

To begin the dimensional modelling of Eq. 2.1, first the following half sine wave solution forms are assumed [96]:

$$\begin{aligned}
v_{static} &= a\sin\left(\frac{\pi x}{l}\right) & v(t) &= f\sin\left(\frac{\pi x}{l}\right) & \dot{v}(t) &= \dot{f}\sin\left(\frac{\pi x}{l}\right)\\
v'_{static} &= \frac{a\pi}{l}\cos\left(\frac{\pi x}{l}\right) & v'(t) &= \frac{f\pi}{l}\cos\left(\frac{\pi x}{l}\right) & \ddot{v}(t) &= \ddot{f}\sin\left(\frac{\pi x}{l}\right)\\
v''_{static} &= -\frac{a\pi^2}{l^2}\sin\left(\frac{\pi x}{l}\right) & v''(t) &= -\frac{f\pi^2}{l^2}\sin\left(\frac{\pi x}{l}\right) & &\\
v''''_{static} &= \frac{a\pi^4}{l^4}\sin\left(\frac{\pi x}{l}\right) & v''''(t) &= \frac{f\pi^4}{l^4}\sin\left(\frac{\pi x}{l}\right) & &
\end{aligned} \tag{2.4}$$

where $a$ is the initial displacement of the midspan of the beam due to the static load $P_{static}$, and $f$ is a dimensionless time dependent displacement, also at midspan.

By substituting these solutions, together with Eq. 2.2 and 2.3 into Eq. 2.1, the

equation of motion now becomes:

$$m\ddot{f}\sin\left(\frac{\pi x}{l}\right)+c\dot{f}\sin\left(\frac{\pi x}{l}\right)+\frac{EI\pi^4}{l^4}f\sin\left(\frac{\pi x}{l}\right)-\frac{P_{static}\pi^2}{l^2}a\sin\left(\frac{\pi x}{l}\right)$$
$$-\frac{P_{dynamic}\cos\Omega t\pi^2}{l^2}a\sin\left(\frac{\pi x}{l}\right)+\frac{EA}{2l}\left(\frac{\pi^2a^2}{2l}\right)a\frac{\pi^2}{l^2}\sin\left(\frac{\pi x}{l}\right)-\frac{P_{static}\pi^2}{l^2}f\sin\left(\frac{\pi x}{l}\right)$$
$$-\frac{P_{dynamic}\cos\Omega t\pi^2}{l^2}f\sin\left(\frac{\pi x}{l}\right)+\frac{EA}{2l}\left(\frac{\pi^2f^2}{2l}\right)f\frac{\pi^2}{l^2}\sin\left(\frac{\pi x}{l}\right)=0 \tag{2.5}$$

For simplification, the condition that $\sin\left(\frac{\pi x}{l}\right)\neq 0$ for $x\in(0,l)$ is used. Hence Eq. 2.5 may be reduced to:

$$m\ddot{f}+c\dot{f}+\frac{EI\pi^4}{l^4}f-\frac{P_{static}\pi^2}{l^2}a-\frac{P_{dynamic}\cos\Omega t\pi^2}{l^2}a+\frac{EA\pi^4}{4l^4}a^3$$
$$-\frac{P_{static}\pi^2}{l^2}f-\frac{P_{dynamic}\cos\Omega t\pi^2}{l^2}f+\frac{EA\pi^4}{4l^4}f^3=0 \tag{2.6}$$

After which, dividing through by $m$ leads to:

$$\ddot{f}+\frac{c}{m}\dot{f}+\frac{EI\pi^4}{ml^4}f-\frac{P_{static}\pi^2}{ml^2}a-\frac{P_{dynamic}\cos\Omega t\pi^2}{ml^2}a+\frac{EA\pi^4}{4ml^4}a^3$$
$$-\frac{P_{static}\pi^2}{ml^2}f-\frac{P_{dynamic}\cos\Omega t\pi^2}{ml^2}f+\frac{EA\pi^4}{4ml^4}f^3=0 \tag{2.7}$$

In the current configuration all terms should be in acceleration units. By creating definitions and grouping terms together, the complete equation of motion for the beam in Fig. 2.1 can be described as:

$$\ddot{f}+\beta\dot{f}+\frac{\pi^2}{ml^2}\left[P_{crit}-P_{static}-P_{dynamic}\cos\Omega t\right]f+\frac{EA\pi^4}{4ml^4}f^3$$
$$-\frac{\pi^2}{ml^2}\left[P_{static}+P_{dynamic}\cos\Omega t\right]a+\frac{EA\pi^4}{4ml^4}a^3=0 \tag{2.8}$$

where $\beta=\frac{c}{m}$, with typical linear viscous damping defined by $c=2\zeta m\omega_n$. The critical buckling load of the beam is $P_{crit}=\frac{EI\pi^2}{l^2}$.

Upon further inspection of Eq. 2.8 it can be seen that both the static and the dynamic responses of the system are governed by sets of terms containing $a$ and $f$

respectively. Hence the static response, $a$, of the beam is described by:

$$\frac{EA\pi^4}{4ml^4}a^3 - \frac{\pi^2}{ml^2}\left[P_{static}\right]a = 0 \tag{2.9}$$

where $P_{static}$ is the load relevant to the static displacement of the mid-span, $a$, and the dynamic loading term $P_{dynamic}\cos\Omega t$ has been ignored due to its time-varying nature.

Whereas the dynamic response, $f$ is described by:

$$\ddot{f} + \beta\dot{f} + \frac{\pi^2}{ml^2}\left[P_{crit} - P_{static} - P_{dynamic}\cos\Omega t\right]f + \frac{EA\pi^4}{4ml^4}f^3 = 0 \tag{2.10}$$

where it can be seen that $P_{crit}$ has an effect upon $f$, and so subsequently $P_{static}$ will also.

It is the dynamic response of the system that is of most interest for the purposes of energy harvesting, and so this forms the focus of the remaining analysis.

### 2.2.1 Expressing for the Fundamental Natural Frequency

Defining the natural frequency of the beam is essential for exploring the behaviour of the response when subjected to various forms of excitation, especially if attempting to achieve resonant conditions. To obtain the terms to describe $\omega_n$, Eq. 2.10 must first be multiplied back through by $m$, such that:

$$m\ddot{f} + c\dot{f} + \frac{\pi^2}{l^2}\left[P_{crit} - P_{static} - P_{dynamic}\cos\Omega t\right]f + \frac{EA\pi^4}{4l^4}f^3 = \tag{2.11}$$

Now consider that $P_{static}$ and $P_{dynamic}$ can be both zero and nonzero. If $(P_{static}, P_{dynamic}) = (0, 0)$, then only the fundamental stiffness of the beam remains which is given by $k = \frac{P_{crit}\pi^2}{l^2}$. Hence an expression for $\omega_n$ can be derived for unloaded conditions using this fundamental stiffness and dividing back through by $m$:

$$\omega_n = \sqrt{\frac{k}{m}} = \sqrt{\frac{\pi^2}{ml^2}P_{crit}}, \qquad ; \qquad (P_{static}, P_{dynamic}) = (0, 0) \tag{2.12}$$

When $(P_{static}, P_{dynamic}) \neq (0, 0)$, there are additional terms to include in the

derivation of $\omega_n$. Complications begin to arise because of the time-variant nature of $P_{dynamic}$ included in the parametric excitation terms that will lead to a time-varying expression for $\omega_n$. Therefore, for simplicity, the analysis will continue under the assumption that $P_{dynamic}$ will not be used in the computation of $\omega_n$, thus:

$$\omega_n = \sqrt{\frac{\pi^2}{ml^2}\left[P_{crit} - P_{static}\right]}, \qquad ; \qquad P_{crit} > P_{static} \tag{2.13}$$

Eq. 2.13 describes the natural frequency of the system for conditions where $P_{crit} > P_{static}$. However, it is known that to satisfy the conditions required by a bistable system, the overall linear stiffness must be negative, such that $P_{crit} < P_{static}$. This condition gives rise to a complex number that can be difficult to compute in practice. Therefore, in order to avoid this, the terms in Eq. 2.10 can be manipulated in such a way that all the prerequisites required by the system, including a negative linear stiffness and $P_{static} > P_{crit}$, can be achieved without the formation of complex numbers. The approach is as follows:

$$\ddot{f} + \beta\dot{f} - \left(\frac{\pi^2}{ml^2}\left[P_{static} - P_{crit}\right] - \frac{\pi^2}{ml^2}\left[P_{dynamic}\cos\Omega t\right]\right) f + \frac{EA\pi^4}{4ml^4} f^3 = 0 \tag{2.14}$$

where the minus sign applied to the bracketed 3$^{\text{rd}}$ set of terms has been introduced to ensure that the resulting sign of $P_{crit}$ and $P_{static}$ remain consistent with that shown in Eq. 2.10. Also, note that the sign of the dynamic forcing terms, $P_{dynamic}$ is unimportant because of the oscillating cosine operator.

Now the natural frequency in loaded conditions can now be defined as:

$$\omega_n = \sqrt{\frac{\pi^2}{ml^2}\left[P_{static} - P_{crit}\right]}, \qquad ; \qquad P_{static} > P_{crit} \tag{2.15}$$

In this way, a negative linear stiffness can be defined so that real values for the natural frequency are obtained whilst continuing to neglect the dynamic component.

In order for the system to be computed when $P_{static}$ is both less and greater than $P_{crit}$, it is proposed to use piecewise functions to define which form the the equation of motion takes depending on the instantaneous condition of $P_{static}$. Therefore the full

behaviour of the system could be analysed numerically by the following:

$$0 = \begin{cases} \ddot{f} + \beta\dot{f} + \left({\omega_n}^2 - \dfrac{\pi^2}{ml^2}\left[P_{dynamic}\cos\Omega t\right]\right) f + \dfrac{EA\pi^4}{4ml^4} f^3 \; ; \; P_{static} < P_{crit} \\ \ddot{f} + \beta\dot{f} - \left({\omega_n}^2 - \dfrac{\pi^2}{ml^2}\left[P_{dynamic}\cos\Omega t\right]\right) f + \dfrac{EA\pi^4}{4ml^4} f^3 \; ; \; P_{static} > P_{crit} \end{cases} \tag{2.16}$$

where:

$$\omega_n = \begin{cases} \sqrt{\dfrac{\pi^2}{ml^2}\left[P_{crit} - P_{static}\right]} \; ; \; P_{static} < P_{crit} \\ \sqrt{\dfrac{\pi^2}{ml^2}\left[P_{static} - P_{crit}\right]} \; ; \; P_{static} > P_{crit} \end{cases} \tag{2.17}$$

It is interesting to observe the relationship $\omega_n$ has with other constituents of its defining terms, particularly $l$ and $P_{static}$ since they may be considered as the simplest parameters through which to affect control upon the system in practice. Fig. 2.2(a) is a 3-dimensional plot that has been hued to convey height and depth to show the combined influence that both $l$ and $P_{static}$ have upon $\omega_n$. A trough of $\omega_n = 0$ is clearly evident sweeping across the $l$, $P_{static}$ plane and is explained by the 'snap-through' behaviour as the system transitions from one static bistable well to the other. By superimposing the relationship of $P_{crit}$ vs. $l$ on top of a contour plot of $P_{static}$ vs. $l$ (see Fig. 2.2(b)) it can be seen that this curve matches the trough precisely. The nature of this can also be deduced from Eq. 2.17 where it can be seen that if $P_{static} = P_{crit}$ then $\omega_n = 0$, which is precisely at the onset of a snap-through.

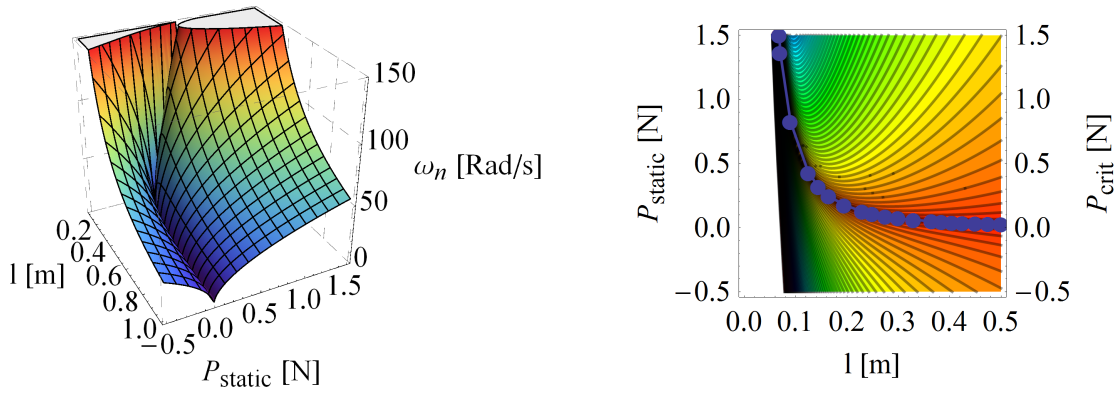


(a) 3-Dimensional plot showing the response of $\omega_n$ vs. $l$ & $P_{static}$.

(b) Contour plot of $P_{static}$ vs. $l$ that has been hued to indicate magnitude of $\omega_n$, with relationship between $P_{crit}$ vs. $l$ superimposed.

Figure 2.2: Relationship of $\omega_n$ for a fibre glass epoxy beam with $l$ and $P_{static}$ when cross-sectional area, $A = 2.5 \times 10^{-6}\text{m}^2$, Young's modulus, $E = 13\text{GPa}$ and density, $\rho = 1900\text{kg/m}^3$.

## 2.3 Expressing the Effective Potential of the Periodically Excited System

Some of the qualitative behaviour of the system described by Eq. 2.16 and Eq. 2.17 can be observed by examining the complete effective potential of the system, $V(f)$, such that $f'' = -\frac{\partial V(f)}{\partial f}$ is defined as:

$$V(f) = \begin{cases} -\frac{1}{2}\left({\omega_n}^2 - \frac{P_{dynamic}\pi^2}{ml^2}\cos\Omega t\right) f^2 + \frac{1}{4}\left(\frac{EA\pi^4}{4ml^4}\right) f^4 \; ; \; P_{static} < P_{crit} \\ \frac{1}{2}\left({\omega_n}^2 - \frac{P_{dynamic}\pi^2}{ml^2}\cos\Omega t\right) f^2 + \frac{1}{4}\left(\frac{EA\pi^4}{4ml^4}\right) f^4 \; ; \; P_{static} > P_{crit} \end{cases} \tag{2.18}$$

where again, $\omega_n$ is defined by Eq. 2.17.

First, by examining the system under static loading conditions the transition between a uni-stable system and a bistable system may be observed. When $P_{static} \neq 0$

and $P_{dynamic} = 0$, Eq. 2.18 is reduced to:

$$V(f) = \begin{cases} -\frac{{\omega_n}^2}{2} f^2 + \frac{1}{4}\left(\frac{EA\pi^4}{4ml^4}\right) f^4 \,;\; P_{static} < P_{crit} \\ \frac{{\omega_n}^2}{2} f^2 + \frac{1}{4}\left(\frac{EA\pi^4}{4ml^4}\right) f^4 \,;\; P_{static} > P_{crit} \end{cases} \tag{2.19}$$

Fig. 2.3(a) depicts the resulting behaviour for various $P_{static}$. When $P_{static} = 0$, the system exists with only one stable well such that the beam will be unbuckled at rest with zero initial conditions. And indeed, if $P_{static} < 0$, then a tensile force will be applied axially to the beam that manifests itself with a narrower single well. The result of this is that the beam becomes more stable in its pre-tensioned state, making it more difficult for lateral oscillations to generate a displacement. This is precisely the behaviour that should be discouraged in the context of an energy harvester.

When $P_{static} > 0$, i.e. when a compressive load is applied axially to the beam, there begins the formation of a bistable system which is evident from the presence of a double well potential. Therefore the beam will be attracted to either well which manifests itself by buckling to either respective side of the *unstressed zero reference line*. By increasing $P_{static}$ even further the bistable wells become deeper still.

However, in terms of increasing the throughput of the energy harvester, a system with deeper potential wells would required larger magnitudes of excitation from $P_{dynamic}$ to increase the likelihood of the response jumping from one well to the other. If the system is able to regularly jump between both wells, then the displacement of the response will be greatly enhanced. Hence, it may be the objective for the energy harvesting approach to select a suitable value for $P_{static}$ so that bistability is achieved. To demonstrate this approach, Fig. 2.3(b) is a plot of the effective potentials described by Eq. 2.18 for given conditions.

This shows that $P_{dynamic}$ can produce a similar effect as $P_{static}$, such that the configuration of the system may be changed to a bistable system depending upon the magnitude of the applied force. The difference here is that the depth of bistability is time varying. It can be that certain values of $P_{static}$ may facilitate this process, and as such, the relationship between $P_{static}$ and $P_{dynamic}$ will be further explored later.

Of course, the effectiveness of the dynamic forcing terms is highly dependent upon

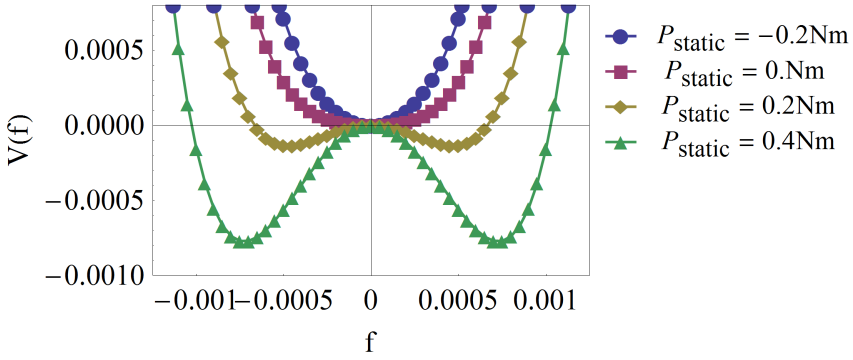


(a) Effective potential of the beam described by Eq. 2.19 when length, $l = 0.35$m, cross-sectional area, $A = 2.5 \times 10^{-6}$m$^2$, Young's modulus, $E = 13$GPa and density, $\rho = 1900$kg/m$^3$.

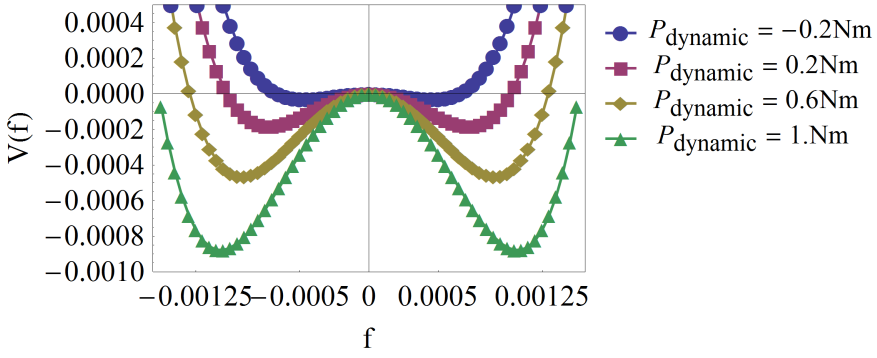


(b) Effective potential of the beam described by Eq. 2.18 when length, $l = 0.35$m, cross-sectional area, $A = 2.5 \times 10^{-6}$m$^2$, Young's modulus, $E = 13$GPa, density, $\rho = 1900$kg/m$^3$, $P_{static} = 0.5$N and modulating frequency, $\Omega = \pi$rad/s.

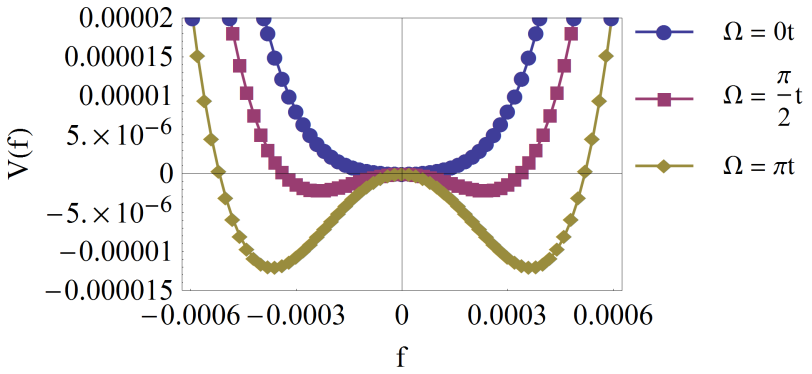


(c) Effective potential of the beam described by Eq. 2.18 when length, $l = 0.35$m, cross-sectional area, $A = 2.5 \times 10^{-6}$m$^2$, Young's modulus, $E = 13$GPa, density, $\rho = 1900$kg/m$^3$, $P_{static} = 0.5$N and $P_{dynamic} = 0.1$N.

Figure 2.3: Effective potential plots for various loading scenarios.

the modulating frequency, as will also be explored further on. For a preliminary understanding, Fig. 2.3(c) shows how the potential barrier can be oscillated by $P_{dynamic}$ at a frequency of $\Omega$. What must also be considered here is that the response of the system to the dynamic forcing will be always be at its greatest at resonance. In the case of parametrically excited systems such as the Euler strut, PPR occurs at $\Omega \approx 2\omega_n$ when the system is linear. However, as previously mentioned, inherent nonlinearities will prevail in the current system since full nonlinearity has been maintained throughout the derivation. This will cause the precise location of PPR to shift depending on the nature of the governing nonlinear stiffnesses. In *soft* systems the shift occurs towards the left of $2\omega_n$, and to the right in *hard* systems.

## 2.4 Defining the Energy Throughput of the Periodically Excited System

To be able to assess the performance of the harvester and observe the influences that particular system parameters have, it is desirable to express this in the terms of the energy able to be harvested. To this end, an expression that describes the net energy dissipated through the system must be derived. To do this, a similar approach used by Stephen (2006) [52], and subsequently McInnes *et al* (2008) [90], is adopted.

Firstly, an expression for the total energy of the system is obtained by multiplying Eq. 2.16 through by $\dot{f}$:

$$\dot{f}\ddot{f} - {\omega_n}^2 \dot{f} f + \frac{EA\pi^4}{4ml^4}\dot{f} f^3 = -\beta \dot{f}^2 - \frac{P_{dynamic}\pi^2}{ml^2}\cos\Omega t \dot{f} f \tag{2.20}$$

Note that only the condition where $P_{static} > P_{crit}$ is being considered for now in the derivation process. Following this, it will then be shown how the resulting expression is applicable to both conditions of $P_{static} > P_{crit}$ and $P_{static} < P_{crit}$.

Rewriting the left hand side terms as a total derivative will produce expressions for both the kinetic and potential energies, such that:

$$\frac{d}{dt}\left[\frac{1}{2}\dot{f}^2 - \frac{1}{2}{\omega_n}^2 f^2 + \frac{1}{4}\left(\frac{EA\pi^4}{4ml^4}\right) f^4\right] = -\beta \dot{f}^2 - \frac{P_{dynamic}\pi^2}{ml^2}\cos\Omega t \dot{f} f \tag{2.21}$$

where the system kinetic energies and potential energies are defined as:

$$T = \frac{1}{2}\dot{f}^2 \tag{2.22}$$

$$U = V(f) = -\frac{1}{2}{\omega_n}^2 f^2 + \frac{1}{4}\left(\frac{EA\pi^4}{4ml^4}\right) f^4 \tag{2.23}$$

Eq. 2.19 and Eq. 2.23 are of the same form, and the total energy, $E_{total}$ of the system may be described as:

$$E_{total}(t) = \frac{1}{2}\dot{f}^2 + V(f) \tag{2.24}$$

Eq. 2.21 represents the conservation of power in the system [52], not withstanding the accepted premise of a strictly conservative system, showing that the instantaneous power being dissipated by the damper plus the time rate of change of the kinetic and potential energies must be equal to the instantaneous power in the system, hence:

$$\dot{E}(t) = -\beta \dot{f}^2 - \frac{P_{dynamic}\pi^2}{ml^2} \cos \Omega t \dot{f} f \tag{2.25}$$

When considering the instantaneous power that there is available to be harvested, it will be assumed that only the power dissipated via damping, $\beta \dot{f}^2$ can in fact be harvested. In this way, the damping terms are being used to represent some form of power take-off device. This approach is sufficient for the current analysis because it will still fully capture changes in performance through the system as it is attempted to enhance the response. Future studies could improve this approach by modelling the physical characteristic of an actual power take-off device, but the analysis will proceed under the assumption that $\beta \dot{f}^2$ will be positive to represent the total available power. Studies by many researchers have investigated the use of piezoelectric strips attached to vibrating beam structures to convert mechanical energy into electrical energy [3,98–102] and it is envisioned that this too would be the most appropriate transducer type.

The sign of the rate of work done in modulating the beam, $\frac{P_{dynamic}\pi^2}{ml^2} \cos \Omega t \dot{f} f$ will oscillate due to the cosine function. However, as the periodic force, $P_{dynamic}$ is to be considered as *freely* harvestable from the environment, it should not be included as contributing to the available instantaneous power to be harvested. Moreover, this is the instantaneous power being delivered into the system. Therefore, the net available instantaneous power, $P_{net}(t)$ that is available to be harvested can be expressed as:

$$P_{net}(t) = \beta \dot{f}^2 \tag{2.26}$$

As only the power dissipated via damping is to be available for harvesting, and because the nature of these terms is the same for both static loading conditions where $P_{static} < P_{crit}$ & $P_{static} > P_{crit}$, it can be accepted that Eq. 2.26 is applicable in both conditions. Therefore, there is no requirement to repeat the same derivation process for when $P_{static} < P_{crit}$.

## 2.5 System Response in the Time Domain and Phase Space

Now that a method for measuring the performance of the system has been developed, it is possible to begin numerical simulations of the periodically excited Euler strut system described by Eq. 2.16. This can be done using different computational software, including *Mathematica* which is popular in the fields of science, mathematics and engineering. This is the preferred software used throughout these studies and makes use of the **NDSolve** command that finds numerical solutions to differential equations. Whilst the precise operation of this function is a closely guarded secret within *Wolfram*, it will employ a range of integrating routines in order to gain convergence, and is also capable of changing between them when calculations appear to be inexorably heading towards a numerical instability or singularity. Typically, such integrators make use of Runge-Kutta calculations, with Gear and Merson variants for systems where the dynamics are highly nonlinear, and many more that **NDSolve** may well call upon, and it is this degree of robustness that makes it a popular choice.

Note that within Eq. 2.16, it is possible to define the material properties and geometry of the Euler strut. Whilst many materials are realisable in practice, the proceeding analysis have all been based upon a fibre glass epoxy material of Young's modulus, $E = 13\text{GPa}$ and density, $\rho = 1900\text{kg/m}^3$ for simplicity. This beam has an arbitrarily chosen cross-sectional area of $A = 2.5 \times 10^{-6}\text{m}^2$ and length, $l = 0.35\text{m}$, unless otherwise stated.

First the response of the system under static forcing conditions only will be explored, where $P_{static} \neq 0\text{N}$ and $P_{dynamic} = 0\text{N}$. The rationale behind this is to be able to observe the response as it moves from a uni-stable state to a bistable state. As previously noted, the system will only be forced into a bistable state when $P_{static} \geq P_{crit}$, where $P_{crit} = \dfrac{EI\pi^2}{l^2}$. In this case the static response of the beam will be attracted to either potential well manifested by the beam physically buckling into the respective side of the *unstressed zero reference line*.

### 2.5.1 Responses to Static Forcing Conditions

Shown in Fig. 2.4 is the response $f$ within the given time domain under static loading conditions. It is often found in systems that are axially forced that the beam may be unable to escape its zero position without being initially perturbed in some way. A simple method by which to achieve this without significantly influencing the behaviour is to use non-zero initial conditions. In Fig. 2.4 the initial conditions of $f(0) = 1 \times 10^{-5}$m, $\dot{f}(0) = 0$rad/s, were shown to perform well and are used throughout.

Whilst not immediately clear within Fig. 2.4(a), the initial conditions produce a transient response immediately from $t = 0$ that quickly settles to the static steady-state shown by each respective $P_{static}$ curve. Under the given conditions $P_{crit} = 0.055$N, it can be seen in Fig. 2.4(b) that when $P_{static} < P_{crit}$ the response remains at zero. Only when $P_{static} > P_{crit}$ does a response register as the beam buckles to either side (into the positive domain in these examples due to the positive sign of $f(0)$) measured laterally from the *unstressed zero reference line*. As $P_{static}$ is increased, so too does the lateral displacement, and it can seen that this happens at a much greater rate immediately after $P_{crit}$ is exceeded.

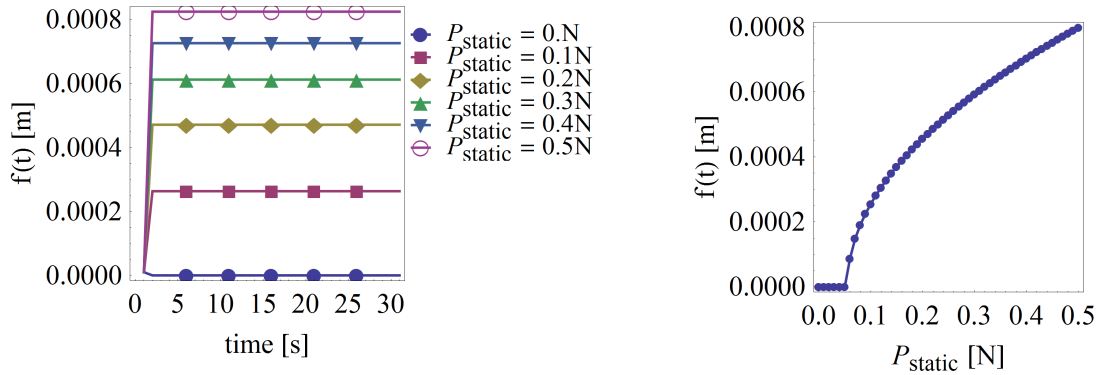


(a) (b)

Figure 2.4: Responses to static loading conditions where $P_{crit} = 0.055$N, $A = 2.5 \times 10^{-6}$m $^2$, $l = 0.35$m, $E = 13$GPa, $\rho = 1900$kg/m$^3$, $P_{dynamic} = 0.0$N, $\zeta = 0.3$, $\Omega = 0$rad/s, $f(0) = 1 \times 10^{-5}$m, $\dot{f}(0) = 0$rad/s and $0 \leq t \leq 30$s.

### 2.5.2 Responses to Dynamic Forcing Conditions

Now the response of the system will be observed under dynamic forcing conditions only. In this sense, it could be said that this is how the harvester would perform in its most fundamental form, and later it will be seen how the throughput of the system can be improved by introducing $P_{static}$. Also, as it is intended that the harvester will collect energy from the $P_{dynamic}$ terms that are considered to be available freely from the environment, it will be possible to make predictions via Eq. 2.26 as to how much energy can be harvested.

To begin with, the excitation frequency has been arbitrarily set to $\Omega = 100$rad/s without any attempt to achieve resonance at this stage. It is important to note that because it has been shown that $P_{static}$ intrinsically affects the location of $\omega_n$, defining $\Omega$ with a fixed frequency for now (as opposed to the approach as a ratio of $\omega_n$) will ensure that simulations where $P_{static}$ is varied will not subsequently affect $\Omega$.

Fig. 2.5 shows the responses of the system to small values of $P_{dynamic}$ and shows the onset of bistable behaviour in the beam. In order to be able to see the precise details of the oscillatory responses, only a very short time domain of three seconds has been plotted because of the high frequencies.

As shown by Fig. 2.5(a) there is a zero response when $P_{dynamic} < P_{crit}$ which was to be expected. As $P_{dynamic}$ increases it reaches the point where $P_{dynamic} > P_{crit}$ and the beam begins to oscillate to either side of the *unstressed zero reference line*. By observing the responses in phase space, the underlying characteristics of this may be observed. In Fig. 2.5(e) it can be seen that the trajectory of the response primarily orbits an attractor located at the origin, but with evidence of two outer potential wells beginning to form (note the skewed shapes). The attractor at the origin is located in the *unstressed position*, but the two outer wells are forming as the state of the beam approaches some form of bistability. As demonstrated previously, bistable conditions would be manifested in practice by the beam buckling to one side and remaining there. The key difference now is that the motion is oscillatory and the response may instead orbit about numerous attractors as opposed to becoming trapped and governed by a single one.

It is shown that when $P_{dynamic} = 0.55$N, the trajectory becomes very unstable with

evidence of multiple periods occurring at different points in time. It could be said that the system is oscillating in and out of a bistable state here. However, when $P_{dynamic}$ is increased to 0.8N, a stable response is again seen, but with the trajectory primarily orbiting about the *unstressed position* and the positive bistable attractor (see Fig. 2.5(k)).

Continuing to increase $P_{dynamic}$ and observing the response at much higher values of $P_{dynamic}$ shows that again multiple periods of attraction form. This demonstrates the complicated and unpredictable responses these systems are capable of in such configurations. The greatest evidence of this is in Fig. 2.6(l) where the response is shown to orbit multiple attractors at irregular periods in time. Such behaviour would result in continually fluctuating instantaneous powers being dissipated through the system and is something to be avoided unless some external form of external rectification process can be performed.

It could be thought that the greatest throughput would be achieved if the trajectory could be manipulated to orbit the two outermost bistable attractors in a steady-state because this would result in the greatest displacement $f$ of the beam. Without making any definitive conclusions about this at this stage, it is observed in Fig. 2.6 that the commonality between simulations has been an attractor located at the *unstressed position*. This is explained by the fact that as $P_{dynamic}$ modulates it will oscillate above and below the value of $P_{crit}$, thus transitioning between a uni-stable and a bistable state. However, as demonstrated in Section 2.5.1, $P_{static}$ can be used to force the beam into an initial bistable state, and by doing so, it is possible to remove the formation of this attractor at the origin. The advantage of doing so would be that the response of the beam could potentially oscillate directly between both outermost attractors, which would result in the enhanced lateral displacements which are sought.

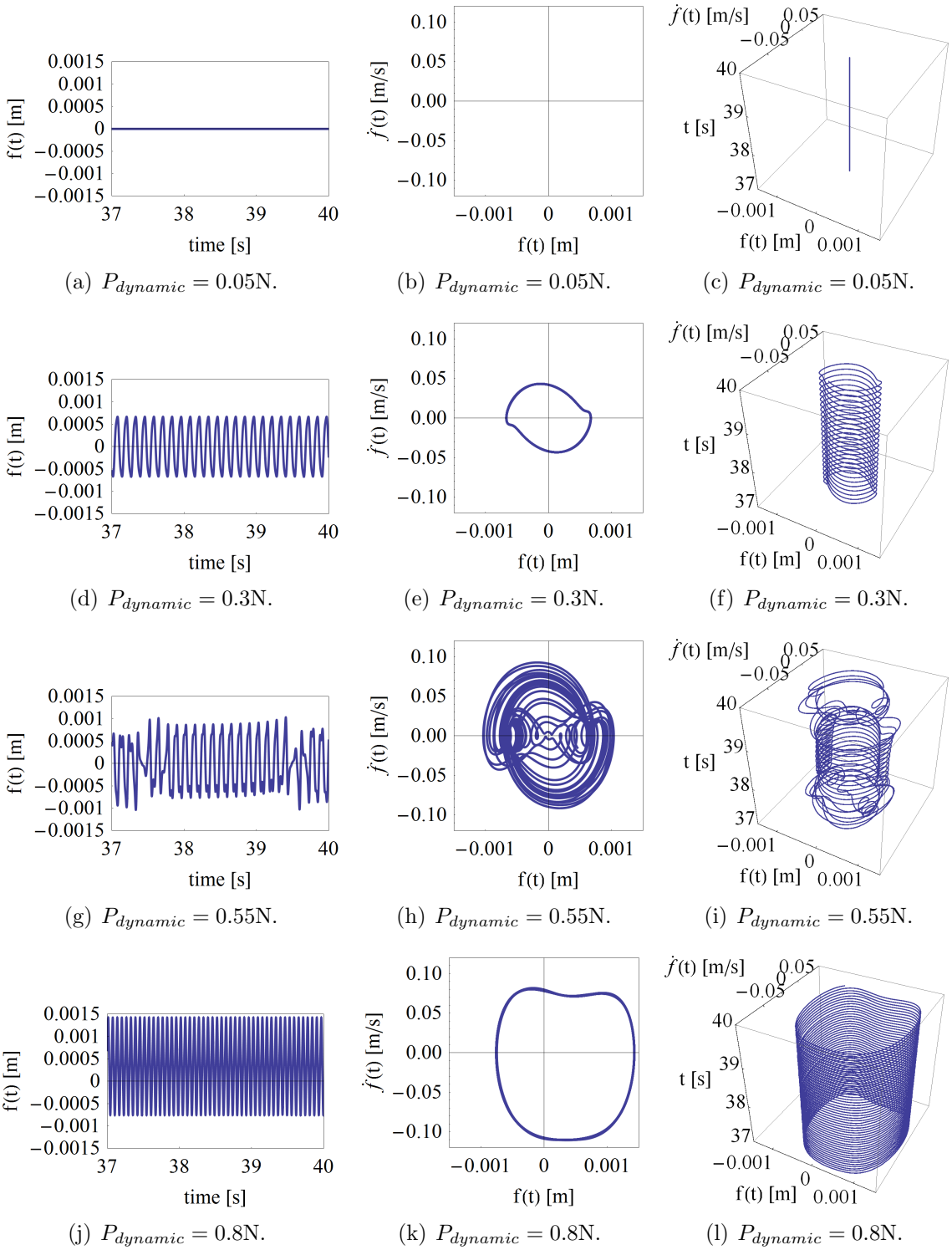


(a) $P_{dynamic} = 0.05$N. (b) $P_{dynamic} = 0.05$N. (c) $P_{dynamic} = 0.05$N.

(d) $P_{dynamic} = 0.3$N. (e) $P_{dynamic} = 0.3$N. (f) $P_{dynamic} = 0.3$N.

(g) $P_{dynamic} = 0.55$N. (h) $P_{dynamic} = 0.55$N. (i) $P_{dynamic} = 0.55$N.

(j) $P_{dynamic} = 0.8$N. (k) $P_{dynamic} = 0.8$N. (l) $P_{dynamic} = 0.8$N.

Figure 2.5: Time domain and phase space responses to small dynamic loading conditions where $P_{crit} = 0.055$N, $P_{static} = 0.0$N, $A = 2.5 \times 10^{-6}$m $^2$, $l = 0.35$m, $E = 13$GPa, $\rho = 1900$kg/m$^3$, $\zeta = 0.3$, $\Omega = 100$rad/s, $f(0) = 0.00001$m, $\dot{f}(0) = 0$rad/s and $37 \leq t \leq 40$s.

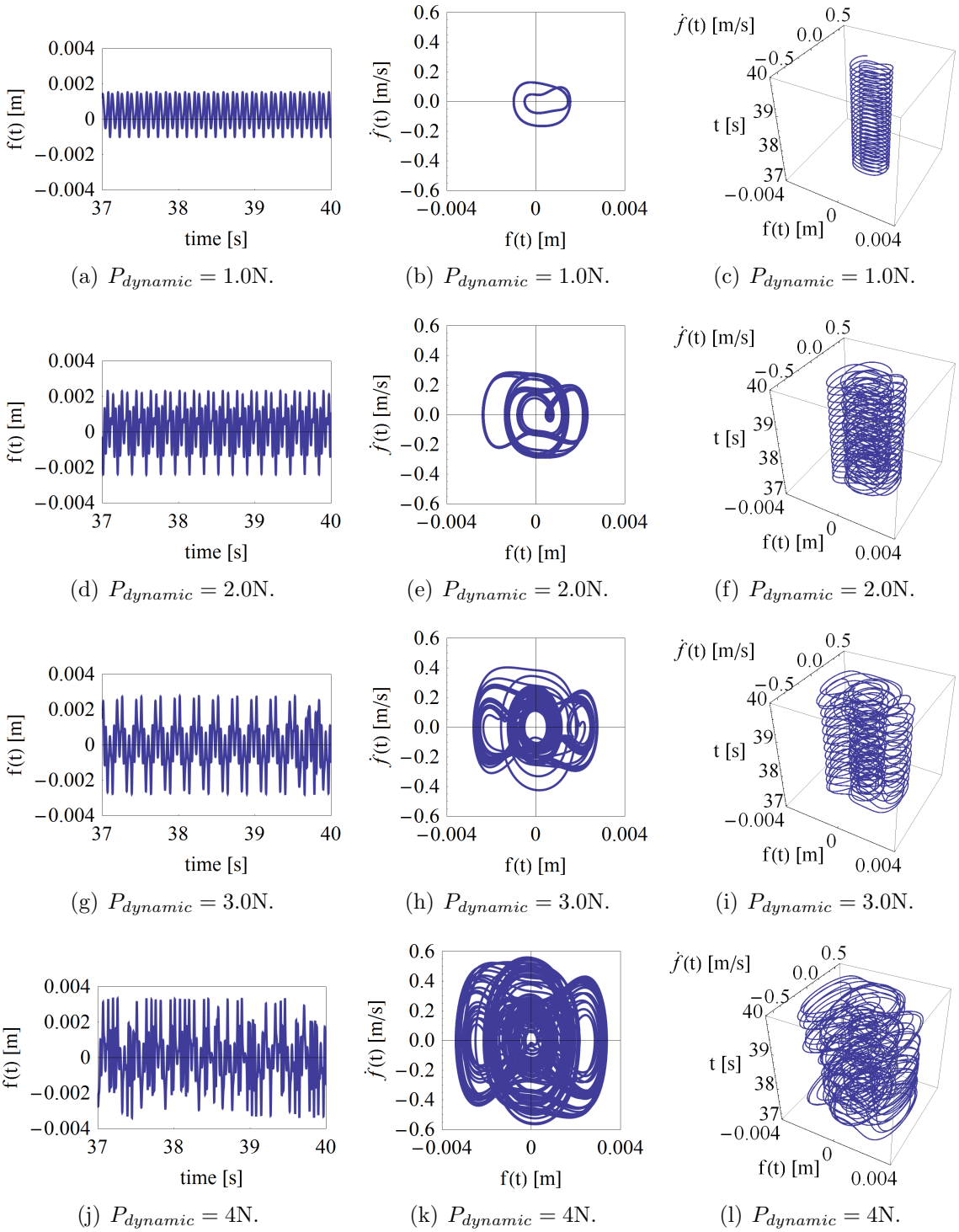


(a) $P_{dynamic} = 1.0$N. (b) $P_{dynamic} = 1.0$N. (c) $P_{dynamic} = 1.0$N.

(d) $P_{dynamic} = 2.0$N. (e) $P_{dynamic} = 2.0$N. (f) $P_{dynamic} = 2.0$N.

(g) $P_{dynamic} = 3.0$N. (h) $P_{dynamic} = 3.0$N. (i) $P_{dynamic} = 3.0$N.

(j) $P_{dynamic} = 4$N. (k) $P_{dynamic} = 4$N. (l) $P_{dynamic} = 4$N.

Figure 2.6: Time domain and phase space responses to large dynamic loading conditions where $P_{crit} = 0.055$N, $P_{static} = 0.0$N, $A = 2.5 \times 10^{-6}$m$^2$, $l = 0.35$m, $E = 13$GPa, $\rho = 1900$kg/m$^3$, $\zeta = 0.3$, $\Omega = 100$rad/s, $f(0) = 0.00001$m, $\dot{f}(0) = 0$rad/s and $37 \leq t \leq 40$s.

### 2.5.3 Responses to Static and Dynamic Forcing Conditions

To demonstrate that $P_{static}$ may be used to enhance the $f$ response of the system by preventing the formation of the uni-stable attractor at the *unstressed position* and creating a bistable state, simulations were performed for various values of $P_{static}$ with an arbitrarily chosen $P_{dynamic} = 0.2$N and $\Omega = 100$rad/s.

In the first loading case where $P_{static} = 0.05$N, the trajectory of the response remains trapped within the uni-stable attractor because the coupling effect with $P_{dynamic} = 0.2$N is not enough to generate bistability. The measured $f$ for this condition barely registers a response at all. However, by only increasing $P_{static}$ to 0.15N where $P_{static} > P_{crit}$, it can be seen that bistability has been achieved and a measurable response is generated. Interestingly, the responses here orbit either attractor for a number of periods before crossing to the other (see Fig. 2.7(d)).

When $P_{static} = 0.25$N it can be seen from Fig. 2.7(h) that the desired behaviour is achieved where the response periodically orbits about both bistable attractors in a steady-state, thus $f$ could be considered as greatly enhanced. It should be noted that this form of enhancement has been achieved passively and that no power is required to maintain this level of static preload. This behaviour is not enough to conclude that the energy throughput of the system will also be enhanced. Actual measurements of the energy available for harvesting will have to be taken in order to form such opinions.

Fig. 2.7(j) demonstrates that with further increases to $P_{static}$, the response can begin to oscillate about a single attractor again. When $P_{static} = 0.35$N, it can be seen that the potential difference between the two attractors is approaching too great for $P_{dynamic}$ to overcome the potential barrier between wells consistently, hence the trajectory orbits either attractor for a number of periods once more. If $P_{static}$ were to be increased even further still, then the response would eventually become trapped within a single attractor of the bistable system and would require significantly more energy from $P_{dynamic}$ in order to cross the potential barrier. Clearly then, there must exist an optimum value of $P_{static}$ that can be applied to system under the given conditions to achieve the greatest displacement, $f$. In order to find this point, it is perhaps more useful to observe the response in terms of the energy being dissipated by power take-off terms.

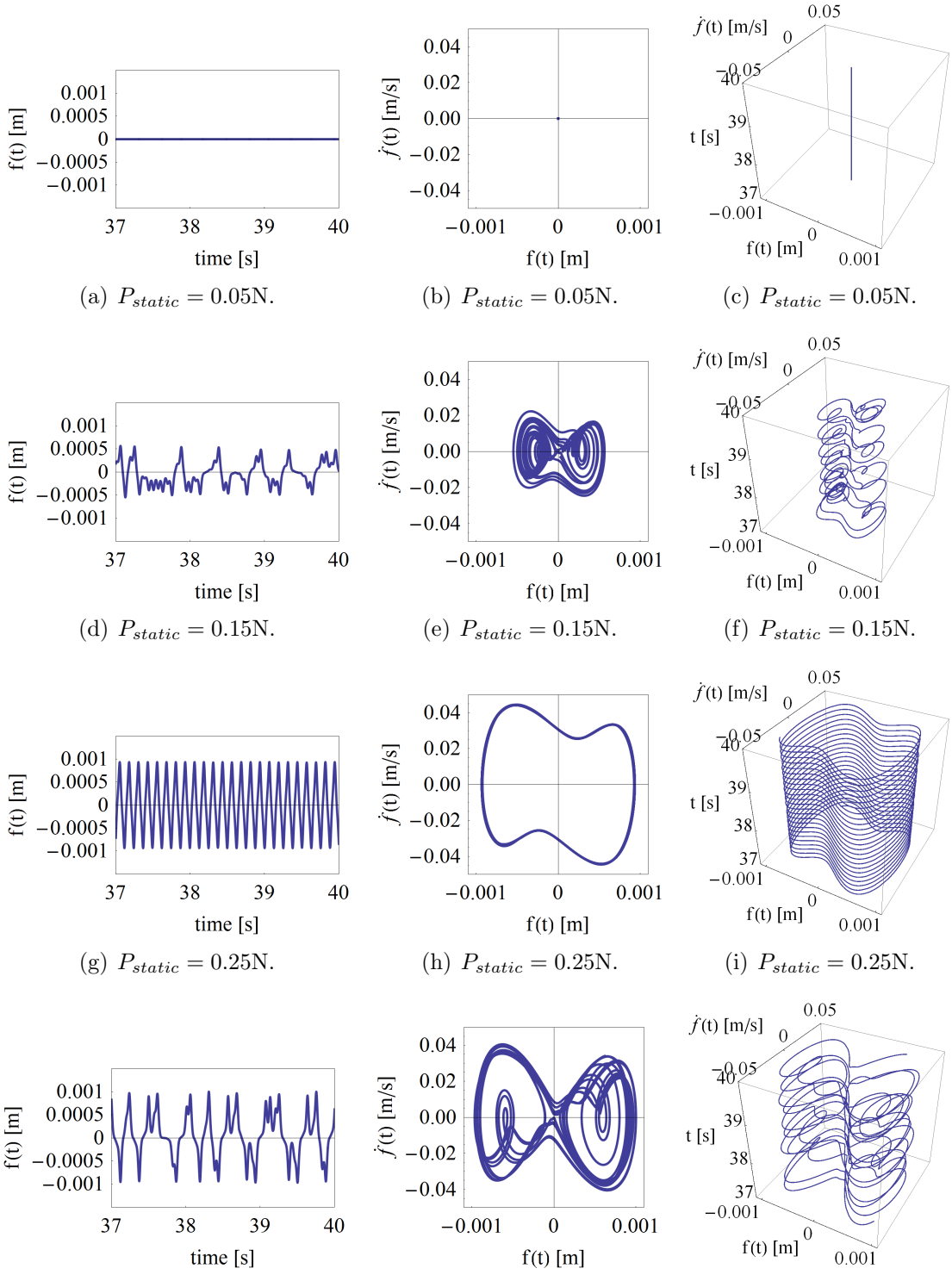


(a) $P_{static} = 0.05$N. (b) $P_{static} = 0.05$N. (c) $P_{static} = 0.05$N.

(d) $P_{static} = 0.15$N. (e) $P_{static} = 0.15$N. (f) $P_{static} = 0.15$N.

(g) $P_{static} = 0.25$N. (h) $P_{static} = 0.25$N. (i) $P_{static} = 0.25$N.

(j) $P_{static} = 0.35$N. (k) $P_{static} = 0.35$N. (l) $P_{static} = 0.35$N.

Figure 2.7: Time domain and phase space responses to static and dynamic loading conditions where $P_{crit} = 0.055$N, $P_{dynamic} = 0.2$N, $A = 2.5 \times 10^{-6}$m $^2$, $l = 0.35$m, $E = 13$GPa, $\rho = 1900$kg/m$^3$, $\zeta = 0.3$, $\Omega = 100$rad/s, $f(0) = 0.00001$m, $\dot{f}(0) = 0$rad/s and $37 \leq t \leq 40$s.

## 2.6 Energy Available for Harvesting from the Periodic Harvester

The previous time domain and phase space simulations alluded to the potential benefits that careful manipulation of various system parameters could have. However, to focus on the context of energy harvesting, a more appropriate way in which to assess the performance of harvester would be in terms of the energy dissipated, and hence the energy that the harvester will be able to collect from the ambient vibrational sources.

As discussed in Section 2.4, the instantaneous power dissipated by the system can be described by Eq. 2.26, repeated below:

$$P_{net}(t) = \beta \dot{f}^2$$

In this situation the damping terms are used to represent some form of mechanical take-off device, such as a piezoelectric strip for example. Note that as the energy consumed in forcing the system is considered to be harvested freely from the environment, it is not necessary subtract this from $P_{net}$. This will still achieve a conservative estimate. For simplicity, and neglecting any other forms of mechanical losses, it will be assumed that all energy dissipated via the damping can be available for harvesting.

Fig. 2.8 shows simulations measuring the instantaneous power, $P_{net}(t)$ that repeats the conditions from Fig. 2.7 in Section 2.5.3. This corroborates the previous observation that when $P_{static} = 0.05$N barely any response is registered. This is shown by barely any power being dissipated through the system under these conditions. Then as $P_{static}$ is increased, a marked improvement in $P_{net}(t)$ is seen. This improvement has been achieved passively since no power is required to maintain the value of $P_{static}$. It can be seen that the only steady-state response is generated when $P_{static} = 0.25$N in Fig. 2.8(c). This also appears to provide the greatest peak $P_{net}(t)$ of approximately 0.068W, and is associated with the trajectory that orbited the two outer attractors that produced the greatest $f$ in Fig. 2.7(h).

However, actually drawing definitive conclusions from observations of the instantaneous power dissipated is difficult, and a more improved method by which to assess

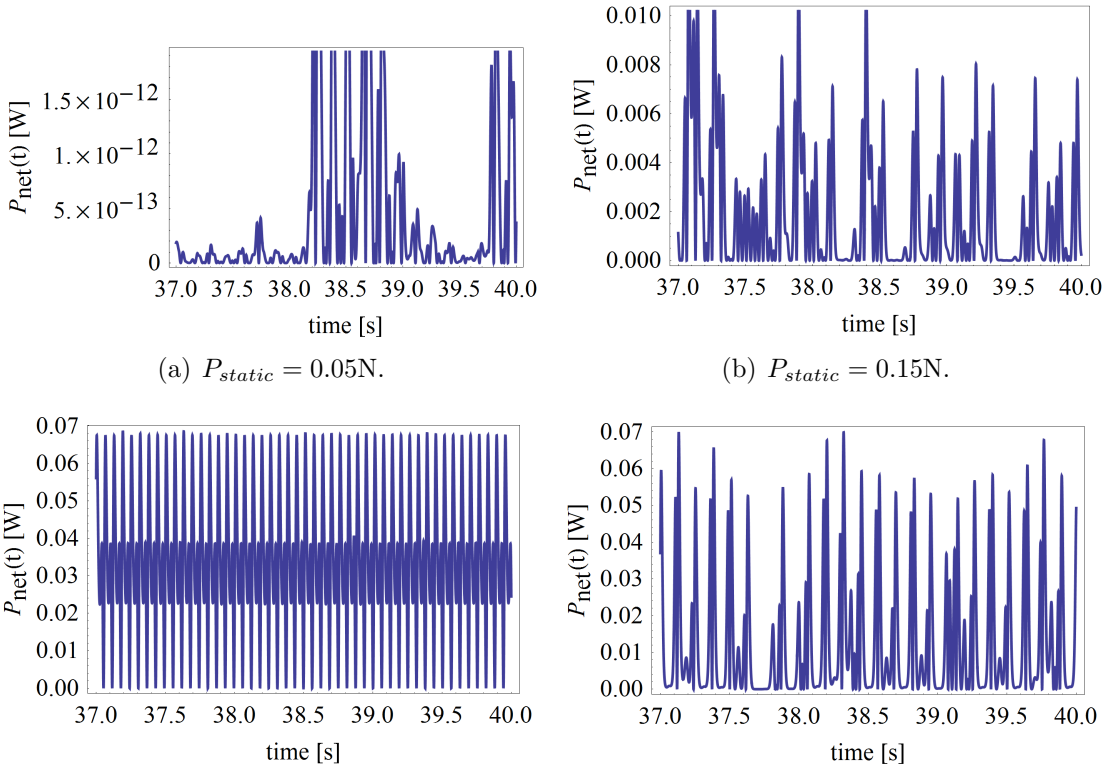


(a) $P_{static} = 0.05$N. (b) $P_{static} = 0.15$N.

(c) $P_{static} = 0.25$N. (d) $P_{static} = 0.35$N.

Figure 2.8: Instantaneous power dissipated by $\beta\dot{f}^2$ where $P_{crit} = 0.055$N, $P_{dynamic} = 0.2$N, $A = 2.5 \times 10^{-6}$m $^2$, $l = 0.35$m, $E = 13$GPa, $\rho = 1900$kg/m$^3$, $\zeta = 0.3$, $\Omega = 100$rad/s, $f(0) = 0.00001$m, $\dot{f}(0) = 0$rad/s and $37 \leq t \leq 40$s.

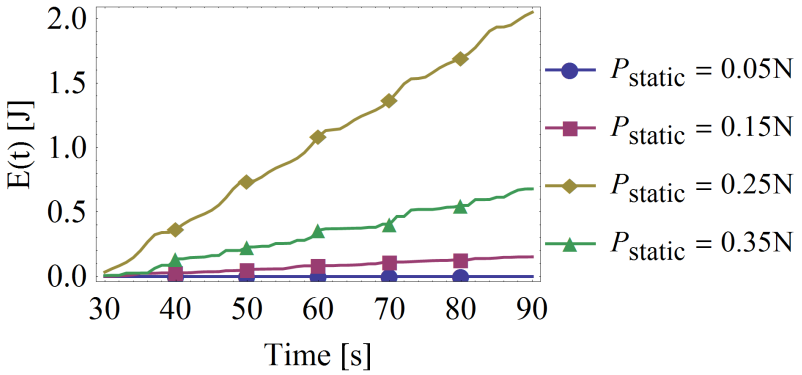


Figure 2.9: Accumulated energy, $E(t)$ via $\beta\dot{f}^2$ where $P_{crit} = 0.107$N, $P_{dynamic} = 0.1$N, $A = 2.5 \times 10^{-6}$m $^2$, $l = 0.25$m, $E = 13$GPa, $\rho = 1900$kg/m$^3$, $\zeta = 0.3$, $\Omega = 100\frac{\text{rad}}{\text{s}}$, $f(0) = 0.00001$m, $\dot{f}(0) = 0$rad/s and $30 \leq t \leq 90$s.

the performance of the harvester would be by the amount of energy that has been collected over a given time period. This can be done by simply integrating $P_{net}(t)$ over the time period in order to produce a plot like that in Fig. 2.9 where energy has been accumulated over a sixty second period which would be more practical should any future experimental measurements be taken.

This plot clearly shows the relationship $P_{static}$ has with the energy throughput of the harvester, where positive gradients refer to positive rates of energy being available for harvesting. Clearly the greatest energy throughput does occur when $P_{static} = 0.25$N for the measured range of $P_{static}$ only. This confirms previously made observations. Note that no negative gradients exist because in the present scenario, no energy is being consumed in forcing the system. $P_{static}$ is a form of passive manipulation and $P_{dynamic}$ is freely sourced from ambient conditions.

Now that the previous methods for observing the response of the system have all alluded to a peak response being generated somewhere in the region of $P_{static} = 0.25$N, it would be more useful to be able to perform parameter sweeps to observe the true nature of the responses. With an approach such as this, the performance of the system can be measured by the energy that is available for harvesting, $E_{acc}$ at the end of a given time period, where:

$$E_{acc} = \int_{t_0}^{t_n} [P_{net}(t)]\, dt \tag{2.27}$$

where $t_0$ and $t_n$ are the upper and lower limits of the time period respectively.

This is the equivalent of measuring the area under the $P_{net}(t)$ curves from Fig2.8 and each data point represents the measured energy accumulated from each such curve. Repeating this process across a range of the chosen parameter being studied will produce a swept plot. It must be noted that each simulation must be performed over the same time period for all subsequent parameter sweeps in order to produce results that may be fairly compared.

### 2.6.1 Parameter Sweeps of Static Axial Loads

First, a $P_{static}$ sweep is performed in the hope to observe a peak response in the region of $P_{static} = 0.25\text{N}$ which would corroborate with previous simulations, see Fig. 2.10. Note that the same conditions of $P_{dynamic} = 0.2\text{N}$ and $\Omega = 100\text{rad/s}$ have been maintained.

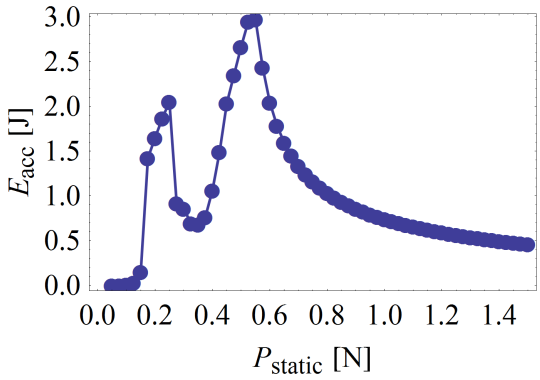


Figure 2.10: Accumulated energy, $E_{acc}$ available across $P_{static}$ where $P_{crit} = 0.055\text{N}$, $P_{dynamic} = 0.2\text{N}$, $A = 2.5 \times 10^{-6}\text{m}^2$, $l = 0.35\text{m}$, $E = 13\text{GPa}$, $\rho = 1900\text{kg/m}^3$, $\zeta = 0.3$, $\Omega = 100\text{rad/s}$, $f(0) = 0.00001\text{m}$, $\dot{f}(0) = 0\text{rad/s}$ and $30 \leq t \leq 90\text{s}$.

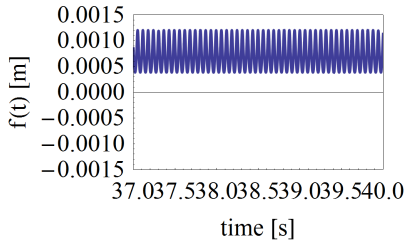


(a) $P_{static} = 0.55\text{N}$.

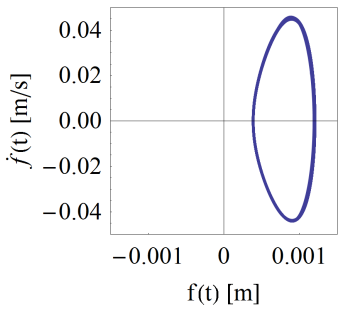


(b) $P_{static} = 0.55\text{N}$.

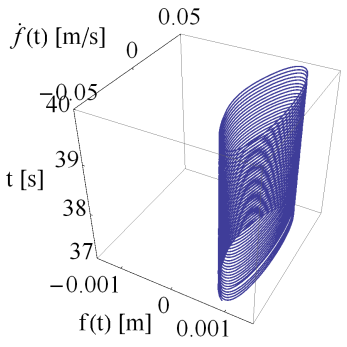


(c) $P_{static} = 0.55\text{N}$.

Figure 2.11: Time domain and phase space responses to static and dynamic loading conditions where $P_{crit} = 0.055\text{N}$, $P_{dynamic} = 0.2\text{N}$, $A = 2.5 \times 10^{-6}\text{m}^2$, $l = 0.35\text{m}$, $E = 13\text{GPa}$, $\rho = 1900\text{kg/m}^3$, $\zeta = 0.3$, $\Omega = 100\text{rad/s}$, $f(0) = 0.00001\text{m}$, $\dot{f}(0) = 0\text{rad/s}$ and $37 \leq t \leq 40\text{s}$.

This is a very interesting response because it in fact shows evidence of two peaks in performance; one at the suspected location of approximately $P_{static} \approx 0.25\text{N}$, and the second at $P_{static} \approx 0.55\text{N}$. The time domain responses in Fig. 2.11 at the location of the second peak shed some light how this second peak may be forming. Despite this only showing a trajectory that orbits about a single bistable attractor, it appears that the velocity response, $\dot{f}$ is greater than it is when $P_{static} = 0.25\text{N}$. By referring back

to Eq. 2.26 it can be seen that it is $\dot{f}^2$ that contributes to $P_{net}(t)$ and so response like this would have a much greater influences of the energy throughput.

Therefore, it must be concluded that it may not always be the case that greater displacements in response will lead to greater performances, albeit the first peak is located at the site of greatest displacement in the shown simulations. Moreover it is the velocity of the response that should be of primary concern when optimising the throughput of the harvester as this contributes more towards the instantaneous power being dissipated.

### 2.6.2 Excitation Sweeps of the Periodically Excited System

Up until now, all previous simulations have been performed with a fixed excitation frequency of $\Omega = 100$rad/s such that the excitation frequency does not track resonant conditions as constituents are varied. Typically for linear parametric systems, PPR occurs at $\Omega = 2\omega_n$, but knowing that full nonlinearity has been maintained for the current system, this location may have been shifted somewhat. Based upon the conditions at the location of the larger $2^{\text{nd}}$ peak response in Fig. 2.10 where $P_{static} = 0.55$N, $P_{crit} = 0.055$N, $l = 0.35$m and $m = 0.00475$kg, then the associated fundamental natural frequency is equal to $\omega_n = 91.67$rad/s, or $\frac{\Omega}{\omega_n} = 1.09$. This is clearly far removed from the linear location of PPR and is evidence of stiffness nonlinearities within the system.

By performing an excitation ratio sweep, the underlying characteristics governing this behaviour are revealed.

Fig. 2.12 does indeed show evidence of softening nonlinearities present within the system, evident by the response curve leaning towards the left of the plot. It also shows the peak response generated in the approximate location of $P_{static}$ that was expected by previous results. Further to this, Fig. 2.13 shows that for increasing values of $P_{static}$ in this range, the effect upon the nonlinear behaviour is minimal. This is observed by the peak responses occurring at approximately the same location for the simulations in Fig. 2.13.

Another feature to be noted from this is that provided resonant conditions are maintained, then increasing $P_{static}$ has the effect of increasing the throughput of the

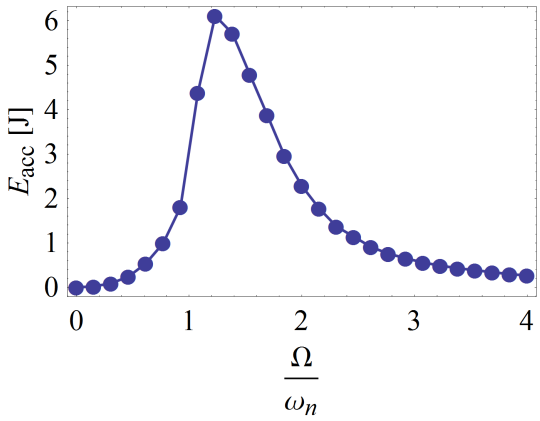


Figure 2.12: Excitation frequency sweeps at location of second peak, where $P_{crit} = 0.055\text{N}$, $P_{static} = 0.55\text{N}$, $P_{dynamic} = 0.2\text{N}$, $A = 2.5 \times 10^{-6}\text{m}^{\,2}$, $l = 0.35\text{m}$, $E = 13\text{GPa}$, $\rho = 1900\text{kg/m}^3$, $\zeta = 0.3$, $f(0) = 0.00001\text{m}$, $\dot{f}(0) = 0\text{rad/s}$ and $30 \leq t \leq 90\text{s}$.

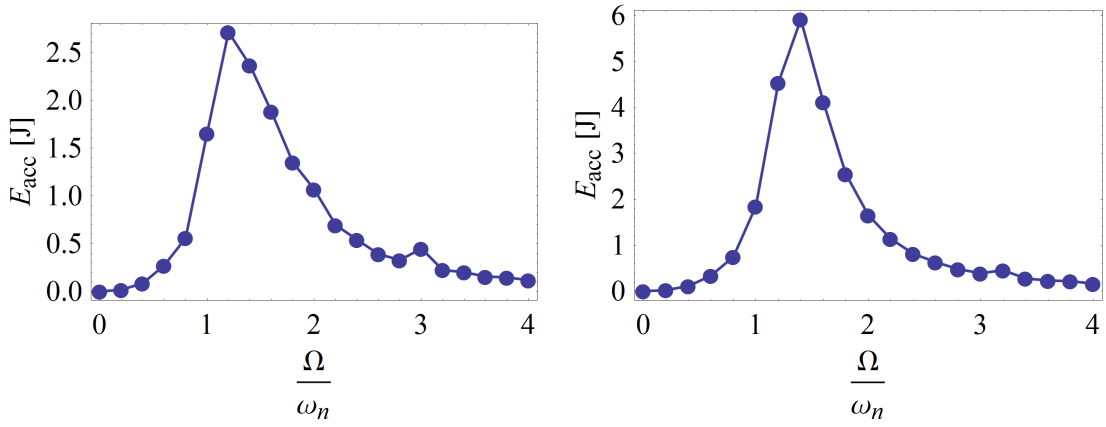


(a) $P_{static} = 0.5\text{N}$.




(b) $P_{static} = 1.0\text{N}$.

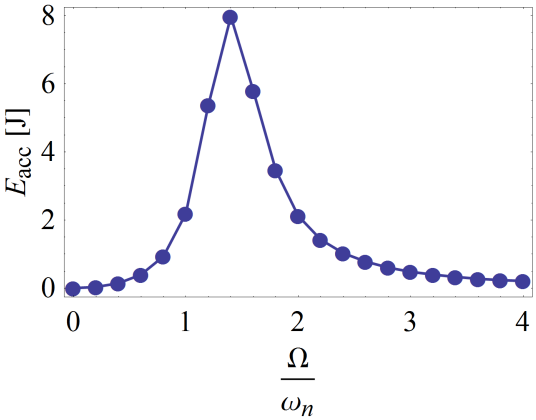


(c) $P_{static} = 1.5\text{N}$.

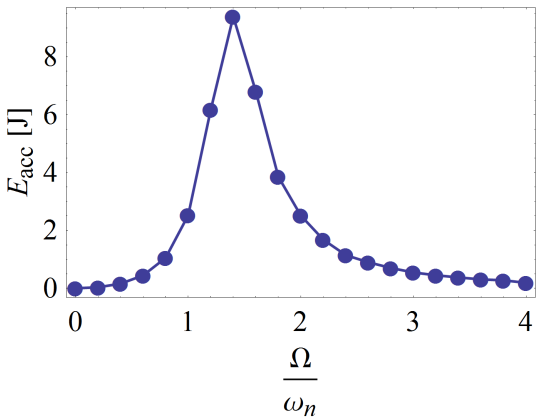


(d) $P_{static} = 2.0\text{N}$.

Figure 2.13: Excitation frequency sweeps for increasing values of $P_{static}$, where $P_{crit} = 0.055\text{N}$, $P_{dynamic} = 0.2\text{N}$, $A = 2.5 \times 10^{-6}\text{m}^{\,2}$, $l = 0.35\text{m}$, $E = 13\text{GPa}$, $\rho = 1900\text{kg/m}^3$, $\zeta = 0.3$, $f(0) = 0.00001\text{m}$, $\dot{f}(0) = 0\text{rad/s}$ and $30 \leq t \leq 90\text{s}$.

system. This is because $\omega_n$ is a function of $P_{static}$ and so this acts as a tuning mechanism. Given that in this form of sweep where the excitation is a ratio of the natural frequency, then higher values of $P_{static}$ will result in the excitation frequency at resonance being higher too, hence more energy becomes available for harvesting.

However, given that the excitations that the harvester will be collecting in practice will be sourced from ambient conditions, it is unlikely that they will be controllable without some form of active tuning (which in itself would consume power). In this study it will be the harvester that will have to be *passively* tuned to the source vibrations and hence there will remain a peak value of $P_{static}$ for the given fixed excitation.

To further explore the nonlinear influences that $P_{static}$ may have, the behaviour as the system changes from a uni-stable state to a bistable state is observed. This is done by repeating the previous simulation for values of $P_{static}$ in the region of $P_{crit}$, where $P_{crit} = \frac{EI\pi^2}{l^2}$.

Fig. 2.14 shows that at low values of $P_{static}$ in the region of $P_{crit}$ the system response moves from one that is governed by hardening stiffnesses, to one that is governed by softening stiffnesses. In practice, this means that when the beam has no initial pre-curvature applied to it, it exists as a hard system with much higher frequencies required to generate peak responses. But as $P_{static}$ is made much greater than $P_{crit}$ and a pre-curvature is formed, the system softens with resonance occurring at lower frequencies. It is interesting to observe that the greatest throughput of the harvester only seems to be seen when the system is predominately soft, such as in Fig. 2.13, and that the extent of the softening appears to approach the approximate location of $\frac{\Omega}{\omega_n} = 1.0$.

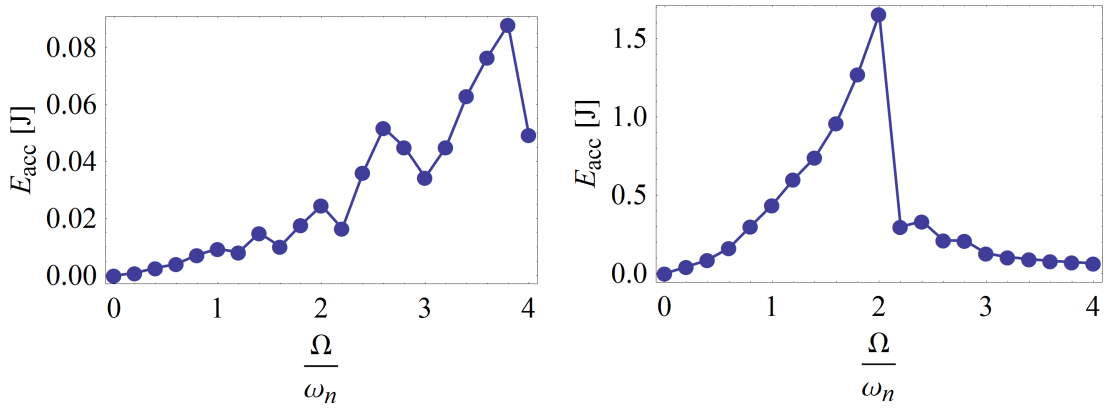


(a) $P_{static} = 0.05$N. (b) $P_{static} = 0.2$N.

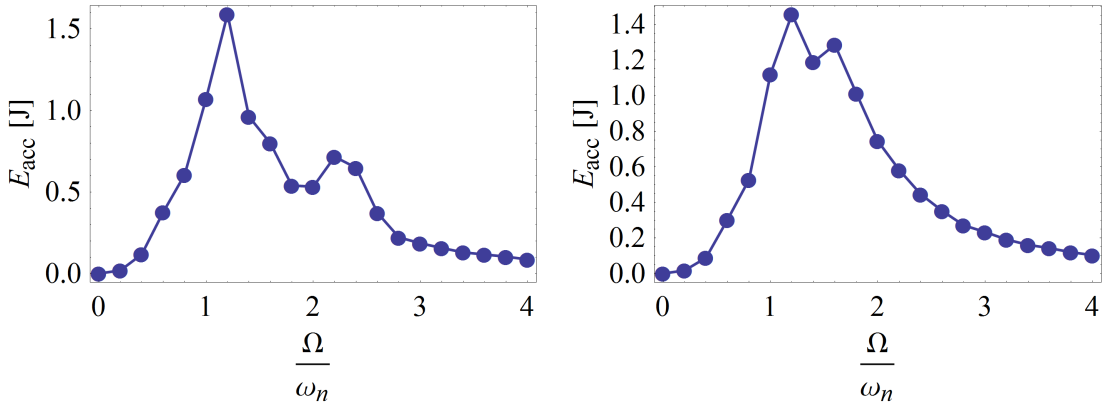


(c) $P_{static} = 0.3$N. (d) $P_{static} = 0.4$N.

Figure 2.14: Excitation frequency sweeps for increasing values of $P_{static}$ in the region of $P_{crit}$, where $P_{crit} = 0.055$N, $P_{dynamic} = 0.2$N, $A = 2.5{\times}10^{-6}\text{m}^{\,2}$, $l = 0.35$m, $E = 13$GPa, $\rho = 1900\text{kg/m}^3$, $\zeta = 0.3$, $f(0) = 0.00001$m, $\dot{f}(0) = 0$rad/s and $30 \leq t \leq 90$s.

### 2.6.3 Influences of Amplitude of Dynamic Forcing

Next the effects of $P_{dynamic}$ are assessed to see if there exists a peak value when operated at a fixed frequency. $\Omega = 100$rad/s has been used again for consistency with previous simulations. Clearly Fig. 2.15 shows starkly different behaviour to that seen before, where now increasing values of $P_{dynamic}$ lead to ever increasing values of $E_{acc}$. However, such behaviour is perhaps not unexpected. It is known that $P_{dyanmic}$ terms have not been included within the derivation of $\omega_n$ and is therefore independent of the location of resonance. But more importantly, the excitation frequency $\Omega$ itself remains fixed during the course of the simulation and therefore by increasing the amplitude at this fixed frequency, the amount of energy being fed into the system can only increases too. Considering that the power take-off terms are represented by the damping within the system, if more power is fed into the system then more power will be available for harvesting. From observed time domain responses, chaotic motions are evident for some values of $P_{dynamic}$, and these can be attributed to the fluctuations in $E_{acc}$ across the shown plot. However, the predominant trend appears to be approximate linear between $P_{dynamic}$ and $E_{acc}$ as seen in Fig. 2.15.

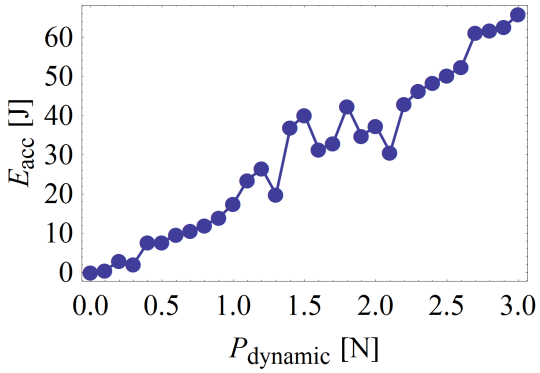


Figure 2.15: Accumulated energy, $E_{acc}$ available across $P_{dynamic}$ where $P_{crit} = 0.055$N, $P_{static} = 0.55$N, $A = 2.5 \times 10^{-6}$m $^2$, $l = 0.35$m, $E = 13$GPa, $\rho = 1900$kg/m$^3$, $\zeta = 0.3$, $\Omega = 100$rad/s, $f(0) = 0.00001$m, $\dot{f}(0) = 0$rad/s and $30 \leq t \leq 90$s.

The same conclusions made about the control of the excitation frequencies, $\Omega$, can again be made with $P_{dynamic}$ in that this is sourced from the environment and as a result is likely non-controllable. Even if effort was made to control the amplitude of the harvestable vibrations, this would consume energy in the active process, whilst also wasting the maximum potential of the source.

It is for these reasons that the study will now explore methods for optimising the response of the harvester subjected to particular excitation conditions. There exist three readily modifiable parameters for the given design:

- $P_{static}$, the effects of which have already been discussed.
- $\zeta$, which is used to control the level of damping within the system that subsequently affects the strength of the energy dissipation of the representative power take-off.
- $l$, which controls the length of the harvester that subsequently affects the location of resonance.

### 2.6.4 The Effects of Damping within the Harvester

The response may also be affected via the level of damping within the system, which may be controlled by the damping ratio, $\zeta$ where $\beta\dot{f}^2$ and $\beta = 2\zeta m\omega_n$. As previously discussed, these terms have been defined to represent some form of power-take off device. Increasing $\zeta$ would allow the damper to dissipate more of the energy fed into the system by the harvestable source, but crucially at the cost of inherently affecting the resulting response. This could be likened to increasing the thickness of a piezoelectric strip attached to the beam of the harvester. Therefore, one may expect there to be an optimum level of damping through which to dissipate energy from the system.

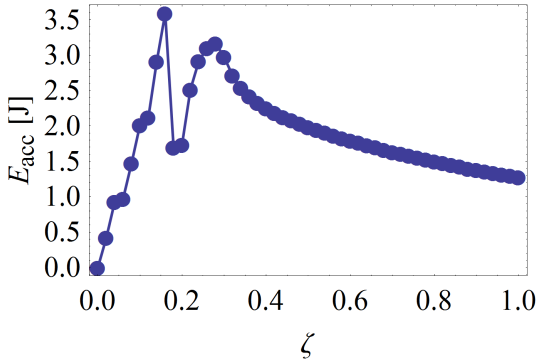


Figure 2.16: Accumulated energy, $E_{acc}$ available across $\zeta$ where $P_{crit} = 0.055$N, $P_{static} = 0.55$N, $P_{dynamic} = 0.2$N, $A = 2.5 \times 10^{-6}$m $^2$, $l = 0.35$m, $E = 13$GPa, $\rho = 1900$kg/m$^3$, $\zeta = 0.3$, $\Omega = 100$rad/s, $f(0) = 0.00001$m, $\dot{f}(0) = 0$rad/s and $30 \leq t \leq 90$s.

In fact, two peak values of $\zeta$ are presented in Fig. 2.16. The first, when $P_{static} = 0.55\text{N}$, $P_{dynamic} = 0.2\text{N}$ and $\Omega = 100\text{rad/s}$, appears to be located at $\zeta \approx 0.15$ and from time domain responses is shown to orbit about both bistable attractors, see Fig. 2.17(a). The second peak response is shown to be when $\zeta \approx 0.275$, and is associated with trajectory orbiting about a single attractor in a similar manner as observed in Section 2.6.1, only now the peak velocity is lower and accounts for the lower peak $E_{acc}$, see Fig. 2.17(b).

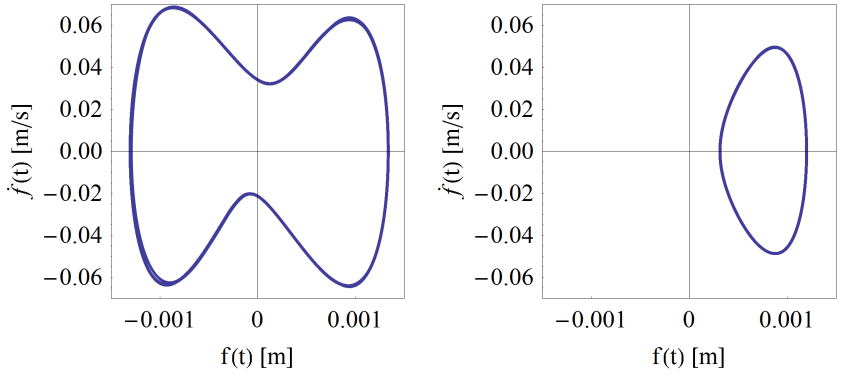


(a) $\zeta = 0.15\text{N}$. (b) $\zeta = 0.275\text{N}$.

Figure 2.17: Time domain and phase space responses to static and dynamic loading conditions where $P_{crit} = 0.055\text{N}$, $P_{static} = 0.55\text{N}$, $P_{dynamic} = 0.2\text{N}$, $A = 2.5 \times 10^{-6}\text{m}^2$, $l = 0.35\text{m}$, $E = 13\text{GPa}$, $\rho = 1900\text{kg/m}^3$, $\Omega = 100\text{rad/s}$, $f(0) = 0.00001\text{m}$, $\dot{f}(0) = 0\text{rad/s}$ and $37 \leq t \leq 40\text{s}$.

To assess whether $\zeta$ imparts any nonlinear effects upon the system, numerous sweeps were performed in Fig. 2.18. All the simulations shown look very similar in nature with the peak response occurring within the same region, suggesting that the effects of damping are independent of the inherent nonlinear stiffnesses in the system. However, what is clear is that $\zeta$ is capable of increasing the operational bandwidth of the harvester. This can be a very beneficial feature because in the event that $\Omega$ may fluctuate over time, it would be advisable to have a wide bandwidth, and hence select a higher value of $\zeta$ in order to maintain increased performance. This would of course be at the cost of a lower peak operating response, and so this would have to be judged upon the excitation conditions in practice.

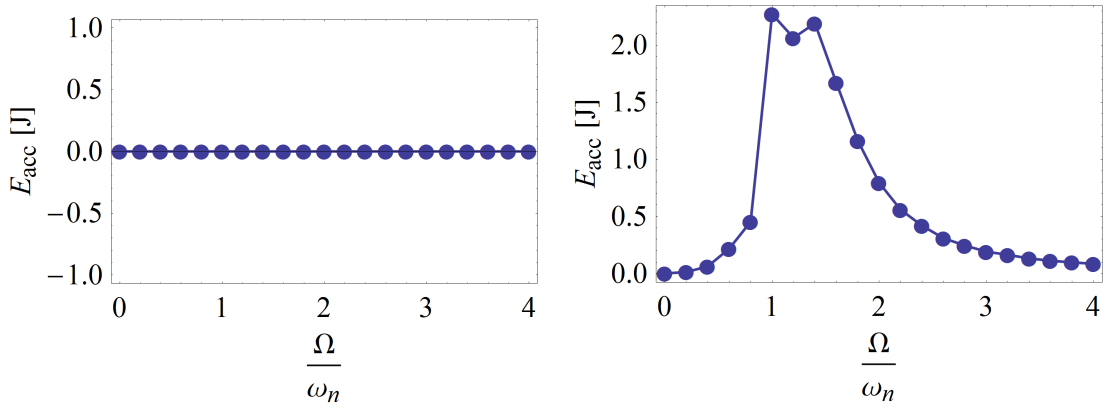


(a) $\zeta = 0.0$N.




(b) $\zeta = 0.2$N.

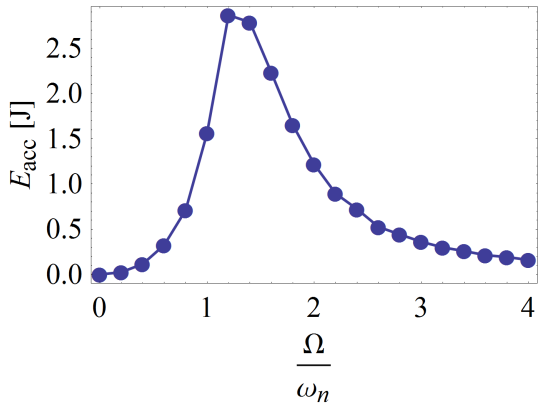


(c) $\zeta = 0.4$N.

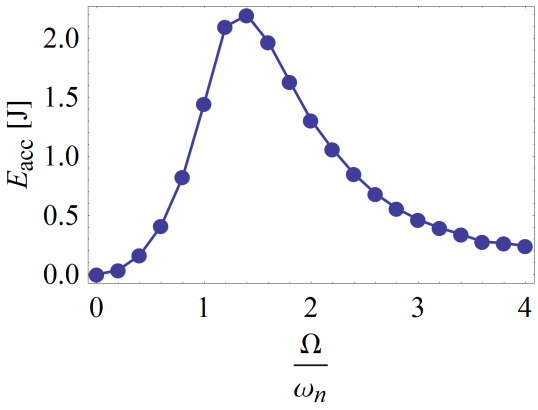


(d) $\zeta = 0.6$N.

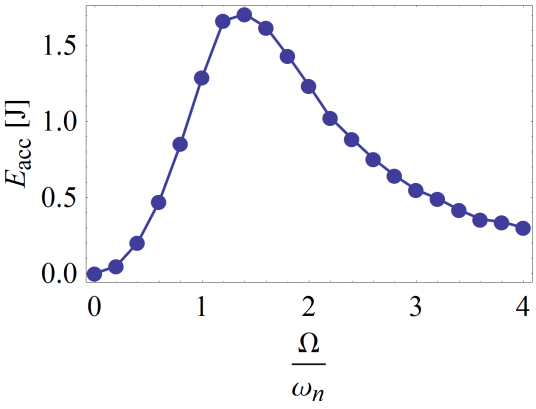


(e) $\zeta = 0.8$N.

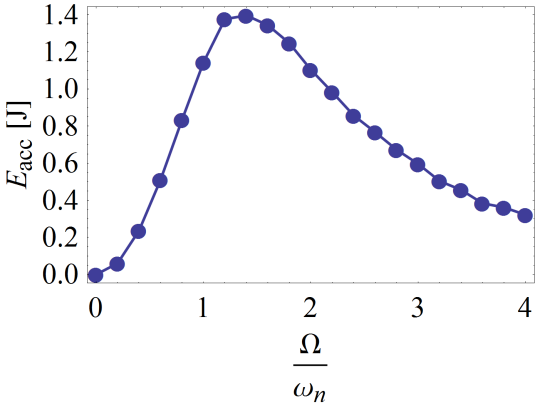


(f) $\zeta = 1.0$N.

Figure 2.18: Excitation frequency sweeps for increasing values of $\zeta$, where $P_{crit} = 0.055$N, $P_{static} = 0.55$N, $P_{dynamic} = 0.2$N, $A = 2.5 \times 10^{-6}$m $^2$, $l = 0.35$m, $E = 13$GPa, $\rho = 1900$kg/m$^3$, $f(0) = 0.00001$m, $\dot{f}(0) = 0$rad/s and $30 \leq t \leq 90$s.

### 2.6.5 The Effects of the Length of the Harvester

The effective length, $l$ of the harvester beam is another property that will affect the response of the system. So too will varying the cross-sectional area, $A$, but given that the length of the beam could be considered a more viable mechanism by which to affect the system in practice, attention is given to this. It has already been shown by Eq. 2.17, and depicted in Fig. 2.2 that manipulation of $l$ will affect the value of $\omega_n$ and so it is again expected that a peak value of $l$ will exist.

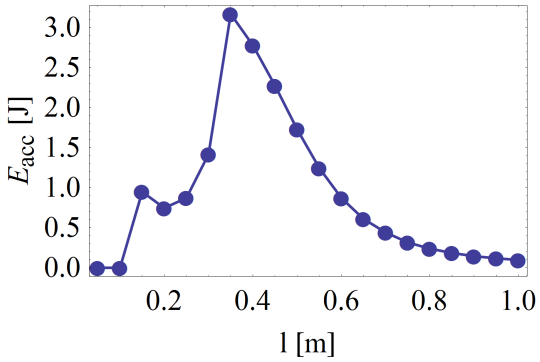


Figure 2.19: Accumulated energy, $E_{acc}$ available across $l$ where $P_{crit} = 0.055$N, $P_{static} = 0.55$N, $P_{dynamic} = 0.2$N, $A = 2.5 \times 10^{-6}$m $^2$, $E = 13$GPa, $\rho = 1900$kg/m$^3$, $\zeta = 0.275$, $\Omega = 100$rad/s, $f(0) = 0.00001$m, $\dot{f}(0) = 0$rad/s and $30 \leq t \leq 90$s.

Following the same processes used with the previous parameter studies, a sweep of $l$ is performed first where $P_{static} = 0.55$N, $P_{dynamic} = 0.2$N, $\Omega = 100$rad/s together with the new optimum value of $\zeta = 0.275$ that was discovered in Section 2.6.4.

Fig. 2.19 shows a peak value of $l = 0.35$m for the given conditions, which is the value that has been used in all the previous simulations. This result was perhaps to be expected if one considers that processes up to this point may have acted as an informal optimisation process. This in itself is very encouraging.

However, the multiple excitation sweeps in Fig. 2.20 do suggest some effect of the nonlinearities of the system at low values of $l$. It can be seen in Fig. 2.20(c) that the system response is governed by hardening stiffnesses when $l = 0.1$m. However, by increasing $l$ by as little as 0.1m so that $l = 0.2$m, it can be seen that the system response becomes soft. From this point on the location of resonance remains more or less unaffected in the position that has come to be expected. This is very interesting and closely resembles behaviour seen when $P_{static}$ is within the region of $P_{crit}$. In fact,

this is precisely what is happening because when $l = 0.1$m, the associated $P_{crit} = 0.69$N where $P_{crit} = \frac{EI\pi^2}{l^2}$. Now consider that in the simulation $P_{static} = 0.55$N, the result is that the beam possesses no initial pre-curvature and thus manifests itself as a hard system. However, when $l = 0.2$m and the associated $P_{crit} = 0.17$N, then $P_{static}$ is now large enough to apply an initial pre-curvature in the beam and the system becomes predominately soft.

This is the same effect that has been shown to be brought about by varying $P_{static}$ within the region of $P_{crit}$ (see Section 2.6.1). It must still be concluded that from all previous simulations, including this one, the peak performance of the harvester occurs when the system is governed by softening nonlinearities, and that these conditions should be sought after in practice. Once more, it appears that the location of peak performance is tending towards $\frac{\Omega}{\omega_n} = 1.0$.

This is certainly a very interesting feature, and certainly one that warrants further investigation. To this end, the author does suggest doing so, but that this will take place at a future date. As such, suggestions towards this body of work will be discussed in Chapter 7, to which the reader is referred.

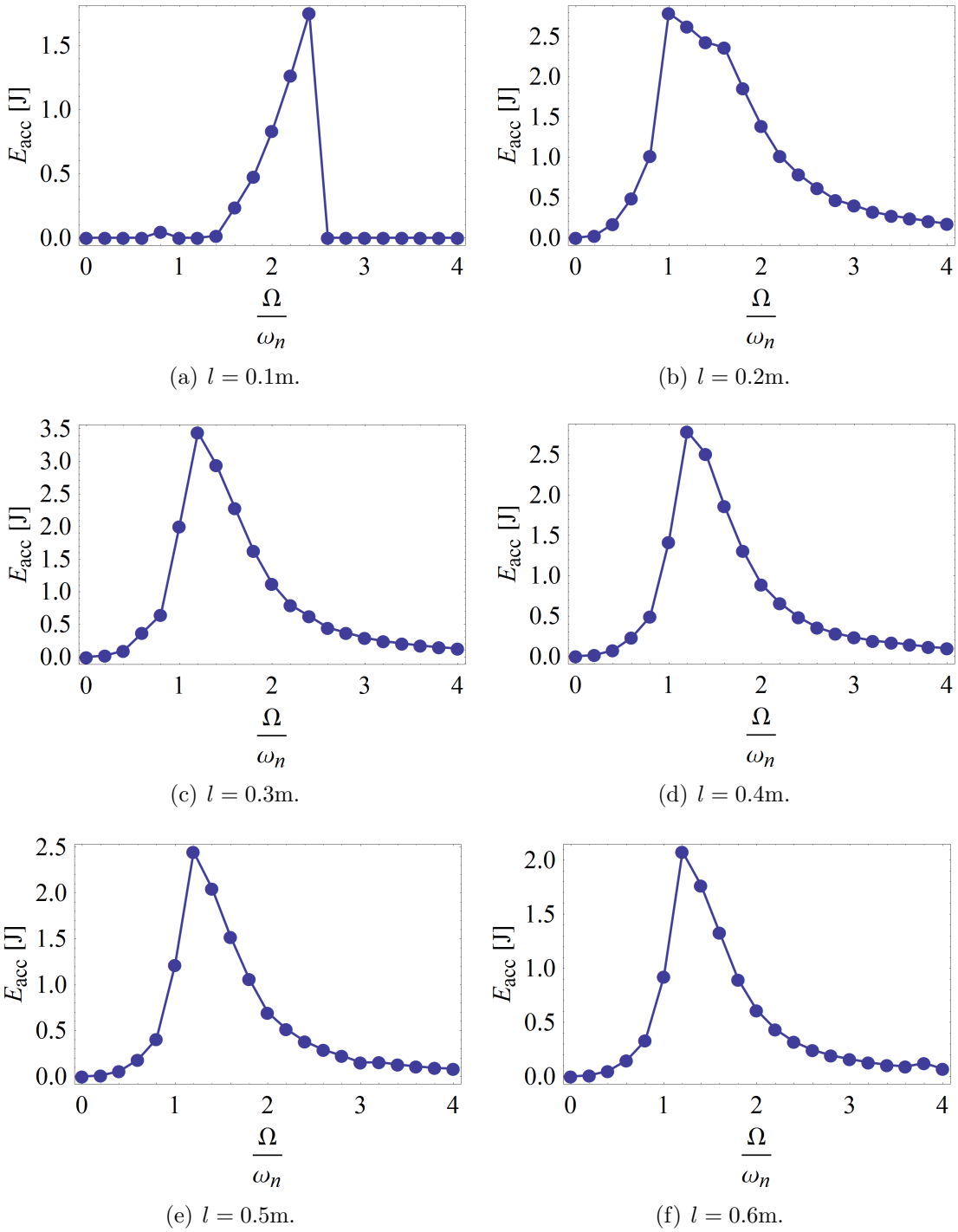


(a) $l = 0.1$m. (b) $l = 0.2$m.

(c) $l = 0.3$m. (d) $l = 0.4$m.

(e) $l = 0.5$m. (f) $l = 0.6$m.

Figure 2.20: Excitation frequency sweeps for increasing values of $l$, where $P_{crit} = 0.055$N, $P_{static} = 0.55$N, $P_{dynamic} = 0.2$N, $A = 2.5 \times 10^{-6}$m $^2$, $E = 13$GPa, $\rho = 1900$kg/m$^3$, $\zeta = 0.275$, $f(0) = 0.00001$m, $\dot{f}(0) = 0$rad/s and $30 \leq t \leq 90$s.

## 2.7 Summarising Remarks for the Periodic Euler Strut Energy Harvester

An Euler strut based energy harvester has been proposed that could be used to harvest *known* steady-state periodic vibrations from ambient conditions in the environment. The performance of the system was assessed in numerous capacities. Firstly, the response of the system was observed under static loading conditions and it was shown that no lateral displacements were generated when $P_{static} < P_{crit}$. This was to be expected and it was shown that a response only formed when the critical buckling capacity in the beam was exceeded. This lent credit that the governing equation of motion that was derived was functioning correctly.

Following this, it was shown that under dynamic loading conditions only, $P_{dynamic}$ could be used to oscillate the system in and out of a bistable state, but that a basin of attraction always existed at the *unstressed position*. By applying an initial pre-load to the beam in the form of $P_{static}$, this unstressed attractor could be removed. Provided that $P_{dynamic}$ was large enough to surmount the potential barrier between the two potential wells in the now bistable system, the response would be able to oscillate between the bistable attractors resulting in an increased lateral displacement. However, if $P_{static}$ was made larger yet, then the response of the system was shown to become trapped within a single potential well, but that this could generate a response with greater velocity responses.

By observing the energy throughput of the system it was shown that a $P_{static}$ sweep would produce a curve with two peaks; one located at the site of greatest displacement response, $f$, and the other at the site of greatest velocity response, $\dot{f}$. The peak associated with the greater velocity response was shown to be the largest for the given conditions, and therefore this would be the optimum operating value of $P_{static}$. This successfully showed that the response of the harvester could be enhanced *passively* considering that no power was required to maintain this response.

It was also shown that the inherent nonlinearity of the system could be controlled via $P_{static}$. When $P_{static} < P_{crit}$, the beam would have no initial pre-curvature and the system was governed by hardening stiffnesses. However, as $P_{static}$ was increased above

$P_{crit}$, softening nonlinearities would become dominant and the peak response appeared to tend towards a resonant condition of $\frac{\Omega}{\omega_n} = 1.0$. Further investigations are required to conclusively state this, but the results are indicative.

Considering that the power take-off of the harvester was being represented by damping, numerous simulations were performed to assess the influence that the damping ratio would have upon the performance of the system. This could be considered equivalent to increasing the thickness of a piezoelectric strip attached to the beam if this was the chosen power take-off device. A peak value was noted, and also that increased values of $\zeta$ were able to increase the operational bandwidth of the harvester. This of course came at the cost of producing lower peak responses and it was suggested that a compromise would have to be reached based upon the actual excitation conditions in practice.

Finally, the effects that the length of the beam had upon the system were also explored. Once again, a peak value of $l$ existed for the given conditions, but further to this, similar behaviours were seen to that when $P_{static}$ was applied within the region of $P_{crit}$. When $l$ was set low, hardening stiffnesses governed the system response. But when $l$ increased, the response become predominately soft again, once more tending towards the peak location of $\frac{\Omega}{\omega_n} = 1.0$. This was because varying $l$ has the subsequent effect of varying $P_{crit}$. Therefore, when $l$ was low enough so that the applied $P_{static}$ was less than $P_{crit}$, the same behaviour as previously noted occurred. And of course, as $l$ was increased, $P_{crit}$ subsequently decreased until $P_{static}$ was able to buckle the beam and the system became soft.

The most promising observation from the parameter study of $l$ was that the peak value occurred almost precisely at the value that had been applied in all previous simulations. This was because within all the earlier parameter studies, the system was been continually optimised until the point where the final parameter of $l$ was explored, the system was already in an optimised condition. This was achieved passively and showed that indeed the energy throughput of the periodically excited Euler strut harvester could be greatly enhanced using the discussed techniques.

# Chapter 3

# Stochastic Vibrational Energy Harvestering

In Chapter 2 the concept of harvesting vibrational energy using an Euler strut based harvester was explored. This particular harvester was periodically excited axially and had the facility to apply an initial pre-curvature to the beam using a static axial load which was demonstrated to be able to enhance the response passively. However, the underlying restriction of the system was that it was excited by steady-state 'known' vibrations, and albeit methods were explored that would enable the user to control the operational bandwidth, the harvester was ultimately restricted to excitations of this form. Furthermore, such stable vibrations could be difficult to find naturally occurring in practice, and therefore the application of the harvester itself would be limited. If non-steady-state vibrations were the intended target of the energy harvester, then it would be desirable to seek an alternative approach that was able to circumvent this particular restriction altogether.

To this end, this chapter will now seek to propose a new concept of harvester that has the potential to benefit from the cumulative effects of both deterministic and stochastic inputs into a parametric system. Not only would this form of active manipulation relieve the requirement for stable frequencies of excitation because the source vibrations would be stochastic in nature, but by conditioning the system to become bistable in a similar way as previously shown, the enhancing effects of stochastic resonance (SR) may possibly be exploited.

However it must be noted that it was during this particular phase of study that the author was presented the opportunity to collaborate with industry on two funded feasibility studies (see Appendix D for details) of a completely separate and novel form of pendulum based energy harvesting system, of which will be discussed fully in following chapters. It is for this reason that the scope of work in the current chapter does not entail as a comprehensive analysis of the stochastic Euler strut harvester as previously undertaken in Chapter 2. Moreover, it presents and details the derivation of the system inclusive of a preliminary study of the time domain responses sought after. This is followed by a discussion regarding possible methods for measuring the energy throughput with a number of potential future works that would be of high interest to pursue.

The proposed energy harvester is in fact a modified version of the previous periodically excited Euler strut, which in itself was inspired by the early work of Watt and Cartmell (1994) [95] as was discussed. However, both Chapter 2 and the original work by Watt and Cartmell (1994) [95] highlight the sensitivity that all externally loaded parametric systems have to excitation frequencies, where even minor shifts may result in significant drops in response. This presents a practical limitation in the field of energy harvesting unless the excitation frequency of the harvestable source vibration is well known and understood to be steady; the conditions required by the previously discussed periodic harvester.

Unfortunately this set of requirements limits the functionality and flexibility of the device itself and therefore, in an attempt to circumvent the strict limitation for a very narrow band or deterministic source of excitation, the use of stochastically resonant systems was investigated.

The underlying mechanisms involved in the phenomena observed by McInnes *et al* (2008) is a subtle coupling between PPR and SR, and it is precisely this that inspired the paradigm shift in the present study for using a bistable parametric system for harvesting energy from stochastic sources. The rationale behind this was that instead of being limited to harvesting vibrations at a known frequency, a parametric system with its potential to produce large responses could instead be subjected to stochastic vibrations in a mutually beneficial approach. Hence, the parametric oscillations would

no longer be the subject of harvested vibrations, but would instead be used as a potential well modifier to enhance the throughput of the system excited by stochastic vibrations. The objective was to observe a similar coupling effect seen by McInnes *et al* (2008), where the net gain in throughput can be greatly offset by the power consumed in artificially forcing the parametric system periodically.

## 3.1 Description of the Proposed System for Harvesting Stochastic Excitations

As shown by Fig. 3.1, the proposed stochastically excited vibrational energy harvester is very similar to the periodically excited Euler strut based energy harvester discussed in Chapter 2, but instead of harvesting axially applied steady-state vibrations, now lateral stochastic vibrations are harvested from ambient environmental conditions. Again, the system has the facility to apply both a static and a dynamic load axially, where the static load can once more be used to apply an initial pre-curvature to the beam to force a bistable state, whilst the dynamic load is now used to modulate the potential barrier between the two stable states. The intention is that by modulating the potential barrier separating the two potential wells, the likelihood of transitions may be increased in a mutually beneficial manner. This is known as SR and the reader is referred to Section 1.5.4, which discusses this phenomena in greater detail.

In Fig. 3.1, the Euler strut is constrained within a structure free to move laterally with respect to the beam and is hinged at both ends with static and dynamic loads applied axially. The beam itself is modelled as having a lumped mass at the centre to capture the essential behaviour of the harvester. As discussed, the static axial load is used to exceed the inherent buckling point of the beam to produce a pre-curvature. As the beam (planar in this example) must buckle to either one of two sides of the *unstressed zero reference line*, bistability can thus be achieved. The dynamic load can also be applied in the form of parametric oscillations to modulate the potential barrier between the two stable states. Finally, the encasing structure is excited by stochastic vibrations acting laterally to the beam (whether orientated vertically as shown, or horizontally). These stochastic vibrations are to be considered as sourced

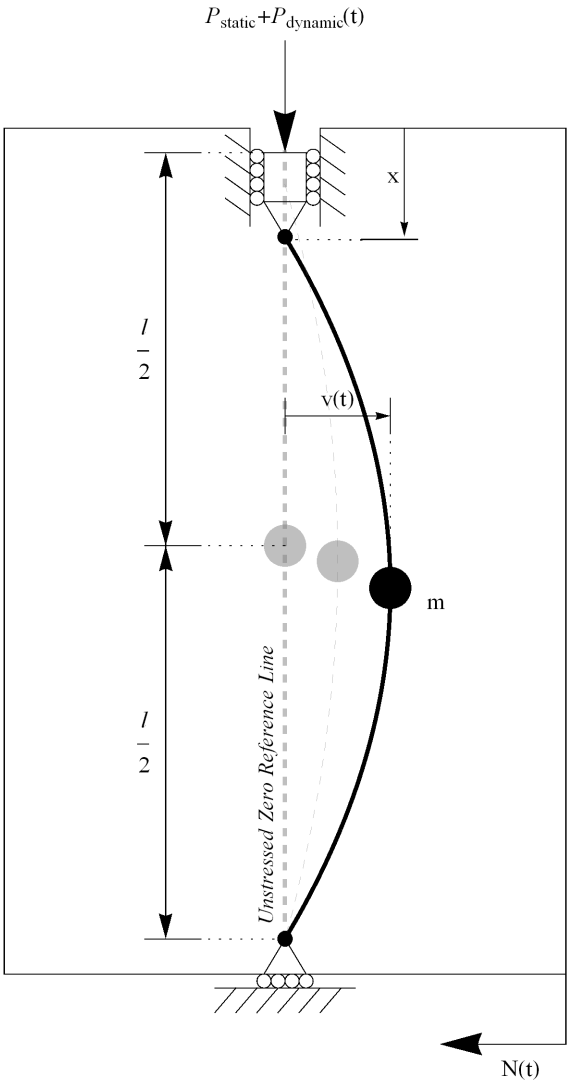


Figure 3.1: An encased buckled beam of length, $l$, with lumped mass, $m$, hinged at both ends, with static and dynamic loads applied axially, $P_{static}$ and $P_{dynamic}$ respectively. The stochastic element, $N(t)$ is also applied laterally to the encasing structure itself, and is considered to be sourced from the environment.

*freely* from the environment and are the subject of the harvestable energy. Once more, the response of the system is measured as lateral displacements of the lumped mass centre of the beam relative to the *unstressed zero reference line*, and hence in this sense the displacement of the casing due to the stochastic input is not measured directly, only its influence upon the response of the beam.

## 3.2 Governing Equation of Motion of the Stochastically Excited Euler Strut

It has been mentioned that the stochastically excited energy harvester is very similar in construct to the periodically excited harvester described in Chapter 2. The result is that the derivation of the equation of motion follows mostly the same form. In fact the only addition to the derivation is the inclusion of the lateral stochastic term. Therefore, for simplicity only the key steps of the derivation will now be repeated, but the reader is referred to Chapter 2 for a more detailed derivation process. The crucial addition here when compared to the harvester form Chapter 2 is $N(t)$, which is the function used to represent the stochastic *noise* input.

By applying Newtons 2$^{\text{nd}}$ Law, the system can be described by:

$$\frac{\partial^2 M}{\partial x^2} + \left[P - \frac{EA}{2l}\int_0^l \left(\frac{\partial v_0}{\partial x}\right)^2 dx\right]\frac{\partial^2 v_0}{\partial x^2} + \left[P - \frac{EA}{2l}\int_0^l \left(\frac{\partial v}{\partial x}\right)^2 dx\right]\frac{\partial^2 v}{\partial x^2} - q = -m\ddot{N} \tag{3.1}$$

The dynamic response of the system, $f$ is only form that is of interest for the following analysis again, which is governed by:

$$\ddot{f} + \beta\dot{f} + \frac{\pi^2}{ml^2}\left[P_{crit} - P_{static} - P_{dynamic}\cos\Omega t\right] f + \frac{EA\pi^4}{4ml^4} f^3 = -\ddot{N}(t) \tag{3.2}$$

### 3.2.1 Obtaining an Expression Describing the Natural Frequency of the Stochastically Excited Energy Harvester

Of course, an expression describing the natural frequency of the system must be derived in order to perform any comprehensive analysis.

As can be seen by Eq. 3.2, the natural frequency of the system is not in any way governed by the additional terms used to define the stochastic input, $\ddot{N}(t)$, and therefore the operations by which an expression for $\omega_n$ was obtained in Chapter 2 stands true for the present harvester. Of the loading conditions, the natural frequency is only to be a affected by $P_{static}$ in order to avoid a complicated time-varying expression.

For a more complete understanding of how the following was obtained, the reader is referred to Section 2.2.1. Accepting this, the final equation of motion and natural frequency for the stochastically excited energy harvester are described by:

$$-\ddot{N}(t) = \begin{cases} \ddot{f} + \beta\dot{f} + \left({\omega_n}^2 - \frac{\pi^2}{ml^2}\left[P_{dynamic}\cos\Omega t\right]\right) f \\ \qquad + \frac{EA\pi^4}{4ml^4} f^3 \quad ; \; P_{static} < P_{crit} \\ \ddot{f} + \beta\dot{f} - \left({\omega_n}^2 - \frac{\pi^2}{ml^2}\left[P_{dynamic}\cos\Omega t\right]\right) f \\ \qquad + \frac{EA\pi^4}{4ml^4} f^3 \quad ; \; P_{static} > P_{crit} \end{cases} \tag{3.3}$$

where:

$$\omega_n = \begin{cases} \sqrt{\frac{\pi^2}{ml^2}\left[P_{crit} - P_{static}\right]} \; ; \; P_{static} < P_{crit} \\ \sqrt{\frac{\pi^2}{ml^2}\left[P_{static} - P_{crit}\right]} \; ; \; P_{static} > P_{crit} \end{cases} \tag{3.4}$$

In Eq. 3.4, $P_{dynamic}$ has again been excluded to avoid complications that would arise from a time varying expression for $\omega_n$. The equation of motion has also been suitably manipulated to satisfy the requirements for a negative overall linear stiffness under both conditions where $P_{static} > P_{crit}$ & $P_{static} < P_{crit}$. This has been captured with the implementation of the piecewise conditions shown.

## 3.3 Expressing the Effective Potential of the Stochastically Excited System

An important feature of a bistable stochastic resonator, such as the one being modelled, is the ability to modulate the potential barrier between the two stable states (where $P_{static} > P_{crit}$). In the present system, $P_{dynamic}$ is used to provide this actively controlled modulation to the barrier to effectively increase the likelihood of transitions between these two states. The actual ability for $P_{dynamic}$ to modulate the potential barrier was observed in Section 2.3 by computations of the expression describing the effective potential, $V(f)$, such that $f'' = -\frac{\partial V(f)}{\partial f}$ is defined as:

$$V(f) = \begin{cases} -\frac{1}{2}\left({\omega_n}^2 - \frac{P_{dynamic}\pi^2}{ml^2}\cos\Omega t\right) f^2 + \frac{1}{4}\left(\frac{EA\pi^4}{4ml^4}\right) f^4 \; ; \; P_{static} < P_{crit} \\ \frac{1}{2}\left({\omega_n}^2 - \frac{P_{dynamic}\pi^2}{ml^2}\cos\Omega t\right) f^2 + \frac{1}{4}\left(\frac{EA\pi^4}{4ml^4}\right) f^4 \; ; \; P_{static} > P_{crit} \end{cases} \tag{3.5}$$

It can be seen that Eq. 3.5 is identical to that discussed in Section 2.3, and so the reader is again referred to Fig. 2.3 for a visual demonstration of how the potential barrier may be manipulated.

However, as $P_{dyanmic}$ is being used as an active method by which to modulate the system, it will require work to do so that should be subtracted from the energy dissipated via the power take-off device to obtain a conservative estimate for the net harvestable energy. It is considered likely that the peak performance of the dynamic forcing terms will be located at the site of resonance associated with the current system that will be a complicated coupling between deterministic and stochastic inputs.

## 3.4 Defining the Stochastic Input

Given that an understanding of how the effective potential can be modulated by the artificial axial loads, the derivation is almost at the point where time domain simulations can be performed to assess how these modulations can be controlled to affect changes in response that effectively enhance the displacement of the mass centre of the beam. It remains to define the stochastic input $N(t)$.

White noise shall be used for the stochastic vibrations in the proposed scenario. This is defined as a sequence of random number with normal distribution with zero mean and unit variance. An interpolated function can be created to satisfy these conditions using numerical approaches. To this end a *Mathematica* code has been developed that defines and implements the random white noise as a function:

$$\ddot{\mathbf{N}}(\mathbf{t}) = \mathbf{Interpolation}[\mathbf{Table}[\{\mathbf{t}, (\psi_{\mathbf{noise}}(\mathbf{RandomReal@NormalDistribution}[\mathbf{0}, \mathbf{1}]))\}, \{\mathbf{t}, \mathbf{t}_0, \mathbf{t}_n\}]]; \tag{3.6}$$

where $t$ is time, $t_0$ is the start time, $t_n$ the end time and $\psi_{noise}$ is a user defined quantity inserted to control the average magnitude of the applied white noise.

The *Mathematica* 'Interpolation' command, as suggested, interpolates the data collected by the random normal distribution with zero mean and unit variance across the given time domain and creates a function that may be called upon in subsequent numerical integrations. If the time domain for the white noise function is ensured to always match the time limits of subsequent numerical integrations performed upon Eq. 3.3, then the interpolated function may be directly applied as $\ddot{N}(t)$. An example plot of the white noise function, $\ddot{N}(t)$ within a given time domain is shown in Fig. 3.2.

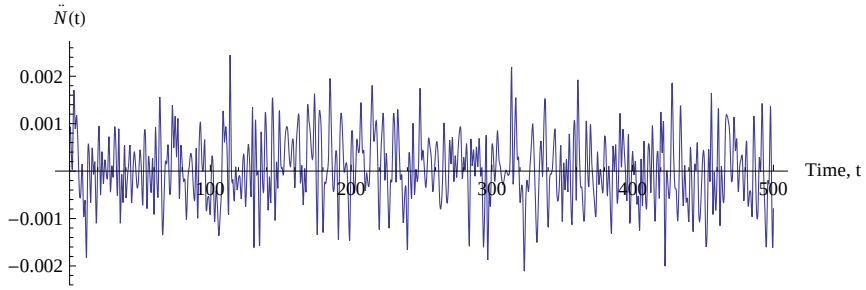


Figure 3.2: Time domain plot of white noise excitation when $\psi_{noise} = 0.5$ which has no units because is it a user defined quantity and $0 \leq t \leq 180$s.

Normally the inherent nature of the *random* normal distribution used to define $\ddot{N}(t)$ can make it difficult to present response data in various forms if doing so requires repeated simulations. Whilst it is possible to statistically predict certain qualities of a random distribution such as the mean and standard deviation for example, the precise

details within the statistical norm remain *random*. Hence, each time the command for the interpolated white noise function is performed, a unique distribution is created. It is possible to store the random function for a chosen time period in order to reuse it if necessary. However, it is important that the same $t_0$ and $t_n$ limits are used in both the normal distribution and any subsequent numerical integrations in order for this to function properly. This is because the random nature of the selected values within the limits of the distribution will produce a new interpolated function for $\ddot{N}(t)$ during each call of the script.

## 3.5 Typical Unforced and Forced Time Domain Responses

Now that the stochastically excited Euler strut harvester concept has been presented and the accompanying equation of motion derived, it is possible to observe time domain responses under various loading conditions. The purpose of this exercise is to demonstrate the typical behaviour that is sought after in a stochastically resonant system. Following this, and given that the extent of this chapter will only be to establish the concept of the particular harvester, approaches to measuring the energy throughput of the system will be developed but with the knowledge and intent that further investigation is required. What is hope for, however, is that this study may open the topic to discussion.

Time domain and phase space plots from numerical integrations performed upon Eq. 3.3 can be useful tools for understanding the characteristic behaviour of an oscillatory system. These can be used to visualise the response of the system subject to stochastic inputs, and subsequently the changes in response when the axial static pre-load or the dynamic forcing terms, or indeed a combination of the two, are added to the system.

Chapter 2 explored a similar system whereby axial periodic vibrations were harvested, whereby in this scenario they are being used to modulate and enhance the response of the system as it is excited laterally by $\ddot{N}(t)$. To maintain some form of consistency between the two different forms of harvester, they are both based upon a fibre glass epoxy Euler strut of Young's modulus, $E = 13\text{GPa}$, density, $\rho = 1900\text{kg/m}^3$

and length, $l = 0.35$m, unless specifically stated otherwise.

It must be noted that a direct comparison of the accumulated energies of the two harvesters cannot be made since the two harvest different forms of source vibrations, and that in the current harvester the periodic forcing is a form of active modulation that must be subtracted from the net available energy. This will be discussed in greater detail later. However, given that when $\ddot{N}(t) = 0$ the equation of motion reduces to exactly that of the previous periodic harvester, under this condition only the observations made in Chapter 2 would apply to both systems if the material and geometric properties remain the same. If this is indeed accepted, then the following analysis is limited to the performance of the system when $\ddot{N}(t) \neq 0$ since only under this condition will there be any energy actually available to be harvested.

### 3.5.1 Stochastically Excited Only Harvester

The harvester could be said to be operating in its most basic form when it is excited by $N(t)$ only. This shows how the system would perform prior to any form of active or passive control targeted at enhancing the throughput. In this form with no initial pre-loads applied in the form of $P_{static}$ the system exists in a uni-stable state with a single basin of attraction that the trajectory of the response will orbit about when excited laterally by $N(t)$.

Fig. 3.3 demonstrates typical time domain and phase space responses to increasing values of $\psi_{noise}$ which is used to control the magnitude of the stochastic excitations. The stochastic nature of the response is clearly evident by the random oscillations that never reach a steady-state within the 60 second period, and orbit mostly about the uni-stable attractor located in the *unstressed position*. In practice, this is manifested as oscillations back and forth across the *unstressed zero reference line* shown in Fig. 3.1.

However, there do exist periods where the response actually oscillates to either side of the *unstressed position* for a number of periods. This suggests the sporadic formation of additional attractors in which the trajectory of the response becomes briefly trapped within. This is more clearly viewed in the phase space responses of Fig. 3.3 where it can be seen that when $\psi_{noise} = 6.0$ the velocity responses within these outer attractors

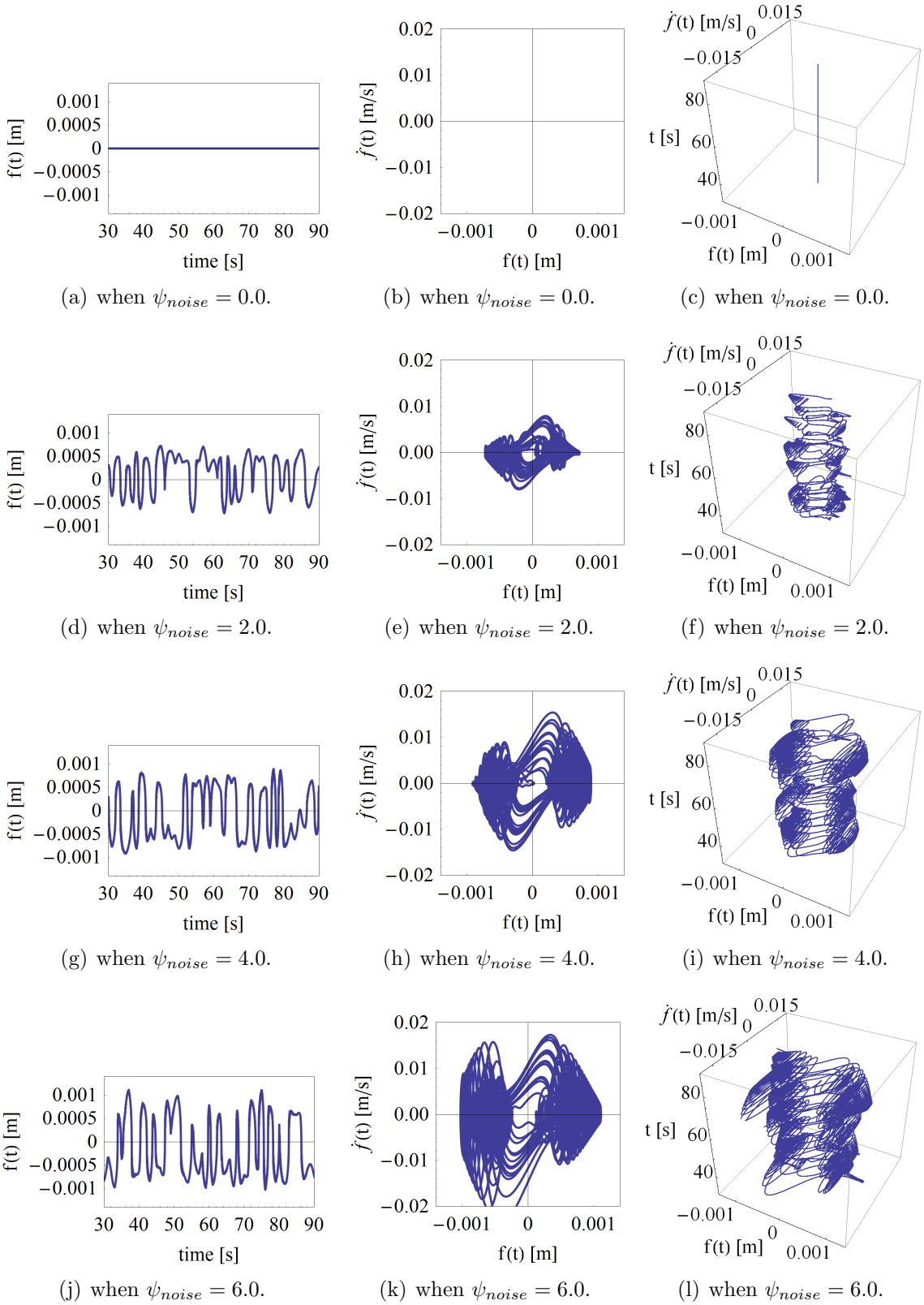


(a) when $\psi_{noise} = 0.0$. (b) when $\psi_{noise} = 0.0$. (c) when $\psi_{noise} = 0.0$.

(d) when $\psi_{noise} = 2.0$. (e) when $\psi_{noise} = 2.0$. (f) when $\psi_{noise} = 2.0$.

(g) when $\psi_{noise} = 4.0$. (h) when $\psi_{noise} = 4.0$. (i) when $\psi_{noise} = 4.0$.

(j) when $\psi_{noise} = 6.0$. (k) when $\psi_{noise} = 6.0$. (l) when $\psi_{noise} = 6.0$.

Figure 3.3: Time domain responses of the uni-stable Euler strut to increasing magnitudes of $\psi_{noise}$, where $A = 2.5{\times}10^{-6}\text{m}^{\,2}$, $l = 0.35$m, $E = 13$GPa, $\rho = 1900\text{kg/m}^3$, $P_{static} = 0.0$N, $P_{dynamic} = 0.0$N, $P_{crit} = 0.055$N, $\zeta = 0.1$, $\Omega = 0.0$, $f(0) = 0.00001$m, $\dot{f}(0) = 0$rad/s and $30 \leq t \leq 90$s.

is very high compared to their relatively short physical displacements.

These additional attractors seem to be forming in the locations that one would typically expect of a bistable system. The conclusion therefore is that the momentum generated by the higher velocities of the mass centre must be intermittently exceeding the buckling capacity of the beam and resulting in the observed behaviour. However, the duration of these trapped oscillations is very short and clearly the trajectory of the response primarily orbits the *unstressed position* attractor.

It is also interesting to observe the actual shape of the trajectory as it orbits the *unstressed* attractor. Again choosing to observe Fig. 3.3(k), the response is skewed somewhat with positive domain trajectories favouring towards the right, and negative domain responses towards the left. This is the result of much greater decelerations in the beam as it reaches its maximum lateral displacement and the restoring forces begin to take precedence, than there are accelerations when the direction of travel reverses. This is expected of such systems and lends confidence to the derived model.

### 3.5.2 Stochastically Excited System Only With Applied Static Preload

Knowing that a bistable system is a prerequisite for the system to achieve stochastic resonance, $P_{static}$ can be used to apply the necessary pre-curvature to the beam when $P_{static} > P_{crit}$ in a similar way to Section 2.5.1. However, now $P_{static}$ is introduced when the beam is excited by $N(t)$ at $\psi_{noise} = 1.0$. Note that in the current configuration of the beam $P_{crit} = 0.055$N.

Fig. 3.4(a), 3.4(b), 3.4(c) show the base response when $P_{static} = 0$N where the response primarily orbits the *unstressed position* attractor with only intermittent oscillations about the additional attractors according to previous observations. In Fig. 3.4(d), 3.4(e), 3.4(f) when $P_{static} = 0.1$N, $P_{crit}$ is exceeded and a bistable system is formed. This manifests itself in the way that has come to be expected, by a number of oscillations trapped within either bistable state, with intermittent jumps in between. However, these transitions do remain irregular, but it is important to note that the *unstressed position* attractor has been removed. Therefore the trajectory must exist in either bistable state which if controlled correctly can be beneficial.

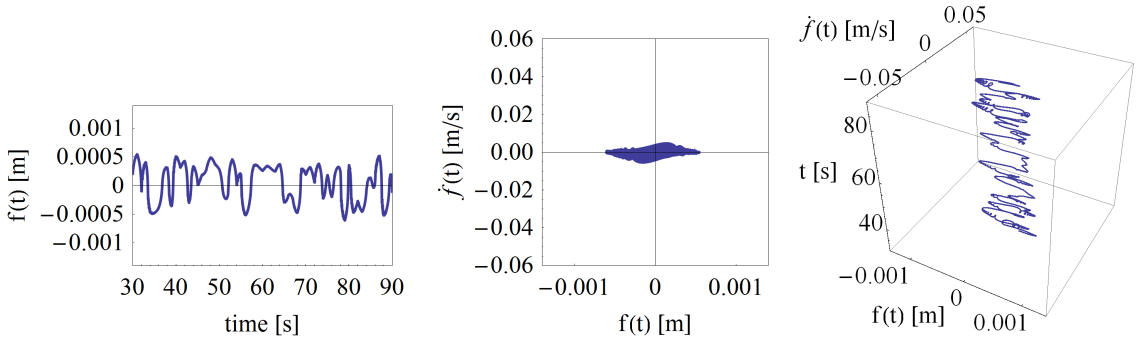


(a) when $P_{static} = 0.0$N. (b) when $P_{static} = 0.0$N. (c) when $P_{static} = 0.0$N.

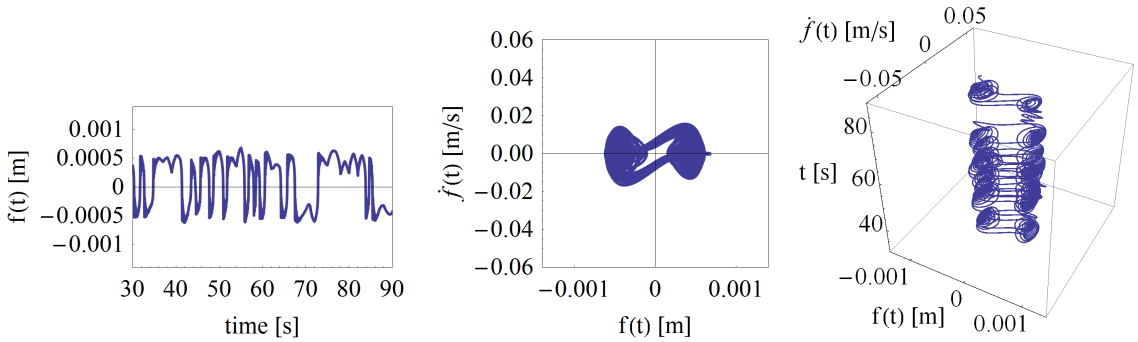


(d) when $P_{static} = 0.1$N. (e) when $P_{static} = 0.1$N. (f) when $P_{static} = 0.1$N.

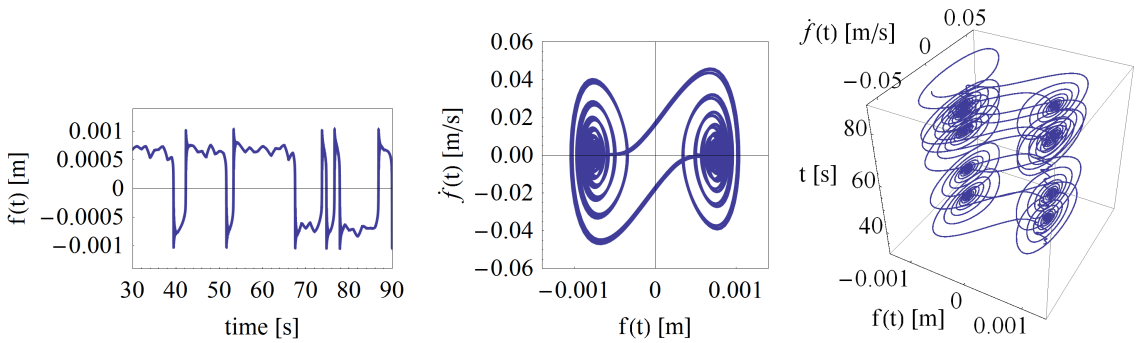


(g) when $P_{static} = 0.3$N. (h) when $P_{static} = 0.3$N. (i) when $P_{static} = 0.3$N.

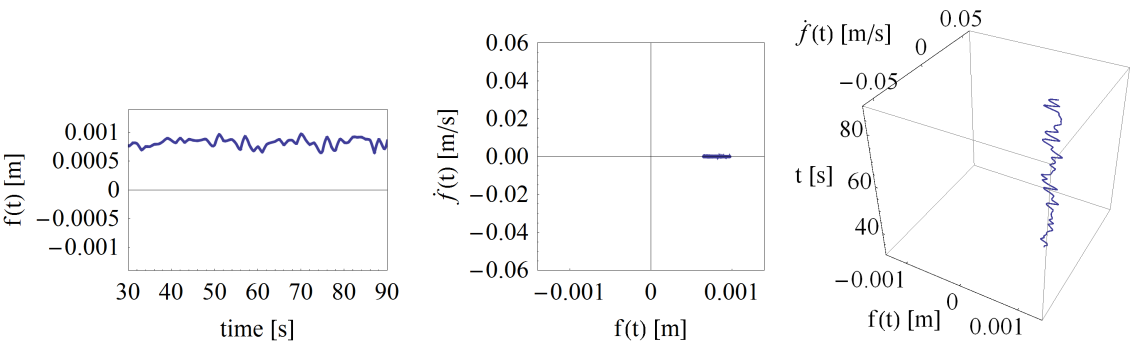


(j) when $P_{static} = 0.5$N. (k) when $P_{static} = 0.5$N. (l) when $P_{static} = 0.5$N.

Figure 3.4: Time domain responses of the uni-stable Euler strut to increasing magnitudes of $P_{static}$, where $A = 2.5\times10^{-6}$m $^2$, $l = 0.35$m, $E = 13$GPa, $\rho = 1900$kg/m$^3$, $P_{dynamic} = 0.0$N, $P_{crit} = 0.055$N, $\zeta = 0.1$, $\Omega = 0.0$, $\psi_{noise} = 1.0$, $f(0) = 0.00001$m, $\dot{f}(0) = 0$rad/s and $30 \leq t \leq 90$s.

When $P_{static}$ is increased to 0.3N, the duration at which the trajectory oscillates within a single outer well increases, and thus the number of jumps between decreases. This is a direct result of $P_{static}$ increasing the depth of the potential wells in the system. However, it should be remembered that if jumps between states can be maintained, the larger values of $P_{static}$ will increase the extent to which the beam displaces to either side of the *unstressed zero reference line*. Clearly in this case where the number of transitions does decrease, the net effect would be a reduction in total displacement, $f$. However, Fig. 3.4(g), 3.4(h), 3.4(i) do clearly show that the velocity response, $\dot{f}(t)$ during the actual transitions has dramatically increased under this magnitude of $P_{static}$ and from conclusions drawn in Section 2.6 of Chapter 2, it is known that this may not necessarily result in a decreased energy throughput, but could in fact enhance the energy performance.

Of course, there will become a point at which values of $P_{static}$ will increase the depth of the potential wells in the system to such an extent that the amplitude of $N(t)$ will no longer be larger enough to instigate transitions at all. This behaviour is seen in Fig. 3.4(j),3.4(k), 3.4(l) when $P_{static} = 0.5$N. The resulting reduction in velocity response is remarkable and clearly the total displacement has been significantly reduced too. There is no question at all that under such conditions the performance of the system will be greatly affected for the worse. Increasing the value of $P_{static}$ any further from this point would only exaggerate the situation further.

These particular simulations have up to this point involved only a passive form of control. Clearly the approach of manipulating $P_{static}$ can affect either a positive or a negative response with respect to the performance of the harvester, but rather than pursuing this approach further, the actual intention now is to introduce $P_{dynamic}$ as a form of active control to enhance the response. First though, the cumulative effects of the system that is excited by $N(t)$ and modulated by $P_{dynamic}$ only are observed.

### 3.5.3 Stochastically Excited System With Forced Modulations

It has been necessary to plot across a 10 second time domain in Fig. 3.5 in order to better observe the modulating process that $P_{dynamic}$ has upon the system response.

The modulating frequency, $\Omega$, has been arbitrarily chosen to be 25rad/s. Note that various other frequencies were also simulated, including 17rad/s, 75rad/s, 125rad/s and 230rad/s, and that the characteristics of the responses were very similar to that produced by $\Omega = 25$rad/s. Therefore, it can be accepted that the following is indicative of the generic behaviour produced under such excitation and loading conditions. It must also be noted that no attempt to seek resonant conditions has been made here. Such will be explored at a later point.

The effect is quite clear when Fig. 3.5(a) (in which $P_{dynamic} = 0$N) is compared to the responses generated when $P_{dynamic} \neq 0$N. It can be seen that the response typically generated by $N(t)$ alone is in fact modulated as it oscillates along its own course trajectory that in the current loading conditions of $P_{static} = 0$N is primarily about the *unstressed* attractor. As $P_{dynamic}$ is increased, so too does the amplitude of these inherent modulations and it can be seen that these themselves can lead to the formation of additional attractors about which the dominant response oscillates intermittently.

Viewing this behaviour in phase space reveals the complicated nature of this type of system, making it clear that a steady-state response is never likely to be reached. It is not possible to discern from these simulations alone whether any gain in energy throughput may have been achieved. However, given that this form of modulation is achieved actively, in that power is consumed to force the system physically in this way, it seems unlikely that any will have from this approach alone. This does however demonstrate how the modulation of the potential barrier is manifested, and so it remains to observe the time domain responses when both $P_{static}$ and $P_{dynamic}$ are applied together in the stochastically excited harvester to assess whether any net gains can be achieved this way.

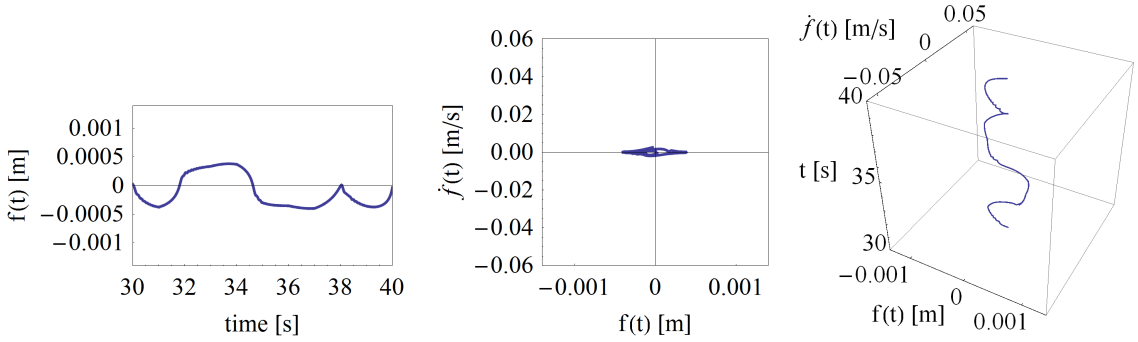


(a) when $P_{dynamic} = 0.0$N. (b) when $P_{dynamic} = 0.0$N. (c) when $P_{dynamic} = 0.0$N.

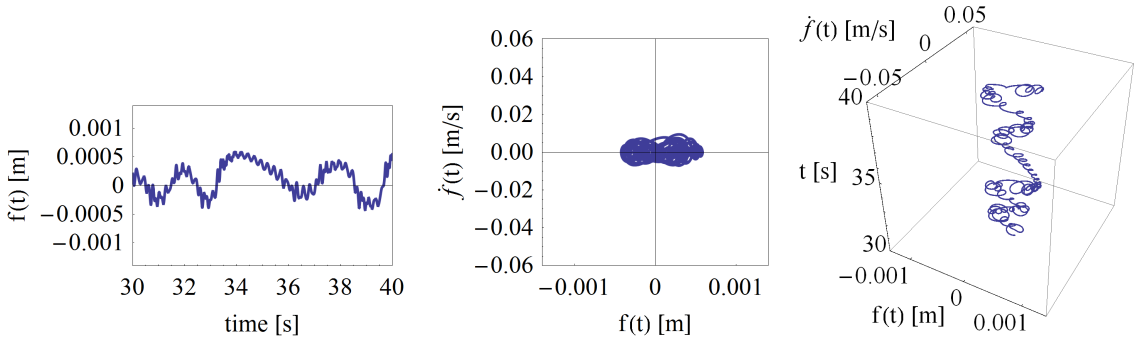


(d) when $P_{dynamic} = 0.05$N. (e) when $P_{dynamic} = 0.05$N. (f) when $P_{dynamic} = 0.05$N.

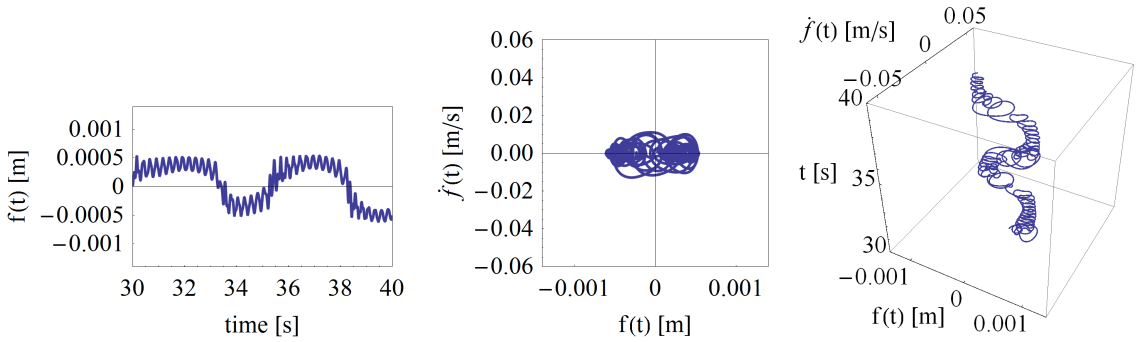


(g) when $P_{dynamic} = 0.1$N. (h) when $P_{dynamic} = 0.1$N. (i) when $P_{dynamic} = 0.1$N.

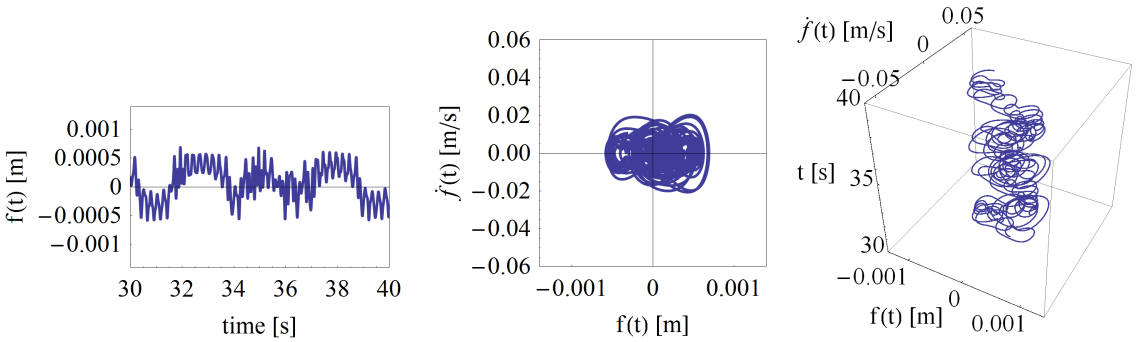


(j) when $P_{dynamic} = 0.15$N. (k) when $P_{dynamic} = 0.15$N. (l) when $P_{dynamic} = 0.15$N.

Figure 3.5: Time domain responses of the uni-stable Euler strut to increasing magnitudes of $P_{dynamic}$, where $A = 2.5 \times 10^{-6}$m $^2$, $l = 0.35$m, $E = 13$GPa, $\rho = 1900$kg/m$^3$, $P_{static} = 0.0$N, $P_{crit} = 0.055$N, $\zeta = 0.1$, $\Omega = 25$rad/s, $\psi_{noise} = 1.0$, $f(0) = 0.00001$m, $\dot{f}(0) = 0$rad/s and $30 \leq t \leq 40$s.

### 3.5.4 Enhanced Response of the Stochastically Excited System

By applying both $P_{static}$ and $P_{dynamic}$ to the system, it is hoped to exploit their cumulative effects to enhance the response of the harvester. In this way, $P_{static}$ is used to provide an initial pre-curvature to the beam to produce a bistable system, whilst $P_{dynamic}$ is used to modulate the potential barrier to increase the likelihood that the lateral excitation $N(t)$ could bring about regular transitions between both stable states. It is expected that this would greatly enhance the displacement of the mass centre, but more importantly that this, that it would lead to an increase in net available energy able to be harvested.

Before developing an approach to measure the actual energy throughput, the time domain responses to static and axial loading is observed. To begin with, the simulations are performed when $P_{static} = 0.5$N since it was shown in Fig. 3.4 that this value results in the system just initially oscillating within a single state as a result of $N(t)$ alone. Following this, it is hoped that increases in $P_{dynamic}$ will induce more regular jumps between states and thus increase the total displacement of the beam. Crucially, when $P_{static} = 0.5$N it is just on the the verge of beginning transitions, and therefore only small values of $P_{dynamic}$ should be required. This is important because one must remember that the work of $P_{dynamic}$ must be subtracted from the net harvestable energy.

Fig. 3.6 demonstrates this concept by increasing $P_{dynamic}$ to the harvester which has the initial pre-curvature resulting form $P_{static} = 0.5$N applied to it. Note that in all the simulations of Fig. 3.6 the frequency of $P_{dynamic}$ has arbitrarily been made equal to $\Omega = 25$rad/s again to maintain consistency with Section 3.5.3 and therefore no claim is being made yet that the applied modulation to the beam is operating at its greatest effectiveness. The effects of the modulating frequency, $\Omega$ will be explored shortly.

Even when $P_{dynamic} = 0.2$N in Fig. 3.6 it can be seen that the modulation has a positive effect and that a total of six transitional jumps has occurred within the 60 second time period alone. By increasing $P_{dynamic}$ further it can be seen that the number of transitions continues to increase. This trend could of course be continued further, but at some point the response will be dominated not by the harvestable excitations from $N(t)$, but instead by the active modulations of $P_{dynamic}$, which as discussed requires

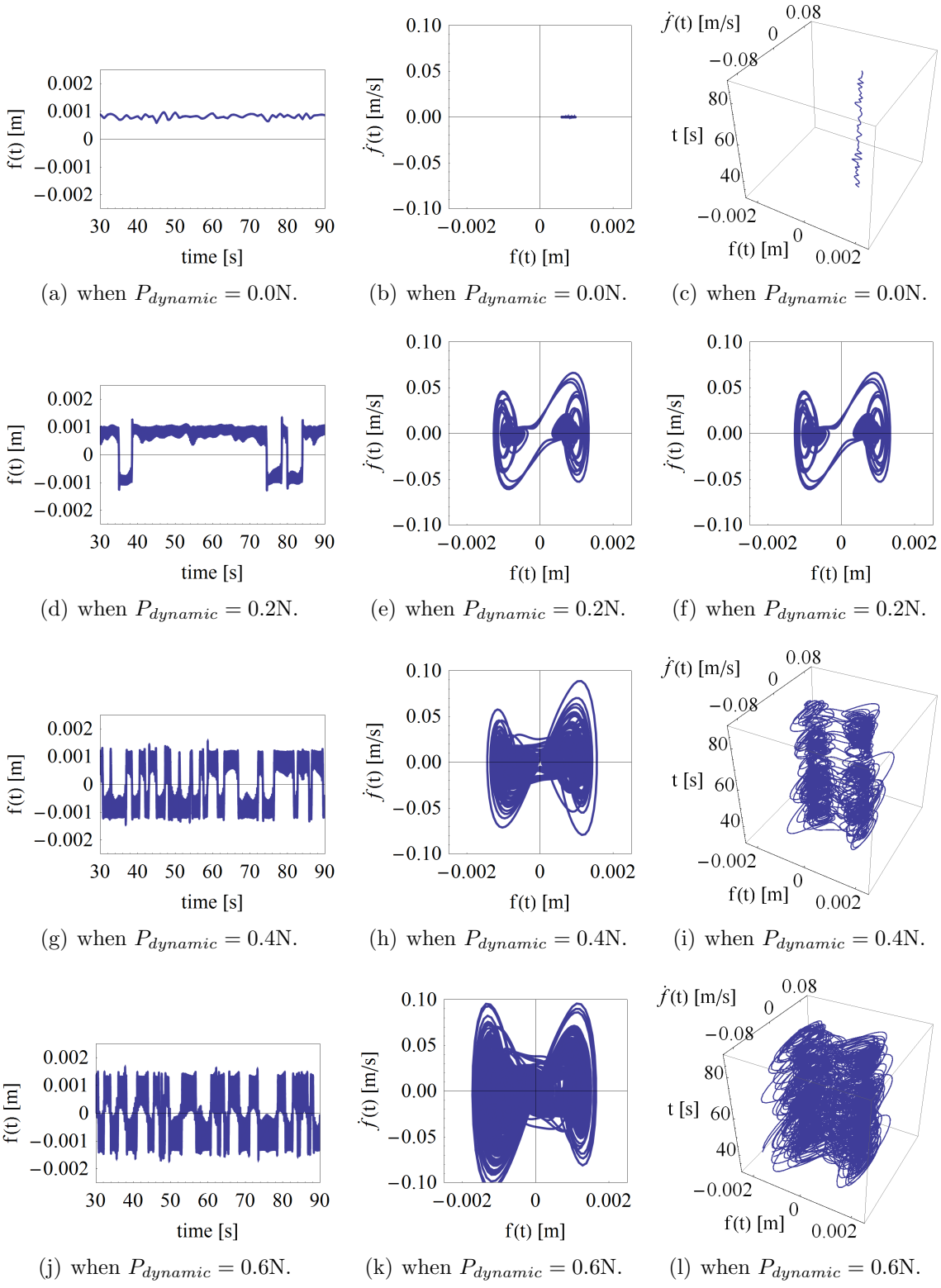


(a) when $P_{dynamic} = 0.0$N. (b) when $P_{dynamic} = 0.0$N. (c) when $P_{dynamic} = 0.0$N.

(d) when $P_{dynamic} = 0.2$N. (e) when $P_{dynamic} = 0.2$N. (f) when $P_{dynamic} = 0.2$N.

(g) when $P_{dynamic} = 0.4$N. (h) when $P_{dynamic} = 0.4$N. (i) when $P_{dynamic} = 0.4$N.

(j) when $P_{dynamic} = 0.6$N. (k) when $P_{dynamic} = 0.6$N. (l) when $P_{dynamic} = 0.6$N.

Figure 3.6: Time domain responses of the uni-stable Euler strut to increasing magnitudes of $P_{dynamic}$ with static axial load, where $A = 2.5 \times 10^{-6}$m $^2$, $l = 0.35$m, $E = 13$GPa, $\rho = 1900$kg/m$^3$, $P_{static} = 0.5$N, $P_{crit} = 0.055$N, $\zeta = 0.1$, $\Omega = 25$rad/s, $\psi_{noise} = 1.0$, $f(0) = 0.00001$m, $\dot{f}(0) = 0$rad/s and $30 \leq t \leq 90$s.

work to apply.

It is therefore paramount that the use of $P_{dynamic}$ always remains energy efficient, and the obvious route to achieving this is to operate at resonant frequencies. In respect to the current stochastic oscillating system, stochastic resonance will occur as a cumulative result of principle parametric resonance from the parametric modulations, and the increase in transitions this would subsequently cause. Given that the full nonlinear description of the system has been maintained during the derivation process, it is known that the precise location of resonance may be shifted from the linear location of PPR ($\frac{\Omega}{\omega_n} = 2.0$) typically seen in parametric systems. Therefore, using the value of $P_{dynamic} = 0.6$N, Fig. 3.7 shows the effect of various modulating frequencies, $\Omega$.

The differences that $\Omega$ brings about are immediately clear. Even operating at $\frac{\Omega}{\omega_n} = 1.0$ results in a marked increase in transitional jumps, but there still remains periods of oscillations within a single well. This is known from the phase space plot in Fig. 3.7(b) which still appears to orbit about individual outer attractors at points, hence there is no formation of an open loop about the origin.

By increasing the frequency of modulation to $\frac{\Omega}{\omega_n} = 2.0$ it can be seen that such a loop does indeed form. This would be manifested in practice by the beam continually oscillating from one buckled extreme to the other with no periods of oscillation in a single well at all. However, when $\frac{\Omega}{\omega_n} = 3.0$ the performance of the system is seen to increase further still with the loop widening and the distance between the inside and outside thinning. Clearly this corresponds with much more stable and complete transitions from one state to the other and could be considered as the peak displacement operating point. It is also shown that the velocity response at this condition has also increased. Further evidence that this is in fact the location of stochastic resonance within the system under the given conditions can be seen when $\frac{\Omega}{\omega_n} = 4.0$ where the response has begun to deteriorate such that the peak location has been passed.

Hence from these simulations alone, one may deduce that for a beam of the given geometrical and material properties with the stochastic input defined in Section 3.4, stochastic resonance has be achieved with a static pre-load of $P_{static} = 0.5$N and a dynamic modulation of $P_{dynamic} = 0.6$N operated at a frequency of $\frac{\Omega}{\omega n} = 3.0$. Note that at this point no claim has been made that a net gain in harvestable *energy* would

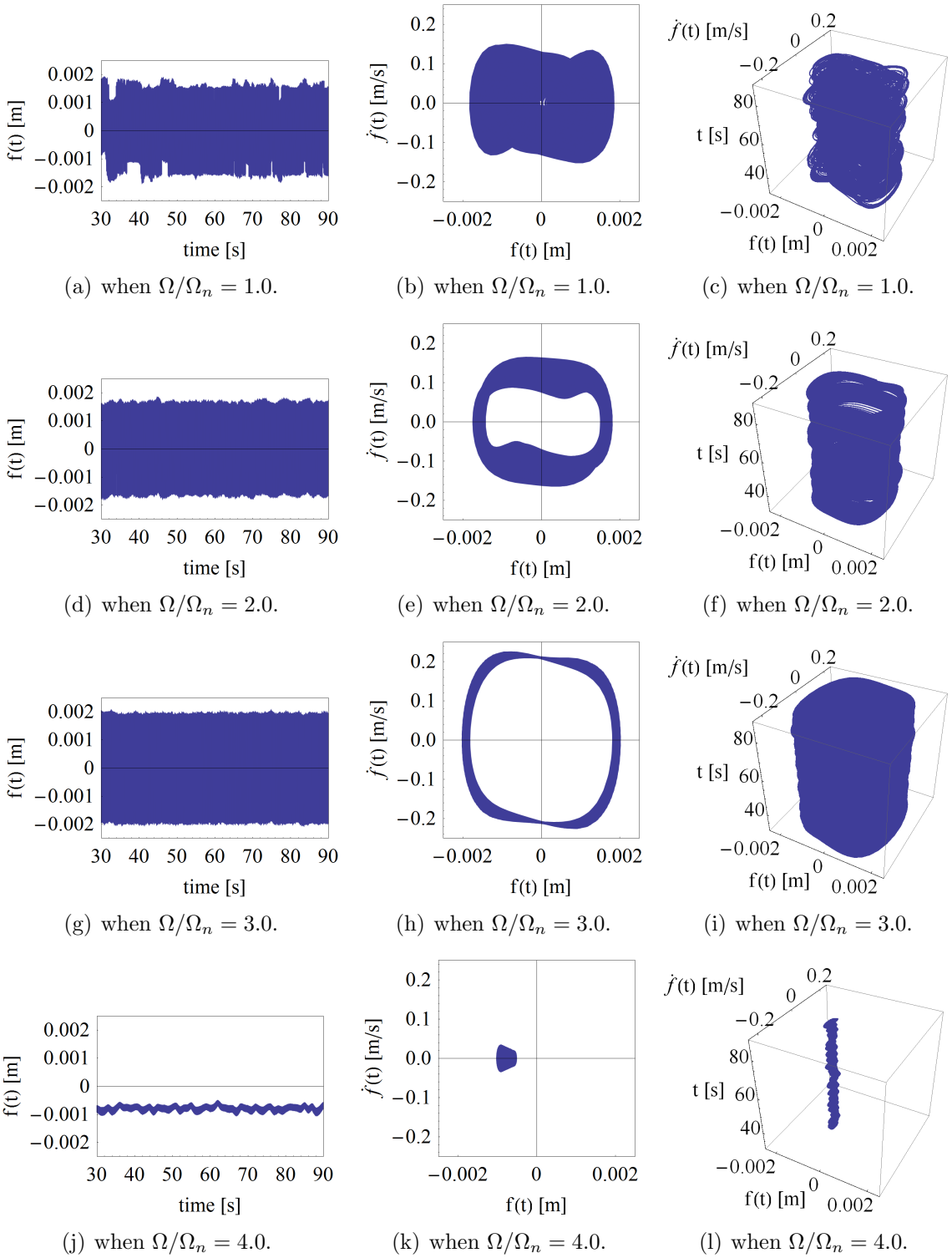


(a) when $\Omega/\Omega_n = 1.0$. (b) when $\Omega/\Omega_n = 1.0$. (c) when $\Omega/\Omega_n = 1.0$.

(d) when $\Omega/\Omega_n = 2.0$. (e) when $\Omega/\Omega_n = 2.0$. (f) when $\Omega/\Omega_n = 2.0$.

(g) when $\Omega/\Omega_n = 3.0$. (h) when $\Omega/\Omega_n = 3.0$. (i) when $\Omega/\Omega_n = 3.0$.

(j) when $\Omega/\Omega_n = 4.0$. (k) when $\Omega/\Omega_n = 4.0$. (l) when $\Omega/\Omega_n = 4.0$.

Figure 3.7: Time domain responses of the uni-stable Euler strut to excitation frequencies with static and dynamic axial loads, where $A = 2.5 \times 10^{-6}\text{m}^{\,2}$, $l = 0.35\text{m}$, $E = 13\text{GPa}$, $\rho = 1900\text{kg/m}^3$, $P_{static} = 0.5\text{N}$, $P_{dynamic} = 0.6\text{N}$, $P_{crit} = 0.055\text{N}$, $\zeta = 0.1$, $\psi_{noise} = 1.0$, $f(0) = 0.00001\text{m}$, $\dot{f}(0) = 0\text{rad/s}$ and $30 \leq t \leq 90\text{s}$.

be obtained under such conditions. It is more likely that this is the type of time domain behaviour that would be likely to do so.

To properly gain insight upon the energy performance at these peak operating conditions, an expression for measuring the harvestable energy from the system would be required. Unfortunately it was at this point in the process that the author was required to begin work on two separate feasibility studies in collaboration with industry, details of which can be found in Appendix D. This was an excellent opportunity that justified concluding the current work for future investigation, but the author considers the work produced to this point as evidence that the concept is viable.

## 3.6 Summarising Remarks for the Stochastically Excited Euler Strut Harvester

An energy harvester has been proposed that has been shown to be capable of harvesting stochastic vibrations from ambient conditions. The purpose of this concept, which is again based upon an Euler strut, is that it effectively relives the dependency seen by the previous periodically excited harvester to known steady-state vibrations which may normally limit the potential applications of the device.

The actual construct of the harvester is very similar to that discussed in Chapter 2 where the beam has the facility to apply both a static and a dynamic axial load, but in this situation the system is excited laterally by an applied stochastic input. It was hoped, and indeed later validated, that the performance of the system could be greatly enhanced via the cumulative effects from both the deterministic and stochastic inputs. In effect, the static pre-load, $P_{static}$ was used to passively force a bistable state which is a prerequisite for stochastic resonance, whilst the dynamic load, $P_{dynamic}$ was used to actively modulate the potential barrier separating the two states at a frequency of $\Omega$. This was to encourage transitional jumps. By doing so, the displacement of the mass centre of the beam could be greatly enhanced whilst the beam was excited laterally by the stochastic vibrations, $N(t)$.

In order to determine the effectiveness of the approach, and to understand how the various combinations of loading and excitation conditions could affect the response

of the system, an iterative analysis was performed. First, by defining the stochastic input as white noise with a zero mean and unit variance, the response to $N(t)$ alone was observed as a base-line condition. It was shown here that the trajectory of the response within time domain simulations would oscillate primarily about the attractor located at the *unstressed* position, but with sporadic formations of additional attractors resembling that typically seen in bistable systems. It was suggested that this could be a result of increased momentum generated by $N(t)$ acting upon the mass centre intermittently exceeding the buckling capacity, $P_{crit}$ of the beam.

By applying $P_{static}$ such that $P_{static} > P_{crit}$, a pre-curvature in the beam could be formed and the system was forced into a bistable state. This had the effect of removing the uni-stable attractor at the *unstressed* position such that the beam was able to oscillate between both stable states at lower values of $P_{static}$. This in effect provided the ability to enhance the response of the system passively in a similar manner to that discussed in Chapter 2. However, the same care had to be taken not to increase $P_{static}$ to the extent that the depth of the potential wells was so deep that the stochastic excitations were not great enough to initiate jumps. In this case the application of $P_{static}$ would be detrimental to the performance of the harvester.

Given that the purpose of the concept is to attempt to achieve stochastic resonance to enhance the energy throughput, the effect $P_{dynamic}$ had upon $N(t)$ was observed. This was able to show the modulation process quite clearly within the time domain plots and provided indications of how this would increase the likelihood of transitions. Unfortunately, it was not possible to discern from this alone whether any increase in throughput would be seen. Note that in this condition the system was uni-stable.

However, by coupling the effects imparted by both $P_{static}$ and $P_{dynamic}$, the improvement in response became immediately clear. Even when the modulation frequency was untuned from the fundamental natural frequency of the beam, the number of transitions would be greatly increased. By gradually varying the modulation frequency, it was shown that the peak displacement and velocity responses, $f$ and $\dot{f}(t)$ respectively, occurred at $\frac{\Omega}{\omega_n} = 3.0$ and resulted in complete and continuous jumps from one stable state to the other. It was therefore concluded that this was in fact the location of stochastic resonance under the given loading and excitation conditions of

the simulated beam.

It was at this point in the study that the author was required to conclude the research, to progress onto the collaborative feasibility studies that were previously mentioned. Therefore, the current chapter concludes with the understanding that stochastic resonance can indeed be achieved with the proposed harvester concept and that this will result in an enhanced energy throughput of the system.

For note, McInnes *et al* (2008) developed an approach to providing a conservative estimate of the energy throughput of a similar system, whereby the energy dissipated by damping, and hence available to be harvested, is reduced by the work done in compressing the beam by an active dynamic load. A similar approach would be required for the concept discussed in this chapter and it is suggested that this possibly be adapted to for use in this system in any future investigation.

# Chapter 4

# Dynamics of a Planar Pendulum Harvester

The remaining chapters will explore a planar pendulum based energy harvester device that may have potential for application in a number of real life scenarios. The principle, as with the previous chapters, is to convert mechanical accelerations emanating from ambient sources into a more useful form of electrical energy. With respect to the pendulum harvester, this would be realised with a suitable power take-off device mounted at the pivot point of the pendulum arm.

The scope of such a device is huge if one considers a similar concept using a spherical pendulum, where accelerations in the full six degrees of freedom could potentially be harvested. In this respect, such a device could be used to harvest the accelerating motion of sea-waves, either as a dedicated device mounted within a buoy, or like, structure deployed at sea. It could even be deployed as a secondary generator mounted within the hull of a vessel. One could even imagine similar purposes in vehicles and aeroplanes and like structures subject to accelerated motions. Personal devices may also be realisable to harness energy lost in human motion to charge portable electronic devices.

The versatility of such a device is evident, and as such, the following study of the planar concept is considered a preliminary effort to what could become a much larger body of work. The study will encompass excitations in the form of accelerations applied in the full three degrees of freedom that may be experienced by the planar

structure; horizontal translation of the absolute frame of reference, vertical translation of the absolute frame of reference and rotation about the origin of the absolute frame of reference. By deriving an equation of motion to describe this system, a detailed understanding of loading characteristics and achievable powers my be compiled.

The first hurdle to overcome within this study is how to adequately describe excitation by rotations of the pendulum. The normally simple derivation is somewhat complicated in such a situation as one must consider carefully how to affect this rotation; be that by introducing torque terms to force rotation about the pendulum pivot point, or by describing the rotation geometrically. Even a geometrical approach introduces questions as to where this rotation originates. The two prominent choices are either about the origin of the absolute frame of reference, or possibly by rotating a second pendulum body frame about the original.

Each approach possess their own merits. The torque induced approach is rather simple in its implementation and easily decoupled from the translational forms of excitation, but one would have to consider how this rotational torque may actually be obtained in reality. This would clearly be dependent on the precise mechanical configuration of the planar pendulum versus what the environment in which it is situated in is capable of providing. These dependencies could either be assumed (as they shall be in the forthcoming analysis) or defined from actual observations and scaled to suit individual applications. Either approach is likely to introduce uncertainties.

The geometrically approaches both have the advantage of showing exactly how the excitation rotations arise and affect the system in practice. But as it will be shown, coupling behaviour between the three forms of excitation may arise if the system is not carefully defined. Whilst not necessarily affecting the behaviour of the response that will intrinsically arise from the geometry of the system, it does limit the level of control the user has over the composition of the excitations themselves. Such complexities are to be discussed in details.

## 4.1 Derivation of Planar Pendulum Device Excitable in Horizontal and Vertical Translations with Torque Induced Rotations

The analysis begins with the derivation of the equation of motion describing a planar pendulum that is excitable in the full three planar degrees of freedom. Typically, the derivation of a pendulum that is excited in translation only is very straightforward. However, as previously eluded to, this derivation is somewhat complicated with the inclusion of terms that introduce rotational excitations to the system. The first approach to this problem is to introduce a torque terms to induce rotations of the pendulum about its pivot point.

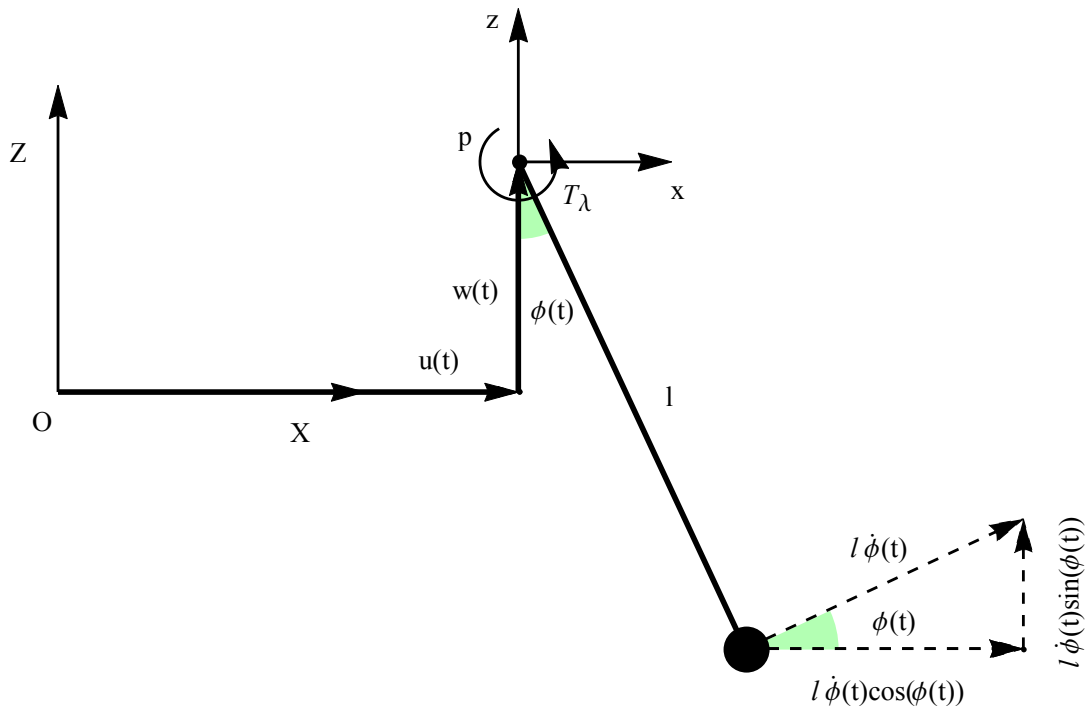


Figure 4.1: Deflected pendulum defining $\phi$ as the permissible degree of freedom with excitations translating in $u$ and $w$ and torque induced rotations about $p$.

Fig. 4.1 depicts a deflected pendulum with constant length, $l$ and concentrated end

mass, $m$. The generalised coordinate $\phi$ represents the permissible degree of freedom for the pendulum arm to swing through where the $\phi$ plane is vertical with respect to the absolute frame $OXZ$. The pendulum may experience rotations through $\phi$ as a result of the excitations in the form of horizontal and vertical translations, denoted by $u$ and $w$ respectively, and by direct rotations of the pendulum that are induced by an externally applied torque about the pendulum pivot point, $p$. The tangential velocity associated with the displacements through $\phi$ is $l\dot{\phi}(t)$, which have horizontal and vertical components of $l\dot{\phi}(t)\cos\phi(t)$ and $l\dot{\phi}(t)\sin\phi(t)$ respectively.

The equations of motion is derived using the preferred method of Lagranges's equations that are:

$$\frac{d}{dt}\left(\frac{\partial T}{\partial \dot{\phi}(t)}\right) - \frac{\partial T}{\partial \phi(t)} + \frac{\partial U}{\partial \phi(t)} = Q_\phi \tag{4.1}$$

where $Q_\phi$ is some generalised force.

To begin formulating the Lagrange's equations for the given system the kinetic and potential energies must first be in the correct form. From Figure.4.1 the kinetic energy can be described as:

$$T = \frac{1}{2}m\left(l^2\dot{\phi}(t)^2 + 2l\dot{u}(t)\dot{\phi}(t)\cos\phi(t) + 2l\dot{w}(t)\dot{\phi}(t)\sin\phi(t) + \dot{u}(t)^2 + \dot{w}(t)^2\right) \tag{4.2}$$

The potential energy of the system is:

$$U = mgw(t) + mgl - mgl\cos\phi(t) \tag{4.3}$$

Next the kinetic energy is differentiated with respect to $\dot{\phi}(t)$:

$$\frac{\partial T}{\partial \dot{\phi}(t)} = \frac{1}{2}m\left(2l^2\dot{\phi}(t) + 2l\dot{u}(t)\cos\phi(t) + 2l\dot{w}(t)\sin\phi(t)\right) \tag{4.4}$$

This is now differentiated with respect to time to become:

$$\frac{d}{dt}\left(\frac{\partial T}{\partial \dot{\phi}(t)}\right) = \frac{1}{2}m\Big(2l^2\ddot{\phi}(t) + 2l\ddot{u}(t)\cos\phi(t) - 2l\dot{u}(t)\dot{\phi}(t)\sin\phi(t) + 2l\ddot{w}(t)\sin\phi(t) + 2l\dot{w}\dot{\phi}(t)\cos\phi(t)\Big) \tag{4.5}$$

Returning to Eq. 4.2 and differentiating with respect to $\phi(t)$ gives:

$$\frac{\partial T}{\partial \phi(t)} = \frac{1}{2}m\Big(2l\dot{w}(t)\dot{\phi}(t)\cos\phi(t) - 2l\dot{u}(t)\dot{\phi}(t)\sin\phi(t)\Big) \tag{4.6}$$

Finally, differentiating the potential energy with respect to $\phi(t)$ gives:

$$\frac{\partial U}{\partial \phi(t)} = mgl\sin\phi(t) \tag{4.7}$$

Hence, the kinetic and potential energies of the system are now in a suitable form for Lagrange's equations to be applied as so:

$$\ddot{\phi}(t) + 2\xi\omega_n\dot{\phi}(t) + \frac{g}{l}\sin\phi(t) + \frac{\ddot{u}(t)}{l}\cos\phi(t) + \frac{\ddot{w}(t)}{l}\sin\phi(t) = Q_\phi \tag{4.8}$$

where linear viscous damping terms, $2\xi\omega_n\dot{\phi}(t)$ have been included for a more realistic system and $\omega_n = \sqrt{g/l}$.

Currently Eq. 4.8 describes a system that can be excited by both horizontal and vertical translations only. The next step is to introduce torque terms to induce rotations of the pendulum about $p$. The reason that this external torque does not arise naturally during the course of the derivation is that it is to be applied as an assumed external load to force rotations, but the precise nature of which are to be assumed. This is a fair assumption to make when one considers that it is the effect that the excitations have upon the system response that is of most interest, but care must be given to ensure that the externally applied torque is practical and achievable in practice.

To ensure that the externally torque is in fact a torque when applied, the inertial units in Eq. 4.8 are multiplied by $ml^2$ to obtain a torque, and $Q_\phi = -\lambda_0\cos\Omega_\lambda t$ is inserted directly. Harmonic expressions are then assumed for the translation terms,

which are:

$$\begin{aligned} u(t) &= U_0 \cos \Omega_u t & w(t) &= W_0 \cos \Omega_w t \\ \dot{u}(t) &= -U_0 \Omega_u \sin \Omega_u t & \dot{w}(t) &= -W_0 \Omega_w \sin \Omega_w t \\ \ddot{u}(t) &= -U_0 {\Omega_u}^2 \cos \Omega_u t & \ddot{w}(t) &= -W_0 {\Omega_w}^2 \cos \Omega_w t \end{aligned} \tag{4.9}$$

By substituting the solutions from Eq. 4.9 into Eq. 4.8, the final form of the equation of motion used to described to the motions of the planar pendulum from Figure.4.1 is:

$$\begin{aligned} \ddot{\phi}(t) + 2\xi\omega_n\dot{\phi}(t) + \frac{g}{l}\sin\phi(t) = \frac{U_0{\Omega_u}^2\cos\Omega_u t}{l}\cos\phi(t) + \frac{W_0{\Omega_w}^2\cos\Omega_w t}{l}\sin\phi(t) \\ - \frac{\lambda_0\cos\Omega_\lambda t}{ml^2} \end{aligned} \tag{4.10}$$

where $\lambda_0$ and $\Omega_\lambda$ are the magnitude and frequency of applied torque respectively.

## 4.2 Numerical Analysis of Torque Induced Rotations System

An initial numerical analysis of the system described by Eq. 4.10 will focus primarily upon the effectiveness of the torque terms used to induce rotations. This is because the dynamics of planar pendulums excited horizontally and vertically are academic and well understood, and it can be seen that Eq. 4.10 contains terms in the usual form used to describe such translating systems. This is demonstrated by the following:

*Simple Planar Pendulum:*

$$\ddot{\phi}(t) + 2\xi\omega_n\dot{\phi}(t) + \frac{g}{l}\sin\phi(t) = 0$$

when $U_0$, $W_0$ and $\lambda_0$ are equal to zero.

*Planar Pendulum Excited Horizontally and Vertically:*

$$\ddot{\phi}(t) + 2\xi\omega_n\dot{\phi}(t) + \frac{g}{l}\sin\phi(t) = \frac{U_0{\Omega_u}^2\cos\Omega_u t}{l}\cos\phi(t) + \frac{W_0{\Omega_w}^2\cos\Omega_w t}{l}\sin\phi(t)$$

when $\lambda_0$ is equal to zero.

*Pendulum Excited by Torque Induced Rotations:*

$$\ddot{\phi}(t) + 2\xi\omega_n\dot{\phi}(t) + \frac{g}{l}\sin\phi(t) = -\frac{\lambda_0\cos\Omega_\lambda t}{ml^2}$$

when $U_0$ and $W_0$ are equal to zero.

Thus, it will be more effective to observe the response of the pendulum system from torque induced rotations only at first in order to ascertain whether the derived terms are functional. This will be conducted in an iterative process.

### 4.2.1 Static Rotations Induced by a Static Torque Load

*Mathematica* has again been used to perform numerical integrations upon the system equation of motion. For simplicity, the analysis begins with static torque loads applied to the system, such that $\lambda_0 \neq 0$ and $\Omega_\lambda = 0$.

Under such conditions, the torque load will remain active under no oscillations since $\cos 0 = 1$. Therefore one could expect the resulting response itself to be static but displaced by some angle $\phi(t)$. A peculiarity of this system is that at $t = 0$, the pendulum is initially unperturbed even when $\lambda_0 \neq 0$, and is only displaced by the torque when $t > 0$. This behaviour is demonstrated in Fig. 4.2 which shows an initial transient phase before the response settles to a steady-state at some particular angle dependent upon the actual value of $\lambda_0$. The cause of this is the chosen initial condition of $\phi(0) = 0$rad which overrides any initial angular displacement induced by $\lambda_0$ at $t = 0$. Hence when $t > 0$s, the response quickly rises to the static response generated by $\lambda_0$, but is preceded by a transient phase. This is typical of a classic step response.

This transient phase may be undesirable depending upon the particular excitation conditions being modelled and can only be mitigated with *prior* knowledge of the

steady-state response. For example, if one were attempting to simulate the pendulum being held at an initial angle $\phi = 11.76°$ at $t = 0$s when $\lambda_0 = -1.0$Nm (see Fig4.2(a)) with no transient phase at all, then the closest approximation to this would be to set the initial condition $\phi(0) = 11.76°$. This has been attempted in Fig. 4.3, but still some initial transient persists despite been greatly reduced in amplitude. Of course, it is possible to reduce the transient phase further by increasing the value of $\xi$ to move from a system that is underdamped to one that is critically, or overdamped. However, this may not be appropriate for all scenarios. This is therefore of limitation of the torque induced approach, and one that does not arise in the geometrically described approach as shall be demonstrated later.

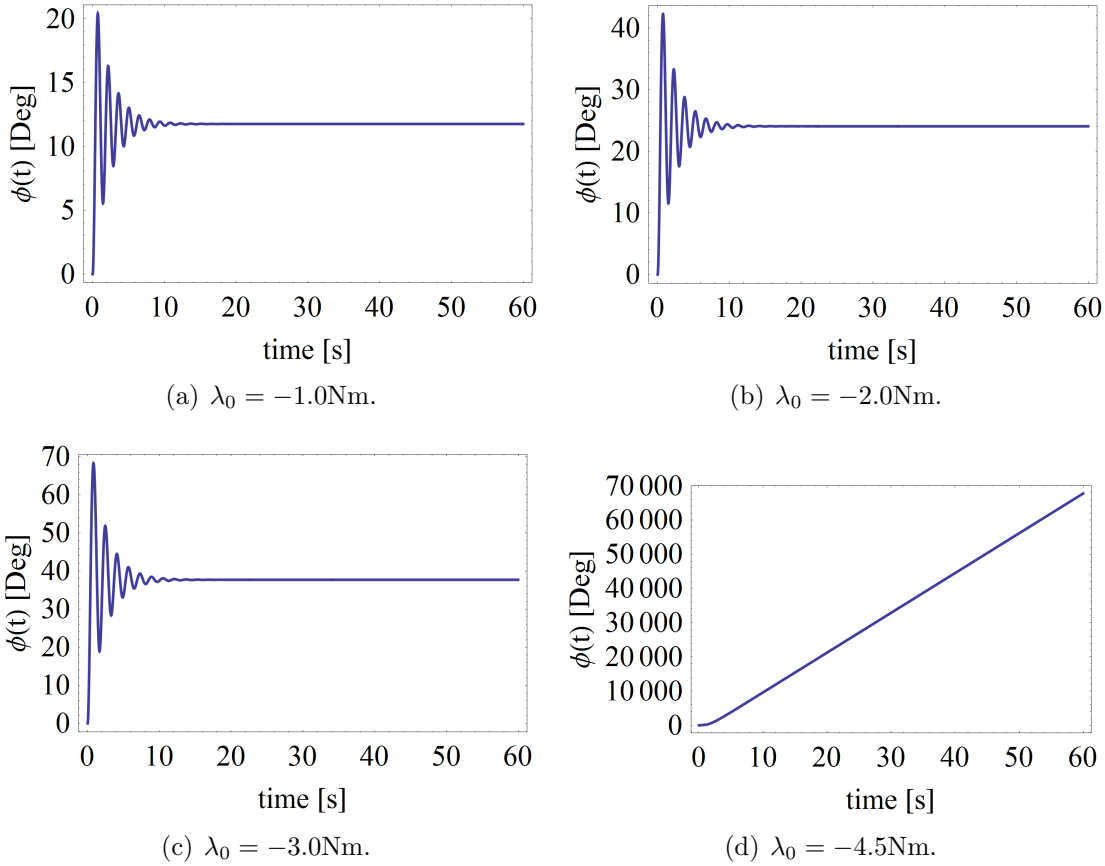


(a) $\lambda_0 = -1.0$Nm. (b) $\lambda_0 = -2.0$Nm.

(c) $\lambda_0 = -3.0$Nm. (d) $\lambda_0 = -4.5$Nm.

Figure 4.2: Time domain responses of the pendulum to increasing magnitudes of $\lambda_0$, where $l = 0.5$m, $m = 1$kg, $\xi = 0.1$, $U_0 = 0$m, $W_0 = 0$m, $\Omega_u = 0$rad/s, $\Omega_w = 0$rad/s, $\Omega_\lambda = 0$rad/s, $\phi(0) = 0$rad, $\dot{\phi}(0) = 0$rad/s and $0 \leq t \leq 60$s.

Despite this issue with an initial transient phase, Fig. 4.2(d) shows a more critical fallacy. It appears that a particular threshold exists after which larger values of $\lambda_0$ cause the response of the system to transition into a full rotational mode, thus becoming a

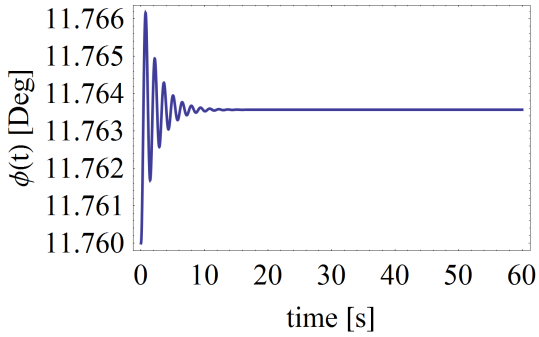


Figure 4.3: Time domain responses of the pendulum when $\lambda_0 = -1.0$Nm, where $l = 0.5$m, $m = 1$kg, $\xi = 0.1$, $U_0 = 0$m, $W_0 = 0$m, $\Omega_u = 0$rad/s, $\Omega_w = 0$rad/s, $\Omega_\lambda = 0$rad/s, $\phi(0) = 11.76°$, $\dot{\phi}(0) = 0$rad/s and $0 \leq t \leq 60$s.

forced-damped rotator instead. This can be explained if one considers a torque arising from gravity acting upon the end mass, $m$ of the pendulum versus the artificially applied torque, $\lambda_0$ used to induced rotations. From Fig. 4.4, the torque generated by gravity, $\tau$ is equal to $mgl \sin \phi(t)$. This will be at its maximum when $\phi = 90°$ or $\phi = 270°$, lowering in amplitude at angular displacements to either side of these points. Therefore, if $\lambda_0 > \tau$ then the pendulum arm will overcome the torque generated by gravity and move into a full rotational mode.

Fig. 4.5 shows how $\tau$ varies with $\phi$ for the pendulum construct shown in Fig. 4.4 and indicates a maximum torque generated by gravity of $\tau \approx -4.9$Nm. However, from Fig. 4.2(d) when $\lambda_0 = -4.5$Nm it shows that still a rotational mode has been achieved. This can be explained by momentum generated during the initial swing of the pendulum starting from $\phi(0) = 0$rad being great enough to cross the before mentioned threshold.

To observe if this is indeed what is happening and to clearly identify the angular displacement $\phi$ beyond which the system enters a rotational mode, a larger value of $\xi$ can be applied to the system to prevent overshoot in the system response. When $\xi = 1.0$ and the system is critically damped, the transition from one mode to the other is very abrupt. When $\lambda_0 = -4.9$Nm (Fig. 4.6(a)) the response $\phi$ tends towards 90° and represents the upper limit at which $\lambda_0$ can be applied. However, by increasing the applied torque by only $-0.1$Nm so that $\lambda_0 = -5.0$Nm, the system enters the rotational mode as predicted. This confirms the assumption that the rotational mode is entered when $\lambda_0$ exceeds the naturally occurring torque from gravity in the system.

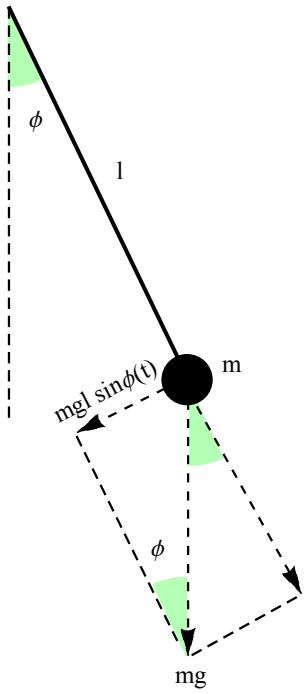


Figure 4.4: Schematic of torque generated by gravity acting upon the end mass of a pendulum.

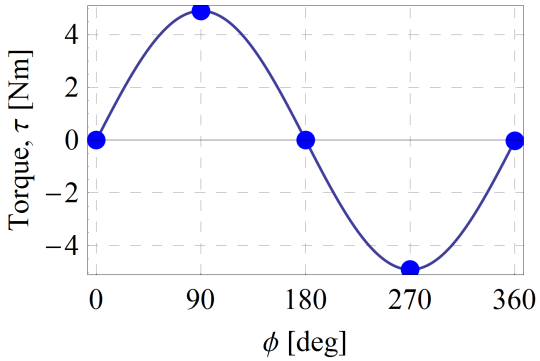


Figure 4.5: Torque generate by gravity acting upon the pendulum end mass versus angular displacement, $\phi$ where $l = 0.5$m and $m = 1$kg.

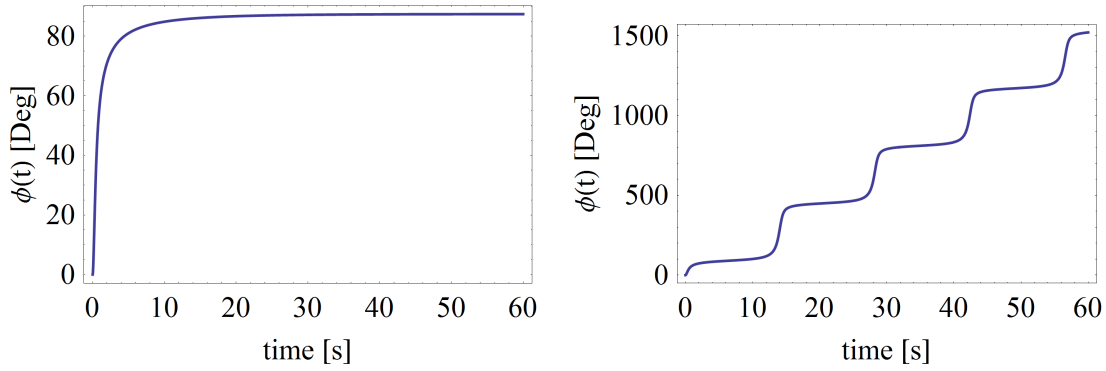


(a) $\lambda_0 = -4.9$Nm. (b) $\lambda_0 = -5.0$Nm.

Figure 4.6: Time domain responses of the pendulum to increasing magnitudes of $\lambda_0$, where $l = 0.5$m, $m = 1$kg, $\xi = 1.0$, $U_0 = 0$m, $W_0 = 0$m, $\Omega_u = 0$rad/s, $\Omega_w = 0$rad/s, $\Omega_\lambda = 0$rad/s, $\phi(0) = 0$rad, $\dot{\phi}(0) = 0$rad/s and $0 \leq t \leq 90$s.

### 4.2.2 Summarising Remarks of the Torque Induced Rotations Method

It has been shown that the torque induced rotations approach has a number of critical limitations. Even under statically loaded conditions the formation of a transient phase reduces the effectiveness with which a user may be able to replicate certain conditions seen in practice. It was shown that this transient phase can be reduced by matching the initial displacement, $\phi(0)$ to that of the steady-state response, but this act itself requires prior knowledge of the response of the system to its environment. Also, the approach of increasing damping within the system may again force one to move away from a realistic system where a lower value of $\xi$ is more appropriate.

Furthermore, it has been demonstrated that an upper $\lambda_0$ threshold exists beyond which the system transitions into a full rotational mode. The angular displacement threshold generated by $\lambda_0$ is shown to be approximately 90° depending on the precise damping conditions. This feature alone renders the approach obsolete since one should be able to exceed this value in practice to cause the system to seize.

It is therefore concluded that this particular approach in its present form should be abandoned for the remainder of the study. Instead the method of the geometrically described rotational excitations will be discussed with the aim of overcoming these limitations in performance.

## 4.3 Derivation of Planar Pendulum Device with Geometrically Described Rotations (Coupled System)

It will be shown how it is possible to define rotational excitations of a pendulum geometrically, which has the advantage of showing exactly how the rotations arise within the system. This differs from the previous torque induced approach where an external torque was assumed to be acting about the pivot point of the pendulum. Whilst this may have been acceptable for analysis purposes only, it remains more desirable to develop an approach where the rotations are fully understood.

There are two perceived methods by which to introduce these rotations geometrically; the first may be to rotate the pendulum body $pxz$ frame about the absolute frame of reference $OXZ$ (see Fig. 4.7), or to rotate a second pendulum body axis about the origin of the principle body frame (see Fig. 4.9).

### 4.3.1 Rotation of the Pendulum Body Frame about the Absolute Frame of Reference

Whilst it may be that the method of rotating the body axis appears the most intuitive, Fig. 4.7 shows that the resulting three forms of excitation will be heavily coupled together. Here, the horizontal, vertical and rotational excitations of $pxz$ about the absolute frame are defined by $u$, $w$ and $\lambda$ respectively. Again $\phi$ represents the permissible degree of freedom through which the pendulum may swing. Note that in this configuration the tangential velocity associated with displacements through $\phi$ is $l\left(\dot{\phi}(t)+\dot{\lambda}(t)\right)$ so that an inertial term for the $\lambda$ coordinate will arise to include the influence that rotations through $\lambda$ have upon the system. This has horizontal and vertical components of $l(\dot{\phi}(t)+\dot{\lambda}(t))\cos(\phi(t)+\lambda(t))$ and $l(\dot{\phi}(t)+\dot{\lambda}(t))\sin(\phi(t)+\lambda(t))$ respectively.

The following derivation of the equation of motion of the system highlights precisely how intrinsically coupled the three excitations are. First, the kinetic, $T$ and potential,

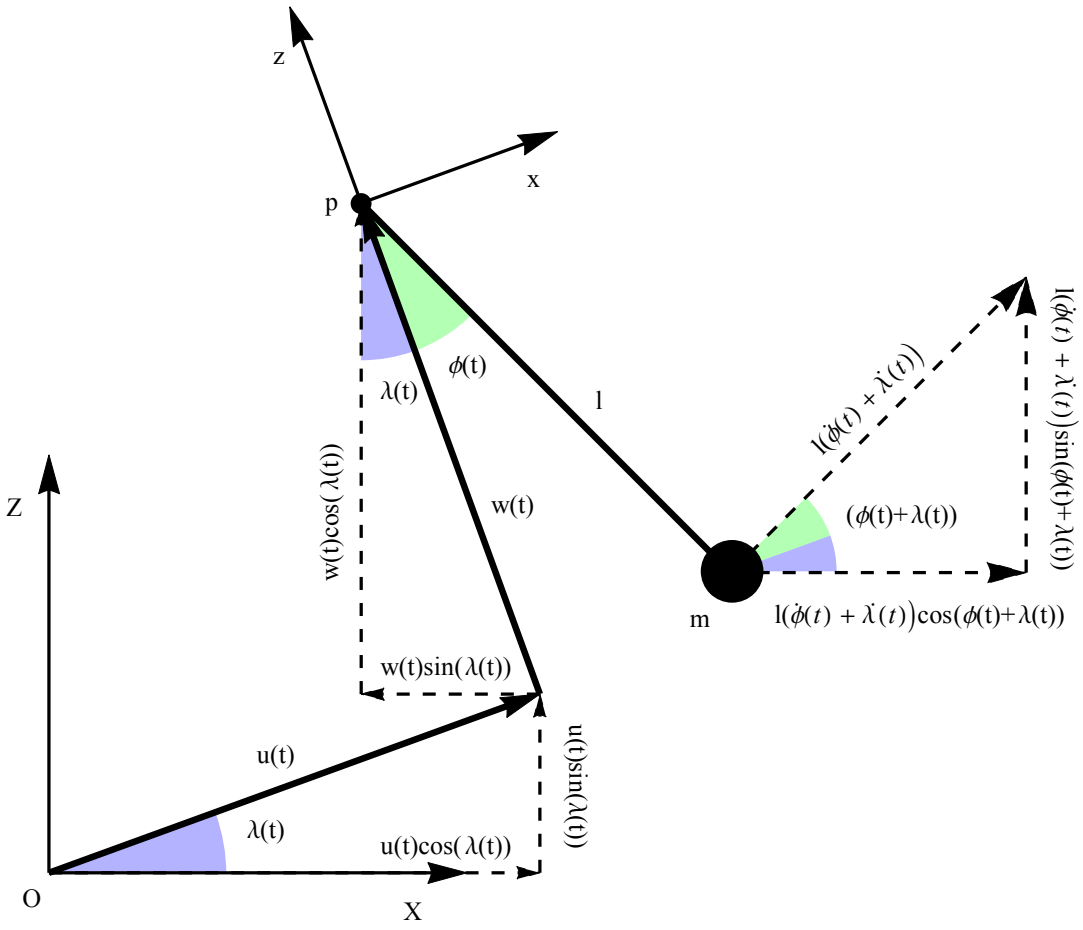


Figure 4.7: Deflected pendulum with horizontal and vertical translating excitations, $u$ and $w$ respectively, and geometrically described rotational excitations about the pivot point, $p$ with $\phi$ as the permissible degree of freedom.

$U$ energies of the system are described by:

$$\begin{aligned} T = \frac{1}{2}m \Big[ & 2l^2\dot{\lambda}(t)\dot{\phi}(t) + l^2\dot{\lambda}(t)^2 + l^2\dot{\phi}(t)^2 \\ & + 2\dot{u}(t)\Big(\dot{\lambda}(t)(l\cos(\phi(t)) - w(t)) + l\dot{\phi}(t)\cos(\phi(t))\Big) \\ & + 2lu(t)\dot{\lambda}(t)\dot{\phi}(t)\sin(\phi(t)) + 2lu(t)\dot{\lambda}(t)^2\sin(\phi(t)) \\ & + 2\dot{w}(t)\Big(\dot{\lambda}(t)(l\sin(\phi(t)) + u(t)) + l\dot{\phi}(t)\sin(\phi(t))\Big) \\ & - 2lw(t)\dot{\lambda}(t)\dot{\phi}(t)\cos(\phi(t)) - 2lw(t)\dot{\lambda}(t)^2\cos(\phi(t))1 \\ & + \dot{u}(t)^2 + u(t)^2\dot{\lambda}(t)^2 + \dot{w}(t)^2 + w(t)^2\dot{\lambda}(t)^2\Big] \end{aligned} \tag{4.11}$$

$$U = -mgl\cos(\lambda(t) + \phi(t)) + mgl + gmw(t) \tag{4.12}$$

Differentiating the kinetic energy with respect to $\dot{\phi}(t)$ gives:

$$\begin{aligned} \frac{\partial T}{\partial\dot{\phi}(t)} = \frac{1}{2}m \Big[ & 2l^2\dot{\lambda}(t) + 2l^2\dot{\phi}(t) + 2l\dot{u}(t)\cos\phi(t) + 2lu(t)\dot{\lambda}(t)\sin\phi(t) \\ & + 2l\dot{w}(t)\sin\phi(t) - 2lw(t)\dot{\lambda}(t)\cos\phi(t)\Big] \end{aligned} \tag{4.13}$$

which, after differentiating with respect to time becomes:

$$\begin{aligned} \frac{d}{dt}\left(\frac{\partial T}{\partial\dot{\phi}(t)}\right) = \frac{1}{2}m \Big[ & 2l^2\ddot{\lambda}(t) + 2l^2\ddot{\phi}(t) + 2l\ddot{u}(t)\cos\phi(t) \\ & + 2l\dot{\lambda}(t)\dot{u}(t)\sin\phi(t) - 2l\dot{u}(t)\dot{\phi}(t)\sin\phi(t) \\ & + 2lu(t)\ddot{\lambda}(t)\sin\phi(t) + 2lu(t)\dot{\lambda}(t)\dot{\phi}(t)\cos\phi(t) \\ & + 2l\ddot{w}(t)\sin\phi(t) - 2l\dot{\lambda}(t)\dot{w}(t)\cos\phi(t) \\ & + 2l\dot{w}(t)\dot{\phi}(t)\cos\phi(t) - 2lw(t)\ddot{\lambda}(t)\cos\phi(t) \\ & + 2lw(t)\dot{\lambda}(t)\dot{\phi}(t)\sin\phi(t)\Big] \end{aligned} \tag{4.14}$$

Differentiating the kinetic and potential energies with respect to $\phi(t)$ now gives:

$$\begin{aligned}\frac{\partial T}{\partial \phi(t)} = \frac{1}{2}m\Big[&2\dot{u}(t)\left(-l\dot{\lambda}(t)\sin\phi(t) - l\dot{\phi}(t)\sin\phi(t)\right) + 2lu(t)\dot{\lambda}(t)\dot{\phi}(t)\cos\phi(t) \\ &+ 2lu(t)\dot{\lambda}(t)^2\cos\phi(t) + 2\dot{w}(t)\left(l\dot{\lambda}(t)\cos\phi(t) + l\dot{\phi}(t)\cos\phi(t)\right) \\ &+2lw(t)\dot{\lambda}(t)\dot{\phi}(t)\sin\phi(t) + 2lw(t)\dot{\lambda}(t)^2\sin\phi(t)\Big] \end{aligned} \tag{4.15}$$

$$\frac{\partial U}{\partial \phi(t)} = mgl\sin(\lambda(t) + \phi(t)) \tag{4.16}$$

Therefore, by substituting Eq. 4.14,4.15 and 4.16 into the Lagrange's equations shown in Eq. 4.1, the following equation of motion is found:

$$\begin{aligned}&\ddot{\phi}(t) + \frac{g}{l}\sin(\phi(t) + \lambda(t)) + 2\omega_n\xi\dot{\phi}(t) - \frac{\dot{\lambda}(t)^2u(t)}{l}\cos\phi(t) + \frac{\ddot{\lambda}(t)u(t)}{l}\sin\phi(t) \\ &\quad + \frac{2\dot{\lambda}(t)\dot{u}(t)}{l}\sin\phi(t) + \frac{\ddot{u}(t)}{l}\cos\phi(t) - \frac{\lambda(t)^2w(t)}{l}\sin\phi(t) - \frac{\ddot{\lambda}(t)w(t)}{l}\cos\phi(t) \\ &\quad - \frac{2\dot{\lambda}(t)\dot{w}(t)}{l}\cos\phi(t) + \frac{\ddot{w}(t)}{l}\sin\phi(t) - \ddot{\lambda}(t) = Q_\phi \end{aligned} \tag{4.17}$$

where, again $Q_\phi$ allows for the provision of some generalised force if required and linear viscous damping terms have been included.

Finally, the following harmonic expressions are again assumed for the excitation terms:

$$\begin{aligned} u(t) &= U_0\cos\Omega_u t & w(t) &= W_0\cos\Omega_w t & \lambda(t) &= \lambda_0\cos\Omega_\lambda t \\ \dot{u}(t) &= -U_0\Omega_u\sin\Omega_u t & \dot{w}(t) &= -W_0\Omega_w\sin\Omega_w t & \dot{\lambda}(t) &= -\lambda_0\Omega_\lambda\sin\Omega_\lambda t \\ \ddot{u}(t) &= -U_0{\Omega_u}^2\cos\Omega_u t & \ddot{w}(t) &= -W_0{\Omega_w}^2\cos\Omega_w t & \ddot{\lambda}(t) &= -\lambda_0{\Omega_\lambda}^2\cos\Omega_\lambda t \end{aligned} \tag{4.18}$$

Hence, with appropriate substitution, the final form of the equation of motion may be

arrived at:

$$\begin{aligned}\ddot{\phi}(t) + \frac{g}{l}\sin\left(\phi(t) + \lambda_0\cos\Omega_\lambda t\right) + 2\omega_n\xi\dot{\phi}(t) &= \frac{{\lambda_0}^2{\Omega_\lambda}^2\sin^2\left(\Omega_\lambda t\right)U_0\cos\left(\Omega_u t\right)}{l}\cos\phi(t) \\ &+ \frac{\lambda_0{\Omega_\lambda}^2\cos\left(\Omega_\lambda t\right)U_0\cos\left(\Omega_u t\right)}{l}\sin\phi(t) - \frac{2\lambda_0\Omega_\lambda\sin\left(\Omega_\lambda t\right)U_0\Omega_u\sin\left(\Omega_u t\right)}{l}\sin\phi(t) \\ &+ \frac{U_0{\Omega_u}^2\cos\left(\Omega_u t\right)}{l}\cos\phi(t) + \frac{{\lambda_0}^2{\Omega_\lambda}^2\sin^2\left(\Omega_\lambda t\right)W_0\cos\left(\Omega_w t\right)}{l}\sin\phi(t) \\ &- \frac{\lambda_0{\Omega_\lambda}^2\cos\left(\Omega_\lambda t\right)W_0\cos\left(\Omega_w t\right)}{l}\cos\phi(t) + \frac{2\lambda_0\Omega_\lambda\sin\left(\Omega_\lambda t\right)W_0\Omega_w\sin\left(\Omega_w t\right)}{l}\cos\phi(t) \\ &+ \frac{W_0{\Omega_w}^2\cos\left(\Omega_w t\right)}{l}\sin\phi(t) - \lambda_0{\Omega_\lambda}^2\cos\Omega_\lambda t \end{aligned} \tag{4.19}$$

This highlights the resulting severity of coupling between all three forms of excitation $U_0$, $W_0$ and $\lambda_0$. The consequences of this are that any rotation affected by $\lambda_0$ will invariably also affect a displacement in $U$ and $W$ when measured from $OXZ$, provided that either $U_0$ or $W_0$ are nonzero. This is further demonstrated in Fig. 4.8 where various combinations of horizontal or vertical excitations are coupled with nonzero rotational excitations. In Fig. 4.8(a) the horizontal translation and rotation introduces an additional vertical displacement despite $W_0 = 0$, and visa versa in Fig. 4.8(b).

Only in the situation where both $U_0$ or $W_0$ are zero can rotational excitations to be applied to the system without subsequently translating the pendulum body in either $u$ or $w$ as demonstrated in Fig. 4.8(c). Eq. 4.19 shows how this condition is reduced to Eq. 4.20 where translation terms are no longer present.

$$\ddot{\phi}(t) + \frac{g}{l}\sin\left(\phi(t) + \lambda_0\cos\Omega_\lambda t\right) + 2\omega_n\xi\dot{\phi}(t) = -\lambda_0{\Omega_\lambda}^2\cos\Omega_\lambda t \tag{4.20}$$

This presents a severe limitation of user control and it was for this reason that the approach was abandoned. Ideally, a method where it would be possible to individually control each excitation term without inherently affect the others is desirable for being able to effectively define particular excitation conditions. Therefore the alternative fully decoupled geometrical approach in which a second body frame of the pendulum is rotated about the origin of the principal body frame will now be explored next.

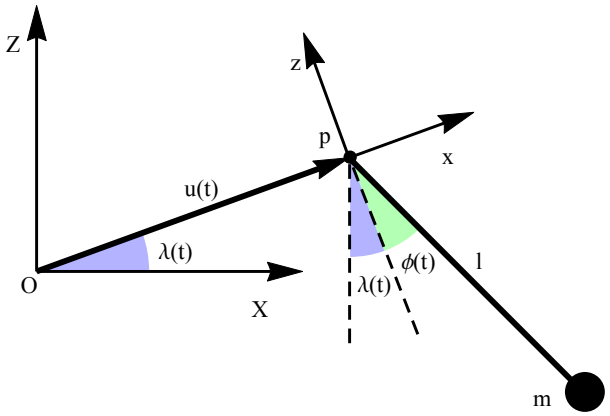


(a) $u_0 \neq 0$m, $w_0 = 0$m and $\lambda_0 \neq 0°$.

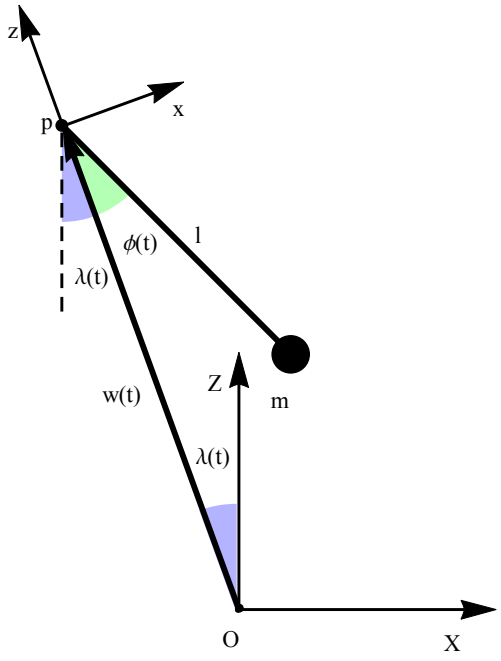


(b) $u_0 = 0$m, $w_0 \neq 0$m and $\lambda_0 \neq 0°$.

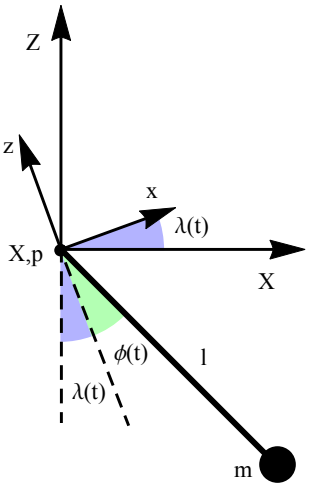


(c) $u_0 = 0$m, $w_0 = 0$m and $\lambda_0 \neq 0°$.

Figure 4.8: Schematics highlighting the inherent coupling between the three forms of excitation for various translation and rotation combinations.

## 4.4 Derivation of Planar Pendulum Device with Geometrically Described Rotations (Decoupled System)

It has been established that it is desirable to fully decouple all three forms of excitation that are realisable for a planar pendulum. By doing so, one provides full control to the user to be able to individually define the excitations without intrinsically affecting the others. This is especially useful when attempting to assess the influence each individually, or in combination, has upon the response of the system. Complications have arisen when attempting to model the rotational excitations in particular where previously these terms have generated heavy coupling with the other two forms of excitation. A new approach to tackle this problem will now be explored.

### 4.4.1 Rotation of a Second Pendulum Body Frame about the Origin of the Principal Body Frame

The deflected planar pendulum shown in Fig. 4.9 is intended to address the issue of coupling between the excitation terms within the system. Again the horizontal and vertical translations and the rotations are defined by $u, w$ and $\lambda$ respectively. In this scenario however, $\lambda$ causes a rotation of a second body frame $p', x', z'$ about $p$ of the original pendulum body frame $pxz$. Both body frames may still be translated by $u$ and $w$ with respect to the absolute frame of reference $OXZ$.

The response of the pendulum remains measured as a displacement through $\phi$ with tangential velocities of $l\left(\dot{\phi}(t) + \dot{\lambda}(t)\right)$.

Again, utilising Lagrange's equations, the kinetic, $T$ and potential, $U$ energies of the decoupled system are defined as:

$$T = \frac{1}{2}m\Big[l^2\left(\dot{\lambda}(t) + \dot{\phi}(t)\right)^2 + 2l\dot{u}(t)\left(\dot{\lambda}(t) + \dot{\phi}(t)\right)\cos(\lambda(t) + \phi(t)) + 2l\dot{w}(t)\left(\dot{\lambda}(t) + \dot{\phi}(t)\right)\sin(\lambda(t) + \phi(t)) + \dot{u}(t)^2 + \dot{w}(t)^2\Big] \tag{4.21}$$

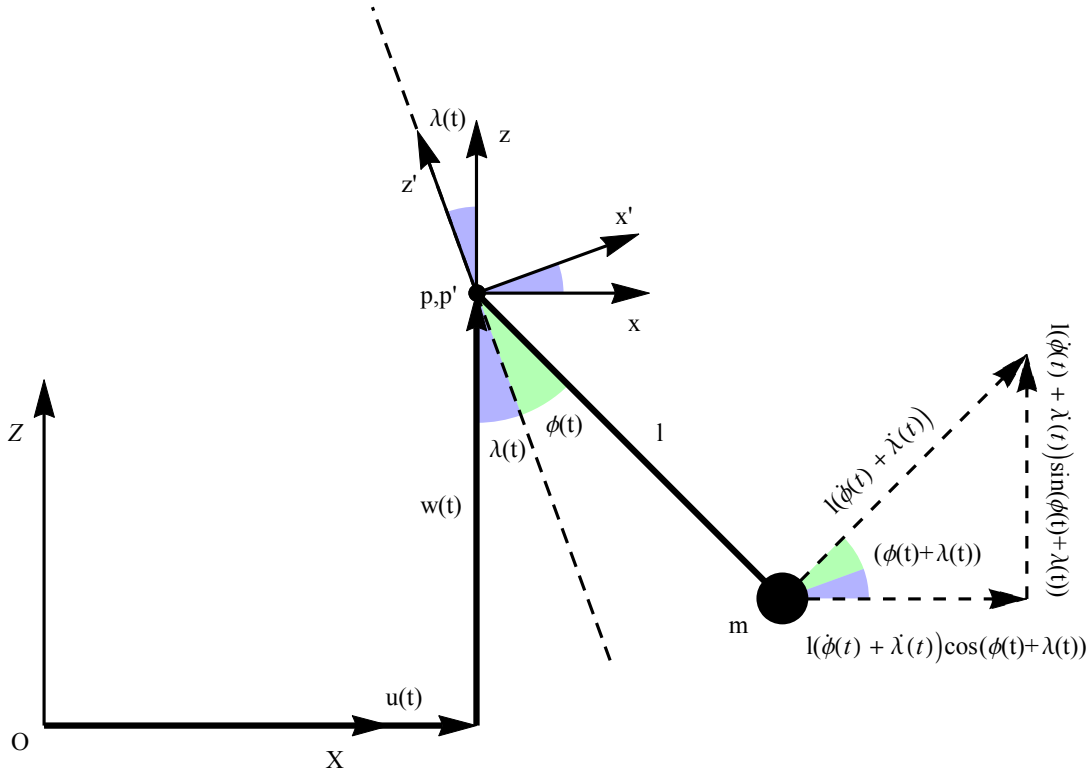


Figure 4.9: Deflected pendulum with fully decoupled forms of excitation of translation in $u$ and $w$ and rotations of $\lambda$ about $p$, with $\phi$ as the permissible degree of freedom in which the swing of the pendulum arm is measured.

$$U = -mgl\cos(\lambda(t)+\phi(t)) + mgl + mgw(t) \tag{4.22}$$

Hence, differentiating Eq. 4.21 with respect to $\dot{\phi}(t)$ yields:

$$\frac{\partial T}{\partial \dot{\phi}(t)} = \frac{1}{2}m\left[2l^2\left(\dot{\lambda}(t)+\dot{\phi}(t)\right) + 2l\dot{u}(t)\cos\left(\lambda(t)+\phi(t)\right) + 2l\dot{w}(t)\sin\left(\lambda(t)+\phi(t)\right)\right] \tag{4.23}$$

which, after differentiating with respect to time becomes:

$$\begin{aligned}\frac{d}{dt}\left(\frac{\partial T}{\partial \dot{\phi}(t)}\right) = \frac{1}{2}m\Big[&2l^2\left(\ddot{\lambda}(t)+\ddot{\phi}(t)\right) + 2l\ddot{u}(t)\cos(\lambda(t)+\phi(t)) \\ &- 2l\dot{u}(t)\left(\dot{\lambda}(t)+\dot{\phi}(t)\right)\sin(\lambda(t)+\phi(t)) + 2l\ddot{w}(t)\sin(\lambda(t) \\ &+\phi(t)) + 2l\dot{w}(t)\left(\dot{\lambda}(t)+\dot{\phi}(t)\right)\cos(\lambda(t)+\phi(t))\Big]\end{aligned} \tag{4.24}$$

Now, differentiating Eq. 4.21 and 4.22 with respect to $\phi(t)$ gives:

$$\begin{aligned}\frac{\partial T}{\partial \phi(t)} = \frac{1}{2}m\Big[&2l\dot{w}(t)\left(\dot{\lambda}(t)+\dot{\phi}(t)\right)\cos(\lambda(t)+\phi(t)) - 2l\dot{u}(t)\left(\dot{\lambda}(t)\right. \\ &\left.+\dot{\phi}(t)\right)\sin(\lambda(t)+\phi(t))\Big]\end{aligned} \tag{4.25}$$

$$\frac{\partial U}{\partial \phi(t)} = mgl\sin(\lambda(t)+\phi(t)) \tag{4.26}$$

And with appropriate substitution into Lagranges equations, shown in Eq. 4.1, the following equation of motion is obtained:

$$\begin{aligned}\ddot{\phi}(t) + 2\xi\omega_n\dot{\phi}(t) + \frac{g}{l}\sin(\lambda(t)+\phi(t)) + \frac{\ddot{u}(t)}{l}\cos(\lambda(t)+\phi(t)) \\ + \frac{\ddot{w}(t)}{l}\sin(\lambda(t)+\phi(t)) + \ddot{\lambda}(t) = Q_\phi\end{aligned} \tag{4.27}$$

where linear viscous damping terms, $2\xi\omega_n\dot{\phi}(t)$ have been inserted.

Finally, by assuming and substituting the harmonic solutions for the excitation terms, shown in Eq. 4.18, the equation of motion may be rewritten as:

$$\begin{aligned}\ddot{\phi}(t) + 2\xi\omega_n\dot{\phi}(t) + \frac{g}{l}\sin\left(\phi(t) + \lambda_0\cos\left(\Omega_\lambda t\right)\right) = &\frac{U_0{\Omega_u}^2\cos\left(\Omega_u t\right)}{l}\cos\left(\phi(t) + \lambda_0\cos\left(\Omega_\lambda t\right)\right) \\ &+ \frac{W_0{\Omega_w}^2\cos\left(\Omega_w t\right)}{l}\sin\left(\phi(t) + \lambda_0\cos\left(\Omega_\lambda t\right)\right) \\ &+ \lambda_0{\Omega_\lambda}^2\cos\left(\Omega_\lambda t\right) \qquad (4.28)\end{aligned}$$

Immediately it is clear from the three sets of right hand excitation terms have been successfully decoupled from one another. The equation of motion is also remarkably simpler that that derived in Eq. 4.19 because of the way in which all the coupled terms cancelled out with one another. This in itself is encouraging.

Furthermore, the schematics shown in Fig. 4.10 demonstrate typical behaviour that these terms may produce under the various stated conditions. It now remains to perform a numerical analysis based upon Eq. 4.28 to assess the actual performance of the derived equation to confirm that the approach for introducing rotational excitations is functional.

### 4.4.2 Static Rotations of the Decoupled System

To begin with, the pendulum will be subjected to static rotations at $t = 0$ such that $\lambda_0 \neq 0°$ and $\Omega_\lambda = 0$rad. It can be seen that this results in a similar response to those reported in Fig. 4.2 when the torque induced rotations method was utilised. However, despite appearances, the response here is actually very different. When $\lambda_0 = -45°$ the response in Fig. 4.11(a) shows that $\phi = 0°$ at $t = 0$. But immediately after this when time is allowed to progress the trajectory enters into oscillatory motion within the negative domain and eventually settles to a steady state at $\phi = 45°$.

This behaviour continues for increasing values of $\lambda_0$ and is attributed to the pendulum being deflected by the prescribed value of $\lambda_0$ at $t = 0$ and subsequently possessing potential energy. It will then fall from this point under the force of gravity when $t > 0$. This results in a response in $\phi$, which of course begins from $\phi = 0°$ at $t = 0$. The final steady state value of $\phi$ is always equal to $-\lambda_0$ when $\lambda_0 < 180°$.

This behaviour produced here is similar to specifying an initial condition such as

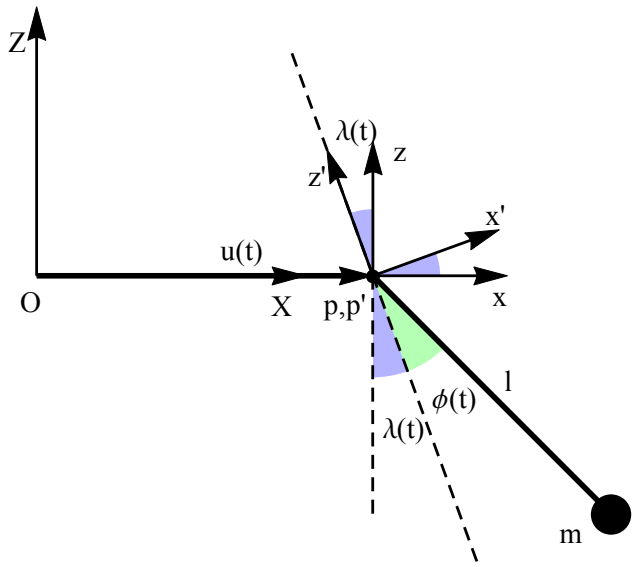


(a) $u_0 \neq 0$m, $w_0 = 0$m and $\lambda_0 \neq 0°$.

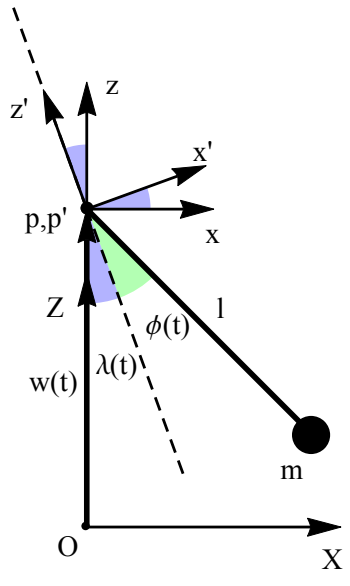


(b) $u_0 = 0$m, $w_0 \neq 0$m and $\lambda_0 \neq 0°$.

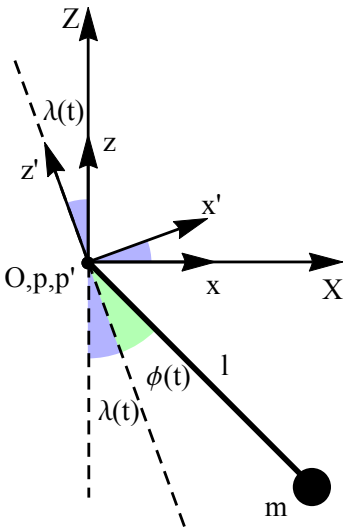


(c) $u_0 = 0$m, $w_0 = 0$m and $\lambda_0 \neq 0°$.

Figure 4.10: Schematics demonstrating the decoupled behaviour between the three forms of excitation.

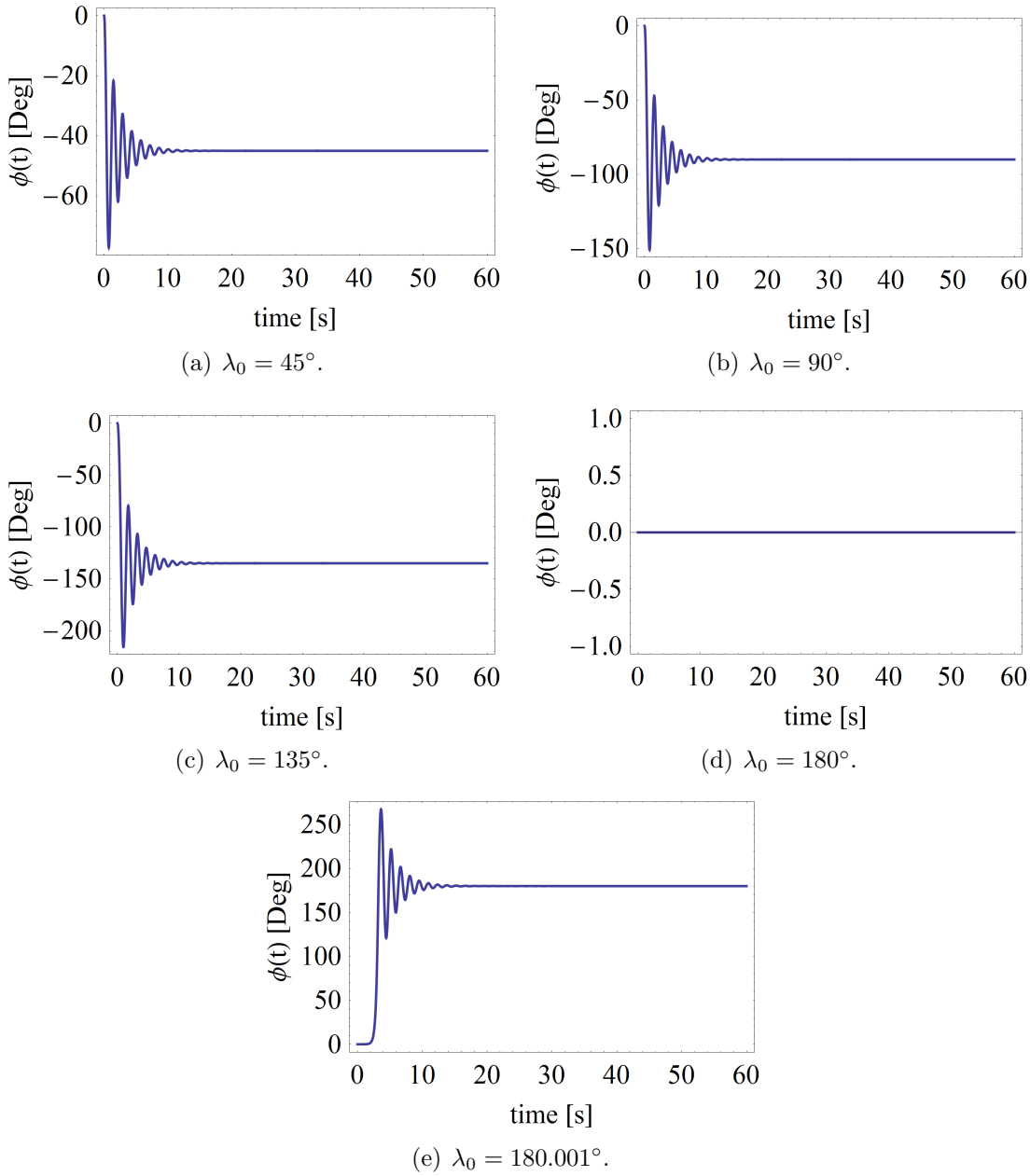


(a) $\lambda_0 = 45°$.

(b) $\lambda_0 = 90°$.

(c) $\lambda_0 = 135°$.

(d) $\lambda_0 = 180°$.

(e) $\lambda_0 = 180.001°$.

Figure 4.11: Time domain responses of the pendulum to increasing magnitudes of $\lambda_0$, where $l = 0.5$m, $m = 1$kg, $\xi = 0.1$, $U_0 = 0$m, $W_0 = 0$m, $\Omega_u = 0$rad/s, $\Omega_w = 0$rad/s, $\Omega_\lambda = 0$rad/s, $\phi(0) = 0$rad, $\dot{\phi}(0) = 0$rad/s and $0 \leq t \leq 60$s.

$\phi(0) \neq 0$, except that here $\phi$ would begin from the defined condition and oscillate before eventually coming to rest at $\phi(t > 0) = 0°$. Note that it is also possible to initially displace the pendulum body frame from the absolute frame via $u$ and $w$ at $t = 0$, but that this will not result in any measured response in $\phi$ since no differences in potential energy will have been created.

An interesting feature is highlighted in Fig. 4.11(d) where it can be seen that no response is produced. What has occurred under these conditions is that the pendulum has initially been rotated through 180° so that it is pointing vertically upwards. This results in gravity acting axially down upon $m$ and with no transverse forces acting upon the system, the pendulum remains stationary. By further increasing the value of $\lambda_0$ by as little as ±0.001°, gravity will no longer be acting axially upon the pendulum and a response is produced. Note that the response of $\phi$ in Fig. 4.11(d) is positive because the pendulum was rotated by more than 180°, causing it to rotate anticlockwise.

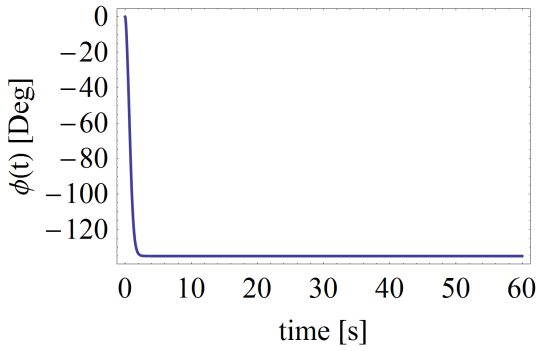


Figure 4.12: Time domain response of the critically damped pendulum where $\lambda_0 = 135°$, $l = 0.5$m, $m = 1$kg, $\xi = 1.0$, $U_0 = 0$m, $W_0 = 0$m, $\Omega_u = 0$rad/s, $\Omega_w = 0$rad/s, $\Omega_\lambda = 0$rad/s, $\phi(0) = 0$rad, $\dot{\phi}(0) = 0$rad/s and $0 \leq t \leq 60$s.

Of course, it is possible to reduce the transient phase of these responses by increasing the level of damping within the system. To highlight this, Fig. 4.12 shows the response of a critically damped ($\xi = 1.0$) system which is released from rest at $\lambda_0 = 135°$. Here no overshoot is evident and the response of the system quickly settles to the appropriate steady state value.

### 4.4.3 Oscillating Rotations of the Decoupled System

Oscillating rotation motion is introduced when $\Omega_\lambda \neq 0$ and initially the excitation is equal to the natural frequency of the system ($\Omega_\lambda = \omega_n$). The influence of damping

is observed in Fig. 4.13 and the majority of these simulations presents what may be perceived as typical behaviour, with the exception of Fig. 4.13(a) where $\xi = 0$. Here the response grows and declines in a periodic fashion. This is because at $t = 0$ the pendulum arm is initially raised due to the nature of the cosine within the excitation terms. Then after $t = 0$ the pendulum begins to fall under gravity whilst $\lambda_0$ oscillates at a frequency of $(\Omega_\lambda = \omega_n)$. Because $\xi = 0$, no energy is dissipated through the system and the pendulum will continue to swing endlessly between $\pm\lambda_0^\circ$. The result is that $\phi(t)$ periodically moves in and out of sync with $\lambda_0$ in the manner indicated by Fig. 4.13(a).

As $\xi$ is increased the response in $\phi$ begins to reduce due to energy being dissipated via the damping and so the response is able to achieve a more stable response after an initial transient phase.

Also, as would be expected, increased values of $\xi$ lead to reduced amplitudes of response. This trend continues as $\xi$ is increased to exaggerated values until in Fig. 4.13(d) the level damping is so large that the response is near zero.

The excitation frequency, $\Omega_\lambda$, also plays a very important role. Whereas previous simulations have been performed at $\Omega_\lambda = \omega_n$, Fig. 4.14 shows the response of the system to a frequency sweep. This sweep was performed by measuring the rectified peak response in $\phi$ when $60 \leq t \leq 90$s for each data point to give an indication of the performance of the system. The specified time domain was to ensure that any transient response was not included within the mean rectification process. This was repeated over a range of damping, $\xi$ values.

This has highlighted that in fact the transmittance of the system decays in the region of $\Omega_\lambda = \omega_n$ and therefore produces a negative effect on the application of energy harvesting.

This behaviour has been confirmed over an extensive range of time domain simulations, and whilst perhaps not intuitively obvious to begin with, it can be explained by the fact that when $\Omega_\lambda = \omega_n$, the swinging motion of the pendulum approaches synchronicity with $\lambda(t)$. The repercussion of this is that the measured displacement of $\phi$ will be greatly reduced and so in order to maximise the response of the system, one must always attempt to ensure that the swinging motion of the

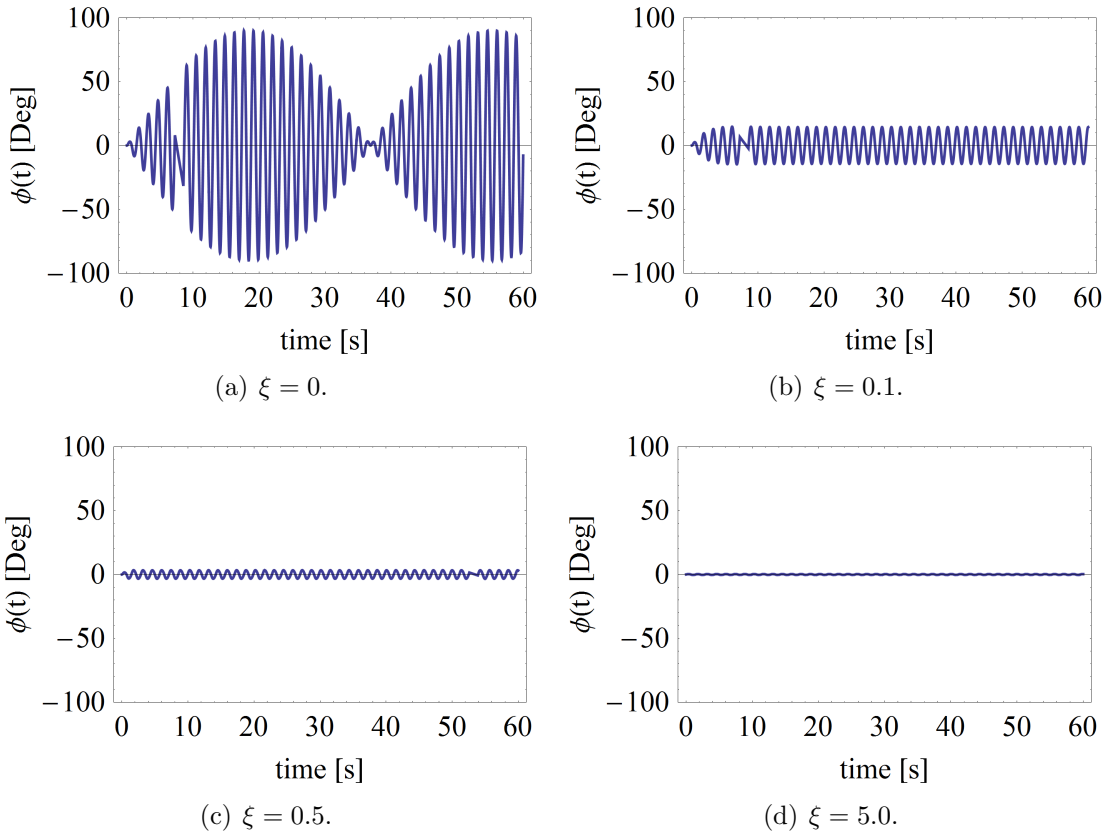


(a) $\xi = 0$.

(b) $\xi = 0.1$.

(c) $\xi = 0.5$.

(d) $\xi = 5.0$.

Figure 4.13: Time domain responses of the oscillating pendulum to increasing magnitudes of $\xi$, where $\lambda_0 = 45°$, $l = 0.5$m, $m = 1$kg, $U_0 = 0$m, $W_0 = 0$m, $\Omega_u = 0$rad/s, $\Omega_w = 0$rad/s, $\Omega_\lambda = \omega_n$, $\phi(0) = 0$rad, $\dot{\phi}(0) = 0$rad/s and $0 \leq t \leq 60$s.

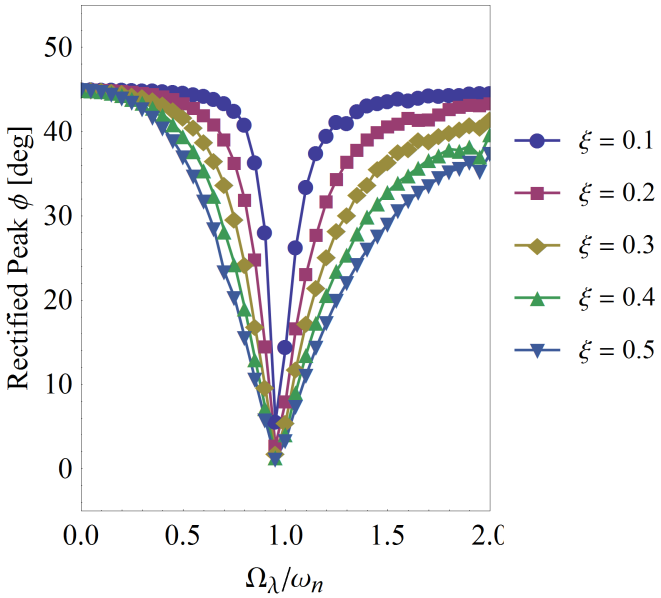


Figure 4.14: Frequency sweep for a range of values of $\xi$, where $\lambda_0 = 45°$, $l = 0.5$m, $m = 1$kg, $U_0 = 0$m, $W_0 = 0$m, $\Omega_u = 0$rad/s, $\Omega_w = 0$rad/s, $\phi(0) = 0$rad, $\dot{\phi}(0) = 0$rad/s and $60 \leq t \leq 90$s.

pendulum and $\lambda(t)$ are as near to 90 degrees out of phase with each other as possible.

### 4.4.4 Combined Translations and Rotations of the System

Whilst it is not the intention of the current study to fully investigate the dynamics of an *unloaded* pendulum (where no terms describing some form of power take-off device have been included), a brief investigation into the combined effects of both translational and rotational excitations was appropriate to be confident that the full derived equation of motion, and indeed the approach to introducing decoupled rotations, was performing adequately. This was done by observing phase portraits of the system response to various excitation combinations and profiles. These are shown in Fig. 4.15 and 4.16.

The trajectories seen when either $U_0 \neq 0$ or $W_0 \neq 0$ alone indicate typical responses with no other significant observations to be made other than the excitations appear to be functional. Note that with respect to vertical excitations $\Omega_w = 2\omega_n$ because in this configuration the system is parametric in nature and so this would be the appropriate resonant condition. Perhaps the most interesting behaviour in these examples occurs in Fig. 4.16 with the formation of additional periods when $\Omega_\lambda$ is equal to $0.5\omega_n$ and

$1.5\omega_n$. This is further evidence of interesting dynamics taking place within the system. Unfortunately, as previously stated, investigations of this type do not fall within the remit of the current study where the purpose is to assess the performance of a planar pendulum as an energy harvesting device and how throughput can be improved.

From these responses no anomalous behaviour is evident, which is exactly what was hoped and so it is assumed that the current approach to exciting the pendulum in the full three degrees of freedom is functioning properly and with the desired level of control afforded to the user. Effort will now be directed towards applying an external load in order to be able to represent a suitable form of power take-off device to convert the mechanical motion of the system into useful electrical energy, and to make predictions of the expected harvestable powers for a given configuration. That said, it is suggested that future research be conducted on the interesting dynamics hinted at here to gain a better understanding of the complicated relationship between all three forms of excitation. This is expected to be an extensive undertaking given the almost limitless possible combinations.

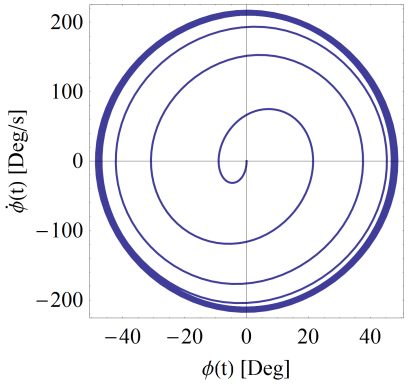


(a) $U_0 = 0.1$m, $W_0 = 0$m, $\lambda_0 = 0°$, $\Omega_u = \omega_n$rad/s, $\Omega_w = 0$rad/s, $\Omega_\lambda = 0$rad/s.

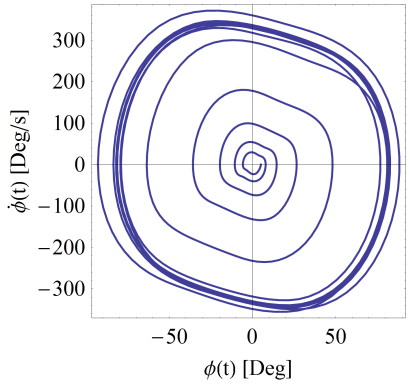


(b) $U_0 = 0$m, $W_0 = 0.1$m, $\lambda_0 = 0°$, $\Omega_u = 0$rad/s, $\Omega_w = 2\omega_n$rad/s, $\Omega_\lambda = 0$rad/s. (Note that $\phi(0) = 5°$ here only).

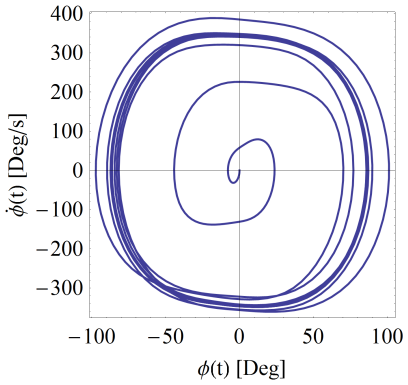


(c) $U_0 = 0.1$m, $W_0 = 0.1$m, $\lambda_0 = 0°$, $\Omega_u = \omega_n$rad/s, $\Omega_w = 2\omega_n$rad/s, $\Omega_\lambda = 0$rad/s.

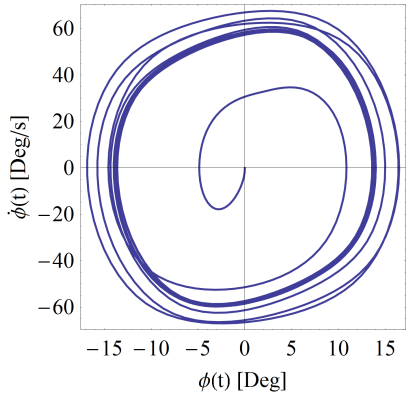


(d) $U_0 = 0.1$m, $W_0 = 0$m, $\lambda_0 = 45°$, $\Omega_u = \omega_n$rad/s, $\Omega_w = 0$rad/s, $\Omega_\lambda = \omega_n$rad/s.

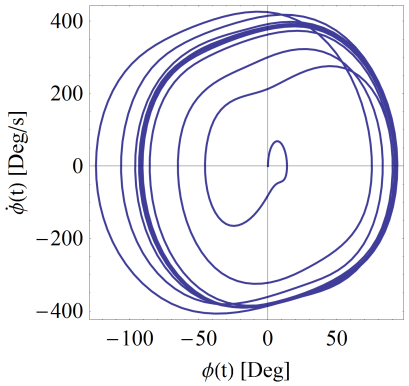


(e) $U_0 = 0$m, $W_0 = 0.1$m, $\lambda_0 = 45°$, $\Omega_u = 0$rad/s, $\Omega_w = 2\omega_n$rad/s, $\Omega_\lambda = \omega_n$rad/s.

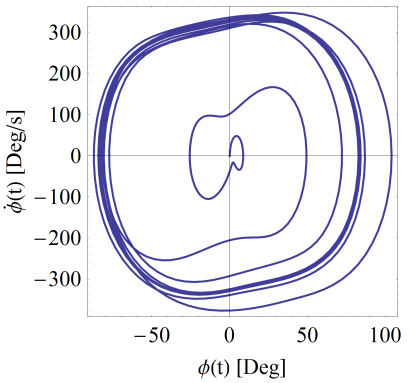


(f) $U_0 = 0.1$m, $W_0 = 0.1$m, $\lambda_0 = 45°$, $\Omega_u = \omega_n$rad/s, $\Omega_w = 2\omega_n$rad/s, $\Omega_\lambda = \omega_n$rad/s.

Figure 4.15: Phase portraits of the oscillating pendulum to various excitation conditions where $l = 0.5$m, $m = 1$kg, $\phi(0) = 0$rad, $\dot{\phi}(0) = 0$rad/s and $0 \leq t \leq 60$s.

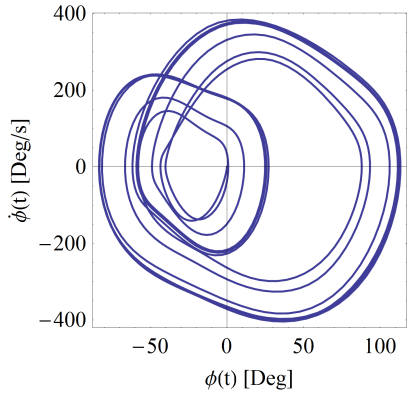


(a) $U_0 = 0.1$m, $W_0 = 0.1$m, $\lambda_0 = 45°$, $\Omega_u = \omega_n$rad/s, $\Omega_w = 2\omega_n$rad/s, $\Omega_\lambda = 0.5\omega_n$rad/s.

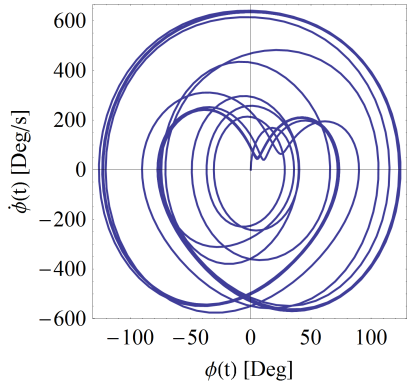


(b) $U_0 = 0.1$m, $W_0 = 0.1$m, $\lambda_0 = 45°$, $\Omega_u = \omega_n$rad/s, $\Omega_w = 2\omega_n$rad/s, $\Omega_\lambda = 1.5\omega_n$rad/s.

Figure 4.16: Continued phase portraits of the oscillating pendulum to various excitation conditions where $l = 0.5$m, $m = 1$kg, $\phi(0) = 0$rad, $\dot{\phi}(0) = 0$rad/s and $0 \leq t \leq 60$s.

## 4.5 Summarising Remarks for the Derivation of a Geometrically Described Planar Pendulum

A planar pendulum that is excitable in the full three degrees of freedom has been derived. The purpose was to be able to introduce rotations as excitations together with horizontal and vertical translations. To do this two approaches were investigated; firstly by rotating the pendulum body frame ($pxz$) about the absolute frame of reference ($OXZ$), secondly by introducing a second body frame ($p'x'z'$) and rotating this about the origin of ($pxz$). In both approaches $pxz$ could be translated horizontally and vertically with respect to $OXZ$.

The outcome of the first approach was an equation of motion that was very complicated that resulted in heavily coupled terms. Given the lack of flexibility that this would impart upon the user when designing or replicating particular excitation environments, it was concluded that this approach was ineffective and therefore was abandoned in favour of the second approach.

The second approach produced a very simple equation of motion in which the excitation terms were fully decoupled from each other. Numerical simulations were used to perform performance checks with specific attention given to the rotational excitation terms. These were shown to produce behaviour that may be intuitively predicted in practice. It was also highlighted the important role that damping plays in

such systems where higher levels were shown to restrict the measured response in $\phi$ in the usual manner. Because $\phi$ would be the harvestable response for energy harvesting purposes, this would clearly reduce the throughput of the system and demonstrates the importance of making every effort to reduce the inherent damping within any energy harvesting system.

It was also shown that the response of $\phi$ when excited rotationally only is lowest at resonant conditions when $\Omega_\lambda \approx \omega_n$. This was attributed to the swing of the pendulum synchronising with the excitation, thus leading to a lower measured response in $\phi$. It was therefore suggested that effort must be given to maintain an excitation frequency that is 90° out of phase with $\omega_n$ to maximise the response of the system.

Finally, a brief investigation highlighted the potentially interesting and complicated behaviour when more than one form of excitation was introduced at same time. This was a very brief study, but it is suggested that future effort be given to studying these dynamics in greater depth. However, given the intended purpose of the planar pendulum as a vibrational energy harvesting device, the performance of the system may be better understood by measuring the harvestable energy. To this end, it is necessary to define an external load by which to extract energy from the current system. This external loading will be used to represent a suitable power take-off device that may be realised in practice.

# Chapter 5

# Response Based External Loading Terms

A method has now been developed that is capable of exciting a planar pendulum in the full three degrees of freedom realisable by such systems. It remains however, to develop an approach for measuring the amount of energy that such a device would be capable of harvesting from ambient conditions. By developing a set of appropriate external loading terms representing a power take-off device, it would be possible to measure the energy throughput of the system. Furthermore, the concept behind the pendulum-based harvester is for it to be able to harvest accelerating motion in both directions of swing of the pendulum arm about its pivot point, which requires the response to be rectified in some way. Devices capable of performing this function are readily available in practice, including those that mechanically rectify the instantaneous principal plane of motion either from a single plane (planar pendulum), or indeed two principal planes of motion mutually rotated 90 degrees from one another (spherical pendulum). The present analysis focusses upon the external loading of a planar pendulum only.

Previous studies by Watt and Cartmell (1994) [95] developed an approach to model the resistive torque produced by a ratchet and pawl mechanism that lifted a known mass as a suitable power take-off device for a parametric oscillator in the form of a torsional pendulum. The author investigated the possibility of developing this approach for the pendulum energy harvester, of which is included in Appendix A for the readers interest, but ultimately the method was proven unsuitable for the present application.

It was shown that a pre-assigned frequency based set of loading terms, such as those proposed in [95], are inherently difficult for maintaining synchronicity with the response of a loaded system. In such circumstances, it can be that the intended loading terms intermittently switch between acting as an energy sink, to an energy source, thereby at times driving the system instead. This was shown in Appendix A to be more prominent during non-resonant conditions, and was predicated to be further exaggerated when additional excitation terms were introduced. It was also shown that a phase changed would occur when the response of the system crossed zero, thereby again turning the load into an energy source.

The clear solution to these problems would be to base the frequency of any external loading terms used to represent a power take-off device directly upon the response itself, such that the load always provides a resistance against the motion of the pendulum. The following will attempt to develop loadings terms capable of this and explore the resulting performance under various conditions.

## 5.1 Development of Square Wave Response Based Loading Terms

In order to produce a torque that is always resistive to the motion of the pendulum, it is essential to know the direction of said swing. To identify this Fig. 5.1 shows the angular displacement, $\phi(t)$ and the angular velocity, $\dot{\phi}(t)$ of a generic response of the pendulum system that is excited horizontally only. From this it can be seen that as expected $\dot{\phi}(t) = 0$ when $\phi(t)$ reaches a maximum in either domain. Therefore this represents the point in which a change in direction occurs. Hence, the sign of $\dot{\phi}(t)$ reveals the direction of motion.

Not only does this provide information on the direction of motion, but it presents the opportunity to produce a full square wave as opposed to the approximated square wave defined by Eq. A.4. Therefore, a new square wave loading term may be defined as:

$$L_{square} = -T_0 \times \text{Sign}\left[\dot{\phi}(t)\right] \tag{5.1}$$

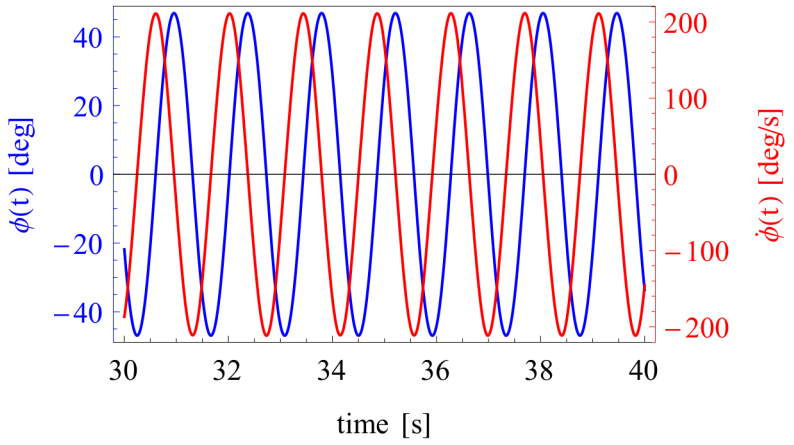


Figure 5.1: Superimposed $\phi(t)$ and $\dot{\phi}(t)$ responses, where $l = 0.5$m, $m = 1$kg, $\xi = 0.1$, $U_0 = 0.1$m, $W_0 = 0$m, $\lambda_0 = 0°$, $\Omega_u = \omega_n$rad/s, $\Omega_w = 0$rad/s, $\Omega_\lambda = 0$rad/s, $\phi(0) = 0$rad, $\dot{\phi}(0) = 0$rad/s and $30 \leq t \leq 40$s.

where again $T_0$ is the magnitude of the applied torque with units, $Nm$.

Note the sign of $T_0$ in Eq. 5.1. This is to ensure that it always acts as a resistance to the direction of $\dot{\phi}(t)$.

After inserting this into the physical form of the equation of motion of the planar pendulum to ensure that torque units are maintained, and subsequently working this back into the preferred form, the new equation of motion describing the loaded pendulum is:

$$\begin{aligned}\ddot{\phi}(t) + 2\xi\omega_n\dot{\phi}(t) + \frac{g}{l}\sin\left(\phi(t) + \lambda_0\cos\left(\Omega_\lambda t\right)\right) = &\frac{U_0{\Omega_u}^2\cos\left(\Omega_u t\right)}{l}\cos\left(\phi(t) + \lambda_0\cos\left(\Omega_\lambda t\right)\right) \\ &+ \frac{W_0{\Omega_w}^2\cos\left(\Omega_w t\right)}{l}\sin\left(\phi(t) + \lambda_0\cos\left(\Omega_\lambda t\right)\right) \\ &+ \lambda_0{\Omega_\lambda}^2\cos\left(\Omega_\lambda t\right) \\ &- \text{Sign}\left[\dot{\phi}(t)\right]T_0 \end{aligned} \tag{5.2}$$

Fig. 5.2 shows the resulting torque profile this new term produces. It shows that the load approach does indeed match the frequency of the response and that a perfect square waveform has been produced that is successful in reducing the response with higher values of $T_0$. Fig. 5.2(c) does show a skewing effect occurring to the response, $\dot{\phi}(t)$, and also evidence of erratic jumps in $L_{square}$ as it appears to respond to small oscillations of $\dot{\phi}(t)$ about zero. Upon closer inspection, it is revealed that the response

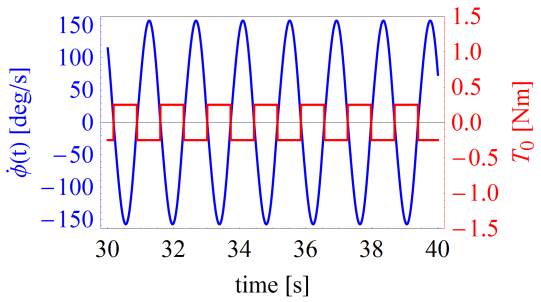


(a) $T_0 = 0.25$Nm.

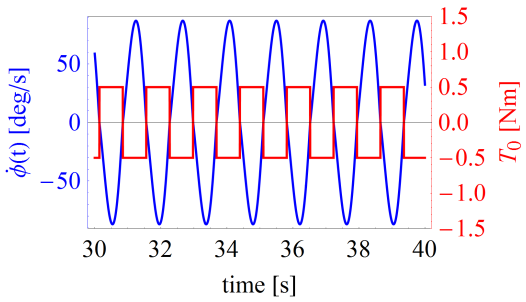


(b) $T_0 = 0.5$Nm.

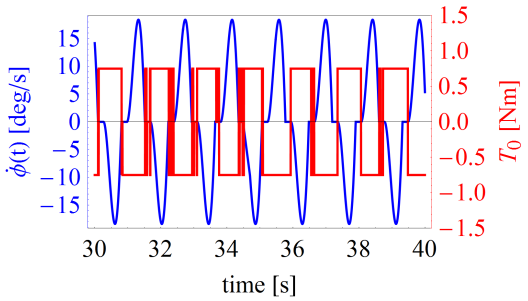


(c) $T_0 = 0.75$Nm.

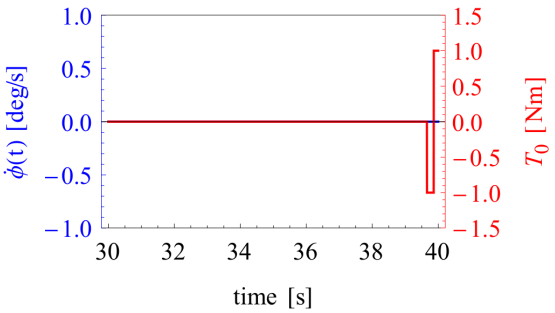


(d) $T_0 = 1.0$Nm.

Figure 5.2: $\dot{\phi}(t)$ responses to increasing values of $T_0$ with *Load* superimposed, where $l = 0.5$m, $m = 1$kg, $\xi = 0.1$, $U_0 = 0.1$m, $W_0 = 0$m, $\lambda_0 = 0°$, $\Omega_u = \omega_n$rad/s, $\Omega_w = 0$rad/s, $\Omega_\lambda = 0$rad/s, $\phi(0) = 0$rad, $\dot{\phi}(0) = 0$rad/s and $30 \leq t \leq 40$s.

does oscillate very closely about zero for these short periods, and accounts for the constant switching of the load.

Fig. 5.2(d) shows a response where the motion of the pendulum appears to have seized. This is shown by the absence of responses in $T_0$ and this is a very encouraging result because the previous loading approaches were incapable of achieving this. Two spikes in $T_0$ do appear just towards the end of the shown time period that could be a result of an integration error, but in the opinion of the author, it is more likely that a response was attempting to grow again. This of course, would be immediately resisted by the presence of $T_0$ again and explains the presence of these spikes in load.

It should be noted that Fig. 5.2 has been plotted at resonant conditions for horizontal excitations, such that $\Omega_u = \omega_n$. This means that the performance of the loading approach discussed in Appendix A, $L_{Fourier}$ can be directly compared to $L_{square}$ since it was shown that $L_{Fourier}$ was functional under resonant condition provided that $\Omega = \Omega_u = \omega_n$.

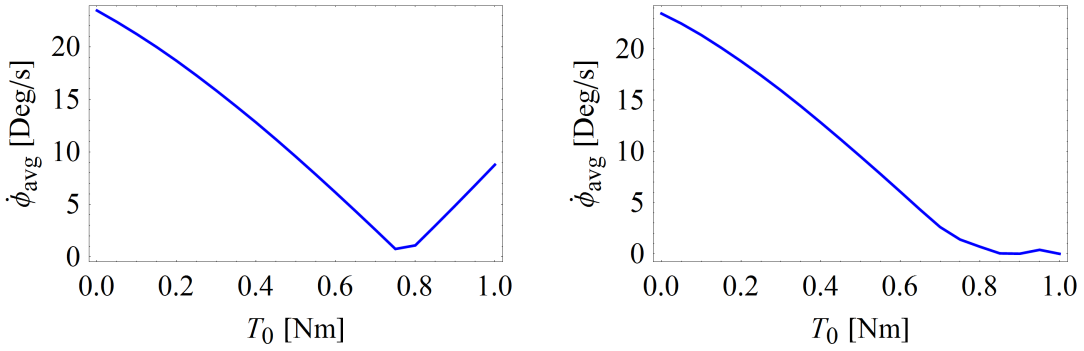


(a) when the external load is defined by $L_{Fourier}$.

(b) when the external load is defined by $L_{square}$.

Figure 5.3: $T_0$ sweeps versus the average angular velocity, $\dot{\phi}_{avg}$ collected over the given time frame, where $l = 0.5$m, $m = 1$kg, $\xi = 0.1$, $U_0 = 0.1$m, $W_0 = 0$m, $\lambda_0 = 0°$, $\Omega_u = \omega_n$rad/s, $\Omega_w = 0$rad/s, $\Omega_\lambda = 0$rad/s, $\Omega = \Omega_u$, $\phi(0) = 0$rad, $\dot{\phi}(0) = 0$rad/s and $30 \leq t \leq 40$s.

Data points have been collected in Fig. 5.3 by summing the absolute values of $\dot{\phi}(t)$ over the given time domain, and dividing this by the time period such that an average angular velocity is obtained as follows:

$$\dot{\phi}_{avg} = \frac{\sum_{t_0}^{t_n} |\dot{\phi}(t)|}{t_n - t_0} \tag{5.3}$$

The results are very similar which in itself lends credence to both approaches when employed in the given conditions. When $T_0 = 0$Nm the average angular velocity, $\dot{\phi}_{avg}$ is at its maximum. Then as $T_0$ increases, both response decrease at similar rates until a minimum is reached at $T_0 \approx 0.8$Nm.

What is important to note is that the point in Fig. 5.3(a) at which the response begins to grow again, showing that there was a phase change in $L_{Fourier}$ such that it became an energy source, is not replicated in Fig. 5.3(b). Instead now the response remains approximately at zero, suggesting that the pendulum has come more or less to a complete halt because the energy fed into the system from the horizontal excitation is no longer great enough to overcome the resistive load. In fact, observations of Fig. 5.4 show this to remain so at much higher values of $T_0$ which confirms that $L_{square}$is incapable of acting as an energy source.

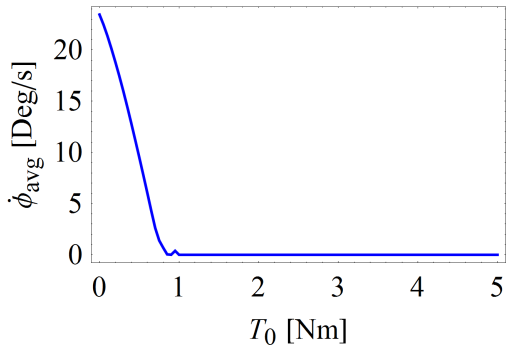


Figure 5.4: $T_0$ sweep versus the average angular velocity, $\dot{\phi}_{avg}$ collected over the given time frame for the $L_{square}$ loading approach, where $l = 0.5$m, $m = 1$kg, $\xi = 0.1$, $U_0 = 0.1$m, $W_0 = 0$m, $\lambda_0 = 0°$, $\Omega_u = \omega_n$rad/s, $\Omega_w = 0$rad/s, $\Omega_\lambda = 0$rad/s, $\phi(0) = 0$rad, $\dot{\phi}(0) = 0$rad/s and $30 \leq t \leq 40$s.

## 5.2 Power Capacity of the Pendulum Energy Harvester

Now that a suitable set of terms representing the square waveform of the power take-off have been developed, and appear to be sufficiently functional, it would be appropriate to measure the energy that can be harvested by $Load_{sqaure}$. By doing so, a parameter study could then be performed to assess the optimal conditions under which the pendulum harvester can operate.

During the motion of the pendulum end mass, $m$, it is producing *work* in the form of a torque travelling through an angular displacement, $\phi(t)$:

$$Work = \int_{\phi_0}^{\phi_n} \tau d\phi \tag{5.4}$$

where $\tau$ is the torque produced by the end mass, $m$ and $\phi_0$ and $\phi_n$ are the initial and final angular positions of $m$ between which the *work* has been produced.

A portion of this *work* will be consumed when acting against the externally applied torque $L_{square}$, and it is this that will be harvestable. No mechanically or electrical inefficiencies of the actual power take-off will be assumed at this point, and so the full proportion of $L_{square}$ contributes to the harvestable energy. Therefore, given that *power* is work per unit time, then the power dissipated via the power take-off will be:

$$P(t) = |L_{square}\dot{\phi}(t)| \tag{5.5}$$

where *Load* is the chosen loading scheme in torque units, $Nm$.

The modulus of $P(t)$ is taken because power is harvested in both domains of motion of the pendulum due to some external rectification process, be that a form of mechanical or electrical rectification. Continuing to use the loading approach define by $L_{square}$, and with further mathematical simplifications, Eq. 5.5 becomes:

$$P(t) = \left|T_0\dot{\phi}(t)\right| \tag{5.6}$$

Note that the above only applies in the context of a external square load waveform.

Fig. 5.5 shows simulations that repeat the conditions from Fig. 5.4 using Eq. 5.6. The instantaneous power, $P(t)$ has been plotted within the time domain and indicates similar characteristics to Fig. 5.4 with $P(t) \rightarrow 0$ as $T_0$ increases. Once more the response drops to zero when $T_0 \approx 0.8$Nm, see Fig. 5.5. Given that this is a measure of the power being dissipated by the power take-off, it confirms that $L_{square}$ only acts as an energy sink because $P(t)$ never crosses zero. Under these steady-state conditions it can be seen that the peak power harvested is approximately 0.8 Watts when $T_0 = 0.4$Nm.

Fig. 5.6 demonstrates another method to view this data. Here it is observed how energy is collected over time and positive fitted gradients refer to energy being harvested. The steeper the positive gradient relates to greater rates of energy being dissipated, hence greater powers capacities. Note that no negative gradients are present. It can be seen that trends in both Fig. 5.5 and Fig. 5.6 are in agreement with one another.

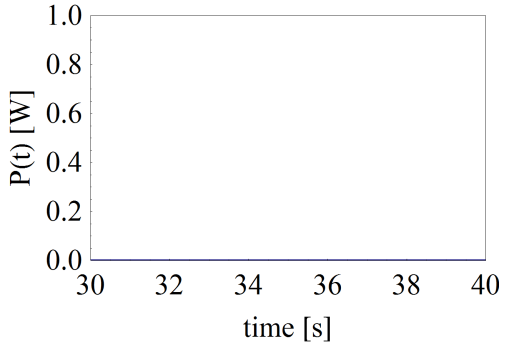


(a) $T_0 = 0$Nm.

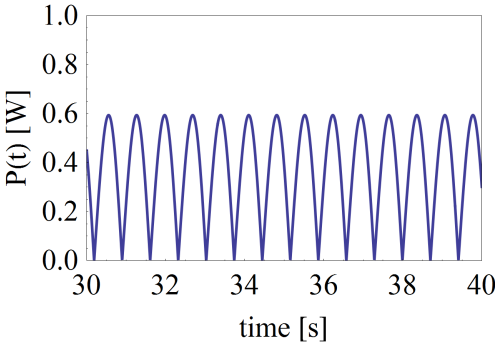


(b) $T_0 = 0.2$Nm.

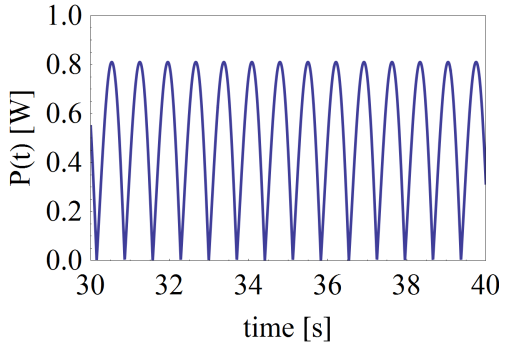


(c) $T_0 = 0.4$Nm.

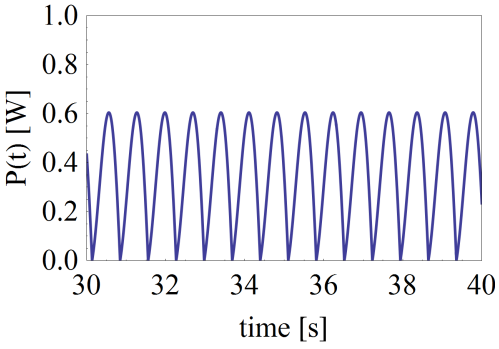


(d) $T_0 = 0.6$Nm.

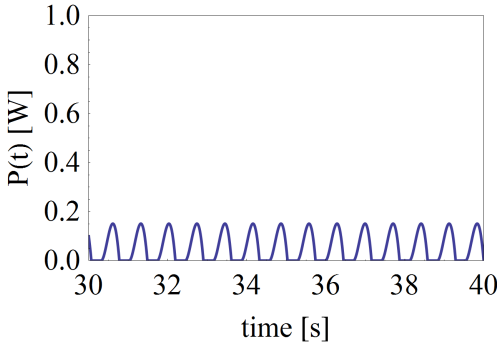


(e) $T_0 = 0.8$Nm.

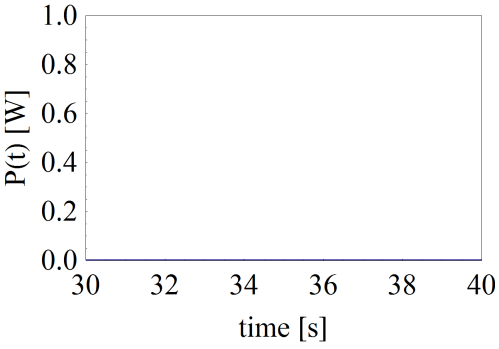


(f) $T_0 = 1.0$Nm.

Figure 5.5: Instantaneous power, $P(t)$ dissipated by the power take-off terms, where $l = 0.5$m, $m = 1$kg, $\xi = 0.1$, $U_0 = 0.1$m, $W_0 = 0$m, $\lambda_0 = 0°$, $\Omega_u = \omega_n$rad/s, $\Omega_w = 0$rad/s, $\Omega_\lambda = 0$rad/s, $\phi(0) = 0$rad, $\dot{\phi}(0) = 0$rad/s and $30 \leq t \leq 40$s.

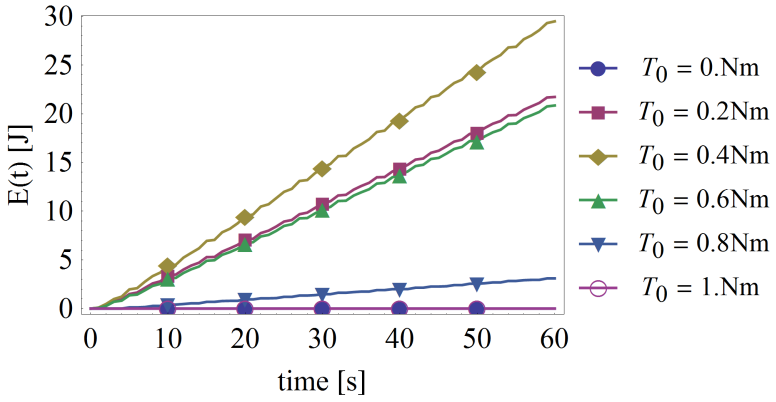


Figure 5.6: Accumulating energy, $E(t)$ collected via the power take-off terms, where $l = 0.5$m, $m = 1$kg, $\xi = 0.1$, $U_0 = 0.1$m, $W_0 = 0$m, $\lambda_0 = 0°$, $\Omega_u = \omega_n$rad/s, $\Omega_w = 0$rad/s, $\Omega_\lambda = 0$rad/s, $\phi(0) = 0$rad, $\dot{\phi}(0) = 0$rad/s and $0 \leq t \leq 60$s.

## 5.3 Parameter Sweeps for Optimisation of the Harvester

With a method for measuring the energy throughput of the harvester established, it is perhaps more effective to observe the influence various parameters have upon the performance of the system. By doing so, approaches for optimising the throughput of the system may be devised and an understanding of the peak performance can be found.

Firstly, it must be defined how to represent the measurable value of performance. The method to measure the instantaneous power will not be appropriate since this is dependent upon the instantaneous time in which the measurement is taken. It would be better to measure the amount of energy accumulated over a given time period and call it $E_{acc}$. This can be done in a similar way to that used in Chapters 2 and 3, such that:

$$E_{acc} = \int_{t_0}^{t_n} [P(t)]\, dt \tag{5.7}$$

This produces a value that can be compared between simulations without introducing errors due to differences in trajectories at instantaneous moments. However, to be a fair comparison, all simulations should be of the same time period.

Fig. 5.7 is an example of a $T_0$ sweep that was performed using the above approach.

This clearly shows the characteristics in response that were before eluded to by Fig. 5.5 and Fig. 5.6. It can be seen that indeed the peak performance of the pendulum with the given conditions does occur when $T_0 \approx 0.4$Nm with an associated $E_{acc} \approx 30$J.

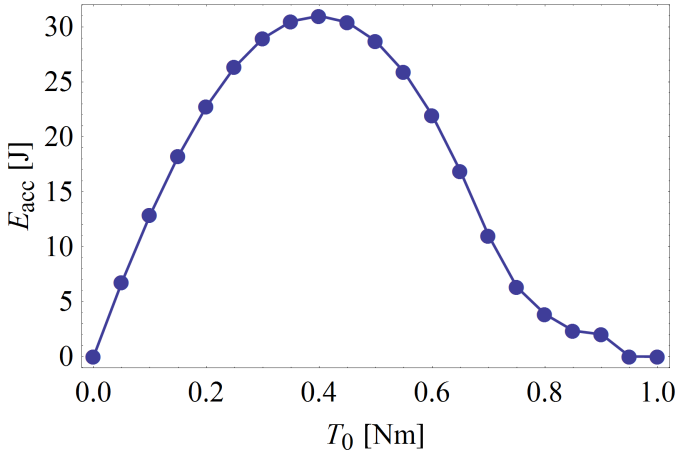


Figure 5.7: A sweep of $T_0$ showing the $E_{acc}$ produced, where $l = 0.5$m, $m = 1$kg, $\xi = 0.1$, $U_0 = 0.1$m, $W_0 = 0$m, $\lambda_0 = 0°$, $\Omega_u = \omega_n$, $\Omega_w = 0$rad/s, $\Omega_\lambda = 0$rad/s, $\phi(0) = 0$rad, $\dot{\phi}(0) = 0$rad/s and $30 \leq t \leq 90$s.

### 5.3.1 The Effects of the Frequency of Horizontal Excitation Only

It is now known that for a pendulum with an end mass, $m = 1$kg, arm length, $l = 0.5$m and damping ratio, $\xi = 0.1$ that is excited horizontally at resonance where $U_0 = 0.1$m and $\Omega_u = \omega_n$, the average energy accumulated by the system is $E_{acc} \approx 30$J. One may typically expect the greatest throughput of the system to occur at resonant conditions, and that any deviation from the condition will result in a drop in response, and hence power. However, Fig. 5.8(a) shows that this is not the case.

In fact, what is happening is very interesting. There is evidence of a peak in $E_{acc}$ in the region of $\Omega_u = \omega_n = 1.0$, and the fact that the response builds rapidly immediately prior to this location suggests that resonant conditions do produce much greater responses in such systems as one would expect. However, beyond this point it can be seen that the response continues to grow steadily. It has been observed that no transitions into full rotational modes occur within this region and so this is not the cause of this behaviour. What does happen in fact is that as $\Omega_u$ increases, the inertia

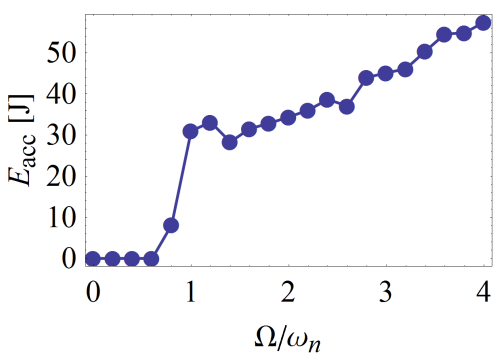


(a) when $T_0 = 0.4$Nm.

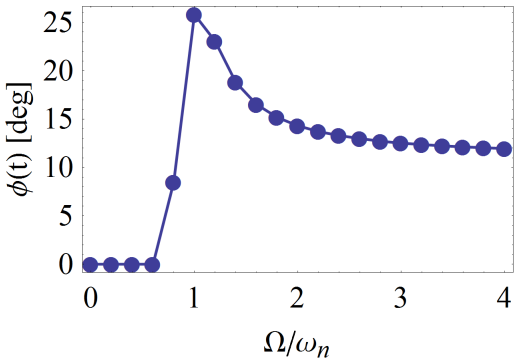


(b) $T_0 = 0.4$Nm.

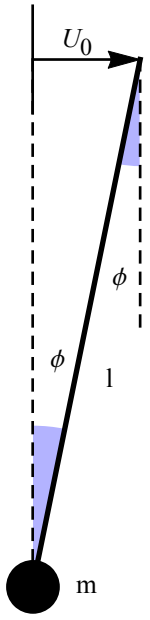


(c) Approximated displaced pendulum when $U_0 = 0.1$m and $\Omega_u >> \omega_n$

Figure 5.8: Sweep of excitation frequency, $\Omega_u$ showing the $E_{acc}$ produced and peak $\phi(t)$, and a schematic of a displaced pendulum, where $l = 0.5$m, $m = 1$kg, $\xi = 0.1$, $U_0 = 0.1$m, $W_0 = 0$m, $\lambda_0 = 0°$, $\Omega_w = 0$rad/s, $\Omega_\lambda = 0$rad/s, $\phi(0) = 0$rad, $\dot{\phi}(0) = 0$rad/s and $30 \leq t \leq 90$s.

in the $m$ must reach a point that the mass itself almost remains horizontally static and the pivot point deflects to either side in the manner shown in Fig. 5.8(c). Knowing that $U_0 = 0.1$m and $l = 0.5$m, the angular displacement associated with such a scenario is calculated using trigonometry as $\phi = 11.54°$. Comparing this to Fig. 5.8(b) that shows an excitation sweep plotting the peak responses of $\phi(t)$, then it can be seen that indeed the system does tends towards this angular displacement.

The consequence of this is that at higher frequencies when the inertia of $m$ becomes so great, then $\phi(t)$ is directly affected by the excitation displacement, $U_0$, which in these simulations remains fixed. However, if the $\Omega_u$ continues to increase, then the frequency of the response will also increase, thus more power becomes available for harvesting in the way indicated by Fig. 5.8(a).

It may be that these increasingly large values of $\Omega_u$ become unreasonable in practise.

### 5.3.2 The Effects of the Frequency of Vertical Excitation Only

Performing a similar method to that above will allow the influence of vertical excitations to be understood. First, the peak value of $T_0$ is determined under the assumption that this will occur somewhere in the region of $\Omega_w = 2\omega_n$, since in this configuration the system is parametric in nature. As shown before, the pendulum has to be initially perturbed to initiate a response since to transverse forces act upon $m$ when excited axially only. $\phi(0) = 15°$ was arbitrarily chosen for this process. From Fig. 5.9(a) it can be seen that an optimum value of $T_0 \approx 0.16$Nm exists for the given conditions. Interestingly, beyond this point the response of the system drops almost immediately to zero a likely result of inherent nonlinearities within the system that in the current excitation configuration, is parametric in nature. Parametric systems are known to be sensitive to loading conditions, as demonstrated by this figure.

Further insight into this behaviour is given by Fig. 5.9(b) where the effects of softening nonlinearities that were alluded to are present, evident by the curve leaning towards the left. The peak of this response when $T_0 = 0.16$Nm exists at $\Omega_w = 2\omega_n$ as predicted, and at frequencies immediately prior to this the response is at approximately zero. This supports the observations from Fig. 5.9(a).

To uncover the true sensitivity to the loading conditions, multiple sweeps were

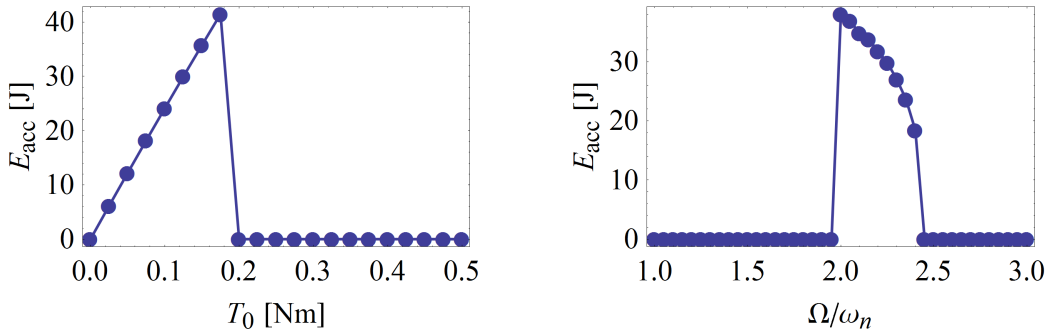


(a) $\Omega_w = 2\omega_n$. (b) $T_0 = 0.16$Nm.

Figure 5.9: Sweeps of $T_0$ and $\Omega_w$ showing the $E_{acc}$ produced, where $l = 0.5$m, $m = 1$kg, $\xi = 0.1$, $U_0 = 0.0$m, $W_0 = 0.1$m, $\lambda_0 = 0°$, $\Omega_u = 0$rad/s, $\Omega_\lambda = 0$rad/s, $\phi(0) = 15°$, $\dot{\phi}(0) = 0$rad/s and $30 \leq t \leq 90$s.

performed under various values of $T_0$ in Fig. 5.10. This shows that at low values of $T_0$, these softening nonlinearities have a greater influence upon the system. One advantage of this is that it can be seen that the operating bandwidths of the peak responses are increased. What is very peculiar however, is that it appears that this system cannot exist when hardening nonlinearities are dominant. This is suggested because it can be seen that when $T_0 = 0.2$Nm the shape of the peak is approaching that of a linear response. However, when $T_0 = 0.25$Nm the system, which if the observed trend continues, would be forced into a hard state. Instead of this however, the response drops to zero, and is perhaps a consequence of the parametric system not being able to exist in such a state, particularly when externally loaded.

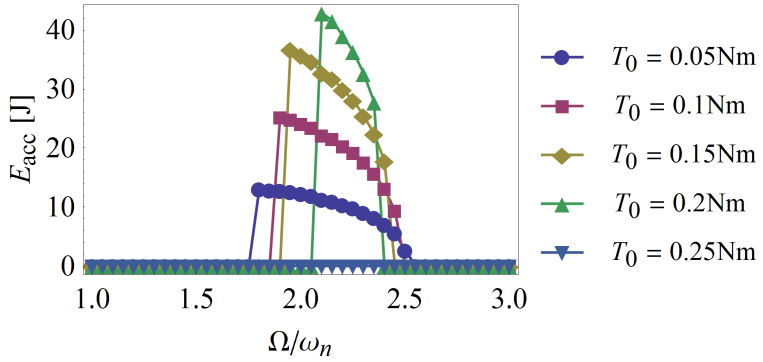


Figure 5.10: Multiple sweeps of excitation frequency, $\Omega_w$ showing the $E_{acc}$ produced for various values of $T_0$, where $l = 0.5$m, $m = 1$kg, $\xi = 0.1$, $U_0 = 0.0$m, $W_0 = 0.1$m, $\lambda_0 = 0°$, $\Omega_u = 0$rad/s, $\Omega_\lambda = 0$rad/s, $\phi(0) = 15°$, $\dot{\phi}(0) = 0$rad/s and $30 \leq t \leq 90$s.

### 5.3.3 The Effects of the Frequency of Rotational Excitation Only

Simulations observing the influence of rotational excitations again reveals interesting behaviour possibly akin to that seen where the pendulum was excited horizontally at high frequencies. Firstly, the optimum value of $T_0$ was determined from Fig. 5.11(a) using an arbitrarily chosen value of $\lambda_0 = 10°$. The excitation frequency was set to $\Omega_\lambda = 2\omega_n$ because of the observations made in Fig. 4.14 which showed that the response of a system excited rotationally was at it lowest when $\Omega_\lambda = \omega_n$, and so this condition is avoided.

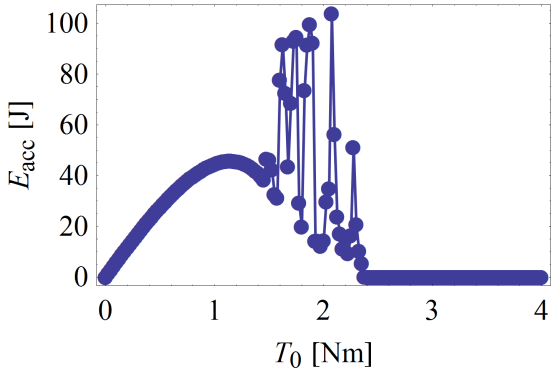


(a) $\Omega_\lambda = 2\omega_n$.

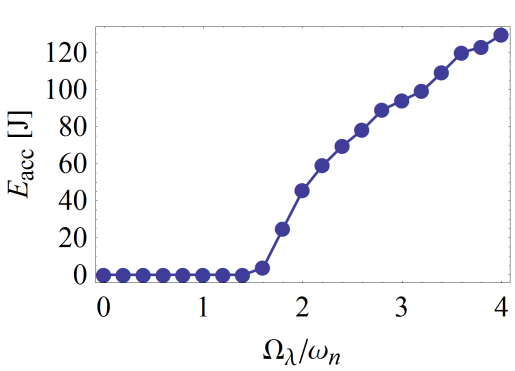


(b) $T_0 = 1.1$Nm.

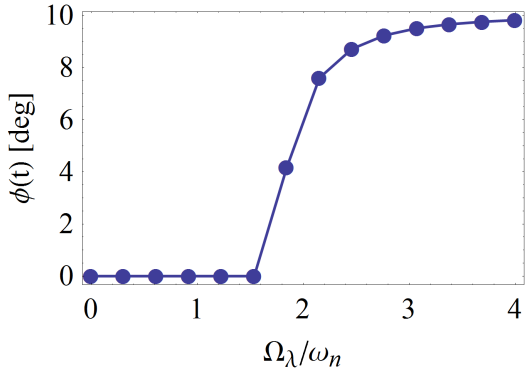


(c) $T_0 = 1.1$Nm.

Figure 5.11: Sweeps of $T_0$ and $\Omega_\lambda$ showing the $E_{acc}$ produced and peak $\phi(t)$, where $l = 0.5$m, $m = 1$kg, $\xi = 0.1$, $U_0 = 0.0$m, $W_0 = 0.0$m, $\lambda_0 = 10°$, $\Omega_u = 0$rad/s, $\Omega_w = 0$rad/s, $\phi(0) = 0$rad, $\dot{\phi}(0) = 0$rad/s and $30 \leq t \leq 90$s.

The response in Fig. 5.11(a) shows consistent behaviour for $0 \leq T_0 \leq 1.5$Nm, where the response increases to a peak and then begins to drop again. However, there is the

appearance seemingly random spikes within the response when $1.5 \leq T_0 \leq 2.3$Nm that could be attributed to integrations errors within the numerical computation process, or even chaotic behaviour. However, given the regularity of the response up to and including the peak located at $T_0 \approx 1.1$Nm, this value has been selected to perform an excitation frequency sweep that reveals similar behaviour seen in Fig. 5.8(a). This can once more possibly be attributed to the inertia of $m$ becoming so large that the response is purely generated by the excitation itself. Knowing that $\lambda_0 = 10°$, Fig. 5.11(c) reveals this to be the case since at higher frequencies of excitation, the peak angular displacement of the response, $\phi(t)$ approaches 10° which is equal to the chosen $\lambda_0$. Therefore, as the value of $\lambda_0$ remains fixed and $\Omega_\lambda$ increases, there will be more energy available for harvesting via $L_{square}$ in the manner indicated by Fig. 5.11(b). Once more, physically achieving such high excitation frequencies in practice may not be practical.

### 5.3.4 The Effects of Magnitude of Excitation

It is important to also understand how the magnitude of the excitation terms will affect the performance of the system. If it is accepted that the frequency of the excitation remains constant across these simulations, then it would be expected that larger displacements would result in more power available for harvesting. That is indeed the behaviour suggested by the simulations in Fig. 5.12.

The response in Fig. 5.12(a) grows more rapidly at lower values of $U_0$, but then does continue to grow almost linearly as $U_0$ is increased further. The response for vertical excitations in Fig. 5.12(b) is somewhat different as there appears to be a large drop in response in the region of $W_0 = 0.2$m, which is followed by a short period of rapid growth, further followed by a almost level response. There is also evidence of further growth at the much higher values of $W_0$. It is not immediately clear what the cause of this response is, but it is likely due to complicated behaviour arising from the inherent nonlinearities within the system.

The response of Fig. 5.12(c) is in itself very interesting because of the linear appearance of the response. This suggests that $\lambda_0$ and $E_{acc}$ are directly proportional to one another, and it is suggested the reason for this is because there is no horizontal

or vertical translation of the system when it is excited in this way. Therefore there is very little change in kinetic or potential energy of $m$ other than that instigated by the inherent damping of the system. Therefore, almost all of the energy being delivered into the system by the excitation terms will be dissipated by the loading terms, and hence $E_{acc}$ increases this way. This is in keeping with the observations from Fig. 5.11 where above excitation frequencies of $\Omega_\lambda > 2\omega_n$ the response in $E_{acc}$ began to grow linearly.

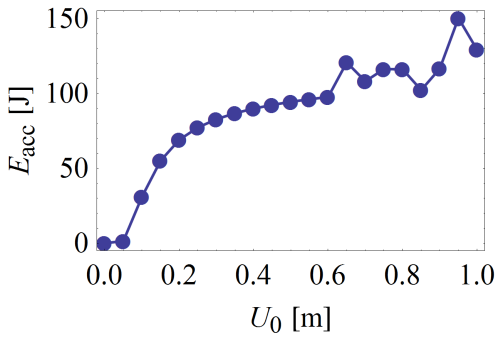


(a) $T_0 = 0.4$Nm, $\Omega_u = \omega_n$, $\Omega_w = 0$rad/s and $\Omega_\lambda = 0$rad/s.

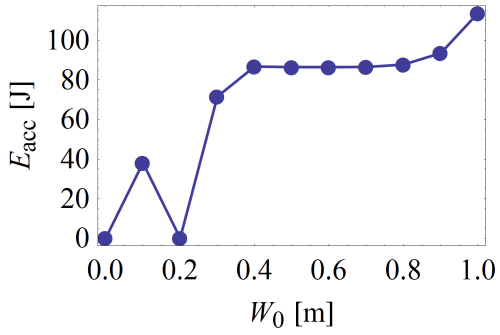


(b) $T_0 = 0.16$Nm, $\Omega_u = 0$rad/s, $\Omega_w = 2\omega_n$, $\Omega_\lambda = 0$rad/s and $\phi(0) = 15°$.

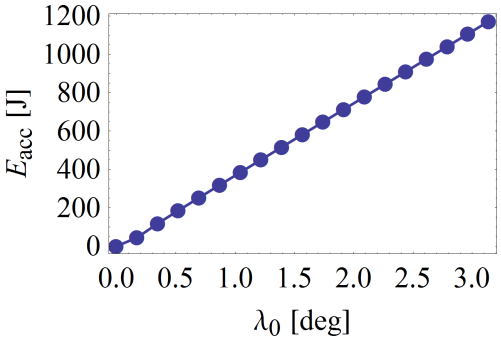


(c) $T_0 = 1.1$Nm, $\Omega_u = 0$rad/s, $\Omega_w = 0$rad/s and $\Omega_\lambda = 2\omega_n$.

Figure 5.12: Sweeps of magnitude of excitation in different forms showing the $E_{acc}$ produced with the following conditions (unless otherwise stated), $l = 0.5$m, $m = 1$kg, $\xi = 0.1$, $\phi(0) = 0$rad, $\dot{\phi}(0) = 0$rad/s and $30 \leq t \leq 90$s.

### 5.3.5 The Effects of Damping within the Harvester

The use of damping in the planar pendulum energy harvester plays a different role than that used in previous chapters concerning the Euler strut based harvester where the damping terms were used directly to dissipate energy for harvesting. Now damping

is used purely to simulate mechanical losses such as friction and sound. In practice one would attempt to limit the inherent damping within the system since any energy dissipate this way is not available for harvesting. To briefly demonstrate how damping affects the system, various scenarios are presented to assess the performance of the system.

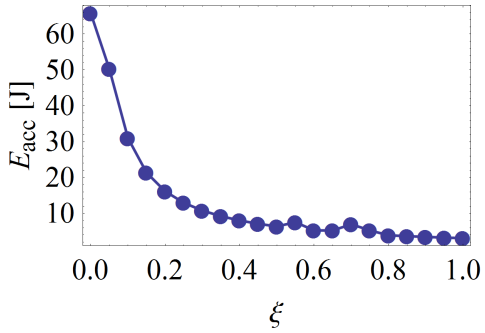


(a) $T_0 = 0.4$Nm, $U_0 = 0.1$m, $\Omega_u = \omega_n$, $\Omega_w = 0$rad/s and $\Omega_\lambda = 0$rad/s.

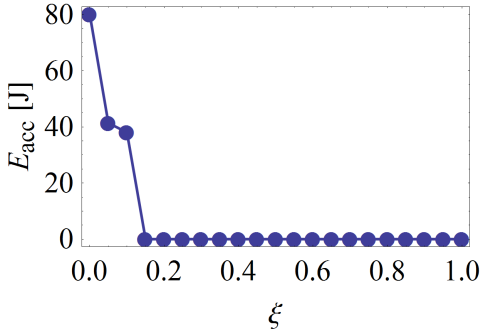


(b) $T_0 = 0.16$Nm, $W_0 = 0.1$m, $\Omega_u = 0$rad/s, $\Omega_w = 2\omega_n$, $\Omega_\lambda = 0$rad/s and $\phi(0) = 15°$.

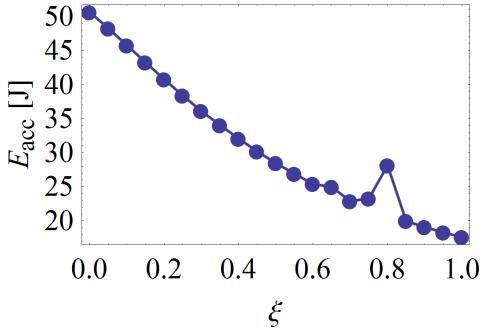


(c) $T_0 = 1.1$Nm, $\lambda_0 = 10°$, $\Omega_u = 0$rad/s, $\Omega_w = 0$rad/s, $\Omega_\lambda = 2\omega_n$.

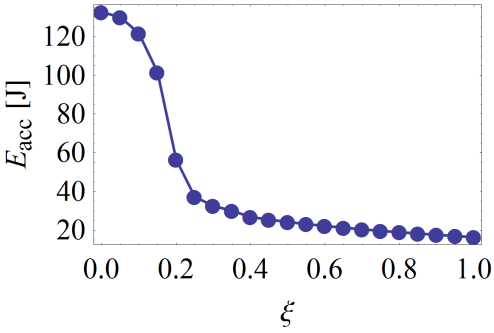


(d) $T_0 = 0.5$Nm, $U_0 = 0.1$m, $W_0 = 0.1$m, $\lambda_0 = 10°$, $\Omega_u = \omega_n$, $\Omega_w = 2\omega_n$ and $\Omega_\lambda = 2\omega_n$.

Figure 5.13: Sweeps of $\xi$ showing the $E_{acc}$ produced with the following conditions (unless otherwise stated), $l = 0.5$m, $m = 1$kg, $U_0 = 0.0$m, $W_0 = 0.0$m, $\lambda_0 = 0°$, $\Omega_u = 0$rad/s, $\Omega_w = 0$rad/s, $\Omega_\lambda = 0$rad/s, $\phi(0) = 0$rad, $\dot{\phi}(0) = 0$rad/s and $30 \leq t \leq 90$s.

In all four simulations shown from Fig. 5.13 it can be seen that indeed larger values of damping, as controlled by the damping ratio, $\xi$, do lead to lower values of $E_{acc}$. It can be seen in Fig. 5.13(b) that a vertically excited system is far more sensitive to damping effects compared to horizontal or rotational excitations, where the response falls to zero as low as when $\xi \approx 0.17$. Conversely, a system that is excited rotationally only is by far the most tolerant to damping. The final simulation shows the coupled behaviour when all three forms of excitation are applied simultaneously, each with the

same conditions as used in their respective individual simulations.

The conclusion from these $\xi$ sweeps is that, as would be typically expected, significant throughput benefits can be afforded when the inherent damping within the energy harvester, as indeed with all forms of energy harvesters, is kept at an absolute minimum to prevent energy being dissipated as waste.

## 5.4 Optimisation of the System for Under Various Scenarios

The parameters that have been studied so far are mostly related to the excitation conditions. However, these parameters in practice would be determined by the vibrations originating from the environment that are to be harvested, be they man-made or naturally occurring. The fact is that these may not be controllable, and any effort to do so would likely waste energy. It is therefore the harvester that should be tuned to suit these excitation conditions, and not the other way about. A study will now be performed where the controllable parameters of the pendulum will be identified and a suitable method will be developed by which these can be used to maximise the energy throughput of the harvester.

From inspection of the equation of motion of the system defined by Eq. 5.2, there are three parameters that may in practice be controlled by the user to manipulate the response of the system. These are:

- Length, $l$; can be used to manipulate the natural frequency to potentially tune the system to frequencies of peak performance.
- Mass, $m$; will affect the inertial properties of the system.
- Externally applied torque, $T_0$; will directly affect both the response of the system and the amount of power that can be harvested. This value in practice will be defined by the physical power take-off device and the effects that this term has already been discussed.

In reality, all three of these parameters will have physical implications towards the mass and volume that is feasible for the particular environment that the device is

deployed within. For example, a end mass of 100kg would be impracticable for a 10cm pendulum arm length without causing mechanical failure. This is an exaggerated example, but the principle holds true. Actual engineering design implications are not the focus for the current study, but an attempt at realism will be maintained throughout.

### 5.4.1 Development of an Optimisation Process for Various Excitation and Loading Conditions

Due to the shear scope of the number of variations possible from a system with three decoupled forms of excitation; horizontal, vertical and rotational, a method will now be detailed that will allow for the optimum operating conditions to be more easily identified for each unique case. This will be applied to a number of arbitrarily chosen excitation profiles to demonstrate its effectiveness.

The rational behind this approach is that in practice the actual excitation conditions could be measured and understood, and therefore may be applied to this model for optimisation. It is also suggested that the resistive torque of the power take-off device would be known depending on the capacity of the device itself, and therefore applied to this same model. Therefore, the optimisation method focuses on determining the optimum values for the mass and length of the harvester.

The approach developed performs a dual sweep of both $m$ and $l$ under the 'known' conditions where $E_{acc}$ is again measured to characterise the throughput. The suggestion is that given the excitation conditions and the resistive torque of the power take-off, the mass and length of the pendulum can be tailored to maximise throughput.

A number of examples are now presented to demonstrate this process, but are in no way representative of a complete catalogue of possible configurations. It has also been necessary to make a number of assumptions. These are that effort will have been made to reduce the inherent damping as far as possible and so a value of $\xi = 0.1$ has been chosen throughout, and also that the amplitudes and frequencies of excitations are not prone to fluctuations. The last assumption is particularly important because it means that the excitation frequencies will not track the varying natural frequency of the system as $l$ is itself varied. This means that $l$ itself is used to track the natural

frequency towards resonant conditions.

As mentioned, there are endless possibilities for sample simulations that could be performed, but those shown in Fig. 5.14 demonstrate the technique for increasing the performance of the harvester. It is interesting to observe the various shapes of the responses, from those with tall but narrow bandwidths such as Fig. 5.14(a) & 5.14(b), and those with much broader bandwidths such as Fig. 5.14(c).

The previous parameter studies have given insight into how such shapes are produced by varying the value of $T_0$, and therefore it becomes discretionary to the user as to whether a wider bandwidth with lower throughput is preferred, or one that is narrower but with higher achievable powers. Ultimately this would be dictated by the relative stability of the excitation conditions. If the excitations are known to be stable, then narrower bandwidths may be acceptable. However, if the excitations have a tendency for drift then wider bandwidths would be the obvious solution.

What is shown across all simulations is that there is a saturation point with respect to the mass where the relative gain for increasing $m$ begins to level off. It is suggested that there would have to be a compromise between the actual mass of the system and the practicalities that come from implementing it in practice. There exists a point where additional mass will compromise the integrity of the structure, or make it difficult to deploy in its intended location.

It can be concluded from these simulations that the developed approach does indicate preferable properties for increasing the throughput of the harvester.

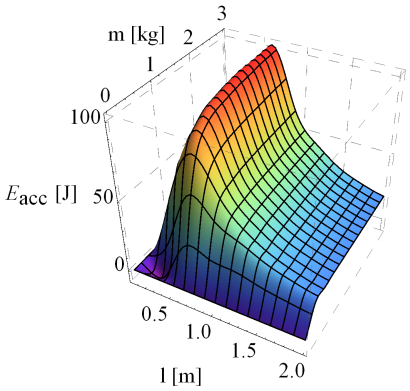


(a) $T_0 = 0.5$Nm, $U_0 = 0.3$m, $W_0 = 0.1$m, $\lambda_0 = 15°$, $\Omega_u = 4$rad/s, $\Omega_w = 1$rad/s, and $\Omega_\lambda = 0.5$rad/s.

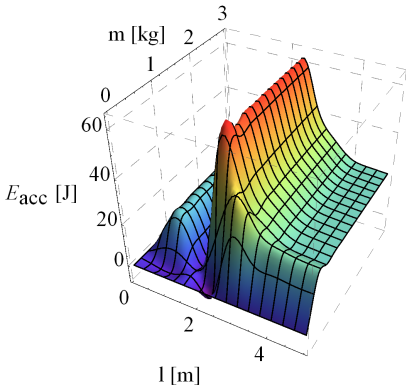


(b) $T_0 = 0.5$Nm, $U_0 = 0.1$m, $W_0 = 0.3$m, $\lambda_0 = 30°$, $\Omega_u = 2$rad/s, $\Omega_w = 4$rad/s, and $\Omega_\lambda = 2$rad/s.

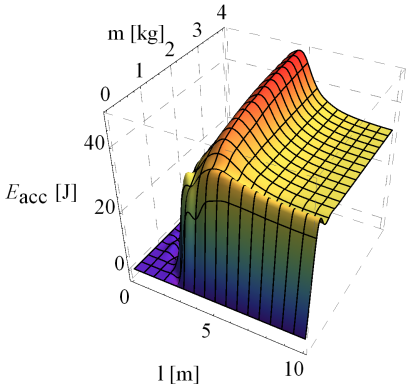


(c) $T_0 = 1.5$Nm, $U_0 = 0.5$m, $W_0 = 0$m, $\lambda_0 = 10°$, $\Omega_u = 1.5$rad/s, $\Omega_w = 0$rad/s, and $\Omega_\lambda = 3$rad/s.

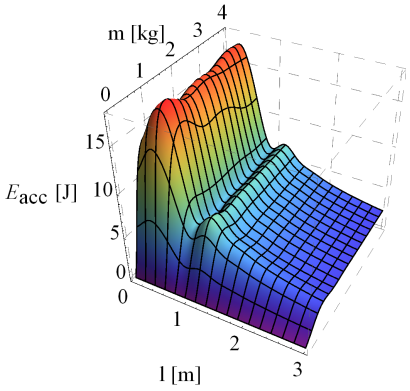


(d) $T_0 = 0.05$Nm, $U_0 = 0.6$m, $W_0 = 0.03$m, $\lambda_0 = 0°$, $\Omega_u = 5$rad/s, $\Omega_w = 1$rad/s, and $\Omega_\lambda = 0$rad/s.

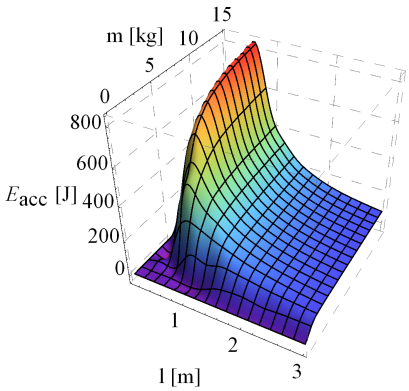


(e) $T_0 = 5$Nm, $U_0 = 0.25$m, $W_0 = 0.3$m, $\lambda_0 = 25°$, $\Omega_u = 4$rad/s, $\Omega_w = 2$rad/s, and $\Omega_\lambda = 0.25$rad/s.

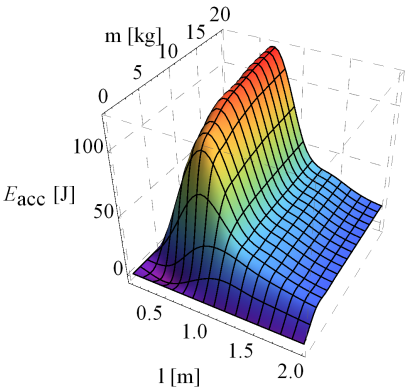


(f) $T_0 = 1.5$Nm, $U_0 = 0.1$m, $W_0 = 0$m, $\lambda_0 = 0°$, $\Omega_u = 4$rad/s, $\Omega_w = 0$rad/s, and $\Omega_\lambda = 0$rad/s.

Figure 5.14: Dual sweeps of $l$ and $m$ showing the $E_{acc}$ produced, where $\xi = 0.1$, $\phi(0) = 0$rad, $\dot{\phi}(0) = 0$rad/s and $30 \leq t \leq 90$s.

## 5.5 Summarising Remarks for the Response Based Loading Approach

A response based square wave loading approach, $L_{square}$ has been developed that is capable of applying a resistive torque to the pendulum regardless of the frequency of the response. This new approach is also capable of producing a fully square waveform to better model the loading characteristics of the discussed ratchet and pawl mechanism that could be used to lift a mass on a winding drum. A comparison of the angular velocity response behaviour was made between the revised response based load and the Fourier series based approximation developed in Chapter A. This was performed at resonant conditions where the latter approach was shown only to be functional, and the results were very comparable. This simulation also showed that the new approach was not susceptible to the phase change anomaly where previously $L_{Fourier}$ could transition from acting as an energy sink to an energy source. Instead when the magnitude of the $L_{square}$ is increased high enough, the response will drop to zero and remain there, simulating a seized system.

Confident that the new approach was functioning in the desired manner, a method for measuring the harvested energy from the pendulum was developed. Using this it was possible to perform a parameter study to show how behaviour is affected by various properties. It was shown that there exists a peak value for $T_0$ when all three forms of excitation were studied individually. It was also shown that $T_0$ could be directly used to control the bandwidth of the system by varying the nonlinear properties of the system.

It was also observed how the excitation frequency and magnitude of excitations affected the system. This highlighted some interesting behaviour where in certain conditions the response of the system would behave linearly with the excitation. It was also shown how increased damping will dissipate more energy from the system as expected, which would reduce the harvestable energy from the external load.

Finally, the effects of the mass and length of the system were observed in numerous arbitrarily defined scenarios. The reason for the arbitrary scenarios was because there exist endless possible combinations of excitation conditions, and so the shown

simulations were used to demonstrate a technique that allows for the optimum mass and length properties to be determined for each situation. The three-dimensional plots were used to highlight peak operating conditions, and it was again shown how some of these peaks were wider or narrower than others as a result of the applied $T_0$ controlling the bandwidth of the response.

It was also shown that at some point the increase in harvested energy from increasing $m$ would begin to level off. This therefore indicated that it may not always be a simple case of applying as large a mass as possible to increase throughput of the harvester. Finally, it was discussed how of course there would exist engineering restrictions in practice with respect to both the mass and the length of the pendulum harvester, but that this technique could be used as an indicator to improving the response as far as possible.

# Chapter 6

# Conclusions

During the course this thesis, the author has proposed and developed three forms of vibrational energy harvester: a periodically excited Euler strut harvester, a stochastically excited Euler strut harvester, and a planar pendulum harvester that is excitable by both horizontal and vertical translations and rotations about its own pivot point. All three have focussed upon the field of harvesting mechanical accelerations from ambient conditions, with a view to increasing the normal throughput either by enhancing the response of the system actively or passively, or by optimising the system parameters to compliment the given excitation conditions. In all cases, the analytical and numerical approaches used throughout this thesis have demonstrated the potential of these concepts, and the conclusions made about each will now be summarised.

## 6.1 Periodically Excited Euler Strut Energy Harvesting

In Chapter 2, a parametric oscillator in the form of an Euler strut was proposed as an energy harvesting device that would be capable of harvesting *known* steady-state periodic vibrations applied axially to the beam. This design, whilst somewhat similar in construction to the second proposed device, is intended for application where the harvestable vibrations would not be prone to excessive drifts in frequency. Such drifts were shown to lead to dramatically reduce the throughput of the system, and thus would compromise its effectiveness in practice. As it was assumed that the periodic

vibrations would be sourced *freely* from ambient conditions, the principal focus in the development of the periodically excited harvester was to attempt to enhance its normal functioning throughput, and also to identify a mechanism through which the operational bandwidth could be broadened.

By providing the facility to apply an initial pre-curvature to the beam via an axially applied static pre-load, the system could be switched between a uni-stable state to a bistable one. Furthermore, application of this static load could be considered as a passive form of control because no energy would be required to maintain it. This was the mechanism by which it was proposed to enhance the energy throughput.

It was considered that in the absence of a static pre-load upon the Euler strut, whilst simultaneously being excited by a dynamic axial force, the harvester would be operating in its most basic form. It was observed that whilst the beam would oscillate about a single basin of attraction for small dynamic forcing values, for larger values the critical buckling load of the beam could be intermittently exceeded, and would result in complicated and unpredictable responses. Such responses were presented with multiple periods of attraction, including those that are associated with a bistable system. This behaviour was discussed, but ultimately it could be concluded that such responses would not produce an effective energy throughput for the intended application of the harvester.

In light of this, it was shown that application of a static axial load that exceeded the critical buckling point of the beam would force a pre-curvature and subsequently remove the uni-stable basin of attraction normally located at the unstressed position of the beam. By doing so, it was shown that it is possible to enhance both the displacement and velocity response of the device by manipulating the trajectory to orbit about the bistable basins of attraction in a steady-state. Furthermore, by measuring the energy dissipated via damping within the system, it was possible estimate the energy that would be available for harvesting from the source vibrations. This revealed somewhat surprising behaviour where two peak responses in accumulated energy were prevalent. Upon further analysis, it was concluded that this was a result of two distinct types of response orbit trajectories; one at the point of peak displacement manifested by the response orbiting around the two attractors in the bistable system, and the second that

orbited about a single bistable attractor, but resulted in a peak velocity.

The second peak could be considered as more interesting surprising, because it was manifested by the static pre-load upon the beam when it was sufficiently high enough to force oscillations within a single basin of attraction only. This would be present itself by the beam only oscillating to one side of the unstressed position, and is a consequence of the potential barrier between the two bistable attractors being too great for the dynamic load to surpass. However, observations concluded that despite the effective displacement of this particular response being reduced, the resulting velocity response peaked, and given that the measured power was function of the velocity squared, this was shown to be able to result in a greater energy throughput under particular conditions. Thus, a second energy throughput peak was observed.

A following parameter study was performed upon the periodically excited system, and revealed that the static axial load could be used to control the nonlinearities within the system. In situations where the static load was less than the critical buckling load, the system would be governed by hardening stiffnesses. However, if the static load is increased, then softening nonlinearities become prevalent and it was shown that resonant frequency of the system would tend towards the location of the excitation frequency being equal to the fundamental natural frequency. Whilst the true nature behind this observed behaviour is not yet understood, it is concluded that it may be a result of the precise configuration of the system, or perhaps due to the parametric nature of the system being altered by the increasing dominance of bistability. Note that the same behaviour was produced by varying the length of the beam because the critical buckling load is a function of this parameter, and therefore in effect, varying the length would vary the proximity of the critical buckling load to the static axial load.

It was also shown that increasing the dynamic axial load applied to the beam would result in ever increasing levels of available energy able to be harvested. This was expected and was simply concluded to be a direct result of more energy being introduced to the system, and thus more energy becoming available for harvesting. The relationship between these two qualities is approximately linear.

Finally for the periodic system, it was demonstrated that the damping within

the system could be used to effectively manipulate the operational bandwidth of the harvester. It was observed that lower values of the damping ratio would result in taller, narrower peaks in energy throughput, whilst higher damping values would produce lower, but broader peaks. It was concluded that such a mechanism would be especially useful for tailoring the harvester to particular excitation scenarios in practice. If deployed in an environment that is know to produce vibrations with stable frequencies, then a lower damping ratio would result in a more productive harvester. However, in an situation where the excitation frequency is known to drift, then a higher level of damping could be more effective, despite the subsequent decrease in peak response.

Therefore, in conclusion of the periodically excited harvester, it is indeed possible to both enhance the energy throughput of such a device using a passively applied axial static pre-load, and also to increase the operational bandwidth by varying the inherent damping within the system. In both cases, these improved states of performance may not require energy to be maintained.

## 6.2 Stochastically Excited Euler Strut Energy Harvesting

Whilst the periodically excited energy harvester was shown to be a viable concept, the analysis did highlight an underlying sensitivity to excitation frequencies. Given that steady-state periodic vibrations from ambient conditions are perhaps limited, it became desirable to seek alternatives to this approach that circumvented the requirement for stable excitations if broadening of the operational bandwidth would not prove sufficient.

Therefore, another Euler strut energy harvester was proposed in Chapter 3 that is very similar to that discussed in Chapter 2. The only modification was the inclusion of a stochastic input that would now be the source of the harvestable vibrations. Again, the static and dynamic axial loads were implemented, but instead now the dynamic load was used to act as a active form of modulation to attempt to enhance the response of the system. The key difference between the two Euler strut devices is that the first harvests axial vibrations of stable *known* frequency, whereas the next harvester

was to harvest lateral vibrations defined as a sequence of random values with normal distribution with zero mean and unit variance. Hence, the second device is intended for deployment in a more unpredictable environment.

It was shown from time domain responses that when the stochastically excited system was excited by the stochastic input alone, such that the beam existed in an uni-stable state, the response oscillated primarily about the single attractor located at the unstressed position. However, evidence of the sporadic formation of additional attractors was observed at the location typically expected by that of a bistable system. Whilst the precise phase space shape of these trajectories was somewhat different from that observed with the periodic energy harvester (see Chapter 2.5.2) that was excited by the periodic dynamic load only, the underlying mechanism of the two is concluded to be the same. That is that the increased momentum generated by the excitation was enough to intermittently exceed the buckling capacity of the beam. The difference in trajectory shape will be a consequence of the stochastic nature in the excitation of the second harvester.

By introducing an axial static pre-load to the stochastically excited harvester, the uni-stable attractor can again be removed as it was with the periodic harvester. Observations of the effects of this were able to conclude it to be an effective method in passively enhancing the response of the system in a very similar fashion as discussed in Chapter 2, and would therefore be an effective approach to increasing the energy throughput of such a system undergoing stochastic excitations.

However, the purpose of this particular device was to attempt to exploit, and observe, the cumulative effects of both a deterministic and stochastic input, potentially culminating in the enhancing qualities produced by stochastic resonance. This required the inclusion of a dynamic axial load to effectively modulate the potential barrier present in the system when forced into a bistable configuration via the static axial load. This is a form of active control, and its benefits were immediately clear. Even in the situation where the modulating frequency of the dynamic load was well away from the location of principle parametric resonance (which occurs at twice the fundamental natural frequency in linear systems), the result was an increase in transitions between both bistable attractors. This would be manifested in practice by the beam buckling

more often from one side of the unstressed position, to the other, thus increasing the total distance travelled by the mass centre.

Furthermore, it was observed that careful control of the dynamic modulating frequency could further enhance this effect by producing a resonant peak response that was manifested by a steady-state open loop response trajectory about the two bistable attractors. It was concluded that this was the location of stochastic resonance, and by the fact that a steady-state response was produced in the presence of the stochastic input, it can also be concluded that the energy throughput of such a system would also be greatly enhanced and stable.

Unfortunately, it was at this point that research upon this particular harvester had to be concluded so that the author could commence work upon two feasibility studies that were in collaboration with industry. This was an exciting opportunity that merited such a move, but despite this, the author believes that it has been shown that the proposed concept of enhancing the throughput of a stochastically excited Euler strut using *active* measures is very much plausible. The logical next stage of research for this concept should be focussed upon estimating the net energy throughput of the device, so that similar observations can be made to that of the previous periodic harvester. The key difference between these two is, however, that the second harvester uses an *active* form of control that will require energy to perform. Therefore, it is essential that the work done in the compressive stroke of the axial dynamic modulating load be subtracted from the total energy dissipated by the power take-off terms. This would allow for the net available energy for harvesting from the stochastic source to be estimated. The work of McInnes *et al* (2008) proposes a very attractive solution to this, and it is suggested that this could be a logical starting point for future investigation.

## 6.3 Planar Pendulum Energy Harvesting

Following the conclusion of the Euler strut themed energy harvesting devices, the focus of research was placed upon the development of a planar pendulum-based energy harvester. The scope of this research was driven by the development of a novel mechanically rectifying gearbox that by design, was able to rectify rotations out of the

instantaneous plane of motion of a pendulum swing. Therefore, in effect, such a device could replace the pivot point of said pendulum and be used to drive a power take-off device (such as a generator) in a single angular direction to generate useful electrical energy. This would be useful in harvesting mechanical accelerations from ambient sources such as sea waves, vehicular motion and even human motion for example.

To optimise the effectiveness of the planar pendulum harvester, the device had to be able to be excited in the full three degrees of freedom; horizontal translation, vertical translation and rotational excitation. Whilst deriving the equation of motion of a pendulum that is excited by both forms of translation is straight forward and well understood, complications arise when attempting to introduce fully decoupled rotational excitations too.

The first method approached was to introduce an external torque that would effectively induce rotations about the pivot point. It was accepted that such an approach somewhat lacked clarity because such an external torque would have to be assumed or defined from actual measurements, and would clearly be dependent upon what the environment in which the device was deployed would be capable of providing. Accepting this, analysis ultimately showed the approach to be fundamentally flawed. In the situation where initial static rotations were attempted, an initial transient response would always prevail unless countered precisely with opposing initial conditions. Given that this itself would require foreknowledge of the generated response, it was concluded that this would provide inadequate control to the user.

Furthermore, it was demonstrated that it was possible for the rotational torque to force the pendulum to change from a oscillatory mode, to that of a rotator. It was determined that this was a result of the induced torque exceeding the resistive torque generated by gravitational effects upon the end mass, and thus presented a limited range of angles through which pendulum could effectively be rotationally excited.

Due to these limitations, it was ultimately decided to instead describe the rotational excitations using a geometrically described approach. Two methods to achieving this were explored; the first whereby rotations were described by rotating a translated pendulum body axis about the absolute frame of reference, the second by rotating a secondary body axis about the pivot point of an already translated principal pendulum

body axis.

It was quickly concluded that the first approach led to highly coupled excitations terms, such that applying a rotation together with a single translation would intrinsically result in a displacement being affected in the other direction of translation. Thus, this drastically reduces the flexibility for being able to replicate particular excitation profiles (for example, a pendulum in which its axis is rotated as it is simultaneously displaced horizontally would consequently result in an unwanted vertical displacement also).

However, the second geometrical approach whereby a secondary body axis was instead rotated about the principal pendulum body axis, was shown to produce a fully decoupled system and resulted in a very elegant equation of motion. Various parameters were assessed under numerous excitation conditions, and the most important conclusions that were made include: that the issue of achieving static rotations that was reported for the torque induced rotations method was resolved, that some level of damping is required to achieve a more stable response, and that higher levels of damping would dissipate more energy and limit the response (thus demonstrating the need to reduce damping as much as possible in practice). Most importantly however, it was shown that in a system that is excited rotationally only, the measured response from which energy could be extracted would be drastically reduced at resonance. It was observed that this was a result of both the rotational excitation and the swinging response of the pendulum arm entering into phase with one another, thus the measured response approached zero. Therefore, it must be concluded that for a pendulum system that is excited rotationally only, the user must attempt ensure that the system is excited at at frequency as far from resonance as possible.

Following a further brief investigation into the responses generated from combined excitations, which produced some interesting and complicated behaviour, it was concluded that the decoupled geometrical approach was fully functional and suitable for the intended application.

The study progressed to incorporate a set of external torque terms, but in this instance, to model the resistive torque that would be generated by a power take-off device. This differs from the power take-off method adopted with the periodically

excited Euler strut-based harvester, where in that case the damping terms were used to model the energy dissipated by an assumed power take-off device. Instead now it was intended to model the load as an external set of loading terms in-line with the two feasibility studies that this research was been conducted under.

A first approach, that is included in Appendix A, was adapted from earlier work by Watt and Cartmell (1994) [95]. Here a pre-assigned frequency based set of loading terms were used to model the resistance generated by a ratchet and pawl lifting a known mass as a power take-off. This was proven to be ineffectual due the dependence upon a pre-assigned frequency for the load, causing it to enter in and out of phase with the response of the pendulum, thus continually switching between acting as an energy sink and an energy source.

It was therefore concluded that a response based external loading approach would be more appropriate, which was developed in Chapter 5. By measuring the sign of the velocity response of the pendulum, it was possible to ascertain the direction of swing in the pendulum arm. This was used to control the switching of a externally applied torque constant that generated a perfect square wave load that always acted as a sink in energy. With it been concluded that this approach was both elegant and effective, estimates of the energy able to be harvested were subsequently made. This was done by multiplying the modulus of the velocity response with the applied resistive torque of the power take-off terms to produce an expression for instantaneous power.

Further parameter studies similar to that in previous chapters were performed, and it was revealed that there existed a peak operating resistive torque for all free forms of excitation, but also that the operational bandwidth could be controlled by the magnitude of this torque via manipulation of the nonlinear characteristics of the system. Interesting behaviour was noted when the pendulum was excited horizontally only. It was shown that at higher excitation frequencies, the displacement of the end mass of the pendulum could approach zero, such that it appeared static, even though a measured response indicating swinging motion was noted. It was concluded that in these situations with high excitation frequencies, the inertia of the end mass became so large that it began to resist motion and the pendulum arm rotated instead about it. Similar observations were made when the system was excited rotationally only with

increasing magnitudes, but in this instance both the end mass and the pendulum arm approached static behaviour and the pendulum axis now rotated about its pivot point.

Finally, the effects of mass and length in the system were observed together under various arbitrarily defined excitation conditions. This was able to successfully demonstrate that it is possible to optimise the response of the pendulum harvester using these parameters, which could be considered as the most readily controllable in practice. Furthermore, the control upon the operational bandwidth via the magnitude of the resistive power take-off torque was again exhibited in the generated responses, and also that the harvestable energy would begin to level-off with increasing values of end mass. The important conclusion from this observation is that it indicates that there will become a point beyond which very little gains are to be made in comparison to the increased engineering complexity involved with adding additional mass to the pendulum in reality. This would be compounded by the added complexity in physically deploying the structure in location too.

These final observations concluded the study of the planar pendulum based energy harvester, and indeed the thesis. It was shown quite clearly that such a planar device possesses great potential, that could possibly be further increased by adapting the concept to a three-dimensional construction. It is suggested that the loading approach developed within this thesis could easily adapted to such a spherical pendulum, where a different set of power take-off torque terms could be used to harvest energy out of each plane of motion in a three-dimensional device. This will be discussed in the following Chapter 7.

In final conclusion, three individual energy harvesting devices have been proposed and studied. The first two, whilst very similar in construction, are targeted at harvesting different types of vibrational energy, as is reflected throughout; one stable known periodic vibrations, the other unpredictable stochastic vibrations. The Third device is radically different still, both in concept and implementation, but the commonality between all three systems is that it has been shown that with either passive or active controls, or with careful manipulation of system parameters, it is indeed possible to enhance their normal functioning response to benefit their ultimate energy harvesting purposes.

# Chapter 7

# Future Work

The scope of research that was conducted as part of the present thesis can essentially be separated into three bodies of work; the periodically excited Euler strut energy harvester, the stochastically excited Euler strut energy harvester, and the planar pendulum based energy harvester. With this in mind, it is more appropriate to discuss possible future work packages on the basis of each of these individually.

## 7.1 Periodically Excited Euler Strut Energy Harvester

An interesting feature was noted and discussed in relation to the periodically excited Euler strut harvester, whereby it appeared that resonance (the point of peak performance) tended towards $\frac{\Omega}{\omega_n} = 1.0$ as $P_{static}$ was gradually increased. Similar behaviour was also noted when the length of the beam was varied, which was likely a result of the value of $P_{crit}$ being effectively shifted and so the same mechanism was likely being observed. The author believes that it is both interesting and important to investigate this behaviour further to properly ascertain whether this tending location of $\frac{\Omega}{\omega_n} = 1.0$ was due to the precise configuration of the system at the time of these simulations, or whether something more fundamental was occurring between the relationship of $P_{static}$ and $P_{crit}$ whereby the parametric nature of the system was being effectively altered. It is this that requires clarification.

An effective approach to determining this would be to develop a *Mathematica* code

(or similar software) whereby multiple $\frac{\Omega}{\omega_n}$ sweeps are performed whilst logging the peak value of the chosen performance measure and its location. Doing so across a range of $P_{static}$ would indicate quite clearly whether resonant conditions were indeed tending towards $\frac{\Omega}{\omega_n} = 1.0$. Furthermore, by repeating this process for various system configurations would show whether the tending location itself shifted. Such an outcome would itself lead to further need for investigation to identify the underlying mechanism driving this behaviour.

Of course, one of the most important future phases of work in relation to the periodic harvester would be to experimentally validate the simulated data documented within this thesis. To this end, it is strongly recommended that a technology demonstrator be designed and built, preferably based upon the beam geometry and material properties used throughout. The source of the excitations could be provided by a mechanical shaker, whilst a compression spring integrated with a threaded bolt could be used to apply a variable static pre-load to the beam to apply $P_{static}$.

However, such experiments would require a suitable method for measuring the performance of the system, specifically the harvestable energy. In Chapter 2 the performance was assessed by three measures; by the displacement $f(t)$ of the response, the velocity $\dot{f}(t)$ of the response, and the energy dissipated via the chosen power take-off terms.

In any future experimental set-up it would be comparably straightforward to measure $f(t)$ or $\dot{f}(t)$ using an accelerometer mounted at the midpoint of the beam, since it was here that the mass centre from which lateral responses were measured was modelled. If available, it would be more effective to do this using laser vibrometers to avoid the additional mass effects that accelerometers would impart (unless of course this additional mass was suitably incorporated within the analytical model). In order to measure the energy performance of the harvester it was suggested in Chapter 2 that a piezoelectric strip could be physically attached to the beam. This same concept has been proposed and tested by a number of researchers in the past [3, 98–102], and it would be appropriate to implement a similar approach.

Using these three measures of performance, it is hoped that future experimental tests could be used to validate the results presented within the current thesis, or indeed

indicate areas requiring further investigation. In any event, such experiments would in the very least compliment the studies performed up to this point.

## 7.2 Stochastically Excited Euler Strut Energy Harvester

Prior to any experimental tests being performed upon the stochastically excited Euler strut based harvester, it remains to produce energy throughput estimates in order to ascertain the potential effectiveness of the concept, beyond the indicative time domain response discussed in Chapter 3. To this end, it was suggested that previous studies by McInnes *et al* (2008) [90] could prove useful, in that they developed a means by which the total energy available for harvesting from their stochastically enhanced harvester was reduced by the work done from their active form of control. This is essential if a conservative estimate is to be made, and it is suggested that this approach be adapted to the stochastically excited Euler strut-based harvester investigated in this thesis.

Once a suitable method for reducing the net harvestable energy by the work done in forcing the beam has been fully established, it would be then be appropriate to collecte more comprehensive data regarding the effectiveness of the system, and this should include a complete parameter study. Following this, similar experimental approaches as proposed previously for the periodically excited harvester could then be used to validate the acquired results.

In fact, it is envisioned that both experiments could be incorporated into a single experimental apparatus. This is possible because the only additional feature within the stochastically excited system is the lateral stochastic input itself. Therefore, by supporting the Euler strut within a caged structure that also supports a small mechanical shaker providing $P_{dynamic}$ and a spring or known mass to provide $P_{static}$, then the cage structure itself could be excited by a larger mechanical shaker mutually orientated 90 degrees to the beam. A preliminary CAD model of this concept is depicted in Fig.7.1.

It can be seen that this would require the cage structure to be mounted upon a sliding bearing bed to allow the entire structure to translate laterally to the beam.

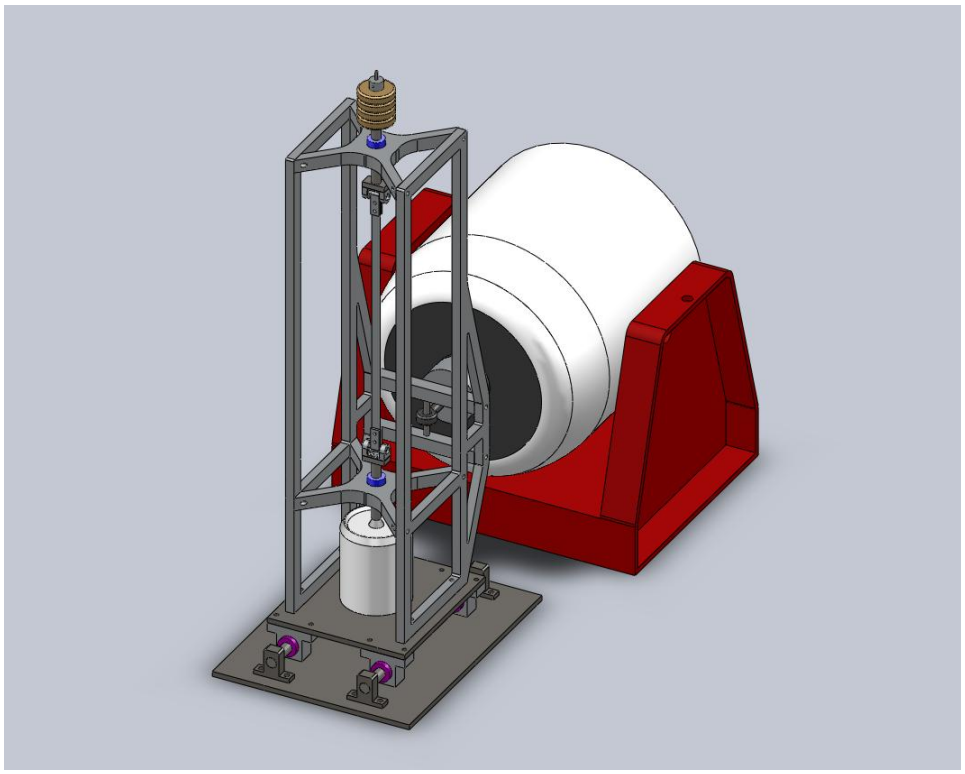

Figure 7.1: Conceptual design for an experimental rig capable of testing both the periodically excited and stochastically excited harvester concepts.

Then, in order to perform experiments testing the periodically excited harvester only, the laterally movement of the rig need only be restrained and the smaller mechanical shaker would then be used to provide the axial periodic excitations alone.

Of course, it is essential to be able to measure the amount of work done in modulating the beam in respect to the stochastically excited harvester, but it would also be useful to understand the energy fed into the system by the respective excitations (of which are to be considered freely sourced from ambient conditions in practice). Both can be measured using a force transducer to measure the applied force and an accelerometer to measuring the displacement of the shaker aperture, thus work done can be calculated. It is unlikely that laser vibrometers will be suitable in this particular scenario due to possible line-of-sight issues.

At this point there should be enough information to form conclusive observations as to whether the stochastically excited harvester is indeed capable of producing net positive energy for harvesting in the way that the simulated data reported within this thesis suggests. Expanding the research further from here would perhaps

involve modelling the characteristics of the power take-off device (the piezoelectric strip) electromechanically. This would provide a much greater level of detail into the understanding of the complete system and subsequently the realisable energy throughput that could be expected under particular conditions. The research by Masana and Daqaq (2011) [69] and Goldschmidtboeing *et al* (2008) [101] would provide useful resource material from which to begin this process from.

## 7.3 Pendulum Based Energy Harvester

The latter portion of this thesis was focussed upon the development of a planar pendulum based energy harvester. The next step to evolving this concept further is to adapt the model into a full spherical pendulum which would be capable of harvesting accelerating motion from the full six degrees of freedom. The author has previously derived the equations of motion of a spherical pendulum that can be excited in three directions of translation, shown below:

$$ml^2\ddot{\phi} + c_\phi m\dot{\phi} + mgl\sin\phi - ml^2\left(\sin\phi\cos\phi\right)\dot{\phi}^2 + ml\left(\cos\phi\cos\theta\right)\ddot{u} + ml\left(\cos\phi\sin\theta\right)\ddot{v} + ml\sin\phi\ddot{w} = Q_\phi \tag{7.1}$$

$$ml^2\sin^2\phi\ddot{\theta} + c_\theta m\dot{\theta} + 2ml^2\left(\sin\phi\cos\phi\right)\dot{\theta}\dot{\phi} - ml\left(\sin\theta\sin\phi\right)\ddot{u} + ml\left(\cos\theta\sin\phi\right)\ddot{v} = Q_\theta \tag{7.2}$$

The reader is referred to Appendix B in which the full derivation process of the above is detailed, but it can be seen that the full swinging motion of the pendulum end mass is captured by two generalised coordinates, $\phi(t)$ and $\theta(t)$ (see Fig.B.1 of AppendixB). This makes it possible to harvest mechanical energy from these two permissible degrees of freedom, but the facility to apply rotational excitations into this model remains to be incorporated. The geometrically described decoupled approach developed in Chapter 4 would therefore have to be adapted into the three-dimensional system in accordance with Euler's rotation theorem.

Accepting this, the actual power take-off of the spherical harvester could be realised in practice using two motor generators and a form of electronic rectification in the way

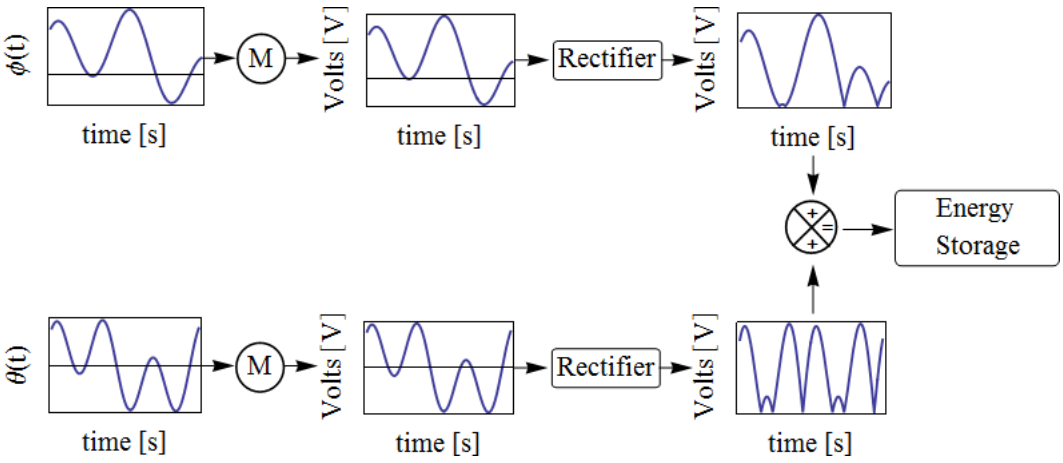


Figure 7.2: Block diagram of the conceptual electrical rectification process of a spherical pendulum energy harvester with two permissible degrees of freedom, $\phi(t)$ and $\theta(t)$.

indicated by Fig.7.2. It is suggested that the two motor generators be mutually rotated 90 degrees from each other and that each be responsible for collecting motion from one of the permissible degrees of freedom, $\phi(t)$ and $\theta(t)$ respectively. By rectifying the voltage produced by each motor individually with a diode bridge, such that only positive voltages are summed, this device could be used to charge an electrical energy storage device such as a battery placed in parallel with a capacitor. It would be important to sum only rectified voltages from each motor to ensure that no positive and negative signals cancel each other out since it would not be possible to ensure that the responses in $\phi(t)$ and $\theta(t)$ remain in phase. A similar rectifying battery charging circuit was used by Sodano *et al* (2005) [103] to rectify the output from a PZT that was attached to an aluminium substrate (see Fig.7.3), and so suggests that the proposed method is viable.

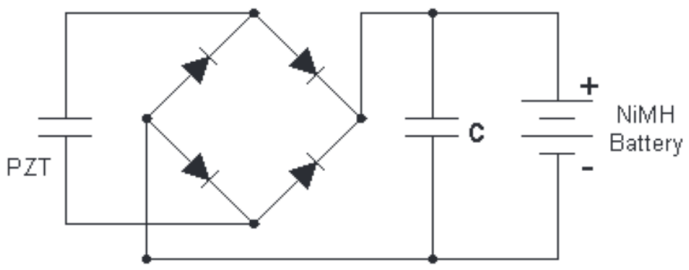


Figure 7.3: Schematic of a battery charging unit developed by Sodano *et al* (2005) [103].

What is elegant about this experimental solution is the fact that is does provide the ability to harvest motion out of the two permissible degrees of freedom of the

spherical pendulum and to integrate these together in a cumulative manner. Given that swinging motion in $\phi(t)$ and $\theta(t)$ is itself generated by accelerations from the six degrees of freedom, this form of harvester would have the potential to harvest the full range of motion realisable in practice by a three-dimensional system in ambient conditions such as sea-waves or vehicular motion for example. To this end, the external loading approach developed in Chapter 5 could be directly integrated into the new system for each generalised coordinate to represent appropriate power take-off devices. Following this, it would be possible to produce energy throughput estimates for the complete system.

Finally, the author proposes to investigate different external loading waveforms aimed at representing different types of power take-off device. A square waveform loading approach was developed in Chapter A and Chapter 5 to model the external loading applied by a simple ratchet and pawl system that lifts a known mass. However, it may be the case that a sinusoidal loading waveform may be more appropriate in some situations. It was shown in this thesis that it is essential for any loading characteristic to be intrinsically linked to the velocity response of the system so that the load only ever acts as an energy sink, and never an energy source. Unfortunately the development of a response based sinusoid can be more complicated to achieve, but the author does suggest the possible use of an $ArcTan$ operator implemented in the following way:

$$Q_{\phi} = T_0 \frac{2ArcTan\left(\dot{\phi}(t)/\epsilon\right)}{\pi} \tag{7.3}$$

$$Q_{\theta} = T_0 \frac{2ArcTan\left(\dot{\theta}(t)/\epsilon\right)}{\pi} \tag{7.4}$$

where $T_0$ again is the value of the applied torque, and $\epsilon$ is a quantity used to control the *roundness* of the desired loading waveform.

Fig.7.4 depicts numerous loading profiles generated by the above $ArcTan$ based loading approach when applied to the established planar pendulum system that is excited horizontally only. Note that the properties of the planar pendulum are similar

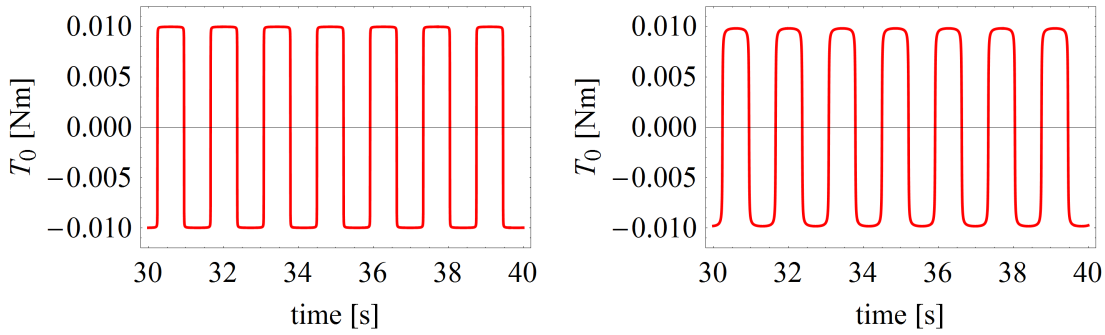


(a) where $\epsilon = 0.01$.




(b) where $\epsilon = 0.1$.

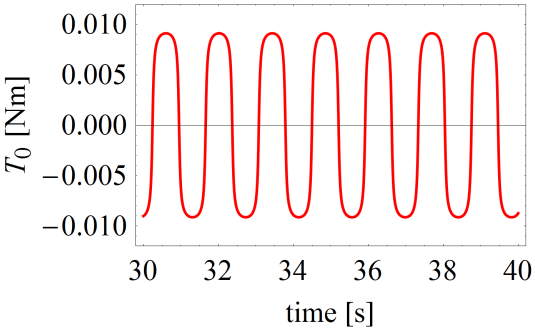


(c) where $\epsilon = 0.5$.

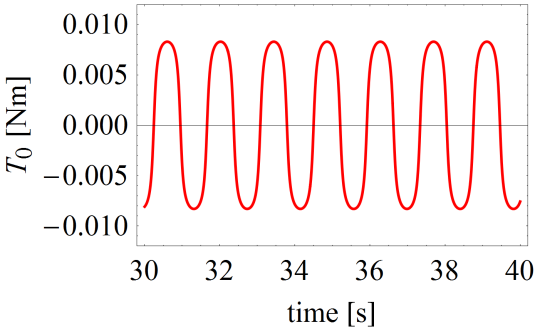


(d) where $\epsilon = 1.0$.

Figure 7.4: Loading profiles of $ArcTan$ based waveform for increasing values of $\epsilon$, where length, $l = 0.5$m, mass, $m = 1$kg, $\xi = 0.1$, $T_0 = 0.01$N, $U_0 = 0.1$m, $W_0 = 0$m, $\lambda_0 = 0°$, $\Omega_u = \omega_n$rad/s, $\Omega_w = 0$rad/s, $\Omega_\lambda = 0$rad/s, $\phi(0) = 0$rad, $\dot{\phi}(0) = 0$rad/s and $30 \leq t \leq 40$s.

to those used previously in the current thesis. It can be seen from this that when the value of $\epsilon$ is very low, such as $\epsilon = 0.01$, the resulting waveform approaches that of a square wave and could be used in the same way discussed in Chapter 5. By increasing $\epsilon$, the roundness of the corners of the waveform can be exaggerated and the profile begins to take a form similar to that of a traditional sinusoidal wave.

This is only a preliminary demonstration, but it does indicate the potential for an $ArcTan$ operator to produce a response based sinusoidal loading waveform if desired. However, it is clear that further investigation is required before forming any definitive conclusions on this, and that care should be given when selecting a value for $\epsilon$. It can be seen from Fig.7.4(d), where $\epsilon = 1.0$, that the peak value of $T_0$ has decreased from the targeted value of $T_0 = 0.01$N. However, if this loading approach is adopted to make estimates of the energy available for harvesting, then by applying the product of these terms for use in the estimation and not simply the value specified for $T_0$, the implications of this feature will be mitigated. It may be though that larger values of $T_0$ would have to be specified to replicate the same resultant load of a square waveform.

The author strongly suggests further investigation into this to determine its effectiveness, and to compare it with that of the square wave loading approach that was developed within this thesis.

# Appendix A

# External Loading of the Planar Pendulum

A pendulum-based energy harvester was proposed in Chapter 4 that seeks to convert mechanical accelerations sourced from the environment into more useful electrical energy. With a suitable equation of motion having been derived that has the facility to excite the system in the full three degrees of freedom that may be experienced by the planar device, the following appendix chapter will discussed the derivation of an external loading approach which was undertaken as an expansion upon earlier work by Watt and Cartmell (1994) [95].

However, this approach used a pre-assigned load to model the resistive torque applied by a ratchet and pawl power take-off torque that ultimately was not able to provide the flexibility required by the planar pendulum energy harvesting device that was proposed in Chapter 4. The following appendix chapter is therefore included to provide an in-depth understanding behind this reasoning.

## A.1 Derivation of Square Wave External Loading Terms

Watt and Cartmell (1994) [95] previously developed a set of square wave loading terms to model a ratchet and pawl power take-off device that was implemented in their novel torsional pendulum. In this example, the ratchet was used to lift a mass on the end

of a winding drum, and therefore the full cycle of the principal inertia comprised of a power take-off stroke when the angular velocity of the pendulum was greater than zero, and a recovery stroke when the angular velocity was equal to, or less than zero. It was decided to adopt a similar square waveform loading approach for the planar pendulum based harvester discussed within this thesis, and so the approach by Watt and Cartmell (1994) [95] was investigated.

The equation of motion developed in Section.4.4 is repeated below for reference before modifying it to include suitable loading terms:

$$\begin{aligned}\ddot{\phi}(t) + 2\xi\omega_n\dot{\phi}(t) + \frac{g}{l}\sin\left(\phi(t) + \lambda_0\cos\left(\Omega_\lambda t\right)\right) = &\frac{U_0{\Omega_u}^2\cos\left(\Omega_u t\right)}{l}\cos\left(\phi(t) + \lambda_0\cos\left(\Omega_\lambda t\right)\right) \\ &+ \frac{W_0{\Omega_w}^2\cos\left(\Omega_w t\right)}{l}\sin\left(\phi(t) + \lambda_0\cos\left(\Omega_\lambda t\right)\right) \\ &+ \lambda_0{\Omega_\lambda}^2\cos\left(\Omega_\lambda t\right)\end{aligned}$$

A generalised force $Q_\phi$ term is used to represent a torque and is inserted after the above equation of motion has been multiplied by $ml^2$ so that the inertial terms themselves are appropriately torques also. This external torque is to act on the pendulum about the pivot point $p$ and will be used to represent the resistive load applied by the power take-off. First, it shall be assumed that $Q_\phi$ contains both a static and time dependent element such that $Q_\phi = T_0 + T_1(t)$, where $T_0$ and $T_1(t)$ can be either positive or negative so that a Fourier series approximation may be applied at a later stage. Therefore the physical form equation of motion then reduces to:

$$\begin{aligned}\ddot{\phi}(t) + 2\xi\omega_n\dot{\phi}(t) + \frac{g}{l}\sin\left(\phi(t) + \lambda_0\cos\left(\Omega_\lambda t\right)\right) = &\frac{U_0{\Omega_u}^2\cos\left(\Omega_u t\right)}{l}\cos\left(\phi(t) + \lambda_0\cos\left(\Omega_\lambda t\right)\right) \\ &+ \frac{W_0{\Omega_w}^2\cos\left(\Omega_w t\right)}{l}\sin\left(\phi(t) + \lambda_0\cos\left(\Omega_\lambda t\right)\right) \\ &+ \lambda_0{\Omega_\lambda}^2\cos\left(\Omega_\lambda t\right) + \frac{T_0}{ml^2} + \frac{T_1(t)}{ml^2}\end{aligned} \tag{A.1}$$

Eq. A.1 is now dimensionally correct provided that $T_0$ and $T_1(t)$ are torques. If the approach developed by Watt and Cartmell (1994) [95] is applied further to produce a square on/off waveform, then this may be approximated using the first two terms in the Fourier series, those of the form $Q_\phi = T_0 + T_1(t)$ with further details built in later.

By setting $T_1 = -T_p \sin(\Omega t + \alpha)$, both an oscillating load function with frequency $\Omega$ and phase angle $\alpha$ can be introduced. Therefore, Eq. A.1 may take the form of:

$$\begin{aligned}\ddot{\phi}(t) + 2\xi\omega_n\dot{\phi}(t) + \frac{g}{l}\sin(\phi(t) + \lambda_0\cos(\Omega_\lambda t)) = &\frac{U_0{\Omega_u}^2\cos(\Omega_u t)}{l}\cos(\phi(t) + \lambda_0\cos(\Omega_\lambda t)) \\ &+ \frac{W_0{\Omega_w}^2\cos(\Omega_w t)}{l}\sin(\phi(t) + \lambda_0\cos(\Omega_\lambda t)) \\ &+ \lambda_0{\Omega_\lambda}^2\cos(\Omega_\lambda t) \\ &+ \left[\frac{T_0}{ml^2} - \frac{1}{ml^2}T_p\sin(\Omega t + \alpha)\right] \qquad \text{(A.2)}\end{aligned}$$

Noting that $\alpha$ should be equal to 0 or $\frac{\pi}{2}$.

In the original application of this approach by Watt and Cartmell (1994) [95] $T_p$ was made equal to$\frac{2T_0}{\pi}$, and the amplitude of the square wave dc offset was halved, such that dc offset $= T_0/2$, so that the approximating sinusoid fit exactly together. Applying this method to Eq. A.2 leads to:

$$\begin{aligned}\ddot{\phi}(t) + 2\xi\omega_n\dot{\phi}(t) + \frac{g}{l}\sin(\phi(t) + \lambda_0\cos(\Omega_\lambda t)) = &\frac{U_0{\Omega_u}^2\cos(\Omega_u t)}{l}\cos(\phi(t) + \lambda_0\cos(\Omega_\lambda t)) \\ &+ \frac{W_0{\Omega_w}^2\cos(\Omega_w t)}{l}\sin(\phi(t) + \lambda_0\cos(\Omega_\lambda t)) \\ &+ \lambda_0{\Omega_\lambda}^2\cos(\Omega_\lambda t) \\ &+ \frac{1}{ml^2}\left[\frac{T_0}{2} - \frac{2T_0}{\pi}\sin(\Omega t + \alpha)\right] \qquad \text{(A.3)}\end{aligned}$$

Fig. A.1 shows the behaviour of the loaded torque terms, $\left[\frac{T_0}{2} - \frac{2T_0}{\pi}\sin(\Omega t + \alpha)\right]$, where $T_0 = 5$Nm and $\Omega = 1$rad/s have been arbitrarily chosen and $\alpha = 0$ and $\frac{\pi}{2}$. A number of features can be discerned from these loading profiles: that $\alpha$ successfully controls the phase of the load, that a dc offset has been applied, that the measured amplitude of the oscillating load is $\approx T_0$, the recovery cycle falls below 0Nm, and finally that a sinusoidal oscillation has been generated.

It is of course possible to better approximate a square waveform by including more terms from the Fourier series in the derivation. However, Watt and Cartmell (1994) [95] observed that the resulting behaviour generated by the first two terms alone produced very similar results to that generated by higher approximations, such as those used

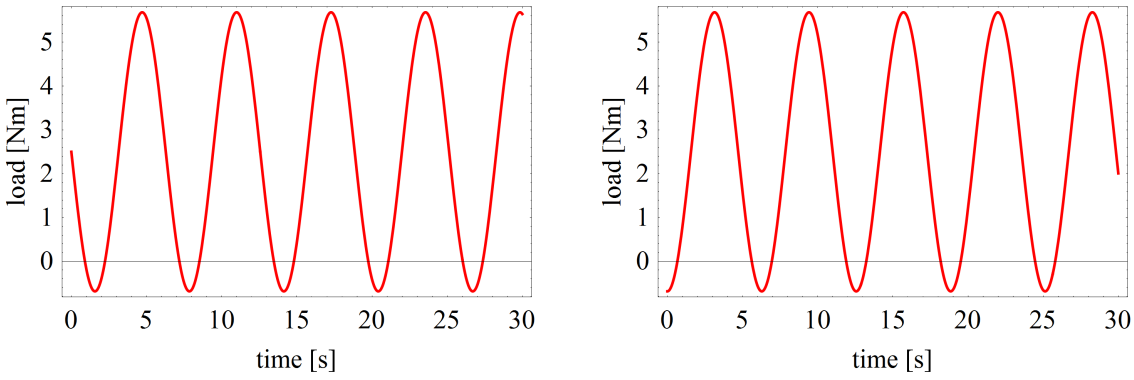


(a) $\alpha = 0$. (b) $\alpha = \frac{\pi}{2}$.

Figure A.1: External loading characteristics simulating an approximated (on/off)square wave torque with half amplitude dc offset, where $T_0 = 5\text{Nm}$, $\Omega = 1\text{rad/s}$ and $0 \leq t \leq 30\text{s}$.

to produce the loading profiles illustrated in Fig. A.2. It is for this reason that the proceeding analysis continues using the two term approximation shown in Eq. A.3.

One must also bear in mind the application with which Watt and Cartmell (1994) [95] originally designed their loading terms. As discussed, these were intended to simulate a half cycle positive power take-off stroke for lifting a mass, followed by a recovery half cycle stroke, as follows:

$$f\left(\dot{\phi}\right) = T_0 \qquad \text{for } \dot{\phi}(t) > 0$$
$$f\left(\dot{\phi}\right) = 0 \qquad \text{for } \dot{\phi}(t) \leq 0$$

However, with respect to the currently proposed planar pendulum harvester, this would have the effect of loading only one half of the cycle i.e. one direction of swing. The repercussions of this would be that the pendulum would be asymmetrically loaded which does not achieved the desired loading conditions. A numerical simulation shown in Fig. A.3 confirms this behaviour. Note that in this simulation all forms of excitation are equal to zero ($U_0 = 0, W_0 = 0$ and $\lambda_0 = 0$) and the response is instead being driven by the on/off load waveform. Clearly the pendulum response resides predominately within the positive domain and it therefore becomes necessary to modify the square wave approximation so that it acts as a symmetrical load with no recovery stroke in between.

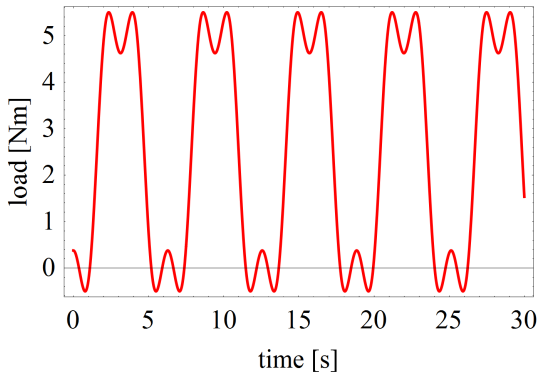


(a) $\frac{T_0}{2} - \frac{2T_0}{\pi}\sin\Omega t + \alpha - \frac{2T_0}{3\pi}\sin 3\Omega t - \alpha$

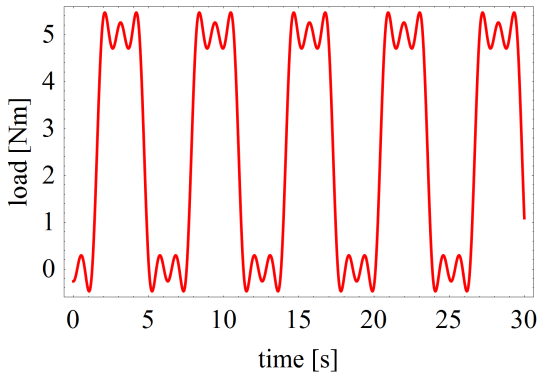


(b) $\frac{T_0}{2} - \frac{2T_0}{\pi}\sin\Omega t + \alpha - \frac{2T_0}{3\pi}\sin 3\Omega t - \alpha - \frac{2T_0}{5\pi}\sin 5\Omega t + \alpha$

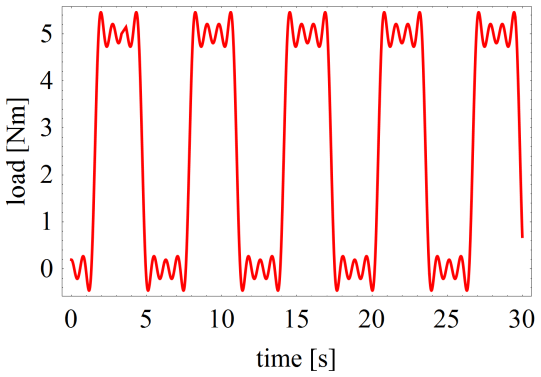


(c) $\frac{T_0}{2} - \frac{2T_0}{\pi}\sin\Omega t + \alpha - \frac{2T_0}{3\pi}\sin 3\Omega t - \alpha - \frac{2T_0}{5\pi}\sin 5\Omega t + \alpha - \frac{2T_0}{7\pi}\sin 7\Omega t - \alpha$

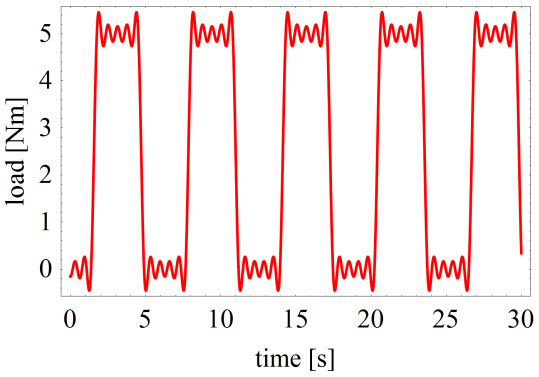


(d) $\frac{T_0}{2} - \frac{2T_0}{\pi}\sin\Omega t + \alpha - \frac{2T_0}{3\pi}\sin 3\Omega t - \alpha - \frac{2T_0}{5\pi}\sin 5\Omega t + \alpha - \frac{2T_0}{7\pi}\sin 7\Omega t - \alpha - \frac{2T_0}{9\pi}\sin 9\Omega t + \alpha$

Figure A.2: External loading characteristics approaching greater approximation of a square (on/off) wave torque with half amplitude dc offset, where $T_0 = 5\text{Nm}$, $\Omega = 1\text{rad/s}$, $\alpha = \frac{\pi}{2}$ and $0 \leq t \leq 30\text{s}$.

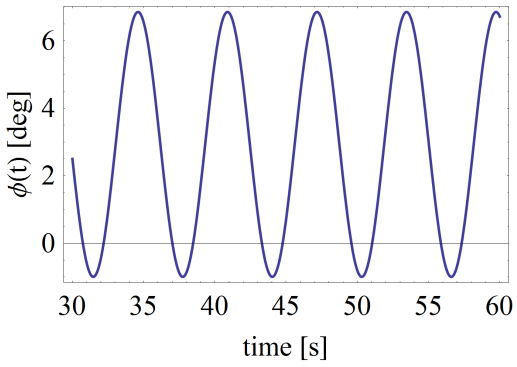


(a)

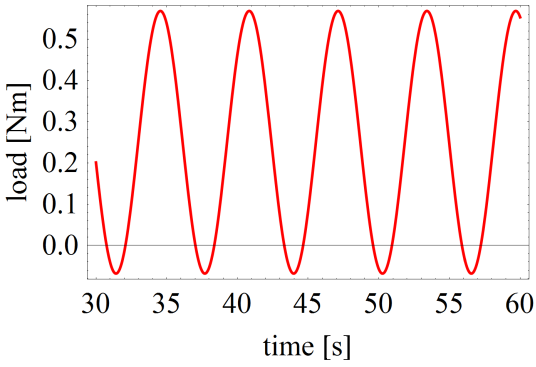


(b)

Figure A.3: Numerical simulation based upon Eq. A.3 (a) pendulum time domain response to (on/off) square wave loading, (b) (on/off) square wave loading profile, where $l = 0.5\text{m}$, $m = 1\text{kg}$, $\xi = 0.1$, $U_0 = 0\text{m}$, $W_0 = 0\text{m}$, $\lambda_0 = 0°$, $\Omega_u = 0\text{rad/s}$, $\Omega_w = 0\text{rad/s}$, $\Omega_\lambda = 0\text{rad/s}$, $T_0 = 0.5\text{Nm}$, $\Omega = 1\text{rad/s}$, $\phi(0) = 0\text{rad}$, $\dot{\phi}(0) = 0\text{rad/s}$ and $30 \leq t \leq 60\text{s}$.

### A.1.1 Modification of Square Wave Loading Terms

It is known that for the planar pendulum energy harvesting device, the power take-off device should be able to harvest mechanical energy in both directions of swing. Therefore, the loading conditions that any square wave approximated loading torque should satisfy are:

$$\begin{aligned} f\left(\dot{\phi}\right) &= -T_0 \qquad \text{for } \dot{\phi}(t) > 0 \\ f\left(\dot{\phi}\right) &= 0 \qquad \text{for } \dot{\phi}(t) = 0 \\ f\left(\dot{\phi}\right) &= T_0 \qquad \text{for } \dot{\phi}(t) < 0 \end{aligned}$$

A method by which to achieve this would be to simply sum two sets of the previous square wave terms, $\left[\frac{T_0}{2} - \frac{2T_0}{\pi}\sin\left(\Omega t + \alpha\right)\right]$ such that their net effect would produce a square waveform that resisted both directions of swing realised by the pendulum through $\phi$. This would be achieved by one set of the terms being 'on' in the positive domain whilst the other is 'off', and visa verca for the negative domain response. This is an attractive solution because it maintains fully the Fourier series approximation without any modification beyond the summation of two sets of terms, and is therefore mathematically more realistic. The modified square wave load may be defined as:

$$L_{Fourier} = \left[\frac{T_0}{2} - \frac{2T_0}{\pi}\sin\left(\Omega t + \alpha\right)\right] - \left[\frac{T_0}{2} - \frac{2T_0}{\pi}\sin\left(\Omega t - \alpha\right)\right] \tag{A.4}$$

Hence the new equation of motion used to describe the pendulum motion is:

$$\begin{aligned} \ddot{\phi}(t) + 2\xi\omega_n\dot{\phi}(t) + \frac{g}{l}\sin\left(\phi(t) + \lambda_0\cos\left(\Omega_\lambda t\right)\right) = {} & \frac{U_0{\Omega_u}^2\cos\left(\Omega_u t\right)}{l}\cos\left(\phi(t) + \lambda_0\cos\left(\Omega_\lambda t\right)\right) \\ & + \frac{W_0{\Omega_w}^2\cos\left(\Omega_w t\right)}{l}\sin\left(\phi(t) + \lambda_0\cos\left(\Omega_\lambda t\right)\right) \\ & + \lambda_0{\Omega_\lambda}^2\cos\left(\Omega_\lambda t\right) \\ & + \frac{1}{ml^2}\left[\frac{T_0}{2} - \frac{2T_0}{\pi}\sin\left(\Omega t + \alpha\right)\right] \\ & - \frac{1}{ml^2}\left[\frac{T_0}{2} - \frac{2T_0}{\pi}\sin\left(\Omega t - \alpha\right)\right] \end{aligned} \tag{A.5}$$

Note that to better approximate a square waveform, additional terms from the Fourier

series may once more be included where necessary in same manner demonstrated in Fig. A.2.

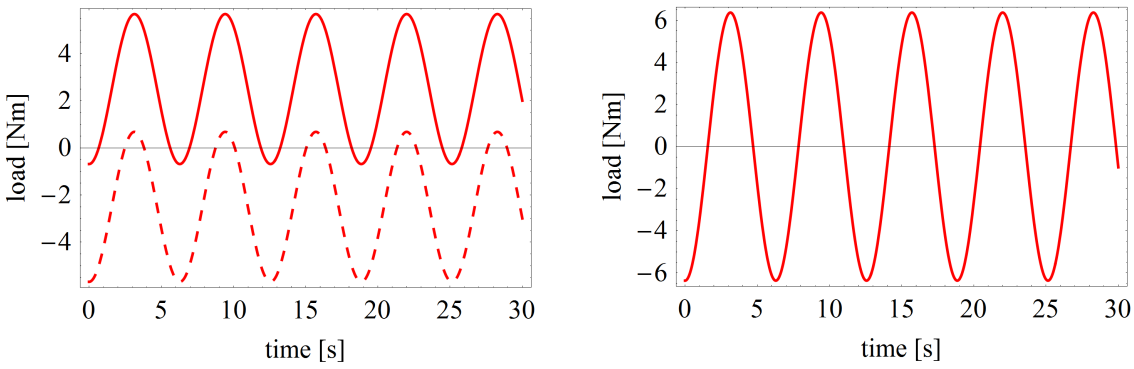


(a) (b)

Figure A.4: External loading characteristics simulating an approximated (on/on) square wave torque (a) solid line positive domain load, dashed line negative domain load, (b) resulting summed loads, where $T_0 = 5\text{Nm}$, $\Omega = 1\text{rad/s}$, $\alpha = \frac{\pi}{2}$ and $0 \leq t \leq 30\text{s}$.

Fig. A.4 shows the resulting torque profile generated by Eq. A.4 that demonstrates how the two sets of terms have been summed to produce the (on/on) square wave approximation. Given that the only modification here is to sum two sets of terms derived previously, the units remain dimensionally consistent. It is very important to note that with $L_{Fourier}$, the phase angle must always be $\alpha = \frac{\pi}{2}$ (or $\alpha = \frac{3\pi}{2}$ which would produce the same effect). The reason for this is that it is necessary for the sign of $\alpha$ to be opposing in either set of terms. Given that a domain sign for zero has no meaning, the previous alternative where $\alpha = 0$ leads to the summed terms cancelling one another out.

By repeating the simulation from Fig. A.3, but instead based upon Eq. A.5, it can be seen in that indeed a symmetrical response has been achieved (see Fig. A.6). Again, the response has been generated by $L_{Fourier}$ alone acting as an energy source as opposed to an energy sink because they have been applied at an arbitrary value and frequency with no other form of excitation and have no response to resist. This in itself is a problem because it should never be the case that the load can act as an energy source. If the pendulum is not being excited by $u$, $w$ or $\lambda$ such that no response should be present, then no load should be experienced either. However, given that the $L_{Fourier}$

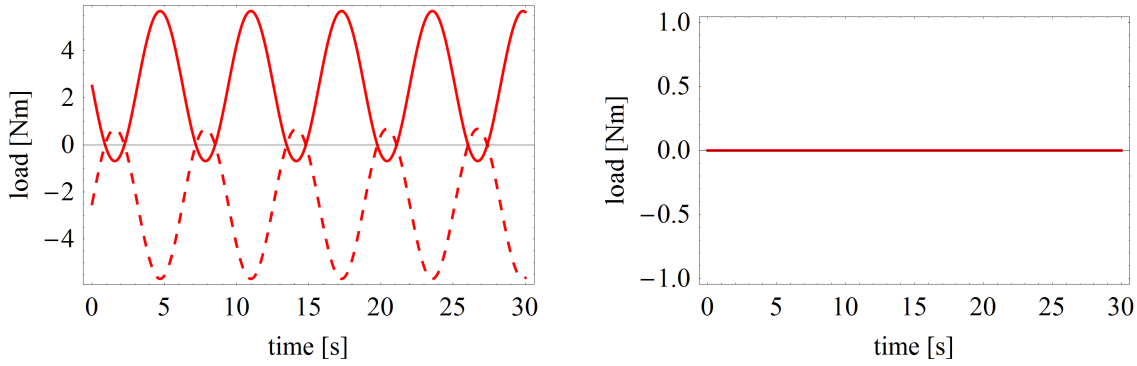


(a) (b)

Figure A.5: External loading characteristics simulating an approximated (on/on) square wave torque (a) solid line positive domain load, dashed line negative domain load, (b) resulting summed loads, where $T_0 = 5\text{Nm}$, $\Omega = 1\text{rad/s}$, $\alpha = 0$ and $0 \leq t \leq 30\text{s}$.

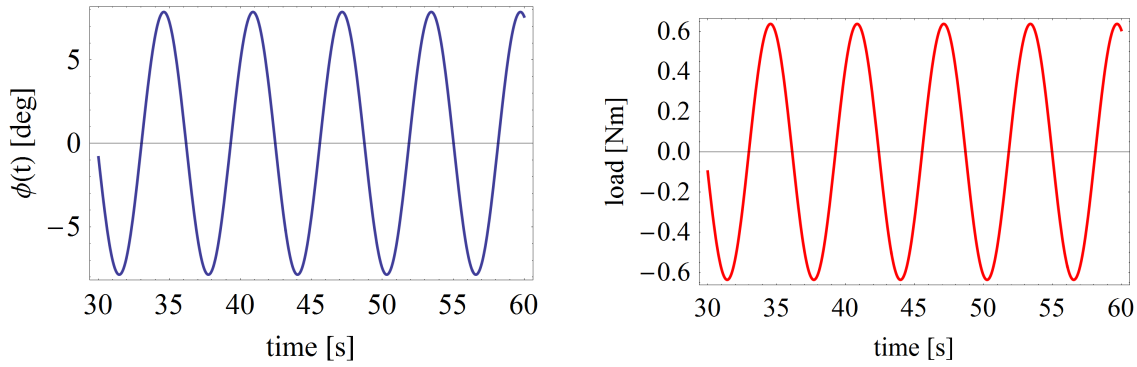


(a) (b)

Figure A.6: Numerical simulation based upon Eq. A.5 (a) pendulum time domain response to (on/on) square wave loading, (b) (on/on) square wave loading profile, where $l = 0.5\text{m}$, $m = 1\text{kg}$, $\xi = 0.1$, $U_0 = 0\text{m}$, $W_0 = 0\text{m}$, $\lambda_0 = 0°$, $\Omega_u = 0\text{rad/s}$, $\Omega_w = 0\text{rad/s}$, $\Omega_\lambda = 0\text{rad/s}$, $T_0 = 0.5\text{Nm}$, $\Omega = 1\text{rad/s}$, $\phi(0) = 0\text{rad}$, $\dot{\phi}(0) = 0\text{rad/s}$ and $30 \leq t \leq 60\text{s}$.

waveform is of the desired form, further numerical simulations will now be performed to properly assess the effectiveness of the loading approach.

## A.2 Simulations Assessing the Performance of the (on/on) Square Wave Loading Approach

For simplicity, the planar pendulum will initially be excited in horizontal translation only. The rational for this is to attempt to introduce as few unknowns as possible into the simulation at first so that the true influence of the derived loading terms may be fully understood. It is also easier to intuitively comprehend the response expected of a pendulum excited this way. Therefore Eq. A.5 may be reduced to:

$$\begin{aligned}\ddot{\phi}(t) + 2\xi\omega_n\dot{\phi}(t) + \frac{g}{l}\sin\phi(t) = {} & \frac{U_0{\Omega_u}^2\cos(\Omega_u t)}{l}\cos\phi(t) \\ & + \frac{1}{ml^2}\left[\frac{T_0}{2} - \frac{2T_0}{\pi}\sin(\Omega t + \alpha)\right] \\ & - \frac{1}{ml^2}\left[\frac{T_0}{2} - \frac{2T_0}{\pi}\sin(\Omega t - \alpha)\right] \end{aligned} \tag{A.6}$$

Simulations based upon this equation reveal some interesting responses. In Fig. A.7 the system is excited by $U_0 = 0.1$m at resonant conditions ($\Omega_u = \omega_n$) which generates the response $\dot{\phi}(t)$. With the introduction of $L_{Fourier}$ it can be seen that this is correctly 90° out of phase with $\dot{\phi}(t)$ and that the response does decrease up to a point as $T_0$ increases. However, when $T_0 > 0.75$Nm there is a phase change in the response such that the load transitions from an energy sink to an energy source resulting in the response increasing again as the load drives the pendulum.

This represents a significant design limitation, but it is to be expected with the current configuration of the load since it is in no way respondent to the response. This can be discerned by the terms themselves. Therefore, if the load is increased to the point that the response approaches zero, $\dot{\phi}(t) \to 0$, there is no facility for feedback to the load and so one may continue to increase $T_0$ and initiate this phase change. For the present it may be considered enough the state that $T_0$ should never exceed the point at which this phase change occurs since the response would be approaching zero

anyway and therefore there would be no energy available for harvesting. This is a weak argument however, and not one to be relied upon.

However, this lack of response dependency gives rise to another fallacy within the current loading approach. Fig. A.7 depicts the response when $\Omega = \Omega_u = \omega_n$, thus the system is being excited at resonance. Because resonant conditions have been achieved, the response and the excitation are in phase with one another and therefore the load is too with a phase shift of 90°. However, if resonance is not achieved or maintained, then the response and excitation move out of phase with one another and so ultimately the performance of the load again breaks down. This is demonstrated in Fig. A.8, where $\Omega = \Omega_u = \frac{4}{5}\omega_n$ which results in the load at times acting as an energy source again.

Further to this, if $\Omega \neq \Omega_u$ then this too renders the effectiveness of the load obsolete. Fig. A.9 shows that when $\Omega_u = \omega_n$ and $\Omega = \frac{4}{5}\Omega_u$ the response becomes erratic, and that at high values of $T_0$ the response becomes primarily driven by the loading terms. One must also consider that matters would become further complicated when the additional excitation terms are included because the frequency of response would be generated by the coupling behaviour between the active excitations and so determining what frequency to set $\Omega$ to would be very difficult and likely time varying. Therefore these observations highlight the requirement for a set of loading terms that are capable of responding to the response of the system directly such that the load always acts as an energy sink and never an energy source. This suggests that the load should not possess a user defined frequency and also be capable of reducing the response of the pendulum to zero (whereby the system would be considered seized). This is the reason and inspiration behind the loading approach developed in Chapter 5 which ultimately proved to be far more effective in applying a resistive torque to the planar pendulum energy harvester.

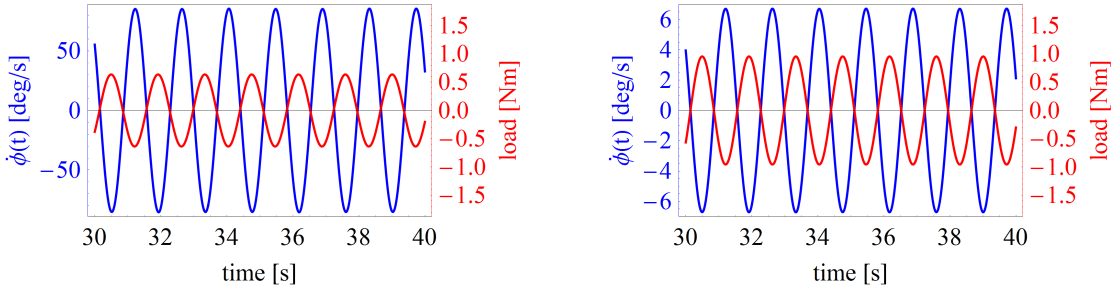


(a) $T_0 = 0.5$Nm.




(b) $T_0 = 0.75$Nm.

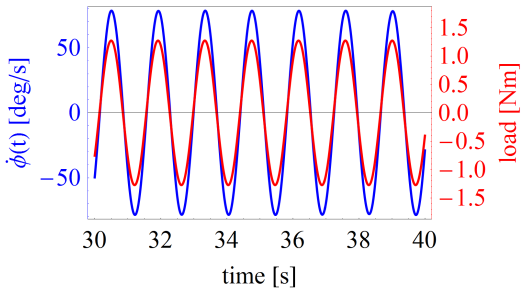


(c) $T_0 = 1.0$Nm.

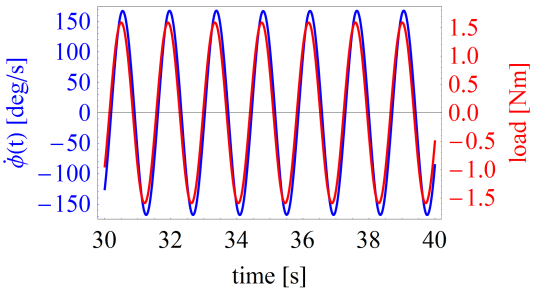


(d) $T_0 = 1.25$Nm.

Figure A.7: $\dot{\phi}(t)$ responses to increasing values of $T_0$ with *Load* superimposed, where $l = 0.5$m, $m = 1$kg, $\xi = 0.1$, $U_0 = 0.1$m, $W_0 = 0$m, $\lambda_0 = 0°$, $\Omega_u = \omega_n$rad/s, $\Omega_w = 0$rad/s, $\Omega_\lambda = 0$rad/s, $\Omega = \Omega_u$rad/s, $\phi(0) = 0$rad, $\dot{\phi}(0) = 0$rad/s and $30 \leq t \leq 40$s.

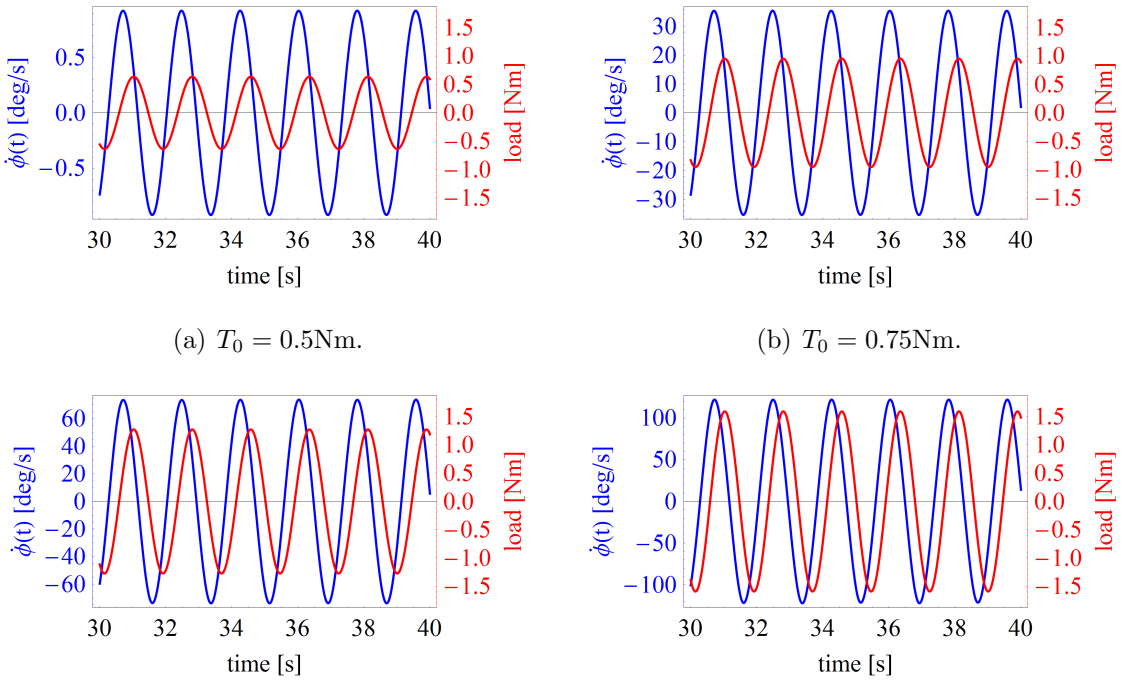


(a) $T_0 = 0.5$Nm.

(b) $T_0 = 0.75$Nm.

(c) $T_0 = 1.0$Nm.

(d) $T_0 = 1.25$Nm.

Figure A.8: $\dot{\phi}(t)$ responses to increasing values of $T_0$ with *Load* superimposed, where $l = 0.5$m, $m = 1$kg, $\xi = 0.1$, $U_0 = 0.1$m, $W_0 = 0$m, $\lambda_0 = 0°$, $\Omega_u = \frac{4}{5}\omega_n$rad/s, $\Omega_w = 0$rad/s, $\Omega_\lambda = 0$rad/s, $\Omega = \Omega_u$rad/s, $\phi(0) = 0$rad, $\dot{\phi}(0) = 0$rad/s and $30 \leq t \leq 40$s.

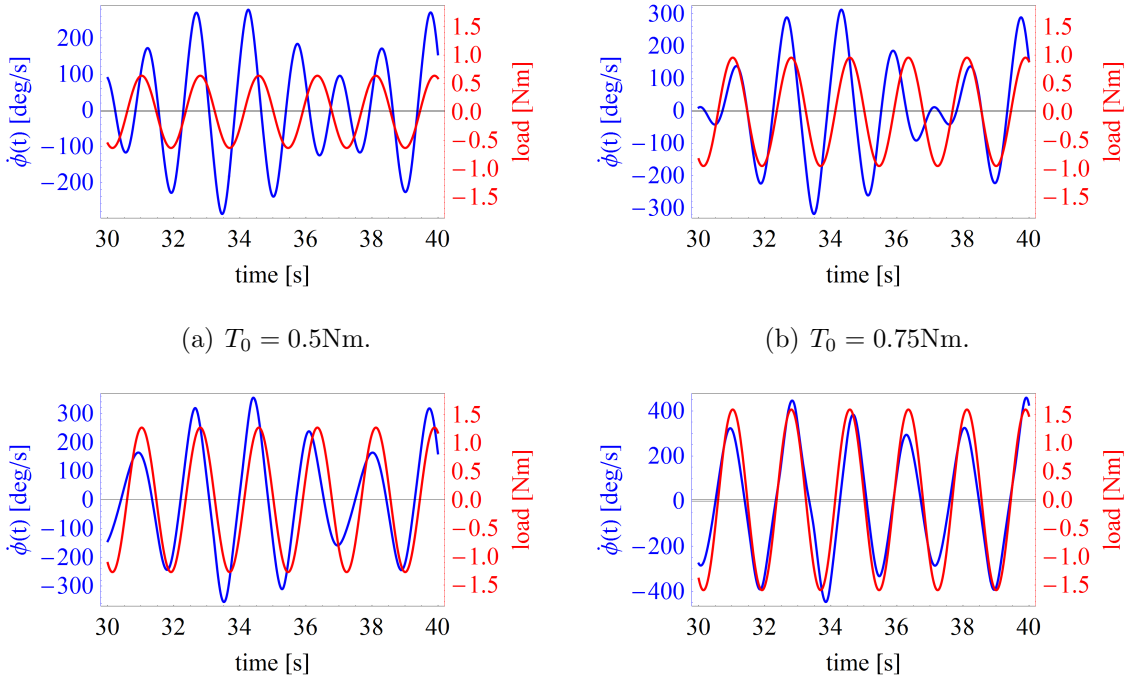


(a) $T_0 = 0.5$Nm.

(b) $T_0 = 0.75$Nm.

(c) $T_0 = 1.0$Nm.

(d) $T_0 = 1.25$Nm.

Figure A.9: $\dot{\phi}(t)$ responses to increasing values of $T_0$ with *Load* superimposed, where $l = 0.5$m, $m = 1$kg, $\xi = 0.1$, $U_0 = 0.1$m, $W_0 = 0$m, $\lambda_0 = 0°$, $\Omega_u = \omega_n$rad/s, $\Omega_w = 0$rad/s, $\Omega_\lambda = 0$rad/s, $\Omega = \frac{4}{5}\Omega_u$rad/s, $\phi(0) = 0$rad, $\dot{\phi}(0) = 0$rad/s and $30 \leq t \leq 40$s.

## A.3 Summarising Remarks for the Square Wave Loading Approaches

A method for representing an externally applied two term Fourier series approximated square wave load has been developed that is capable of modelling model the resistive torque applied to the pendulum system when a suitable power take-off device is used to harvest mechanical accelerations arising from the environment.

First the loading approach developed by Watt and Cartmell (1994) [95] that modelled the loading characteristics of a ratchet and pawl mechanism used to lift a mass was adapted to suit the current application. This comprised of a single set of loading terms derived from a Fourier series approximation to produce an approximated square waveform with a dc offset so that the load resisted motion in one direction only, with the other half cycle for recovery. It was also demonstrated that the square waveform can be better approximated by including more terms from the Fourier series approximation if required. However, given that the present application seeks to harvest the rectified motion of the pendulum, the load terms required modifying to load both directions of swing symmetrically. This led to the development of a modified loading approach that included two sets of the previous terms, but arranged so that their net effect produced a symmetrical load with the desired characteristics.

Initial simulations proved that this approach can successfully load the pendulum in the way expected. However, it was shown that this approach is inherently flawed such that when the response of the system reached zero, the phase between the load and the response could be changed by continuing to increase the magnitude of the load further. The consequence of this is that the load switched from acting as an energy sink to an energy source, thus the response began to rise again. This is not what one would expect in practice where under such conditions the system would normally seize.

Another highlighted fallacy was that the load could not always be maintained in tune with the response of the system. When this occurred then the load would intermittently change between acting as an energy sink, to an energy source. This greatly limits the operating conditions of the loading terms to resonant frequencies alone. Therefore it is proposed that a new robust set of loading terms be developed

that are capable of responding to the response of the system directly in a way that the frequency of the load and response are always matched but 90° out of phase with one another. In this way, full motion of the pendulum could always be harvested even in the event of multiple, or time varying excitation frequencies.

# Appendix B

# Derivation of a Spherical Pendulum

As part of a RenewNet funded feasibility study that was performed by the author in collaboration with industry during the course of this thesis research, the derivation of a spherical pendulum system that could harvest mechanical accelerations out of three directions of translation was performed. Details of this study can be found in Appendix D, but for the purposes of completeness, the derivation process will now be repeated.

Fig.B.1 shows a deflected spherical pendulum with constant length, $l$ and concentrated end mass, $m$ that has been translated by $u$, $v$ and $w$. The two generalised coordinates $\phi$ and $\theta$ represent the two permissible degrees of freedom for the pendulum arm to swing through respectively. Both these generalised coordinates lie on mutually orthogonal planes where the $\phi$ plane is vertical and the $\theta$ plane horizontal. The tangential velocity associated with displacements through $\phi$ is $l\dot{\phi}$, which has a vertical component of $l\dot{\phi}\sin\phi$ and a vertical component of $l\dot{\phi}\cos\phi$.

Whilst the vertical component is clearly vertical with respect to the absolute frame of reference $OXYZ$, the horizontal is not directed along $OX$ because of the coupling with $\theta$. Instead the components lying parallel to $px$ and $py$ of the pendulum body frame, $pxyz$ are taken, $l\dot{\phi}\cos\phi\cos\theta$ and $l\dot{\phi}\cos\phi\sin\theta$ respectively.

Fig.B.1(b) shows the components associated with the tangential velocity $r\dot{\theta}$ where it should be noted that $r$ is shown as $Am$ in Fig.B.1(a), and that this is $l\sin\phi$.

The equations of motion of the spherical pendulum can be obtained using

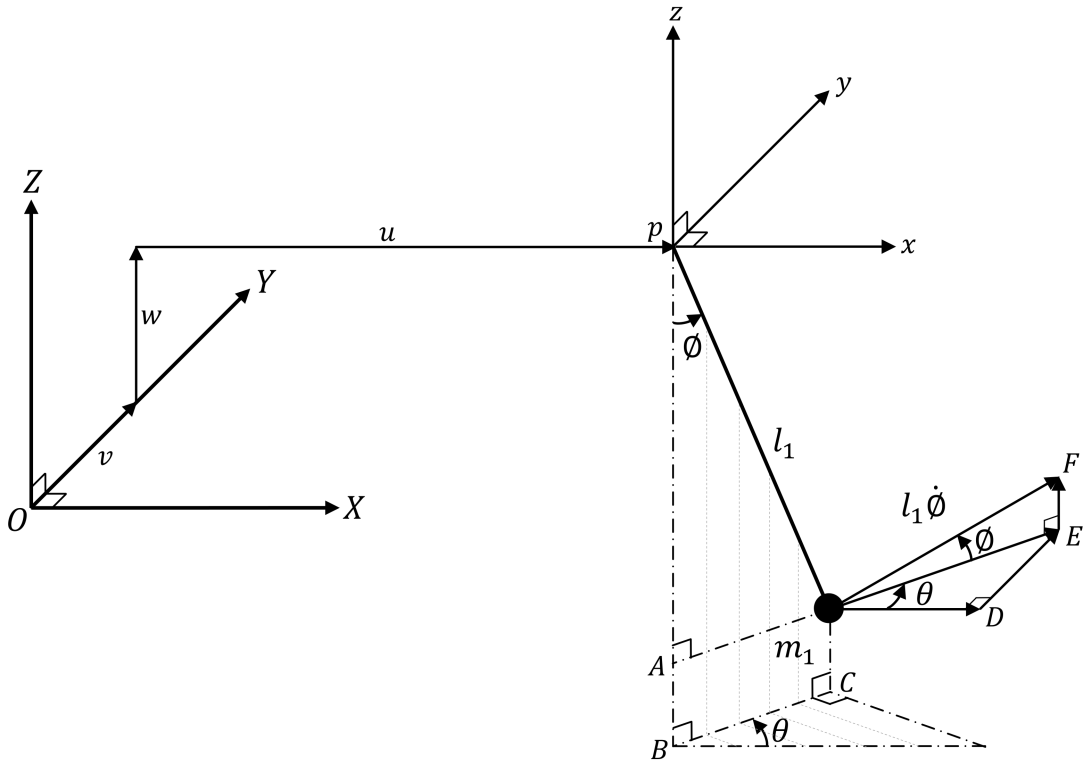


(a)

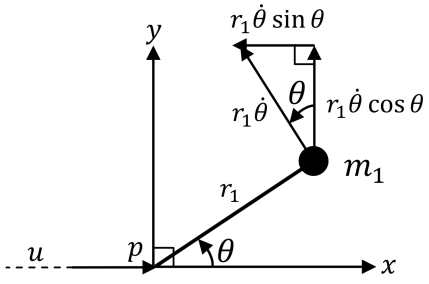


(b)

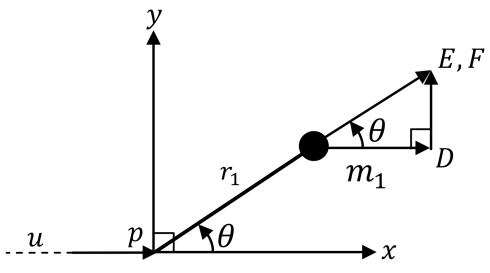


(c)

Figure B.1: Isometric and plan views of a deflected spherical pendulum defining two generalised coordinates as permissible degrees of freedom, $\phi$ and $\theta$.

Lagrange's equations, and as such the kinetic energy of the system is defined by:

$$\begin{aligned} T =& \frac{1}{2}\Big[\Big(\dot{u} - r\dot{\theta}\sin\theta + l\dot{\theta}\cos\theta\cos\phi\Big)^2 + \Big(\dot{v} - r\dot{\theta}\cos\theta + l\dot{\theta}\cos\theta\sin\phi\Big)^2 \\ &+ \Big(\dot{w} + l\dot{\theta}\sin\theta\Big)^2\Big] \end{aligned} \tag{B.1}$$

which after expansion and collection of the terms, the following simplified expression can be reached:

$$\begin{aligned} T =& \frac{1}{2}\Big[\dot{u}^2 + \dot{v}^2 + \dot{w}^2 - 2l\dot{u}\dot{\theta}\sin\theta\sin\phi + 2l\dot{u}\dot{\phi}\cos\theta\cos\phi + l^2\dot{\theta}^2\sin^2\phi + l^2\dot{\phi}^2 \\ &+ 2l\dot{v}\dot{\theta}\cos\theta\sin\phi + 2l\dot{v}\dot{\phi}\sin\theta\cos\phi + 2l\dot{w}\dot{\phi}\sin\phi\Big] \end{aligned} \tag{B.2}$$

The expression for the potential energy in the system is simply:

$$U = mgw + mgl\,(1 - \cos\theta) \tag{B.3}$$

Eq.B.2 and Eq.B.3 are now prepared for insertion into Lagrange's equations by performing the following the necessary differentiations. First the equation of motion describing the motion through $\phi$ will be derived. To do so, the kinetic energy of the system is differentiated with respect to $\dot{\phi}$, such that:

$$\frac{\partial T}{\partial \dot{\phi}} = \frac{1}{2}m\Big[2l\dot{u}\cos\phi\cos\theta + 2l^2\dot{\theta} + 2l\dot{v}\cos\phi\sin\theta + 2l\dot{w}\sin\phi\Big] \tag{B.4}$$

which after differentiating with respect to time becomes:

$$\begin{aligned} \frac{d}{dt}\left(\frac{\partial T}{\partial \dot{\phi}}\right) =& \frac{1}{2}m\Big[2l\ddot{u}\cos\phi\cos\theta - 2l\dot{u}\dot{\phi}\sin\phi\cos\theta - 2l\dot{u}\dot{\theta}\cos\phi\sin\theta + 2l^2\ddot{\phi} \\ &+ 2l\ddot{v}\cos\phi\sin\theta - 2l\dot{v}\dot{\phi}\sin\phi\sin\theta + 2l\dot{v}\dot{\theta}\cos\phi\cos\theta \\ &+ 2l\ddot{w}\sin\phi + 2l\dot{w}\dot{\phi}\cos\phi\Big] \end{aligned} \tag{B.5}$$

Next, differentiating Eq.B.2 with respect to $\phi$:

$$\begin{aligned}\frac{\partial T}{\partial \phi} =& \frac{1}{2}m\Big[-2l\dot{u}\dot{\theta}\sin\theta\cos\phi - 2l\dot{u}\dot{\phi}\cos\theta\sin\phi + 2l^2\dot{\theta}^2\sin\phi\cos\phi \\ &+2l\dot{v}\dot{\theta}\cos\theta\cos\phi - 2l\dot{v}\dot{\phi}\sin\theta\sin\phi + 2l\dot{w}\dot{\phi}\cos\phi\Big]\end{aligned} \tag{B.6}$$

Finally, differentiating the potential energy with respect to $\phi$:

$$\frac{\partial U}{\partial \phi} = mgl\sin\phi \tag{B.7}$$

The above expressions are now ready to be substituted into the appropriate Lagrange's equation for the generalised coordinate in question, which is:

$$\frac{d}{dt}\left(\frac{\partial T}{\partial \dot{\phi}}\right) - \frac{\partial T}{\partial \phi} + \frac{\partial U}{\partial \phi} = Q_\phi \tag{B.8}$$

Therefore, the following equation of motion describing the motion of the system as it swings through $\phi$ can be expressed by:

$$\begin{aligned}&ml^2\ddot{\phi} + c_\phi m\dot{\phi} + mgl\sin\phi - ml^2\left(\sin\phi\cos\phi\right)\dot{\phi}^2 + ml\left(\cos\phi\cos\theta\right)\ddot{u} \\ &+ ml\left(\cos\phi\sin\theta\right)\ddot{v} + ml\sin\phi\ddot{w} = Q_\phi\end{aligned} \tag{B.9}$$

where damping terms, $c_\phi$ have been introduced for a more realistic description.

It remains to repeat the same derivation process with the generalised coordinate $\theta$ as the subject to be inserted into Lagrange's equations. Thus, differentiating Eq.B.2 with respect to $\dot{\theta}$ produces:

$$\frac{\partial T}{\partial \dot{\theta}} = \frac{1}{2}m\Big[-2l\dot{u}\sin\theta\sin\phi + 2l^2\dot{\theta}\sin^2\phi + 2l\dot{v}\cos\theta\sin\phi\Big] \tag{B.10}$$

that after differentiating with respect to time gives:

$$\begin{aligned}\frac{d}{dt}\left(\frac{\partial T}{\partial \dot{\theta}}\right) =& \frac{1}{2}m\Big[-2l\ddot{u}\sin\theta\sin\phi - 2l\dot{u}\dot{\theta}\cos\theta\sin\phi - 2l\dot{u}\dot{\phi}\sin\theta\cos\phi + 2l^2\ddot{\theta}\sin^2\phi \\ &+4l^2\dot{\theta}\dot{\phi}\sin\phi\cos\phi + 2l\ddot{v}\cos\theta\sin\phi - 2l\dot{v}\dot{\theta}\sin\theta\sin\phi \\ &+2l\dot{v}\dot{\phi}\cos\theta\cos\phi\Big] \end{aligned} \tag{B.11}$$

Next, differentiating Eq.B.2 with respect to $\theta$:

$$\begin{aligned}\frac{\partial T}{\partial \theta} =& \frac{1}{2}m\Big[-2l\dot{u}\dot{\theta}\cos\theta\sin\phi - 2l\dot{u}\dot{\phi}\sin\theta\cos\phi - 2l\dot{v}\dot{\theta}\sin\theta\sin\phi \\ &+2l\dot{v}\dot{\phi}\cos\theta\cos\phi\Big] \end{aligned} \tag{B.12}$$

Also, the differential of the potential energy with respect to $\theta$ is equal to:

$$\frac{\partial U}{\partial \theta} = 0 \tag{B.13}$$

Finally, substituting the appropriate terms into the Lagrange's equation describing motion through $\theta$, where:

$$\frac{d}{dt}\left(\frac{\partial T}{\partial \dot{\theta}}\right) - \frac{\partial T}{\partial \theta} + \frac{\partial U}{\partial \theta} = Q_\theta \tag{B.14}$$

produces the following equation of motion:

$$\begin{aligned} &ml^2\sin^2\phi\ddot{\theta} + c_\theta m\dot{\theta} + 2ml^2\left(\sin\phi\cos\phi\right)\dot{\theta}\dot{\phi} - ml\left(\sin\theta\sin\phi\right)\ddot{u} \\ &\quad + ml\left(\cos\theta\sin\phi\right)\ddot{v} = Q_\theta \end{aligned} \tag{B.15}$$

where once more, damping terms, $c_\theta$ have been introduced for a more realistic description.

# Appendix C

# The Suaineadh Experiment

During the course of the thesis research that has been presented, the author was also able to participate in an European Space Agency funded REXUS programme as a member of the Suaineadh experiment. The REXUS (Rocket EXperiments for University Students) programme is an unique opportunity that allows university students from across Europe to fly scientific and technological experiments on sounding rockets powered by an Improved Orion Motor to an altitude of approximately 90km. It was on-board the REXUS-12 rocket that the 'Suaineadh' experiment flew in March 2012.

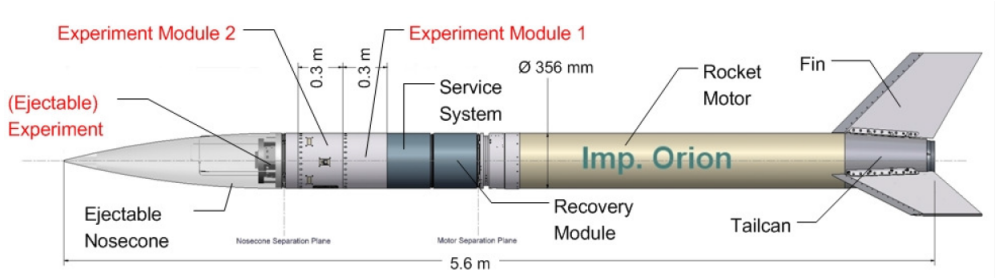


Figure C.1: REXUS standard configuration [104].

Suaineadh, so named for the Gaelic term for 'twisting', was a collaborative project between the University of Glasgow, Strathclyde University and the Royal Institute of Technology in Stockholm. The aim of the project was to design, produce and test the deployment and stabilisation of a space web in a simulated micro-gravity environment by exploiting the centrifugal forces generated by the spinning experiment assembly hub post ejection from the nosecone REXUS-12 at apogee. Control of the web deployment

was to be achieved using active control of an on-board reaction wheel within the hub assembly. Data collected from cameras and inertial measurement units (IMU) was to be transmitted back to the Data Storage Module (DSM) on-board the host REXUS-12 rocket (see Fig.C.1 and C.2) [105–109].

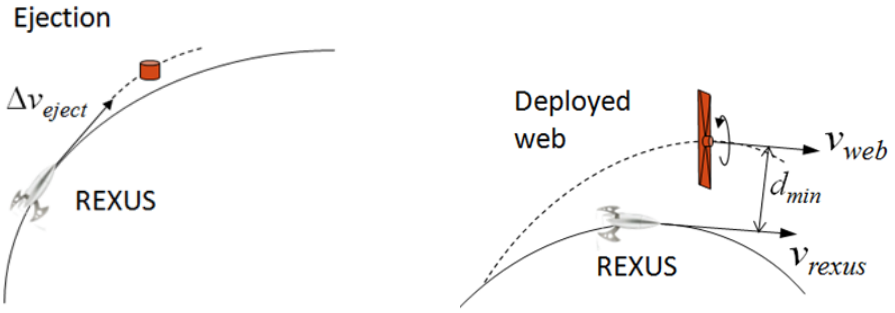


(a) Ejection of experiment from REXUS-12 nosecone.

(b) Deployment and stabilisation of web.

Figure C.2: Conceptual deployment of the Suaineadh experiment from the REXUS nosecone [105].

The main duty of the author within the team was as lead mechanical design engineer and involved the mechanical design of the experiment hardware (shown in Fig.C.3) and coordination of the manufacturing processes, with subsequent environmental testing and validation performed to ESA standards, and also the integration with the electronic architecture fabricated by the other participating universities. This represented a significant workload between December 2010 and March 2012, involving many periods of travel to both ESA and DLR (German Space Agency) facilities across Europe. However, the experiences gained of a real life ESA launch campaign at post graduate level was both unique and invaluable. Beyond just the expansion of engineering skills, it also taught the author a great deal about how to successfully coordinate and manage a multi-national team, to foresee and manage risk, and to deliver a project even under the most demanding circumstances.

Shown in Fig.C.4 is just one of the many rewards from the Suaineadh experiment that shows a selection of the recovered images captured post ejection form REXUS-12, highlighting the curvature of the Earth with the void that is space as a back drop. For more information regarding this project, the reader is referred to a number of publications that were made about the experiment at various stages of development, of which are listed in Appendix D that follows.

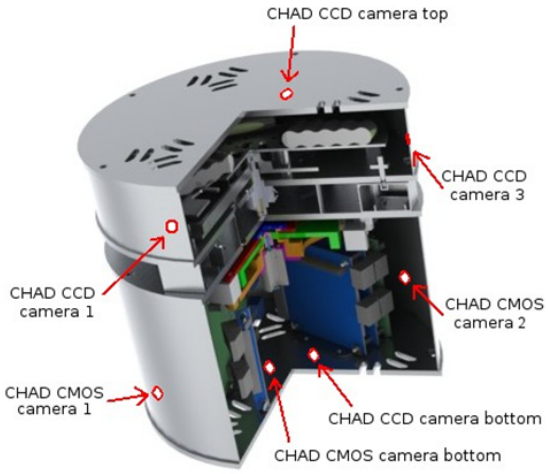


(a) CHAD with sectional cut-out.

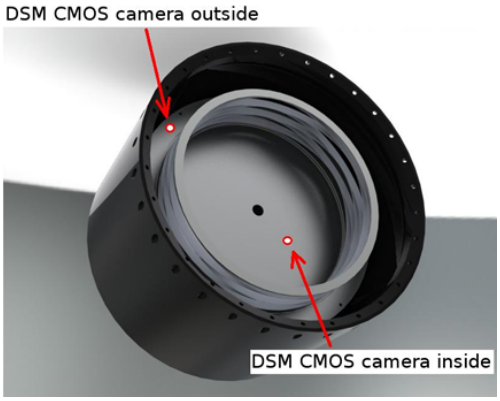


(b) DSM housed within the REXUS-12 nosecone adapter.

Figure C.3: Rendered CAD images of the two sub assemblies of the Suaineadh experiment; Central Hub and Daughter Sections (CHAD), and the Data Storage Module (DSM).

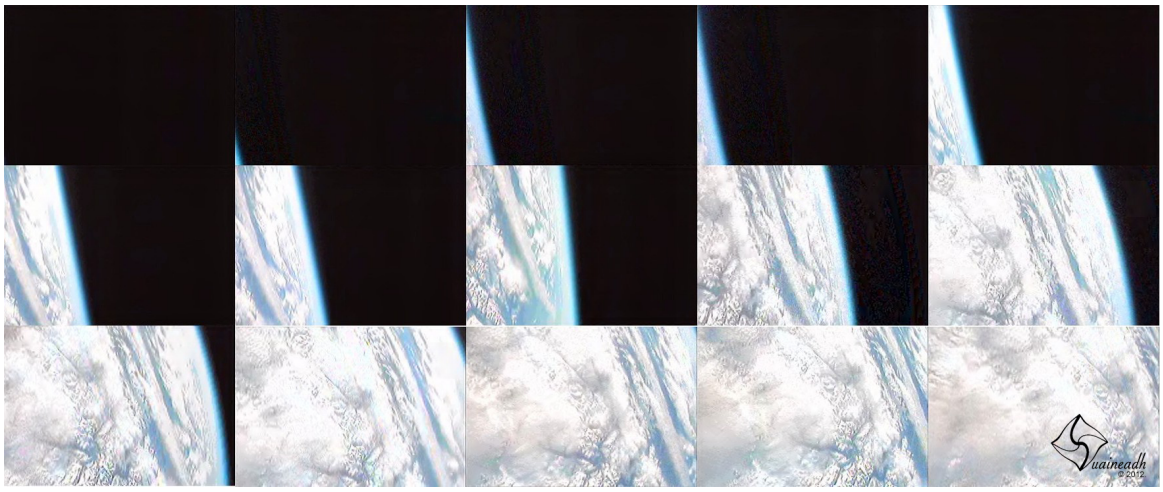

Figure C.4: Images captured by the Suaineadh experiment on the edge of space prior to a loss in wireless communication.

# Appendix D

# List of Publications

- M. McRobb, M. P. Cartmell, C. Cossar, J. Malone, "Feasibility Study of the WITT Power Transmission Device - A Novel Sea-Wave Energy Harvester," *Funding awarded by RenewNet to the University of Glasgow and WITT Energy Solutions Limited*, 2011.
- M. McRobb, M. P. Cartmell, C. Cossar, "TToM Feasibility Report - A study of the dynamics of a pendulum driven WITT transmission," *Funding awarded by TToM to the University of Glasgow and WITT Energy Solutions Limited*, 2012.
- M. Vasile, M. Cartmell, F. Dejene, T. Drysdale, M. Flores, M. Gulzar, N. Ismail, M. Khalid, M. Li, C. Maddock, P. Mallol, A. Mathieson, M. McRobb, J. Berg, P. Reynolds, R. Ritterbusch, W. Sandqvist, L. Summerer, M. Tanveer, G. Tibert, G. Whyte, W. Zafar, and J. Zhang, "The suaineadh project," pp. Paper IAC-10-C3.4, 2010.
- T. Sinn, M. McRobb, A. Wujek, J. Skogby, M. Zhang, M. Vasile, G. Tibert, J. Weppler, A. Feeney, J. Russell, et al., "Rexus 12 suaineadh experiment: deployment of a web in microgravity conditions using centrifugal forces," in *IAC 2011: Proceedings of the 62nd International Astronautical Congress*, pp. IAC-11, 2011.
- T. Sinn, M. McRobb, A. Wujek, J. Skogby, F. Rogberg, J. Wang, M. Vasile, and G. Tibert, "Results of rexus12's suaineadh experiment: Deployment of a spinning space web in micro gravity conditions," in *63rd International Astronautical Congress*, 2012.
- T. Sinn, R. Brown, M. McRobb, A. Wujek, C. Lowe, J. Weppler, T. Parry, D. G. Yarnoz, F. Brownlie, J. Skogby, I. Dolan, T. d. F. Querioz, F. Rogberg, N. Donaldson, R. Clark, and G. Tibert, "Lessons learned from three university experiments onboard the rexus/bexus sounding rockets and stratospheric balloons," in *64th International Astronautical Congress*, 2013.
- T. Sinn, M. McRobb, A. Wujek, J. Skogby, F. Rogberg, J. Wang, M. Vasile, and G. Tibert, "Lessons learned from rexus12s suaineadh experiment: Spinning deployment of a space web in milli gravity," in *21st ESA Symposium on European Rocket and Balloon Programmes and Related Research*, 2013.

# References


[1] S. Roundy, E. Leland, J. Baker, E. Carleton, E. Reilly, E. Lai, B. Otis, J. Rabaey, P. Wright, and V. Sundararajan, "Improving power output for vibration-based energy scavengers," *Pervasive Computing, IEEE*, vol. 4, pp. 28 – 36, jan.-march 2005.

[2] M. Penella and M. Gasulla, "A review of commercial energy harvesters for autonomous sensors," in *Instrumentation and Measurement Technology Conference Proceedings, 2007. IMTC 2007. IEEE*, pp. 1 –5, may 2007.

[3] S. R. Anton and H. A. Sodano, "A review of power harvesting using piezoelectric materials (20032006)," *Smart Materials and Structures*, vol. 16, p. R1, 2007.

[4] H. A. Sodano, D. J. Inman, and G. Park, "A review of power harvesting from vibration using piezoelectric materials," *The Shock and Vibration Digest*, vol. 36, no. 3, pp. 197–205, 2004.

[5] J. Paradiso and T. Starner, "Energy scavenging for mobile and wireless electronics," *Pervasive Computing, IEEE*, vol. 4, pp. 18 – 27, jan.-march 2005.

[6] S. Roundy, P. K. Wright, and J. Rabaey, "A study of low level vibrations as a power source for wireless sensor nodes," *Computer Communications*, vol. 26, no. 11, pp. 1131 – 1144, 2003.

[7] Adnan and Harb, "Energy harvesting: State-of-the-art," *Renewable Energy*, vol. 36, pp. 2641 – 2654, 2011.

[8] *Renewable Energy Projects Handbook*. World Energy Council, 2004.

[9] J. K. Kaldellis and D. Zafirakis, "The wind energy (r)evolution: A short review of a long history," *Renewable Energy*, vol. 36, no. 7, pp. 1887 – 1901, 2011.

[10] B. Drew, A. Plummer, and M. N. Sahinkaya, "A review of wave energy converter technology," *Proceedings of the Institution of Mechanical Engineers Part A Journal of Power and Energy*, vol. 223, no. 8, pp. 887–902, 2009.

[11] R. Baos, F. Manzano-Agugliaro, F. Montoya, C. Gil, A. Alcayde, and J. Gmez, "Optimization methods applied to renewable and sustainable energy: A review," *Renewable and Sustainable Energy Reviews*, vol. 15, no. 4, pp. 1753 – 1766, 2011.

[12] Ibrahim and Dincer, "Renewable energy and sustainable development: a crucial review," *Renewable and Sustainable Energy Reviews*, vol. 4, no. 2, pp. 157 – 175, 2000.

[13] R. Vullers, R. van Schaijk, I. Doms, C. V. Hoof, and R. Mertens, "Micropower energy harvesting," *Solid-State Electronics*, vol. 53, no. 7, pp. 684 – 693, 2009.

[14] G. Nolas, J. Sharp, and H. Goldsmid, *Thermoelectrics: basic principles and new materials developments*. Springer series in materials science, Springer, 2001.

[15] E. Lorenzo, *Solar Electricity: Engineering of Photovoltaic Systems*. PROGENSA, 1994.

[16] C. Solanki, *Solar Photovoltaics : Fundamentals, Technologies and Applications*. PHI Learning, 2011.

[17] A. Luque and S. Hegedus, *Handbook of Photovoltaic Science and Engineering*. John Wiley & Sons, 2011.

[18] M. Green, *Power to the people: sunlight to electricity using solar cells*. University of New South Wales Press, 2000.

[19] S. Thompson, *The Electromagnet and Electromagnetic Mechanism*. Cambridge Library Collection - Technology, Cambridge University Press, 2011.

[20] R. Myers, *The basics of physics*. Basics of the hard sciences, Greenwood Press, 2006.

[21] D. Griffiths, *Introduction to electrodynamics*. Prentice Hall, 1999.

[22] J. Tichỳ, J. Erhart, E. Kittinger, and J. Prívratská, *Fundamentals of Piezoelectric Sensorics: Mechanical, Dielectric, and Thermodynamical Properties of Piezoelectric Materials*. Springer, 2010.

[23] W. Heywang, K. Lubitz, and W. Wersing, *Piezoelectricity: evolution and future of a technology*. Springer series in materials science, Springer, 2008.

[24] R. Hellborg, *Electrostatic accelerators: fundamentals and applications*. Particle acceleration and detection, Springer, 2005.

[25] J. Heilbron, *The Oxford companion to the history of modern science*. Oxford Companions Series, Oxford University Press, 2003.

[26] D. Rowe, *CRC handbook of thermoelectrics*. CRC Press, 1995.

[27] S. Riffat and X. Ma, "Thermoelectrics: a review of present and potential applications," *Applied Thermal Engineering*, vol. 23, no. 8, pp. 913 – 935, 2003.

[28] D. Rowe, *Thermoelectrics handbook: macro to nano*. CRC/Taylor & Francis, 2006.

[29] D. Rowe and G. Min, "Design theory of thermoelectric modules for electrical power generation," *Science, Measurement and Technology, IEE Proceedings* -, vol. 143, pp. 351 –356, nov 1996.

[30] D. Rowe and G. Min, "Evaluation of thermoelectric modules for power generation," *Journal of Power Sources*, vol. 73, no. 2, pp. 193 – 198, 1998.

[31] D.M. and Rowe, "Thermoelectrics, an environmentally-friendly source of electrical power," *Renewable Energy*, vol. 16, no. 14, pp. 1251 – 1256, 1999.

[32] E. F. Thacher, B. T. Helenbrook, M. A. Karri, and C. J. Richter, "Testing of an automobile exhaust thermoelectric generator in a light truck," *Proceedings of the Institution of Mechanical Engineers, Part D: Journal of Automobile Engineering*, vol. 221, no. 1, pp. 95–107, 2007.

[33] J. Yang, "Potential applications of thermoelectric waste heat recovery in the automotive industry," in *Thermoelectrics, 2005. ICT 2005. 24th International Conference on*, pp. 170–174, 2005.

[34] M. Karri, E. Thacher, and B. Helenbrook, "Exhaust energy conversion by thermoelectric generator: Two case studies," *Energy Conversion and Management*, vol. 52, no. 3, pp. 1596 – 1611, 2011.

[35] J. H. Panya Yodovard, Joseph Khedari, "The potential of waste heat thermoelectric power generation from diesel cycle and gas turbine cogeneration plants," *Energy Sources*, vol. 23, no. 3, pp. 213–224, 2001.

[36] S. Chalasani and J. Conrad, "A survey of energy harvesting sources for embedded systems," in *Southeastcon, 2008. IEEE*, pp. 442–447, 2008.

[37] Y. Liang and L. Yu, "Development of semiconducting polymers for solar energy harvesting," *Polymer Reviews*, vol. 50, no. 4, pp. 454–473, 2010.

[38] S. E. International, *Photovoltaics: Design and Installation Manual : Renewable Energy Education for a Sustainable Future*. New Society Publishers, 2004.

[39] L. Mateu and F. Moll, "Review of energy harvesting techniques and applications for microelectronics," in *Proc. SPIE*, vol. 5837, pp. 359–373, 2005.

[40] J. Kimball, B. Kuhn, and R. Balog, "A system design approach for unattended solar energy harvesting supply," *Power Electronics, IEEE Transactions on*, vol. 24, no. 4, pp. 952–962, 2009.

[41] R. Foster, M. Ghassemi, and A. Cota, *Solar Energy: Renewable Energy and the Environment*. Energy and the Environment, Taylor & Francis, 2009.

[42] J. Gordon and I. S. E. Society, *Solar Energy: The State of the Art : ISES Position Papers*. ISES position papers, James & James, 2001.

[43] M. Grätzel, "Photoelectrochemical cells," *Nature*, vol. 414, no. 6861, pp. 338–344, 2001.

[44] M. Boxwell, *Solar Electricity Handbook: A Simple, Practical Guide to Solar Energy : how to Design and Install Photovoltaic Solar Electric Systems*. Greenstream Publishing, 2012.

[45] L. E. Chaar, L. lamont, and N. E. Zein, "Review of photovoltaic technologies," *Renewable and Sustainable Energy Reviews*, vol. 15, no. 5, pp. 2165 – 2175, 2011.

[46] B. Parida, S. Iniyan, and R. Goic, "A review of solar photovoltaic technologies," *Renewable and Sustainable Energy Reviews*, vol. 15, no. 3, pp. 1625 – 1636, 2011.

[47] A. Barnett, J. Rand, R. Hall, J. Bisaillon, E. Delledonne, B. Feyock, D. Ford, A. Ingram, M. Mauk, J. Yaskoff, and P. Sims, "High current, thin silicon-on-ceramic solar cell," *Solar Energy Materials and Solar Cells*, vol. 66, no. 1-4, pp. 45–50, 2001. cited By (since 1996)9.

[48] A. McEvoy, L. Castañer, and T. Markvart, *Solar Cells: Materials, Manufacture and Operation*. Elsevier, 2012.

[49] T. Razykov, C. Ferekides, D. Morel, E. Stefanakos, H. Ullal, and H. Upadhyaya, "Solar photovoltaic electricity: Current status and future prospects," *Solar Energy*, vol. 85, no. 8, pp. 1580 – 1608, 2011. ¡ce:title¿Progress in Solar Energy 1¡/ce:title¿.

[50] M. E. Meral and F. Diner, "A review of the factors affecting operation and efficiency of photovoltaic based electricity generation systems," *Renewable and Sustainable Energy Reviews*, vol. 15, no. 5, pp. 2176 – 2184, 2011.

[51] E. Serrano, G. Rus, and J. Garca-Martnez, "Nanotechnology for sustainable energy," *Renewable and Sustainable Energy Reviews*, vol. 13, no. 9, pp. 2373 – 2384, 2009.

[52] N. Stephen, "On energy harvesting from ambient vibration," 2006.

[53] D. Puccinelli and M. Haenggi, "Wireless sensor networks: applications and challenges of ubiquitous sensing," *Circuits and Systems Magazine, IEEE*, vol. 5, no. 3, pp. 19 – 31, 2005.

[54] S. Roundy, P. Wright, and J. Rabaey, *Energy scavenging for wireless sensor networks: with special focus on vibrations*. Kluwer Academic Publishers, 2004.

[55] C. Williams and R. Yates, "Analysis of a micro-electric generator for microsystems," *Sensors and Actuators A: Physical*, vol. 52, no. 13, pp. 8 – 11, 1996.

[56] S. Beeby, M. Tudor, and N. White, "Energy harvesting vibration sources for microsystems applications," *Measurement Science and Technology*, vol. 17, no. 12, pp. R175–R195, 2006.

[57] N. Dutoit and B. Wardle, "Experimental verification of models for microfabricated piezoelectric vibration energy harvesters," *AIAA Journal*, vol. 45, pp. 1126–1137, May 2007.

[58] J. M. Renno, M. F. Daqaq, and D. J. Inman, "On the optimal energy harvesting from a vibration source," *Journal of Sound and Vibration*, vol. 320, no. 12, pp. 386 – 405, 2009.

[59] C. Eichhorn, R. Tchagsim, N. Wilhelm, and P. Woias, "A smart and self-sufficient frequency tunable vibration energy harvester," *Journal of Micromechanics and Microengineering*, vol. 21, no. 10, p. 104003, 2011.

[60] M. Lallart, S. R. Anton, and D. J. Inman, "Frequency self-tuning scheme for broadband vibration energy harvesting," *Journal of Intelligent Material Systems and Structures*, vol. 21, no. 9, pp. 897–906, 2010.

[61] S. Roundy and Y. Zhang, "Toward self-tuning adaptive vibration-based microgenerators," vol. 5649, pp. 373–384, SPIE, 2005.

[62] D. Zhu, M. J. Tudor, and S. P. Beeby, "Strategies for increasing the operating frequency range of vibration energy harvesters: a review," *Measurement Science and Technology*, vol. 21, no. 2, p. 022001, 2010.

[63] S. G. Adams, F. M. Bertsch, K. A. Shaw, P. G. Hartwell, F. C. Moon, and N. C. MacDonald, "Capacitance based tunable resonators," *Journal of Micromechanics and Microengineering*, vol. 8, p. 15, 1998.

[64] B.-S. L. J.-J. H. Y.-T. P. Wen-Jong Wu, Yu-Yin Chen, "Tunable resonant frequency power harvesting devices," *Smart Structures and Materials 2006: Damping and Isolation*, vol. 6169, pp. 55–62, 2006.

[65] H. Pain, *The physics of vibrations and waves*. John Wiley, 2005.

[66] E. S. Leland and P. K. Wright, "Resonance tuning of piezoelectric vibration energy scavenging generators using compressive axial preload," *Smart Materials and Structures*, vol. 15, no. 5, p. 1413, 2006.

[67] Y. Hu, H. Xue, and H. Hu, "A piezoelectric power harvester with adjustable frequency through axial preloads," *Smart Materials and Structures*, vol. 16, no. 5, p. 1961, 2007.

[68] D. Zhu, S. Roberts, M. J. Tudor, and S. P. Beeby, "Design and experimental characterization of a tunable vibration-based electromagnetic micro-generator," *Sensors and Actuators A: Physical*, vol. 158, no. 2, pp. 284 – 293, 2010.

[69] R. Masana and M. F. Daqaq, "Electromechanical modeling and nonlinear analysis of axially loaded energy harvesters," *Journal of Vibration and Acoustics*, vol. 133, no. 1, p. 011007, 2011.

[70] V. R. Challa, M. G. Prasad, Y. Shi, and F. T. Fisher, "A vibration energy harvesting device with bidirectional resonance frequency tunability," *Smart Materials and Structures*, vol. 17, no. 1, p. 015035, 2008.

[71] V. R. Challa, M. G. Prasad, and F. T. Fisher, "Towards an autonomous self-tuning vibration energy harvesting device for wireless sensor network applications," *Smart Materials and Structures*, vol. 20, no. 2, p. 025004, 2011.

[72] I. Sari, T. Balkan, and H. Kulah, "An electromagnetic micro power generator for wideband environmental vibrations," *Sensors and Actuators A: Physical*, vol. 145146, no. 0, pp. 405 – 413, 2008.

[73] S. C. Stanton, C. C. McGehee, and B. P. Mann, "Nonlinear dynamics for broadband energy harvesting: Investigation of a bistable piezoelectric inertial generator," *Physica D: Nonlinear Phenomena*, vol. 239, no. 10, pp. 640–653, 2010.

[74] B. Mann and B. Owens, "Investigations of a nonlinear energy harvester with a bistable potential well," *Journal of Sound and Vibration*, vol. 329, no. 9, pp. 1215 – 1226, 2010.

[75] M. F. and Daqaq, "Transduction of a bistable inductive generator driven by white and exponentially correlated gaussian noise," *Journal of Sound and Vibration*, vol. 330, no. 11, pp. 2554 – 2564, 2011.

[76] B. Mann and N. Sims, "Energy harvesting from the nonlinear oscillations of magnetic levitation," *Journal of Sound and Vibration*, vol. 319, no. 12, pp. 515 – 530, 2009.

[77] M. Ferrari, V. Ferrari, M. Guizzetti, B. And, S. Baglio, and C. Trigona, "Improved energy harvesting from wideband vibrations by nonlinear piezoelectric converters," *Sensors and Actuators A: Physical*, vol. 162, no. 2, pp. 425 – 431, 2010.

[78] T.-W. Ma, H. Zhang, and N.-S. Xu, "A novel parametrically excited non-linear energy harvester," *Mechanical Systems and Signal Processing*, vol. 28, no. 0, pp. 323 – 332, 2012.

[79] M. F. and Daqaq, "Response of uni-modal duffing-type harvesters to random forced excitations," *Journal of Sound and Vibration*, vol. 329, no. 18, pp. 3621 – 3631, 2010.

[80] A. Nayfeh and D. Mook, *Nonlinear Oscillations*. Physics textbook, John Wiley & Sons, 2008.

[81] S. G. Burrow, L. R. Clare, A. Carrella, and D. Barton, "Vibration energy harvesters with non-linear compliance," in *Society of Photo-Optical Instrumentation Engineers (SPIE) Conference Series*, vol. 6928 of *Society of Photo-Optical Instrumentation Engineers (SPIE) Conference Series*, May 2008.

[82] S. C. Stanton, C. C. McGehee, and B. P. Mann, "Reversible hysteresis for broadband magnetopiezoelastic energy harvesting," *Applied Physics Letters*, vol. 95, pp. 174103 –174103–3, oct 2009.

[83] R. Ramlan, M. Brennan, B. Mace, and I. Kovacic, "Potential benefits of a non-linear stiffness in an energy harvesting device," *Nonlinear Dynamics*, vol. 59, pp. 545–558, 2010.

[84] D. A. W. Barton, S. G. Burrow, and L. R. Clare, "Energy harvesting from vibrations with a nonlinear oscillator," *Journal of Vibration and Acoustics*, vol. 132, p. 021009, 2010.

[85] F. Lim, M. Cartmell, A. Cardoni, and M. Lucas, "A preliminary investigation into optimising the response of vibrating systems used for ultrasonic cutting," *Journal of Sound and Vibration*, vol. 272, no. 35, pp. 1047 – 1069, 2004.

[86] R. Masana and M. F. Daqaq, "Relative performance of a vibratory energy harvester in mono- and bi-stable potentials," *Journal of Sound and Vibration*, vol. 330, no. 24, pp. 6036 – 6052, 2011.

[87] M. Ferrari, M. Ba, M. Guizzetti, and V. Ferrari, "A single-magnet nonlinear piezoelectric converter for enhanced energy harvesting from random vibrations," *Sensors and Actuators A: Physical*, vol. 172, no. 1, pp. 287 – 292, 2011.

[88] B. Mann and B. Owens, "Investigations of a nonlinear energy harvester with a bistable potential well," *Journal of Sound and Vibration*, vol. 329, no. 9, pp. 1215 – 1226, 2010.

[89] L. Gammaitoni, P. Hänggi, P. Jung, and F. Marchesoni, "Stochastic resonance," *Rev. Mod. Phys.*, vol. 70, pp. 223–287, 1998.

[90] C. McInnes, D. Gorman, and M. Cartmell, "Enhanced vibrational energy harvesting using nonlinear stochastic resonance," *Journal of Sound and Vibration*, vol. 318, pp. 655 – 662, 2008.

[91] X. Wu, Z.-P. Jiang, D. Repperger, and Y. Guo, "Nonlinear enhancement of weak signals using optimization theory," in *Mechatronics and Automation, Proceedings of the 2006 IEEE International Conference on*, pp. 66 –71, june 2006.

[92] T. Wellens, V. Shatokhin, and A. Buchleitner, "Stochastic resonance," *Reports on Progress in Physics*, vol. 67, no. 1, p. 45, 2004.

[93] N. I.-V. H. Gammaitoni, L., "Nonlinear oscillators for vibration energy harvesting," *Applied Physics Letters*, vol. 94, no. 16, 2009.

[94] V. H.-G. L. Cottone, F., "Nonlinear energy harvesting," *Physical Review Letters*, vol. 102, no. 8, 2009.

[95] D. Watt and M. Cartmell, "An externally loaded parametric oscillator," *Journal of Sound and Vibration*, vol. 170, no. 3, pp. 339 – 364, 1994.

[96] A. M. Abou-Rayan, A. H. Nayfeh, D. T. Mook, and M. A. Nayfeh, "Nonlinear response of a parametrically excited buckled beam," *Nonlinear Dynamics*, vol. 4, pp. 499–525, 1993. 10.1007/BF00053693.

[97] C. Cartmell, *Introduction to Linear, Parametric and Non-Linear Vibrations*. Springer, 1990.

[98] A. Erturk and D. J. Inman, "An experimentally validated bimorph cantilever model for piezoelectric energy harvesting from base excitations," *Smart Materials and Structures*, vol. 18, no. 2, p. 025009, 2009.

[99] L. Mateu and F. Moll, "Optimum piezoelectric bending beam structures for energy harvesting using shoe inserts," *Journal of Intelligent Material Systems and Structures*, vol. 16, no. 10, pp. 835–845, 2005.

[100] H. A. Sodano, G. Park, and D. J. Inman, "Estimation of electric charge output for piezoelectric energy harvesting," *Strain*, vol. 40, no. 2, pp. 49–58, 2004.

[101] F. Goldschmidtboeing and P. Woias, "Characterization of different beam shapes for piezoelectric energy harvesting," *Journal of Micromechanics and Microengineering*, vol. 18, no. 10, p. 104013, 2008.

[102] E. Lefeuvre, A. Badel, C. Richard, and D. Guyomar, "Piezoelectric energy harvesting device optimization by synchronous electric charge extraction," *Journal of Intelligent Material Systems and Structures*, vol. 16, no. 10, pp. 865–876, 2005.

[103] H. A. Sodano, D. J. Inman, and G. Park, "Generation and storage of electricity from power harvesting devices," *Journal of Intelligent Material Systems and Structures*, vol. 16, no. 1, pp. 67–75, 2005.

[104] EuroLaunch, *REXUS User Manual*, v7.7 ed., September 2012.

[105] M. Vasile, M. Cartmell, F. Dejene, T. Drysdale, M. Flores, M. Gulzar, N. Ismail, M. Khalid, M. Li, C. Maddock, P. Mallol, A. Mathieson, M. McRobb, J. berg, P. Reynolds, R. Ritterbusch, W. Sandqvist, L. Summerer, M. Tanveer, G. Tibert, G. Whyte, W. Zafar, and J. Zhang, "The suaineadh project," pp. Paper IAC–10–C3.4, 2010.

[106] T. Sinn, M. McRobb, A. Wujek, J. Skogby, M. Zhang, M. Vasile, G. Tibert, J. Weppler, A. Feeney, J. Russell, *et al.*, "Rexus 12 suaineadh experiment: deployment of a web in microgravity conditions using centrifugal forces," in *IAC 2011: Proceedings of the 62nd International Astronautical Congress*, pp. IAC–11, 2011.

[107] T. Sinn, M. McRobb, A. Wujek, J. Skogby, F. Rogberg, J. Wang, M. Vasile, and G. Tibert, "Results of rexus12's suaineadh experiment: Deployment of a spinning space web in micro gravity conditions," in *63rd International Astronautical Congress*, 2012.

[108] T. Sinn, M. McRobb, A. Wujek, J. Skogby, F. Rogberg, J. Wang, M. Vasile, and G. Tibert, "Lessons learned from rexus12s suaineadh experiment: Spinning deployment of a space web in milli gravity," in *21st ESA Symposium on European Rocket and Balloon Programmes and Related Research*, 2013.

[109] T. Sinn, R. Brown, M. McRobb, A. Wujek, C. Lowe, J. Weppler, T. Parry, D. G. Yarnoz, F. Brownlie, J. Skogby, I. Dolan, T. d. F. Querioz, F. Rogberg, N. Donaldson, R. Clark, and G. Tibert, "Lessons learned from three university experiments onboard the rexus/bexus sounding rockets and stratospheric balloons," in *64th International Astronautical Congress*, 2013.

[This page is intentionally blank]